



**Materials processing and physical
characterisation of a hybrid composite structure
for bone replacement applications**

A thesis submitted to the Faculty of Science,
Agriculture and Engineering for the Degree of
Doctor of Philosophy

by

Natacha Rodrigues

School of Mechanical and Systems Engineering
Newcastle University

August 2018

Abstract

The development of scaffold-based solutions for large bone defect repair has the potential to overcome the limited efficacy of conventional bone grafting strategies. A promising approach that contemplates the complex bone architecture consists in the development of hybrid scaffolds, composed of distinct but integrated layers able to mimic the different bone regions. The aim of the research presented in this thesis was integrated in the MeDe (Medical Devices innovation) research challenges focused on fabricating a hybrid biopolymer-bioceramic composite structure for mimicking the complex bone-tissue organisation repair, and on developing the manufacturing process required to make them.

The developed manufacturing process consisted in three steps: 1) pre-fabrication of a macroporous polylactic acid (PLA) structure and a microporous apatite wollastonite glass-ceramic (AW) structure, 2) assembly of the pre-fabricated parts to obtain a hybrid PLA-AW composite structure and 3) characterisation of obtained composite interface properties.

A novel two-step fabrication route: 1) 3D printing of a porous bar and 2) laser cutting smaller scaffolds from the 3D printed bar) was developed for creating PLA porous structures with well-defined and open architectures. No decrease in mechanical properties and mass were observed over a 10 weeks' immersion study in PBS, indicating suitability as a trabecular bone analogue.

Concerning the AW porous structure fabrication, the impact of powder blend formulation on the indirect three-dimensional printing route was investigated. Bimodal mixtures with appropriate AW large-small particle ratios (45% large and 25% small) and average particle size values in the 37-61 μ m range resulted in the best printability outcome. Sinterability was mainly affected by the AW powder production route and, to a lesser degree, by particle size distribution and choice of sintering protocol.

Finally, a hybrid PLA-AW composite structure was fabricated through physical interlocking, created by the PLA locally melting and infiltrating into the AW structure. The high interfacial shear strength values obtained in this study (0.5 to 2.5 MPa) indicated that physical bonding might be considered a promising way to avoid delamination in bi-layered scaffold systems. The novel manufacturing route developed in this work has the potential to offer an alternative route to the fabrication of bioactive bone implants which can provide a match to both cortical and trabecular bone properties.

Acknowledgments

Apart from my efforts, the success of this project largely depended on the support and guidelines of many others. In the following lines, I would like to express my gratitude to the people who have powerfully contributed to the successful accomplishment of my postgraduate study.

My deepest and sincere gratitude goes to all my supervisors, Kenny Dalgarno, Mathew Benning and Javier Munguia, for their remarkable supervision, utmost patience, encouragement and continuous support. Overall, they have provided me with both academic and personal guidance throughout the years, and his work and insight were critical towards the goal achievements of this project.

I would like to express my enormous gratitude towards the technical staff for their constant support, assistance and for making me feel welcome at the School of Mechanical and Systems Engineering. It was a pleasure and I am grateful that I had the opportunity to learn out from their experiences and knowledge. I extend my sincere thankfulness to all my colleagues and friends that I made through the years in the laboratory, for their fellowship and endless support. Particularly, Ana Marina Duarte and Piergiorgio Gentile, I will always cherish your valuable advices and the full support you gave me through this research project. Priscila Melo you were the best help that one PhD in the last year can wish for, with your never ending energy and willingness to run the characterisation of AW powders. A great deal of thanks to Cristina Tuinea-Bobe from University of Braford for taking the time to assist and advise me with the ultrasonic welding process, as well as her know-how that always come with kindness and contagious good mood. Chiara Vitale Brovarone and Francesco Baino from Politecnico Di Torino for their contribution in performing the amazing three dimensional characterisation of my scaffolds. As well, to EPSRC Centre for Innovative Manufacture in Medical Devices (MEDE) for the opportunity of developing such an innovative research work. Without the help, expertise and funding from the centre, this project would not be possible.

Finally, I thank my beloved family and friends for their unconditional support throughout this journey. This thesis would not have been possible without the love, eternal encouragement and strength, that kept me going forward and to never give up. Special thanks to my mother and father, that despite being far, they were always there when I needed. You both have encouraged me in a remarkable way all through this far-reaching period. I would like to thank my twin-sister for listening to my constant woes, and for putting up with my grumpiness and endless support to the point that this achievement would not be possible without her.

Table of Contents

Abstract	iii
Acknowledgments	v
Table of Contents.....	vii
List of Figures	xii
List of Tables	xx
List of Abbreviations	xxii
CHAPTER 1. Introduction.....	1
1.1. Background.....	1
1.2. Literature Review	3
1.2.1. Bone anatomy and properties	3
1.2.2. Bone healing clinical approaches	4
1.2.3. Bone Scaffolds.....	5
1.2.4. Multi-layered scaffolds.....	14
1.2.5. Additive Manufacturing (AM)	18
1.2.6. Ultrasonic welding.....	26
1.3. Aim and Objectives	28
1.4. Thesis outline.....	29
CHAPTER 2. Materials and Methods.....	30
2.1. Materials Choice Rationale	30
2.2. Materials	32
2.2.1. Polylactic acid (PLA)	32
2.2.2. Apatite-wollastonite (AW)	32
2.2.3. Maltodextrin (MD)	32
2.2.4. Zb®60 binder	32
2.3. Material Processing	32
2.3.1. PLA.....	32
2.3.1.1. Fused Filament Fabrication (FFF) Process.....	32
2.3.1.2. Laser cutting	35
2.3.2. AW and MD	35
2.3.2.1. Milling and sieving.....	35
2.3.2.2. Roller mixing.....	36

2.3.2.3. Vacuum drying.....	36
2.3.2.4. 3DP Process	37
2.3.2.5. Post-Processing	38
2.3.3. PLA-AW Composite Structures Assembly.....	39
2.3.3.1. Thermal Bonding	39
2.3.3.2. Ultrasonic Welding	40
2.4. Materials Characterisation	40
2.4.1. AW and MD.....	40
2.4.1.1. X-ray Fluorescence (XRF).....	41
2.4.1.2. X-ray photoelectron spectroscopy (XPS)	41
2.4.1.3. Differential Scanning Calorimetry (DSC)	41
2.4.1.4. Hot stage microscopy (HSM)	42
2.4.1.5. Particle size distribution (PSD).....	42
2.4.1.6. Scanning Electron Microscope (SEM)	43
2.4.1.7. X-ray diffraction (XRD)	43
2.4.2. PLA	44
2.4.2.1. Differential Scanning Calorimetry (DSC)	44
2.4.2.2. Gel Permeation Chromatography (GPC)	45
2.4.2.3. Micro Computed tomography (CT)	46
2.4.2.4. Scanning Electron Microscope (SEM)	46
2.4.3. PLA-AW Composite Structures.....	46
2.4.3.1. Interface Morphology	46
2.4.3.2. Interfacial Shear Testing	46
2.5. Statistical analysis	48
CHAPTER 3. Manufacture and Characterisation of PLA Porous Structure.....	49
3.1. Introduction.....	49
3.2. Scaffold fabrication.....	50
3.2.1. Fabrication Route Parameters	50
3.2.2. Material Characterisation.....	51
3.3. Preliminary study: FFF Processing Parameters Investigation	51
3.3.1. Morphology study	52
3.3.2. Tensile testing	53
3.4. Scaffolds Morphological and Mechanical Testing	54
3.4.1. Morphology.....	54

3.4.2. Mechanical Testing.....	55
3.5. In Vitro Degradation Study	55
3.6. Results: Preliminary FFF study	56
3.6.1. Morphology	56
3.6.2. Tensile Testing	59
3.7. Results: Scaffolds Fabrication	60
3.8. Results: Material Characterisation	61
3.9. Results: Morphological and Mechanical Behaviour of PLA scaffold.....	61
3.9.1. Morphology	61
3.9.2. Mechanical properties.....	62
3.10. Results: In vitro Degradation Study	64
3.11. Discussion.....	70
3.11.1. Preliminary study: FFF Processing Parameters Investigation.....	70
3.11.2. PLA scaffold fabrication and characterisation	72
3.11.3. In Vitro Degradation Behaviour	73
3.12. Conclusions	75
<u>CHAPTER 4. Design and characterisation of a 3DP AW structure</u>	<u>77</u>
4.1. Introduction	77
4.2. Materials Processing Route	77
4.2.1. Starting materials processing and characterisation.....	77
4.2.2. Indirect 3DP.....	78
4.2.2.1. Powder Blends Preparation	78
4.2.2.2. 3DP: Powder Blends Printability study.....	79
4.2.2.3. Post-processing: Powder Blends Sinterability Study	79
4.2.2.4. De-binding studies.....	80
4.3. Powder Blends Rationale	80
4.4. Results: Starting Materials Characterisation after Processing.....	81
4.4.1. Morphological (SEM) and Particle size distribution (PSD).....	81
4.4.2. Bulk Chemical characterisation (XRF)	83
4.4.3. Surface Chemical characterisation (XPS)	83
4.4.4. Crystallinity (XRD)	84
4.4.5. Thermal characterisation (DSC).....	85
4.4.6. Hot stage microscopy (HSM)	87
4.5. Results: Indirect 3DP	89

4.5.1. Powder Blends Characterisation	89
4.5.1.1. SEM and PSD	89
4.5.2. 3DP: Powder Blends Printability Study.....	91
4.5.3. Post-Processing: Powder Blends Sinterability Study.....	94
4.5.3.1. Sinterability study	94
4.5.4. De-binding studies	99
4.6. Discussion	101
4.6.1. Comparison with Previous Work.....	101
4.6.2. Processability of different powder blends formulations	103
4.6.2.1 Printability study	103
4.6.2.2. Sinterability Study.....	105
4.6.2.3. AW2.3	112
4.7. Conclusions	112
CHAPTER 5. PLA-AW Hybrid Composite Structure.....	114
5. 1. Introduction.....	114
5.2. Materials.....	115
5.3. Ultrasonic Welding Preliminary Study	115
5.4. Results: Composite Structures Assembly	117
5.4.1. Thermal Bonding	117
5.4.2. Ultrasonic Welding	118
5.4.2.1. Preliminary study	118
5.4.2.2. Final Geometry Assembly	120
5.5. Results: Composite Structures Characterisation	121
5.5.1. Interface Morphology	121
5.5.2. Interfacial Shear Testing	122
5.6. Discussion	124
5.7. Osseointegration Study of PLA-AW Composite Structures.....	127
5.8. Conclusions	128
CHAPTER 6. Final Remarks.....	129
6.1. Outcomes and Novelty.....	129
6.2. Conclusions and Recommendations	133
References.....	134
Appendix.....	153
Appendix A. Academic Contribution	153

Honours and Awards	153
Research Outreach	153

List of Figures

Fig.1. 1. Schematic representation of the hybrid macro scale composite structure approach and how the individual structures meet the bone anatomical regions (Sadat-Shojai 2015).	2
Fig.1. 2. Hierarchical organization of bone tissue at different length scales, from the whole tissue (left) to its smallest components (right). At the macroscopic level compact (cortical) bone with spongy (trabecular) bone at both ends. At microscopic level the osteons (100 μm), that are comprised by concentric layers made of collagen fibres (10-50 μm). At nano level the hydroxyapatite nanocrystals (50 nm x 25 nm in size). Adapted from (Wegst et al. 2014).	3
Fig.1. 3. Summary of bone scaffold desirable properties for bone healing/regeneration applications.	7
Fig.1. 4. Macroscopic examination of implanted scaffolds: the scaffolds were well integrated with the host tissue. Arrows indicate where blood vessel association with the AW scaffolds can be observed, particularly within the central channel, representative images shown.	10
Fig.1. 5. Porous micro-scaffolds from the A/W system still presenting structure collapse depending on the applied heat treatment. The scaffolds on the left side were sintered first, while the scaffolds on the right were sintered with the optimised protocol based in HSM analysis. As identified, the top scaffolds are green parts (before sintering) and the bottom scaffolds are the final parts after sintering.	11
Fig.1. 6. A. Stereoisomers of lactic acid and B. Ring-opening polymerisation of lactides. Adapted from (National Programme on Technology Enhanced Learning) 2014).	14
Fig.1. 7. Schematic representation of some examples of the current scaffolds strategies for osteochondral tissue regeneration: A. Monophasic scaffold with homogeneous material composition, B. Assembled (sutured, glued or pressed together) scaffold with individual scaffolds for cartilage (orange) and bone (purple) before implantation and C. Single scaffold with integrated phases during fabrication, featuring a continuous interface or transition between phases. (adapted from (Li et al. 2014).	15
Fig.1. 8. Iterative layering fabrication process diagram. The iterative layering process is a three-step process which allows the material composition and scaffold micro-architecture in each region of the scaffold to be specifically tailored while producing a resultant scaffold with a seamlessly integrated layer structure (Levingstone et al. 2014).	16

Fig.1. 9. A. Biphasic PLA/HA ceramic scaffold fabrication details: A. Indirect wax molds (left) fabricated on a SolidScape MM2 3D printer and cast ceramic molds (right) for polymer/ceramic biphasic scaffold fabrication; B. Final PLA/HA biphasic scaffold and C. colorized μ CT of biphasic scaffold with portion cut away to depict interdigitation of both phases.	18
Fig.1. 10. Schematic representation of steps in the scaffold fabrication, involving: (a) data acquisition by medical imaging technique; (b, c) 3D computer solid model of tissue defect and biomimetic scaffold; (d, e) layer-by-layer 3D scaffold manufacturing; (f, g) cell seeding and dynamic cell culture of tissue-engineered construct; (h, i) scaffold implantation and tissue regeneration (Mota et al. 2012).	20
Fig.1. 11. Ultrasonic welding process schematic diagram. A. The ultrasonic welding equipment is represented by identifying the main parts and B. The ultrasonic welding process is represented in three steps (numbered 1 to 3), where the blue tip represents the sonotrode/horn, the white arrow the pressure applied direction and the orange and pink parts are the plastic parts being welded. Adapted from (Freudenrich 2011).....	27
Fig.1. 12. Diagrams showing the use of the SonicPin system (Stryker GmbH), a) at implantation, mounted on the ultrasound applicator, b) after ultrasound energy being applied and the applicator, was removed c) showing the ‘melting’ of the pin into the trabecular bone by filling its lacunes (Neumann et al. 2013).	28
Fig.2. 1. Parameters defined during design of a 3D porous model with CAD drawings used for assembling the porous model.	33
Fig.2. 2. Relation between slicing thickness (ST) (defined during build step) and layer height (LH) (defined during design step) resulting in three slices per layer approach.	34
Fig.2. 3. Fused Filament Fabrication machine (FFF) commercially available machine (Ultimaker 2) used for fabricating PLA scaffolds and diagram explaining the process. .	34
Fig.2. 4. A Laser cutting machine (LS3020, HPC Laser LTD, UK) used for fabricating PLA scaffolds from printed porous bar.....	35
Fig.2. 5. Equipment used for preparing MD and AW powder: A. one-bowl ball mill machine and B. Mechanical Sieve shaker.....	36
Fig.2. 6. Roller mixer used for mixing MD and AW powders into a powder blend.....	36
Fig.2. 7. Vacuum drying oven used in this study.	36
Fig.2. 8. 3D Printing process main steps and equipment: A. ZPrinter 310 Plus 3D printer (Z Corp., USA), B. Purging the print head, C. Refilling the binder bottle with ZB60, D.	

Powder compaction, E. Powder spreading from feed to build areas, F. Build area at the end of 3DP process and G. CAD model.	37
Fig.2. 9. Thermal post-processing cycles used in this study to sinter the 3DP green parts: SINT I is the protocol developed by (Xiao et al. 2008) and SINT II and SINT III were developed in this study.....	38
Fig.2. 10. Thermal Bonding of AW and PLA Composite Structures: Top image: set-up and bottom image: schematic diagram: A. AW Preheating, B. Bonding and C. Quenching.	39
Fig.2. 11. Ultrasonic Welding machine from Bradford University used in this study: A. General overview of the set-up, B. square shaped sonotrode and C. oval shaped sonotrode.	40
Fig.2. 12. Typical DSC curve for a polymer: T _g -glass transition, T _c -crystallisation temperature and T _m -Melting temperature.	45
Fig.2. 13. A. Cutting equipment used in this study, IsoMet 5000 Linear Precision Saw from Buehler and B. PLA-AW sample being cross sectioned with a diamond blade.	46
Fig.2. 14. Interfacial strength testing of assembled composite parts: A. Set-up of jig added in a universal testing machine and B. zoom in the personalised jig used.	47
Fig.2. 15. Embedding protocol used for testing interfacial shear: A. Cold embedding 2-part HDPE moulds, B and C. Tape used for avoiding resin infiltration into the porous PLA part and D. Sample ready for testing.....	47
Fig.3. 1. PLA scaffolds manufacturing route steps and parameters that need to be selected for each step.	50
Fig.3. 2. CAD models obtained during porous tensile samples design: A. Dimensions in mm following the ISO standard 527- 2 specifications and B. Obtained tensile specimen with zoom image to highlight porous structure in the testing area.	53
Fig.3. 3. Tensile test set-up with porous sample after failure.	53
Fig.3. 4. 3D model of porous structure with: Top view or XY axes and b) Cross section or XZ axes with a 3-layer approach. PS=pore size and FW= filament width.	54
Fig.3. 5. PLA scaffold in vitro degradation study steps: A. Before air plasma treatment, B. After air plasma treatment, C. Scaffolds immersed in PBS vials and D. Vials inside incubator.....	56
Fig.3. 6. SEM images (top view) obtained during experiment I: printing speed influence on morphology characterisation of porous structures prepared with constant values of FG and LH=0.50 mm, ST=0.25mm, T=210°C.....	58

Fig.3. 7. SEM images (left: top view and right: cross section) obtained during experiment II: temperature influence on morphology of porous structures prepared with constant values of FG and LH=0.50 mm, ST=0.25mm, S=30 mm/s.....	58
Fig.3. 8. SEM images (left: top view and right: cross section) obtained during experiment III: design and build parameters influence on morphology of porous structures prepared with constant values of S=30 mm/s and T=210°C.	59
Fig.3. 9. Effect of printing temperature on tensile properties: A. Apparent Young Modulus and B. Apparent Tensile Strength.	59
Fig.3. 10. Effect of design and build parameters on tensile properties: A. Apparent Young Modulus and B. Apparent Tensile Strength.	59
Fig.3. 11. Structural (porous) versus material(dense) tensile properties: A. Apparent Young Modulus and B. Apparent Tensile Strength. Porous samples design (LH and FG=0.50 mm).....	60
Fig.3. 12. PLA scaffold fabrication process. A. Porous PLA printed bar sample (experiment III) with zoom at edges a1 and a2, B. Laser cut disc from A. with b1. laser cut disc surrounding edges. White scale bar represents 1mm and black bar represents 4mm.	60
Fig.3. 13. Top images: SEM images (40x magnification) of laser cut PLA scaffold. A. Top view, B. Middle cross-section and C. scaffold edges with black arrow pointing towards rounded shape pores. Bottom images: Micro-CT analysis images of laser cut PLA scaffold. a. Top view b. Middle cross-section. c and d. scaffold edges.	62
Fig.3. 14. Stress-strain curve stages of PLA scaffold under compression loading with images acquired during compression testing of PLA scaffolds at a unit cell or pores evolutions level. Each image is identified with the stage and time point (t) that was acquired. Each stage is described in detail in the text below.	63
Fig.3. 15. Compression properties of dense PLA and porous PLA printed and PLA laser cut from a printed bar (PLA scaffold). A. Stress at yield and B. Compressive modulus. Average values were plotted with \pm SD.	64
Fig.3. 16. SEM images of the PLA scaffolds: a. and b: Cross-section SEM images with 40X magnification of laser cut PLA scaffold before (week 0) and after immersion (week 10). A-H: SEM images of laser cut PLA scaffold edges at different PBS immersion times. A and D- before immersion at x30 and x60 magnifications. B, E and G. after 6 weeks at 30x, 60x and 300x magnifications and C, F and H. after 10 weeks at 30x, 60x and 300x magnifications.	65

Fig.3. 17. PLA scaffold in vitro degradation study results obtained for: A. average molecular weight (Mw), B.PBS solution pH variation and C. Dry mass variation of porous PLA scaffolds.	66
Fig.3. 18. Results from in vitro degradation study of PLA scaffolds in PBS at 37°C. A) Compressive modulus and B) Stress at yield. Average values of three replicates were plotted with \pm SD.	66
Fig.3. 19. Images acquired at the end of compression testing of PLA scaffolds at different time points from 0 weeks (no immersion) to 10 weeks (last time point).....	67
Fig.3. 20. Representative stress-strain curves of PLA scaffold during in vitro degradation study at different time points. The curves were divided in stages, as it was done previously: 1) initial linear elastic region followed by 2) plateau of almost constant stress with increasing strain which is terminated by 3) an exponential increase in stress until the test ends.....	67
Fig.3. 21. PLA scaffold edges after 6 weeks of immersion on PBS. Top. SEM image with white arrows pointing towards different pore geometries areas and Bottom: Images acquired during compression testing stages of stress strain curves and time points (t). A. cubic pores with white arrows pointing towards cracks. And B. More rounded pores. ...	68
Fig.3. 22. PLA scaffold edges after 10 weeks of immersion on PBS. Top. SEM image and Bottom: Images acquired during compression testing stages observed in stress-strain curves and time points (t).....	69
Fig.4. 1.Maltodextrin (MD) powder after milling with 400 RPM for 2 min: A) Ceramic bowl with MD melting and B) Milling balls with MD adhesion.....	78
Fig.4. 2. SEM images of AW batches after processing towards specific particle size ranges: A. AW1 54-90 μm , B. AW2 54-90 μm , C AW1 <20 μm and D. AW2 20-53 μm . (The L and W values were not measured for images C and D).	82
Fig.4. 3. SEM images of MD after processing towards specific particle size ranges: A. MD1 < 53 μm after sieving B. MD1 < 20 μm after milling and sieving and C. MD2.20-53 μm after sieving.....	83
Fig.4. 4.Representative survey XPS spectrum of AW1 and AW2 batches.	84
Fig.4. 5. X-ray diffraction pattern of AW batches as received: A. full data was plotted and B. Inset, with hydroxylapatite phase (●) identification.	85
Fig.4. 6. DSC patterns of AW batches with different particle size: A. AW1 and B.AW2. The thermal transitions were identified for the AW1 and AW2 <20 μm , as an example.....	86

Fig.4. 7. Shrinkage of AW1 and AW2 glass samples with different particle sizes obtained by HSM: A. Full temperature range analysed and B. Inset depicting the shrinkage behaviour between 1200°C -1325°C. The main thermal events of samples <20µm are pointed with grey arrows (AW2) and black arrows (AW1).	87
Fig.4. 8. HSM images of a cylindrical AW samples (<20 µm) at different characteristic temperatures during sintering for: A. AW1 and B.AW2. The sintering and expansion events are pointed with arrows for each AW batch.....	88
Fig.4. 9. SEM images of prepared AW powder blends. Powder blends AW1.02 and AW1.03 are not shown here because they could not be processed.....	90
Fig.4. 10. Differential particle size distribution curves of prepared AW powder blends, where main peaks volume density% was quantified.....	91
Fig.4. 11. Representative green parts, 3DP with the following powder blends: A. AW1.01, B. AW1.03 C. AW1.1 and D. Representative sample for AW1.2 AW2.1, AW2.2 and AW2.3.	93
Fig.4. 12..3DP Green parts microstructure prepared with different powder blends formulation.	94
Fig.4. 13. Representative images of obtained consolidation levels: A. Level -1, sintered sample can't be handled, B. Level 0, sintered sample with shrinkage and C. Level 1 and 2, sintered sample with partial and high swelling. GP=green part and SP=sintered part.	95
Fig.4. 14. Microstructure images (SEM) of AW1.1, AW2.1, AW1.2 and AW2.2 parts sintered with SINT II at different magnification: images on the left with a magnification of 200x and images on the right with a magnification of 600x.	96
Fig.4. 15. Microstructure images (SEM) of AW2.1, AW2.2, AW2.3 parts sintered with SINT III for 1hour at different magnification: images on the left with a magnification of 200x and images on the right with a magnification of 600x. Red arrows are pointing towards globular shape particles.	97
Fig.4. 16. Microstructure images (SEM) of AW2.1 and AW2.3 parts sintered with SINT III for 6 hours at different magnification: left (lower) and right (higher).	97
Fig.4. 17. Influence of sintering protocol on the X-ray diffraction (XRD) spectra of AW1 and AW2 batches. From bottom to top: green and light grey spectra are comparing the influence of heating rate on the AW1 sintering process; dark grey and black spectra are comparing the influence of temperature increase on the AW2 sintering process and blue spectra when compared to the dark spectra is showing the influence of time in the	

sintering process of AW2. Crystalline phases identified as: Whitlockite (●), Wollastonite (■) and Hydroxylapatite (▲).	99
Fig.4. 18. Maltodextrin burning study at 10°C/min up to set temperatures as described in each image.	99
Fig.4. 19. Maltodextrin <53 µm pictures after heating up to 330°C at different heating rates: A. 10°C/min, B. 5°C/min and C. 2.5°C/min.	100
Fig.4. 20. Influence of MD particle size (PS) and heating rate (HR) on MD burning out up to 330°C: 0-A. PS=<20 µm and HR=10°C/min, B. PS= 20- 53 µm and HR=10°C/min, C. PS= <20 µm and HR=2.5°C/min and D. PS= 20-53 µm and HR=2.5°C/min.	100
Fig.4. 21. AW1.1 3DP green parts de-biding study at 10°C/min up to different temperatures.	101
Fig.4. 22. Vacuum dried AW1.1 3DP green parts images acquired during de-biding study at 2.5°C/min up.	101
Fig.4. 23. Comparison images of sintered parts prepared with indirect 3DP process in different studies: A. AW4 (70% AW<53 µm and 30% MD<53 µm) (Mancuso et al. 2017), B. AW5 (55% AW 54-90 µm, 15% AW< 53µm and 30% MD<53 µm) (Mancuso et al. 2017) and C. AW1.01 (70% AW<53 µm and 30% MD<53 µm) (this study). Black scale bar represents 4 mm.	102
Fig.4. 24. SEM images of 3DP parts microstructures prepared in different studies , after sintering with the same protocol (SINT I): A. AW4 (70% AW<53 µm and 30% MD<53 µm)(Mancuso et al. 2017). B. AW1.1 (this study).	102
Fig.4. 25. Different consolidation results and microstructure (SEM images) obtained after sintering (SINT I or SINT II) parts prepared with AW1 (top images) and AW2 (bottom images).	108
Fig.5. 1. Porous structures used for the hybrid composite assembly: A. AW discs and B. PLA scaffolds.	115
Fig.5. 2. Images showing the material combinations and geometries used in the preliminary study: A. Dense PLA samples with square and pads geometry, B. PLA dense samples aligned before welding. C. Porous PLA box with a Ø 8.5 mm hole to inset the AW disc, D. Dense PLA-AW and Porous PLA-AW.	116
Fig.5. 3. Preliminary study set-up for welding PLA-AW samples. The AW disc is positioned in between two bars to constrain the sample during the welding process, then the PLA pad is positioned on the top.	117

Fig.5. 4. Thermal images acquired during AW disc heating procedure. AW sample was placed in hot plate pre-heated at 250°C for different heating times: A.10 seconds, B. 15 seconds, C. 25 seconds and D. 35 seconds.	118
Fig.5. 5. Representative image of thermal bonded PLA-AW composite structure.	118
Fig.5. 6. Ultrasonic welding of PLA structures: A and a. Stereomicroscope images of dense PLA-PLA (increasing magnification), B and b. SEM images of porous PLA-PLA (increasing magnification) with red arrows pointing towards the welding line.	119
Fig.5. 7. SEM images of ultrasonic welded porous PLA- AW (2mm thick) composite: A. Cross-section view and B. top view. PLA and AW samples were identified in the image.	120
Fig.5. 8. Ultrasonic welding of dense PLA with AW disc (2.5 mm thick sample): A Stereomicroscope image of obtained structure and B and b. Cross section images of obtained structure (increasing magnification).	120
Fig.5. 9. Stereomicroscope images of ultrasonic welded porous PLA with AW (2.5 mm thick sample): A. Simple PLA squared geometry, B. PLA porous box with AW disc inserted and C and c. Cross section images of structure obtained in B (increasing magnification).	120
Fig.5. 10. Ultrasonic welding set-up used in this study: A. CAD model of designed fixture and B. fabricated fixture with PLA and AW and C. final welding set-up.	121
Fig.5. 11. Cross-section SEM images of thermal bonded PLA-AW composites interface with increasing magnification when AW was pre-heated for: A-C.15 seconds and D-F.25 seconds. No SEM images of sample edges were acquired.	122
Fig.5. 12. SEM images of ultrasonic welded PLA-AW composites interface: A-C cross section with increasing magnification and D. Sample edges.	122
Fig.5. 13. Interfacial shear strength testing of composite structures: A. Structure embedded in resin during testing, with blade hitting the interface. B. Representative force-displacement curves acquired during testing.	123
Fig.5. 14. Average (n=3 or 2) interfacial shear strength values obtained for composite structures prepared with different approaches/parameters.	124
Fig.5. 15. PLA-AW composite structures, assembled with different approaches/parameters, after shear testing: A. thermal bonded (TB) with 15 seconds AW pre-heating, B. Thermal bonded (TB) with 25 seconds AW pre-heating and E. Ultrasonic welded (UW).	124

List of Tables

<u>Table 1. 1.Mechanical Properties Of Bone Tissue (Karageorgiou & Kaplan 2005; Wu Et Al. 2014; Butscher Et Al. 2011).</u>	4
<u>Table 1. 2. Range Of Am Processes Classified Into Seven Categories, Based On How Material Is Joined Together Accordingly To The Iso/Astm 52900-15 Standard. Adapted From (S. Shirazi Et Al. 2015; M. Tarik Arafat Xu Li 2014; Additive Manufacturing Group From Loughborough University 2015).</u>	22
<u>Table 2. 1. Approximate Composition As Percent By Weight (%) Of Binder Zb®60 (Technologies Supplies Ltd.</u>	32
<u>Table 3. 1.Fff And Laser Cutting Processing Parameters Used In The Manufacturing Route.</u>	51
<u>Table 3. 2. Influence Of Fff Processing Parameters Study On The Morphology Of Obtained Porous Pla Structures. Fg=Filament Gap, Lh=Layer Height, St=Slice Thickness, S= Speed, T= Temperature.</u>	52
<u>Table 3. 3.Morphological Features Values Of Fabricated Porous Pla Structures. The Presented Values Are An Average Of 3 Measurements With \pm Sd.</u>	57
<u>Table 3. 4.Values Obtained From Gpc (Mw And Pdi) And Dsc (Tg And Tm) Analysis Of Pla At Different Stages Of Processing.</u>	61
<u>Table 3. 5. Design Parameters And Values Obtained After Fabrication Of Pla Scaffold. The Presented Values Are An Average Of 5 Measurements With \pm Sd. * Mean Pore Size</u>	62
<u>Table 4. 1. Table Describing The Steps Performed During Aw Indirect 3dp Processing.</u>	78
<u>Table 4. 2. Consolidation Levels Classification Used For Powder Blends Sinterability Study.</u>	79
<u>Table 4. 3. Powder Blends (Pb) Formulations Prepared For This Study. *Powder Blends Formulations Reported By (Mancuso Et Al. 2017).</u>	81
<u>Table 4. 4. Particle Size Distribution (Psd) Of Aw1, Aw2 And Md Powders After Processing. Average Values With \pm Sd Were Reported.</u>	82
<u>Table 4. 5. X-Ray Fluorescence Analysis Of Aw Batches (Provided By The Company Gts).</u>	83
<u>Table 4. 6. Surface Elemental Composition (% Atomic Concentration) Of Aw Batches As Measured By Xps Analysis Of Survey Spectra, Without Carbon Peak.</u>	84

<u>Table 4. 7. Thermal Events Summary From Dsc Patterns Of Aw1 And Aw2 With Different Particle Sizes. *Tm Was Selected As The First Melting Peak Temperature And Tx Is The Onset Crystallisation Temperature.</u>	86
<u>Table 4. 8. Thermal Events Summary From Hsm Curves Of Aw1 And Aw2 With Different Particle Sizes.</u>	88
<u>Table 4. 9. Particle Size Distribution (Psd) Of Prepared Powder Blends.</u>	91
<u>Table 4. 10. Summary Of Flowability Results Of Prepared Powder Blends. (*) When Printing Aw2.2 Minor Issues Related With Insufficient Recoating Were Observed.....</u>	92
<u>Table 4. 11. Qualitative Assessment Of Green Parts Quality.</u>	93
<u>Table 4. 12. Consolidation Levels Obtained After Sintering Powder Blends With Different Heating Protocols: -1=No Consolidation, 0=Consolidation With Shrinkage, 1 And 2=Swelling And High Swelling. Vd=Vacuum Dry Powder Before Processing. *Samples Were Stronger</u>	94
<u>Table 4. 13. Thermal Events Obtained From Hsm And Dsc Results Used For Calculating Sinterability (Sc).....</u>	110
<u>Table 5. 1. Ultrasonic Welding Parameters And Values Used In This Study.....</u>	116
<u>Table 5. 2. Influence Of Heating Time On An Aw Disc Surface Temperature Measured With A Thermal Camera.</u>	118
<u>Table 5. 3. Ultrasonic Welding Parameters Values Selected For Each Material And Structure Combination Of Pla And Aw.</u>	119
<u>Table 5. 4. Average Values (N=3 For Tb And N=2 For Uw) Of Interfacial Shear Properties Calculated From Load-Displacement Curves.....</u>	123
<u>Table 6. 1. Summary Of Outcomes And Novelty Obtained In Chapter 3.....</u>	130
<u>Table 6. 2. Summary Of Outcomes And Novelty Obtained In Chapter 4.....</u>	131
<u>Table 6. 3. Summary Of Outcomes And Novelty Obtained In Chapter 5.....</u>	132

List of Abbreviations

A_0 (Initial Area)
 A_T (Area at a specific temperature, T)
3D (Three-Dimensional)
3DP (Three-Dimensional Printing)
AM (Additive Manufacturing)
ASTM (American Society for Testing and Materials)
AW (Apatite-Wollastonite)
BCP (Biphasic Calcium Phosphate)
BJ (Binder Jetting)
CAD (Computer Aided Design)
CAM (Computer-Aided Manufacturing)
CaP (Calcium Phosphate)
Col-I (Collagen-I)
CT (Computer Tomography)
DI (Distilled Water)
DMF (Dimethylformamide)
DSC (Differential Scanning Calorimetry)
ECM (Extracellular Matrix)
EU (European Union)
FDA (Food and Drug Administration)
FFF (Fused Filament Fabrication)
FG (Filament Gap)
FW (Filament Width)
GPC (Gel permeation Chromatography)
HCA (Hydroxy Carbonate Apatite)
HDPE (High-Density Polyethylene)
HR (Heating Rate)
HSM (Hot Stage Microscope)
IJH (Inkjet Head)
ISO (International Organization for Standardization)
L (Length)
LH (Layer Height)

MD (Maltodextrin)
Micro CT (Micro Computed Tomography)
MPa (Mega Pascal)
MRI (Magnetic Resonance Imaging)
MSCs (Mesenchymal Stem Cells)
 M_w (Molecular Weight)
PBF (Powder Bed Fusion)
PBS (Phosphate buffered saline)
PDI (Polydispersity Index)
PGA (Poly (Glycolic Acid))
PHA (PolyHydroxyAlkanoates)
PLA (Poly(Lactic) Acid)
PLGA (Poly (Lactic-co-Glycolic Acid))
PPF (PolyPropyleneFumarate)
PS (Particle Size) or (Pore Size)
PSD (Particle Size Distribution)
RI (Refractive Index)
S (Seconds)
SEM (Scanning Electron microscope)
SLA (Stereolithography)
SLM (Selective Laser Melting)
SLS (Selective Laser Sintering)
ST (Slice Thickness)
T (Temperature)
TB (Thermal Bonding)
Tc1 (First Crystallisation Temperature Peak)
Tc2 (Second Crystallisation Temperature Peak)
TCP (Tricalcium Phosphate)
 T_g (Glass Transition Temperature)
TIPS (Thermal Induced Phase Transformation)
 T_m (Melting Point Temperature)
Tx (Onset Crystallisation Temperature)
USA (United States of America)
UW (Ultrasonic Welding)

VD (Vacuum Drying)

W (Width)

XPS (X-ray photoelectron spectroscopy)

XRD (X-ray Diffraction)

XRF (X-ray Fluorescence)

B-TCP (Beta-Tricalcium Phosphate)

CHAPTER 1. Introduction

1.1. Background

There are almost one million cases of skeletal defects a year reported in both the USA and the EU (Hao & Harris 2008), resulting in severe pain and disability for millions of people worldwide and massive healthcare costs (Deschaseaux et al. 2009). These numbers are expected to increase due to worldwide life expectancy rises. Thus, the management and reconstruction of damaged or diseased skeletal tissues have remained a significant global healthcare challenge (Li et al. 2014).

The limited efficacy of conventional treatment strategies for large bone defects repair, has inspired the development of scaffold-based tissue engineering solutions, with the aim of achieving complete biological and functional restoration of the affected tissue in the presence of a supporting matrix (Li et al. 2014). Several materials have been proposed as bone implants, such as an array of polymers available with varying mechanical properties, degradation times, and physical structures, and ceramics with their inherent strength and biomimetic nature (Baldini et al. 2009; Mateos-Timoneda 2009). However, the varying mechanical properties of bone throughout its volume means that it is difficult for a synthetic implant formed from a single material to match the anisotropic properties in different regions. Furthermore, discrete anatomical regions such as cortical, sub-chondral and trabecular bone each have their own unique mechanical properties and architectures (Li & Aspden 1997; Keaveny & Hayes 1993). Thus, composite systems combining advantages of polymers and ceramics appear as a promising choice, in particular for bone tissue engineering (Khan et al. 2008). The addition of bioactive ceramic phases to polymer phases will not only counteract the poor bioactivity of polymers, but also buffer the acidic degradation products of polymers (Thavornnyutikarn et al. 2014). Ceramic-polymer composites have been proposed as bone implants most commonly as particulate reinforced polymer structures either solid or porous (Rezwan et al. 2006). However, the wide range of variation in properties of natural bone is such that they may be better reproduced by bringing together distinct structures made from different biomaterials into bi- or multi-layered scaffolds (Nooeaid et al. 2012). The formation of a stable interface between layers without occurrence of interfacial deamination has been reported as the primary factor limiting the successful application of stratified scaffolds (Nooeaid et al. 2012). Appropriate scaffold manufacturing techniques represent an important factor to obtain optimal porous structures and suitable mechanical properties of the rather complex stratified scaffolds. The use of Additive Manufacturing (AM) for tissue engineering

has been growing in recent years by overcoming conventional scaffold fabrication techniques (solvent casting and particle leaching, electrospinning and freeze drying) (Holmes et al. 2014). AM techniques offer the ability to directly print 3D porous scaffolds with pre-designed shape, solvent-free, controlled pore size and interconnected porosity. Based on computer-aided design (CAD) models, 3D printers can easily fabricate a predesigned patient specific tissue construct in a layer-by-layer fashion.

Therefore, this project aims to develop new processes for fabricating hybrid polymer-ceramic devices. The overall approach adopted was to pre-fabricated the individual structures and to assemble a macro-scale composite which combined the two structures, and to evaluate these in terms of interface morphology and shear strength. This approach is illustrated in Fig.1. 1 and it is based on the recognition of the different requirements for the anatomical regions in bone regeneration and at the same time prevents delamination of different components because it is an integrated system. The two phases of the composite were a macroporous biopolymer poly(lactic acid) (PLA) structure, with mechanical and morphological properties which match those of trabecular bone (Rodrigues et al. 2016), together with a bioceramic microporous apatite-wollastonite glass-ceramic (AW), with mechanical and morphological properties which approach those of cortical bone (Mancuso et al. 2017).

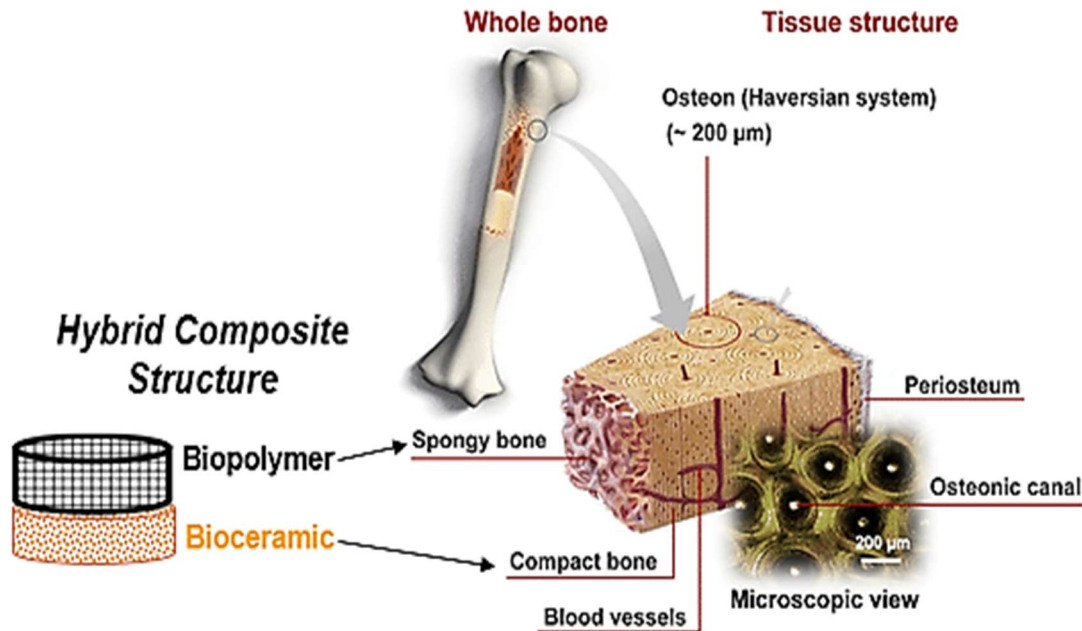


Fig.1. 1. Schematic representation of the hybrid macro scale composite structure approach and how the individual structures meet the bone anatomical regions (Sadat-Shojai 2015).

1.2. Literature Review

1.2.1. Bone anatomy and properties

Bone is a primary structural tissue of the body, which main function is to provide mechanical support and physical protection of soft tissue and organs (Deschaseaux et al. 2009; Florencio-Silva et al. 2015).

From a macro structural perspective, mature bone exists in two forms, as trabecular and cortical bone (Gong et al. 1964). The first one, trabecular bone, is also known as spongy bone (porous size of 0.5-1mm), and it can be found in the interior of small bones, in the ends of long bones, and between the surface of flat bones (Yaszemski et al. 1996). On the other hand, cortical or compact bone, is much denser than trabecular bone, and it is mainly made of cylindrical structures, the osteons (100 μ m). Cortical bone can be found in the outer tubular shell of the long bones, and is adapted to withstand compressive loadings (Yaszemski et al. 1996). The percentage of trabecular bone (~15%) in the body of adult skeleton is smaller than the one for trabecular bone (85%) (Rauch & Schoenau, 2001).

Bone tissue is a complex and hierarchically organised composite material (Fig.1. 2), where structures with multiple size scales (nano to macroscopic levels) co-exist at variable proportions through-out the body to bear different static and dynamic loading conditions. It is made of flexible collagen protein fibers (~10-50 μ m long, 2-3 nm in diameter) reinforced with calcium phosphate plate-shaped nanocrystals (50 nm x 25 nm in size).

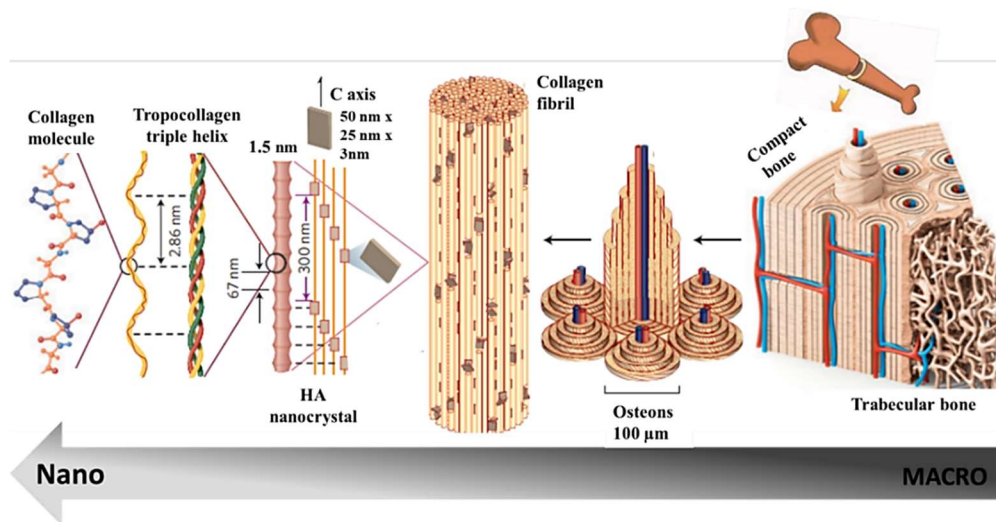


Fig.1. 2. Hierarchical organization of bone tissue at different length scales, from the whole tissue (left) to its smallest components (right). At the macroscopic level compact (cortical) bone with spongy (trabecular) bone at both ends. At microscopic level the osteons (100 μ m), that are comprised by concentric layers made of collagen fibres (10-50 μ m). At nano level the hydroxyapatite nanocrystals (50 nm x 25 nm in size). Adapted from (Wegst et al. 2014).

The bone composition and hierarchical structure, described in Fig.1. 2, are extremely important, mainly because the mechanical properties of the bone will be affected by the combination of the mineralized fibril with non-collagenous proteins and water (Wegst et al. 2014).

Overall, the properties of the bone are influenced by parameters, such as macroscopic tissue composition (trabecular and cortical), structural properties (geometry and distribution), material properties (organic and inorganic), as well as differences in age, nutritional state, activity (mechanical loading) and disease status of individuals (Karageorgiou & Kaplan 2005). Accordingly to previous studies (Karageorgiou & Kaplan 2005; Wu et al. 2014; Butscher et al. 2011), mechanical properties of cortical and trabecular bone have been summarised in Table 1. 1.

Table 1. 1. Mechanical properties of bone tissue (Karageorgiou & Kaplan 2005; Wu et al. 2014; Butscher et al. 2011).

Bone type	Tensile Strength (MPa)	Compressive Strength (MPa)	Young's Modulus (GPa)
Trabecular	5.3-6.8	2-12	0.0005-0.5
Cortical	60-160	30-230	3-30

Unlike other tissues, bone is capable of detecting damaged areas (not completely fractured) and heal/repair them, by a process called bone remodelling (Little et al. 2011; Oryan et al. 2014). Although, under some conditions, bone remodelling can be limited; parameters such as patient age, diseases (bone cancer and infection), anatomical location, and size bone defect can impair bone healing. Previous studies (Bosch et al. 1998; Cowan et al. 2004) have reported critical size of ~2-5mm, meaning that defects larger than this range will need surgery (e.g. bone grafting) to ensure bone healing. Therefore, in the next section clinical approaches to promote bone healing are extensively described/reviewed.

1.2.2. Bone healing clinical approaches

Nowadays, bone grafts are the most utilized clinical approach for stimulating bone repair and regeneration (Blokhuys & Arts 2011). Three clinical approaches of bone grafting have been suggested including, autografts, allografts and xenografts (Nandi et al. 2010; Oryan et al. 2014). Amongst all, the autologous graft has been considered the 'gold standard' for bone reconstruction (Pape et al. 2010; Arnoldi et al. 2012). The main advantage of autogenous grafts is that the graft is harvested from patient's own site, thus it simultaneously reduces the risk of adverse immunoreactions and transmission of infections (Rogers & Greene 2012).

However, as all clinical approaches, autologous grafts are not 100% successful or suitable for all patients with bone deficiency. As described in previous studies (Younger & Chapman 1989; Kumar & Narayan 2014; Goulet et al. 1997), autologous bone grafts have shown some limitations, mostly related to the graft harvesting procedure. Firstly, the quality and amount of bone tissue that can be harvested is mostly limited to small bone effects, especially in the paediatric or elderly population. Moreover, a complication rate of 10-40% at primary surgical site, which includes post-operative pain, hematoma, infection haemorrhage and vascular lesions have been reported (Younger & Chapman 1989; Kumar & Narayan 2014; Goulet et al. 1997).

Allografts (banked bone graft) and xenografts (different species bone graft) have been proposed as an alternative to overcome the problems (e.g. morbidity, inherent limited bone availability) associated with autologous bone grafting. Although allografts and xenografts have showed similar efficacy, other issues such as risk of infection, donor availability issues, tissue rejection and inferior osteoconduction and osteoinduction have been reported (Kurien et al. 2013; Campana et al. 2014).

Accordingly, approaches of bone regeneration that rely on the utilization of conventional bone graft substitutes should be minimized to lessen these problems in the near future.

Therefore, in the last decade research has been focused on alternative novel approaches (Kane & Ma 2013; Castilho et al. 2014), such as the adoption of synthetic bone scaffolds to address the problem of damaged bone regeneration; especially for large defects where a substantial structural scaffold is needed.

1.2.3. Bone Scaffolds

Scaffolds engineering has emerged as a promising approach with great potential to provide the appropriate intervention for the repair and regeneration of bone defects, by overcoming the limitations of the conventional approaches, such as bone grafts (1.2.2. Bone healing clinical approaches) (Da et al. 2013; Sherwood et al. 2002; Grayson et al. 2008; Liu et al. 2013).

By definition, scaffolds are three-dimensional biomaterials that operate as a temporary extracellular matrix (ECM) by guiding and facilitating cells expansion to promote tissue growth; while providing a mechanical support during implantation (Nooeaid et al. 2012). Over time, once the function has been fulfilled, the scaffold degrades and the cells produce their own natural ECM (Jack & Lin 2011; Chan & Leong 2008; O'Brien 2011; Kohane & Langer 2008).

Ideally the scaffold should have features that resemble those of natural bone, thus providing structural support by acting as a natural ECM. Nevertheless, the complexity of the ECM in bone tissue make it difficult to mimic exactly (Chan & Leong 2008). Thus, to achieve this, the scaffold should fulfil range of desirable properties (Fig.1. 3), in which of the most important features are the material choice, design and surface (Schaefer, Martin, G Jundt, et al. 2002; B. Mollon et al. 2013; Grayson et al. 2008). These properties include:

- i) Osteoinductivity and osteoconductivity: the scaffold must have a surface able to recruit and stimulate immature cells to develop into bone-forming cells (osteinduction). Also, the scaffold must support the formation of ECM, adherence and proliferation of bone cells on its surface (by integrating features such as pores, channels or pipes (osteoconduction). Both are essential to achieve a bond between the scaffold and the bone (osteointegration) after implantation (Albrektsson & Johansson, 2001)
- ii) Biocompatibility: After implantation the scaffold should not evoke cytotoxicity and/or an exacerbated inflammatory response that might reduce bone healing or lead to rejection (Almeida et al. 2014).
- iii) Mechanical stability: The scaffold mechanical properties should be adapted to the implantation site. From a clinical perspective, the scaffold needs to be strong enough to allow surgical handling. And after implantation it must maintain its mechanical integrity until bone remodelling process is complete, by providing mechanical support to the adjacent bone (Van Der Stok et al. 2013; Oryan et al. 2014).
- iv) Adequate architecture/design: there must be a balance between architecture and mechanical properties. For example, an appropriate porosity range (diameter 50-1000µm) and interconnectivity (size of interconnections >50µm) are crucial for cell infiltration and vascularisation which are key factors to support bone tissue regeneration (O'Brien 2011; Ikeda et al. 2009; Karageorgiou & Kaplan 2005; M. Tarik Arafat Xu Li 2014; Kalita et al. 2003).
- v) Adequate degradation profile (biodegradability): the scaffold should present a controllable degradation rate, that ideally matches the bone/neotissue formation; Moreover the by-products should not be toxic, and should be easily and rapidly diluted at the implantation site (Hutmacher et al. 2004; Brahatheeswaran Dhandayuthapani Toru Maekawa D. Sakthi Kumar 2011)

- vi) Readily available and easy to manufacture: to become clinically available, the chosen scaffold must be cost effective, easy to process, and possible to scale-up.

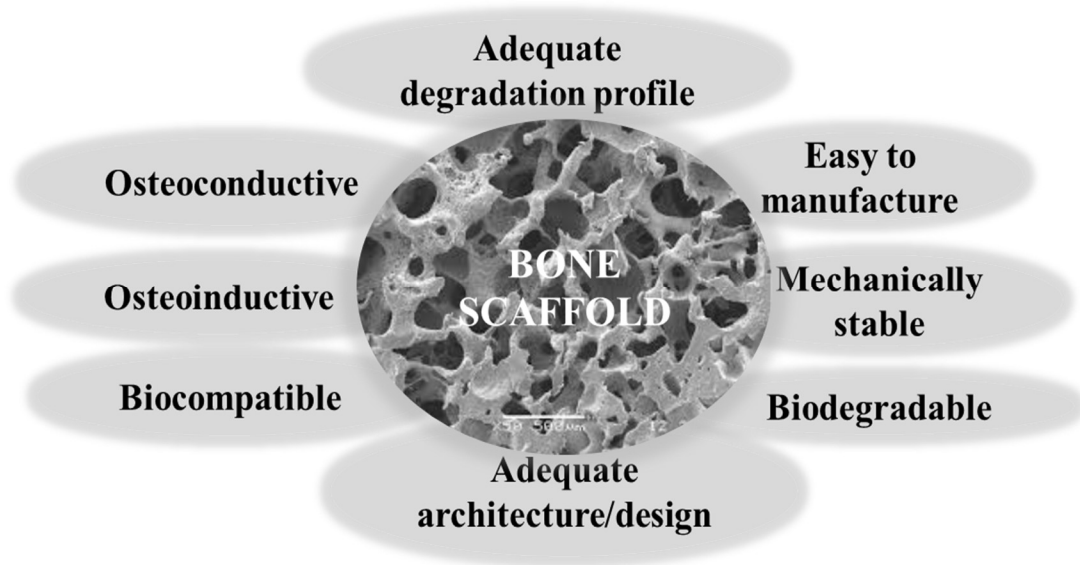


Fig.1. 3. Summary of bone scaffold desirable properties for bone healing/regeneration applications.

Over the past years, a wide range of innovative synthetic materials and/or natural materials have been developed to overcome the problems associated with autologous bone grafts.

Several materials have been used in the field of tissue engineering to fabricate 3D scaffolds, based on bone tissue being a composite material principally formed by an organic phase, consisting of a biopolymer (collagen), and an inorganic phase composed by a bioceramic (natural apatite). Taking that into account, it is easy to explain why biopolymers and bioceramics have been widely used to fabricate scaffolds for bone tissue engineering.

Bioceramics (typically calcium phosphates (CaP), bioactive glasses and glass-ceramics): synthetic CaP materials are approved by US Food and Drug Administration (FDA) and were among the most investigated materials for scaffold composition for over three decades. These materials are inherently bioactive as they share similarities in chemical composition and surface structure with the mineral phase of bone, which consists of plate-like hydroxyapatite crystals (Li et al. 2014). Moreover, most CaP ceramic materials are biocompatible, osteoconductive and can be biodegradable (Samavedi et al. 2013). The osteoconductive properties of CaP support tissue ingrowth, osteoprogenitor cell growth, and the development of bone formation by promoting the attachment, proliferation, differentiation, and migration of bone cells. Their surfaces also allow for a direct, adherent, and strong bond with the bone tissue that can mediate an exchange of calcium (Ca^{2+}) and phosphorus (P) ions between cell matrix and substrate (Pilia et al. 2013; Li et al. 2014). The most widely studied ceramic

scaffolds for clinical bone regeneration include hydroxyapatite (HaP), beta-tricalcium phosphate (β -TCP), biphasic calcium phosphate (BCP), and bioactive glasses and glass-ceramics (specifically composed with silica (SiO_2), calcium oxide (CaO), sodium oxide (Na_2O), and phosphorous pentoxide (P_2O_5)). Clinical reports on bone reconstruction using HaP scaffolds combined with autologous osteoprogenitor cells have demonstrated good scaffold-bone integration in large (4–7 cm) bone defects within 2 months post-implantation, which was maintained over 6–7 years (Li et al. 2014). However, the application of hydroxyapatite in bone reconstruction at load-bearing sites is limited by its low biodegradation, brittleness and low resistance to crack growth, that interfere with bone formation at the implantation site (Li et al. 2014). β -TCP is the stable phase of TCP at low sintering temperatures ($<1100^\circ\text{C}$) with a Ca/P ratio of 1.5. Its high biodegradability allows rapid precipitation of a surface hydroxycarbonate apatite (HCA) layer in physiological fluids, which contributes to the reported osteoconductive and sometimes osteoinductive properties. After implantation in the rat femoral condyle, β -TCP scaffolds showed the presence of new bone formation after seven days and consistent bone formation over 4 weeks (Kondo et al. 2005). A major drawback of β -TCP scaffolds for clinical application, it is the rapid biodegradation that results in the loss of scaffold integrity, which may impede bone formation (Pilia et al. 2013). The high solubility may exceed the rate of tissue regeneration and lead to complicate clinical outcomes such as bone loss at the defect site. Another widely used CaP is named BCP, a two-phase ceramic composed of hydroxyapatite and β -TCP phases, which is obtained by either physically mixing the two powders or chemically sintering calcium-deficient apatite (Ca/P ratio < 1.67) at temperatures above 700°C . The biodegradability of BCP can be tailored to match bone formation, by controlling its reactivity, that increases with the HA β -TCP ratio (Li et al. 2014). When compared to hydroxyapatite or β -TCP scaffolds, BCP scaffolds showed improved osteoinductive properties, by demonstrating superior bone formation in various *in vivo* models, and it was even comparable if not superior to autografts and allografts controls when combined with autologous mesenchymal stem cells (Weinand et al. 2006). Regarding the clinical performance of BCP scaffolds, when employed in a range of orthopaedic procedures, fast integration and bone reconstruction both close to and within the implants, with good to excellent final results were observed. Nevertheless, the application of BCP ceramics in clinical bone reconstruction is restricted to the treatment of bone defects at non-load bearing sites as fillers or particulate forms, due to by their lack of mechanical strength, particularly in the porous forms needed to encourage bone formation and ingrowth (Li et al. 2014). Bioactive glasses or bioglasses consist of a silica network containing element

modifiers bonded to the network via non-bridging oxygen bonds, such as calcium, sodium and phosphorus. The pioneer and most widely investigated bioactive glass composition is Bioglass® 45S5 (45 wt% SiO₂, 24.5 wt% Na₂O, 24.5 wt% CaO and 6 wt% P₂O₅). Other bioactive glass compositions developed over the years contain no sodium (Na) or have additional elements strategically incorporated in the silicate network such as fluorine, magnesium, strontium, iron, silver, boron, potassium or zinc. The typical feature of all bioactive glasses, is their ability to interact with living tissue, in particular forming strong bonds to bone, a property commonly termed bioreactivity or bioactivity. The basis of the bone bonding property of bioactive glasses is the chemical reactivity in physiological body fluids (*in vitro* and *in vivo*) resulting in the formation of a hydroxycarbonate apatite (HCA) layer to which bone can bond (Gerhardt & Boccaccini 2010). The highly glass surface reactivity in physiological environments is explained by the amounts of Na₂O and CaO, as well as the relatively high CaO/ P₂O₅ ratio (Li et al. 2014). Recent studies have proven that ion dissolution and release from bioglasses activate gene expression in osteogenic cells that give rise to enhanced bone regeneration (L. Hench et al. 2000; Perez et al. 2015). However, the brittleness and low fracture toughness remain a major impediment of these materials. On the other hand, glass-ceramics are polycrystalline materials that contain one or more crystal phases embedded into a residual glass and are produced by the controlled heat treatment of certain glasses produced by heating the parent bioactive glass. The heat treatment is usually (but not always) performed in two stages: first, at relatively low temperatures, not far from the glass transition (T_g), to induce internal nucleation, followed by a second stage at a higher temperature to promote the growth of different phases (Montazerian & Dutra Zanotto 2016). In the case of glass-ceramics obtained by a sintering process, during the occurrence of crystallization and densification, the microstructure of the parent glass shrinks, porosity is reduced and the solid structure gains mechanical strength. Bioactive glass-ceramics belong to the group of Class A bioactive materials which are characterized by both osteoconduction (i.e., growth of bone at the implant surface) and osteoinduction (i.e., activation and recruitment of osteoprogenitor cells by the material itself stimulating bone growth on the surface of the material).

AW glass-ceramic, commercially available with the brand name Cerabone® is the most extensively and successfully used bioactive glass-ceramic for bone replacement. Some years ago, Kokubo et al (Kokubo 1991) foreseen that they should develop a glass-ceramic that contains a reinforcing crystal phase, β -wollastonite (CaO SiO₂). Sintering with concurrent crystallization proceeded at 1050° to obtain A-W glass-ceramic with β -wollastonite being

crystallized in the glass with a fine fibrous and needle-like morphology that reinforced the glass-ceramic through activating various toughening mechanisms.

Apatite-wollastonite glass -ceramic (AW GC) is stable *in vivo* and difficult to be resolved when implanted in bone. Although dense AW GC (70 % porosity) has been used as a bone substitute that shows no significant change even after a long implantation period, Fujita et al.(Fujita et al. 2000) reported a total resorption of porous AW intramedullary plugs implanted in the femurs of dogs after 24 months. Teramoto et al. (Teramoto et al. 2005) observed that in comparison with β - TCP, cylinders of porous AW GC have been resorbed more gradually *in vivo* , while β -TCP (75% porosity) had almost completely disappeared by 24 weeks. Due to this material's rapid resorption and relatively poor new bone formation, only a weak mineralized matrix remained in the β -TCP cylinders at 24 weeks. In contrast, abundance of newly formed bone and residual AW GC matrix were observed at 24 weeks, especially in the A-W GC with 70% porosity (Teramoto et al. 2005).

In the study of (Lee et al. 2015) porous AW 3D scaffolds were fabricated with additive manufacturing (AM) technology of selective laser sintering (SLS), together with post SLS heat treatment. The A-W scaffolds were custom-designed to incorporate a cylindrical central channel (1 mm) to increase cell penetration and medium flow to the centre of the scaffolds under dynamic culture conditions during *in vitro* testing and subsequent *in vivo* implantation. The results demonstrated that the macro and micro porous structure has the ability to promote vascularisation, with and without optimised seeding using osteogenic pre-differentiated and undifferentiated MSCs, in a subcutaneous mouse model after 4 weeks (Fig.1. 4).



Fig.1. 4. Macroscopic examination of implanted scaffolds: the scaffolds were well integrated with the host tissue. Arrows indicate where blood vessel association with the AW scaffolds can be observed, particularly within the central channel, representative images shown (Lee et al. 2015) .

AW bioactive porous scaffolds have been produced by powder-based 3D printing (25 to 45 μ m and 45to 100 μ m mixture in 1:1 weight proportion of both powder fractions), however by adopting the same thermal treatment program used for dense geometries and based only on

a conventional sintering curve of technical ceramics (e.g. CaP), the integrity of the final scaffolds structure was compromised. By means of heat microscopy (or HSM), an optimized heating program was found to sinter the delicate struts without losing the structural integrity of the scaffolds (Gomes et al. 2014), as shown in Fig.1. 5.

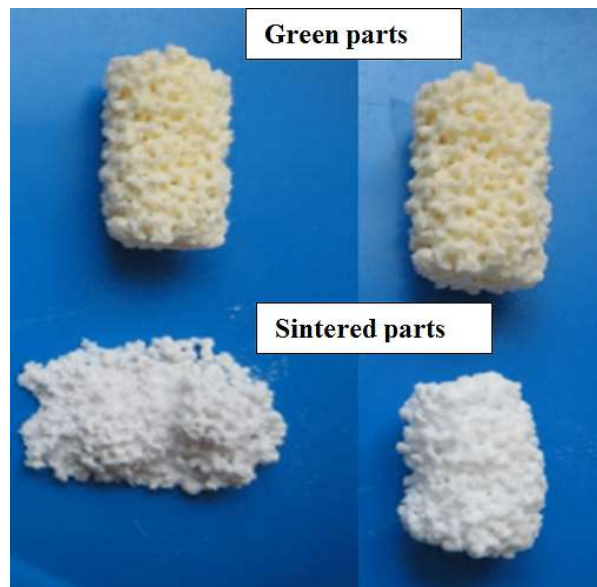


Fig.1. 5. Porous micro-scaffolds from the A/W system still presenting structure collapse depending on the applied heat treatment. The scaffolds on the left side were sintered first, while the scaffolds on the right were sintered with the optimised protocol based in HSM analysis. As identified, the top scaffolds are green parts (before sintering) and the bottom scaffolds are the final parts after sintering (Gomes et al. 2014)

Biopolymers offer several key advantages for promoting bone regeneration at defect sites, such as the ability to tailor mechanical properties and degradation kinetic by tailoring their composition. For instance, polymers can differ in their molecular weight (M_w), polydispersity (PDI), crystallinity, structure and thermal transition, allowing different absorption rates (Razak et al. 2012). Biopolymers are classified into naturally derived and synthetic polymers. Naturally derived polymers, include polysaccharides such as chitosan, chondroitin sulfate, starch, alginate, hyaluronic acid and cellulose and proteins such as collagen, soy, fibrin gels, silk (Saravanan et al. 2016; Martino et al. 2005). They have hydrophilic surfaces that favour cell attachment and differentiation but are characterised by weak mechanical properties. For instance, Collagen-I (Col-I) is the organic component of bone ECM, explaining its biocompatibility and biodegradability, yet it lacks compressive mechanical strength and stiffness. Collagen sponges have attracted attention for bone application owing their ability in supporting cell attachment and growth and in enhancing bone formation by promoting cell differentiation to osteoblasts (Seol et al. 2004). A study concerning the implantation of mesenchymal stem cells (MSCs)–seeded collagen gels into rabbit osteochondral defects led

after 24 weeks to both bone and hyaline cartilage formation in the construct with no evidence of tissue degeneration (Wakitani et al. 1994). Nevertheless, the major problems associated with collagen are its cost, solubility, and lack of commercial sources (Pilia et al. 2013).

In contrast synthetic polymers are the largest family of biopolymers, showing commonly predictable and reproducible physical (e.g. degradation rate) and mechanical properties (e.g. elastic modulus) as result of controlled synthesis process. Additionally, a key advantage offered by this class of polymers is a high control of impurities with respect to the natural polymers, decreasing any possible risks of toxicity or immunogenicity (Varghese & Elisseeff 2006; Rezwan et al. 2006).

Polyesters are the most common synthetic polymers for tissue engineering applications and they can be split in unsaturated and saturated depending on the final chemical structure. Amongst the unsaturated polyesters, the most famous are polypropylenefumarate (PPF) and polyhydroxyalkanoates (PHA) mainly because of the biocompatibility of their degradation products since body can easily remove fumaric acid and propylene glycol upon hydrolysis (Diez-Pascual 2017). PPF consists in a linear polyester incorporating two ester bonds and one unsaturated carbon-carbon double bond and PHA is produced intracellularly by microorganisms as carbon and energy storage compounds under unbalanced growth conditions (Insomphun et al. 2017). Nevertheless, the use of PHA as biomaterial when compared to the other traditional polymers (saturated ones, described next) is limited by their poor mechanical properties, high production cost, limited functionalities, incompatibility with conventional thermal processing techniques and susceptibility to thermal degradation (Li et al. 2016). In order to improve PHA and PPF mechanical properties and spread its range of practical applications, novel approaches need to be developed such as the incorporation of fillers or polymer blending (Diez-Pascual 2017; Shi et al. 2007; Henslee et al. 2012).

The most often utilized biodegradable synthetic polymers for 3D scaffolds in tissue engineering are saturated poly- α -hydroxy esters, including poly (lactic acid) (PLA) and poly (glycolic acid) (PGA), as well as poly(lactic-coglycolide) (PLGA) copolymers and polycaprolactone (PCL). Since the development of the first biodegradable synthetic suture, based on PGA (DEXON®) and clinically applied in 1969, this class of synthetic polymers have been approved by US Food and Drug Administration (FDA) for various applications, resulting in a great variety of biomedical products currently on the market, such as temporary ECM in bone tissue-engineering scaffolds (Rezwan et al. 2006). PCL exists in an elastic state at room temperature, and has a low melting point of 60°C has been shown to have good mechanical properties with fully interconnected pores that increase biocompatibility *in vitro*.

However, due to its semi-crystalline nature and hydrophobicity, degradation of PCL is remarkably slow (years) since the close packed macromolecular arrays retard fluid ingress in the bulk.

PLA is one of the most widely used synthetic polymers in biomedical products for drug delivery, barrier membranes, guided tissue regeneration (in dental applications and orthopaedic), stents and sutures. Furthermore, PLA is the only member of the polyester family that has been used for load bearing applications such as orthopaedic fixation devices (screws and plates), owing to the high mechanical strength of this polymer (Manavitehrani et al. 2016). The properties of PLA depend on its molecular characteristics, crystallinity, morphology and degree of chain orientation.

The process for manufacturing of PLA is a multi-step fermentation process comprises three main steps. The first stage involves the biosynthesis of lactic acid from the starch, that is then converted to dimeric cyclic ester of lactic acid (lactide). The last step is ring-opening polymerization of lactide, that requires heat and a metallic or an organometallic compound as catalyst to convert the lactide to PLA. In more detail, since lactic acid is a chiral molecule that exists in two stereoisomeric forms -L-lactic acid which is optically active and polarizes light to right (denoted by - or d), and D-configuration polarizes light to the left (denoted by + or l), as depicted in Fig.1. 6.A. Since an equimolar mixture of the two lactides is optically inactive, the purity of the monomers can be estimated by measuring their optical activity, that give rise to four morphologically distinct polymers that is P-DD-LA, P-LL-LA (also called PLLA), P-DL-LA (also called PDLA) and a P-meso-LA. For instance, Poly (D-lactic acid) (i.e. PDLA) and poly (L-lactic acid) (i.e. PLLA) can be polymerized by ring opening polymerization of D (+)-lactide and L (-)-lactide, respectively (Fig.1. 6.B).(Rezwan et al. 2006; Razak et al. 2012; National Programme on Technology Enhanced Learning) 2014). Generally, L-PLA is more frequently employed than D-PLA, since the hydrolysis of L-PLA yields L (+)-lactic acid, which is the naturally occurring stereoisomer of lactic acid and it is preferred for load bearing applications, where high mechanical strength and toughness are required. Also, the hydrolysis of amorphous polymers, e.g. PDLA, is faster due to the lack of crystalline regions (Rezwan et al. 2006).

Nevertheless, it is not wise to apply polyesters alone for bone replacement application. The reported drawbacks in the *in vitro* and *in vivo* behaviour such as the degradation products (monomeric or oligomeric hydroxycarboxylic acids) that promote a fast acidification of the surrounding environment, which in turn may accelerate the polyesters degradation and can exacerbate the inflammatory response. The choice of composite materials, mainly Calcium

Phosphate based (CaP), reinforces, has been largely used to solve this problem of acidic degradation. Another disadvantage is that the mechanical properties of the highly porous scaffolds made from polyesters are relatively weak, which limits their use for bone-tissue engineering, especially the *in vivo* implant site (Razak et al. 2012; Manavitehrani et al. 2016)

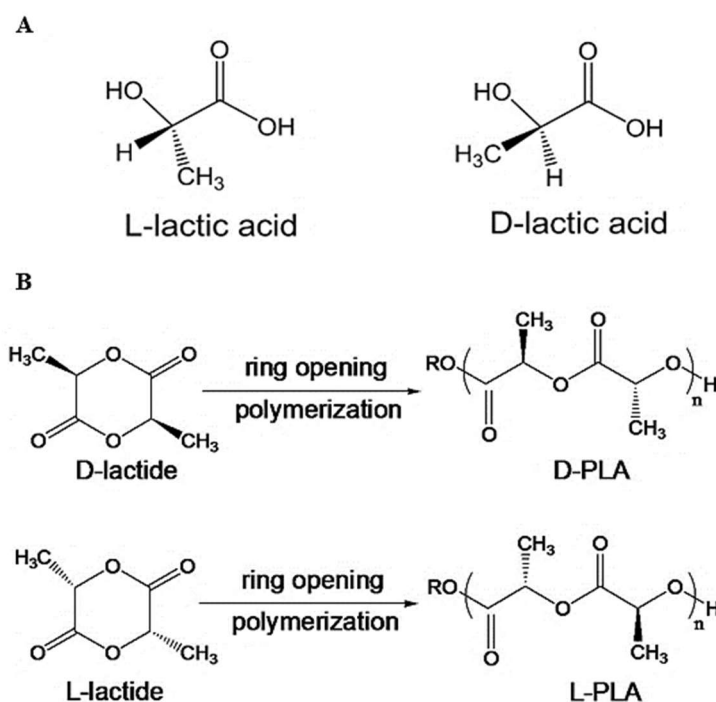


Fig.1. 6. A. Stereoisomers of lactic acid and B. Ring-opening polymerisation of lactides. Adapted from (National Programme on Technology Enhanced Learning) 2014).

None of these materials alone (biopolymers and bioceramics) have had the strength required to withstand static and cyclic loads *in vivo* whilst maintaining sufficiently high porosity (between 60% to 90% with an average pore size of > 150 μm) to facilitate bone ingrowth, vascularisation and the transport of nutrients. The desired scaffold compressive strength should be comparable to that of cortical bone, which is in the range of 30 to 230 MPa (as described in Table 1. 1). Weakness associated with current highly porous scaffolds continues to fuel the demand for a high strength bone scaffold (Prasadh & Wong 2018; Roohani-Esfahani et al. 2016).

1.2.4. Multi-layered scaffolds

Studies involving single-phased or monophasic scaffolds with homogeneous material composition (Fig.1. 7.A) have shown that they have failed on meeting the unique characteristic features of multi-layered tissue organisation such bone and osteochondral unit (interface of bone and cartilage) (Nooeaid et al. 2014). Despite showing fabrication simplicity

and reproducibility, monophasic scaffolds (Fig.1. 7.A) with homogeneous properties typically do not address the different requirements of two tissues, leading to lack of regeneration, particularly in large animal models (Detting et al. 2010; Bernstein et al. 2013).

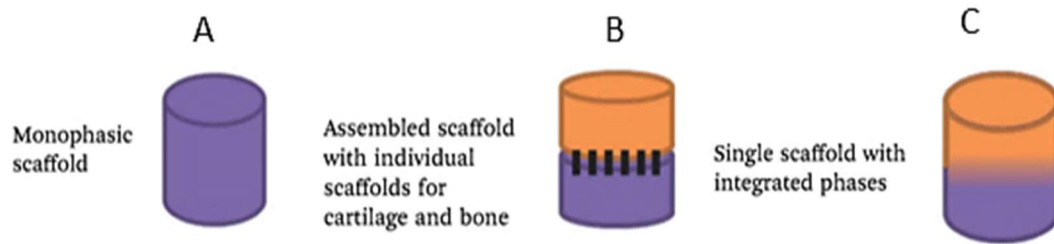


Fig.1. 7. Schematic representation of some examples of the current scaffolds strategies for osteochondral tissue regeneration: A. Monophasic scaffold with homogeneous material composition, B. Assembled (sutured, glued or pressed together) scaffold with individual scaffolds for cartilage (orange) and bone (purple) before implantation and C. Single scaffold with integrated phases during fabrication, featuring a continuous interface or transition between phases. (adapted from (Li et al. 2014).

Aiming at mimicking the structure, architecture and functional properties of complex tissues, like bone, numerous research groups have been developing multi-layered scaffolds obtained by assembling individual scaffolds for each one of the different tissue regions (e.g. Bone and cartilage, as shown in Fig.1. 7.B and C).

In this section, examples of current development on osteochondral scaffolds are reviewed as a reference of complex tissue engineering.

Schaefer et al. (2002) developed a biphasic osteochondral composite by culturing *in vitro* allogeneic chondrocytes on a biodegradable polyglycolide acid (PGA) scaffold and sutured it to a subchondral support with or without bone marrow (Schaefer, Martin, G. Jundt, et al. 2002). Degradation issues were reported due to the continuous presence of hydroxyapatite of the subchondral support which may have slow down the regeneration of the subchondral bone, pointing towards the selection of a biodegradable support instead. Moreover, the engineered cartilage did not integrate well with adjacent host cartilage.

Scotti et al. (2010) also engineered *in vitro* a biphasic osteochondral scaffold based on extensively used biomaterials and the principle of biological bonding of the bony/chondral layers through the extracellular matrix produced by human cells and in clinical practise (Scotti et al. 2010). For the cartilage layer a collagen type I/III matrix (Chondro-Gide®) was seeded with human articular chondrocytes in a fibrinogen solution and combined with a cell-free devitalized bovine trabecular bone cylinder (Tutobone®). To assess the integration strength between the bony/chondral layers, this group developed and validated a peel-off test. It was demonstrated that the chondral scaffolds pre-cultured for 3 days, before its fusion with the bony layer, yielded superior integration forces and were capable of regenerating cartilage and

bone in the osteochondral defects. However due to different shear stresses of bony and chondral layers, scaffolds without artificial fusing are preferred to avoid implant failures. Thus, to overcome biphasic scaffolds limitations, more biomimetic multi-layered scaffolds with an intermediate layer, known as tidemark, have arisen as an option for osteochondral repair. Very recently, it was reported (Levingstone et al. 2014) the development of a collagen based multi-layered scaffold by freeze-drying process, represented in Fig.1. 8.

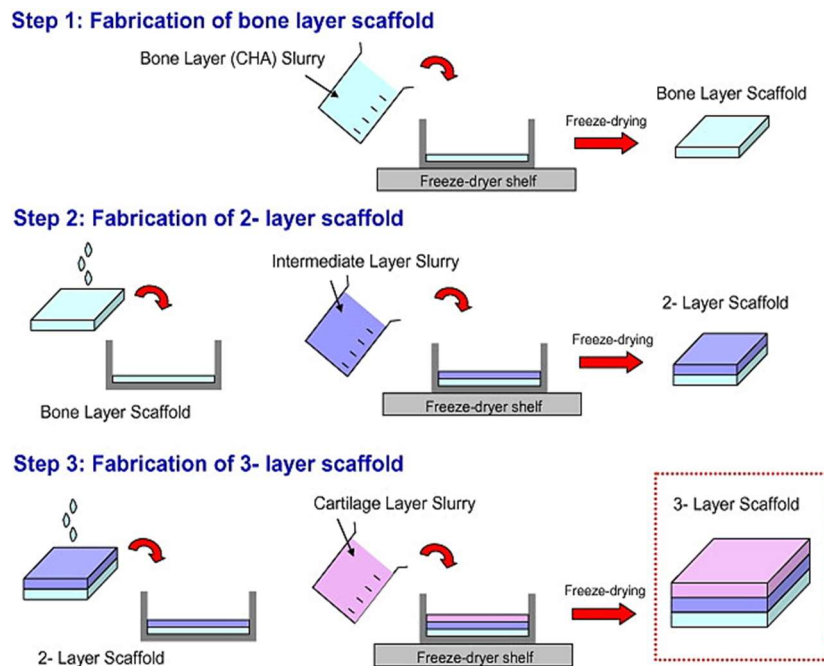


Fig.1. 8. Iterative layering fabrication process diagram. The iterative layering process is a three-step process which allows the material composition and scaffold micro-architecture in each region of the scaffold to be specifically tailored while producing a resultant scaffold with a seamlessly integrated layer structure (Levingstone et al. 2014).

This was achieved by combining a base layer consisting of a collagen-hydroxyapatite (HA) with potential for bone repair with a collagen-HA-glycosaminoglycan intermediate calcified cartilage layer and a top cartilaginous layer composed by collagen-hyaluronic-acid (Levingstone et al. 2014).

In the same study, *in vitro* tests have demonstrated the potential of this multi-layered scaffold as an advanced strategy for osteochondral defect repair which is characterised by an integrated layer structure, with a degree of interconnected porosity throughout the construct. This approach seems promising but as far as we know, this scaffold has not yet been tested in a biological system.

Sherwood et al. (Sherwood et al. 2002) developed a multi-layered cartilage-bone composite scaffold by using a 3D printing process (Theriform™) with a PLGA/PLA cartilage region

(90% porous), a composite of PLGA/TCP cloverleaf-shaped bony portion (55% porous). As well as a transition gradient region between the bony and cartilage section to avoid delamination (Sherwood et al. 2002). After seeding chondrocytes on the scaffold, it was observed that they were preferentially attached to the cartilage region of the device and deposited an extracellular matrix. The measured tensile strength of the bony region was comparable with the trabecular bone and the compressive strength was within one order of magnitude. Still, the reported values were acquired during dry tests and may be somewhat altered at the time of implantation due to the aqueous environment.

Another interesting approach for creating biomimetic biphasic polymer-ceramic scaffolds was developed by coupling additive manufacturing (AM) with conventional sponge scaffold fabrication processes (Taboas et al. 2003). In more detail, the first step consisted in fabricating the ceramic moulds by casting a HA and acrylic slurry in a 3DP mold (made of wax and polysulfonamide), depicted in the left image on Fig.1. 9.A. Then, the obtained cast ceramic pre-mould was subject to a burn out cycle that removed the organic binders and the mold, followed by sintering at 1300°C to obtain the final ceramic mold depicted in the left image on Fig.1. 9.B. The next step was to melt cast the PLA by pre-heating the ceramic mould above the polymer melting point and by pressing them into molten polymer, causing polymer to infiltrate mold pores. Ceramic-free regions within the scaffold were created by selective application of a ceramic solvent, yielding a non-blend, discrete composite with mechanical interdigitation of the ceramic and polymer phases. The biphasic scaffolds with mechanically interdigitated PLA and sintered hydroxyapatite regions were fabricated with 500 and 600 µm wide global pores (Taboas et al. 2003).

With the proposed manufacturing method, the composite materials are interdigitated for increased mechanical integrity, a requisite for structural tissue interface engineering applications. These scaffolds could be used for bone/cartilage interface engineering, as the PLA wall surrounding the periphery of the scaffold serves to entrap seeded chondroblasts and prevent migration of osteoblasts to avoid bone formation where cartilage growth is intended. Conversely, osteoblast migration and bone production is possible in the HA region (Taboas et al. 2003). The main drawbacks associated with the described process are its complexity and time-consuming nature, and the ceramic mould shrinking 50% in volume. While the shrinking could be compensated for before casting, the resulting accuracy needs to be proven by performing future studies.

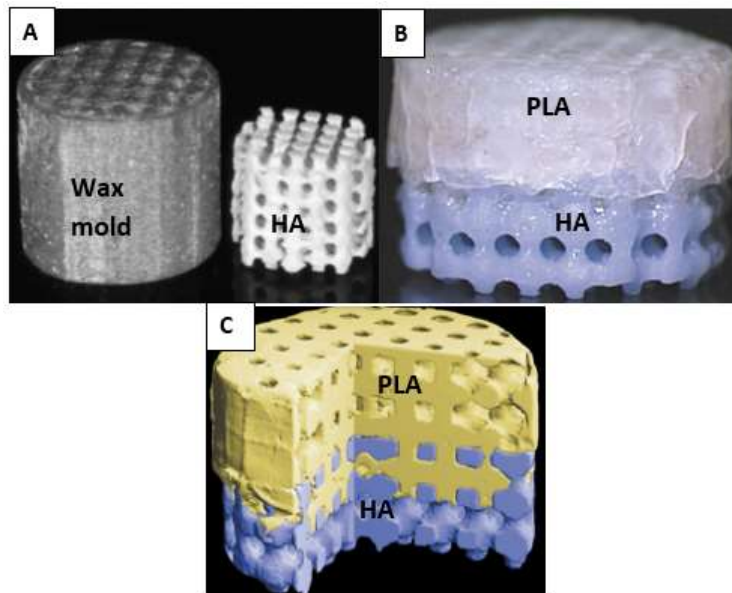


Fig.1. 9. A. Biphasic PLA/HA ceramic scaffold fabrication details: A. Indirect wax molds (left) fabricated on a SolidScape MM2 3D printer and cast ceramic molds (right) for polymer/ceramic biphasic scaffold fabrication; B. Final PLA/HA biphasic scaffold and C. colorized μ CT of biphasic scaffold with portion cut away to depict interdigitation of both phases.

Liu et al. (Liu et al. 2013) claimed that among all suggested designs, single scaffolds with integrated phases (Fig.1. 7.C) are an effective option for treating osteochondral defects, due to their biomimetic architecture, leading to a better regeneration of hyaline-like cartilage and structured bone tissue. It consists in developing a continuous interface from the osseous to the chondral phase with gradient bioactive signals such as growth factors or material composition or combining both, reducing risk of delamination (Mohan et al. 2011). The goal of this approach is to achieve a good interconnectivity between the two phases without artificial fusion such as fibrin glue, suture, or pressing individual parts together (Fig.1. 7.B), where a good integration between phases may be difficult to attain. This leads to lack of gradual transition of properties, with several *in vivo* studies reporting fibrocartilage (scar tissue) regeneration rather than hyaline cartilage (Ho et al. 2010; Miot et al. 2012; Pei et al. 2009). In summary, the incessant development of novel multi-layered scaffold designs taking advantage of different material combinations, methods of fabrication and repair strategies will eventually result in the realisation of simple, effective and robust solutions for the clinical treatment of osteochondral or bone defects to prevent or retard degenerative processes.

1.2.5. Additive Manufacturing (AM)

Depending on scaffolding material and strategy, different processing techniques and methodologies have been proposed to optimize final scaffold performances in terms of

external shape and size, surface morphology and internal architecture. These include the so called conventional fabrication techniques, such as, solvent casting combined with particulate leaching, freeze drying, gas foaming, melt moulding, fibre bonding, phase separation techniques, electrospinning are just some of those that have been used extensively and applied to scaffold production.

For regeneration of complex or structural tissues, scaffolds must possess several structural features that are difficult to achieve using conventional manufacturing methods. For instance, morphological properties (pore size and its distribution and interconnectivity) cannot be precisely controlled with these approaches and some of them require the use of toxic solvents, which are not compatible with biological applications. Morphology control is essential to maximize nutrient diffusion and blood flow that control cell growth and function and to optimise the scaffold mechanical properties to match the regenerated tissue.

While the conventional sponge scaffold manufacturing methods are capable of producing structures with porous internal architectures from a diverse array of materials, the local pores are generally less than 300 μm in diameter. Despite these methods result in interconnected pores, the pore connectivity is not an intentional result of an a priori global design. Instead the morphology is a random product of the processing parameters that cannot provide optimal permeability for tissue ingrowth.

For example, in the study of (Zhang & Ma 2000) PLA scaffolds with two-dimensional (2D) stacked oriented pores by leaching layered meshes made from drawn sugar fibres were fabricated. While control over global pore size and 2D orientation was obtained, the full control over global pore architecture was not attained. Parallely, freeze-drying has emerged as an effective and widely accepted method of producing porous scaffolds from a wide range of materials with the ability to eliminate porogens. Nevertheless, a significant drawback of this process is that any titrants or other intermediate species present during the fabrication of the biomaterial suspension are exceedingly difficult to remove after freeze-drying. These contaminant species become integrally incorporated into the scaffold walls and the removal of these components via leaching or other suitable approaches can compromise the mechanical and microstructural integrity of the scaffold (K. et al. 2009).

Phase separation, such as thermally-induced phase separation (TIPS), is a scaffold fabrication technique capable of fabricating scaffolds with porosities up to 97%. TIPS performed by rapidly heating a polymer-solvent solution with a lower critical solution temperature or cooling one with an upper critical solution temperature. The instability of the solution causes it to separate into polymer-rich and solvent-rich regions. Drawbacks of this process include the

use of organic solvents and the obtained small pore sizes (tens of micrometres), which are often too small for tissue engineering applications.

Electrospinning creates nonwoven meshes of polymeric fibers by drawing dissolved polymer solutions out of a thin syringe tip using a strong electric potential. By modifying processing parameters such as the electric potential, distance to collection substrate, and syringe tip diameter, the diameter of polymer strands and mesh density can be controlled. Fabricated scaffolds lean towards having poor mechanical strengths and it is difficult to build 3D parts with controlled pore shape and toxic organic solvents are often used to dissolve the polymer.(Chartrain et al. 2018). Moreover, scaffolds with tailored porosity for specific defects are difficult to manufacture with most of these approaches.

Unlike these methods, additive manufacturing (AM) has become a popular method for bone scaffolds fabrication. AM refers to a class of manufacturing processes based on the building of a solid object from three-dimensional (3D) model data or CAD model, by joining materials, usually layer upon layer. The 3D model data for scaffold development can be derived from medical imaging techniques used for diagnostic purposes, such as computer tomography (CT) and magnetic resonance imaging (MRI), and are generally treated by computer-aided design (CAD) and computer-aided manufacturing (CAM) software (Mota et al. 2012) (Fig.1. 10).

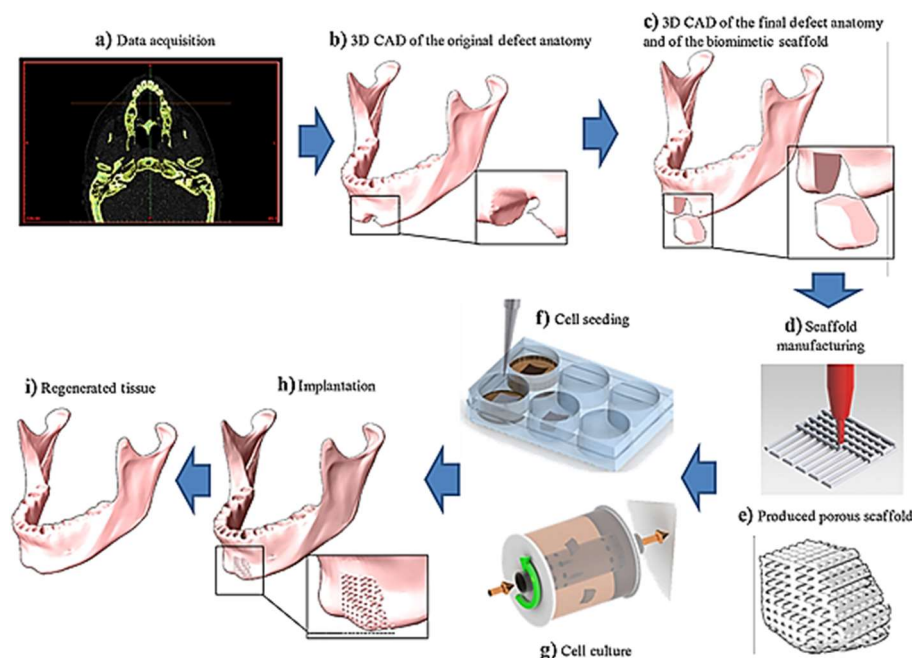
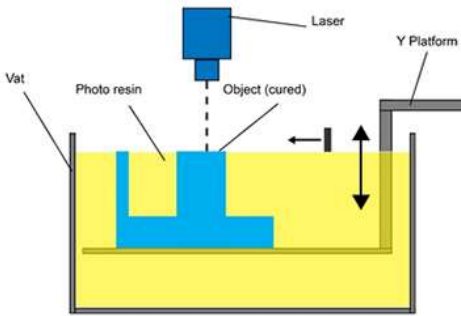
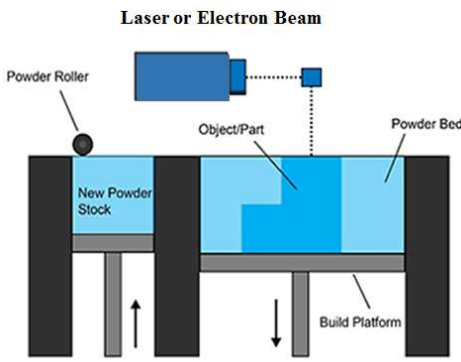


Fig.1. 10. Schematic representation of steps in the scaffold fabrication, involving: (a) data acquisition by medical imaging technique; (b, c) 3D computer solid model of tissue defect and biomimetic scaffold; (d, e) layer-by-layer 3D scaffold manufacturing; (f, g) cell seeding and dynamic cell culture of tissue-engineered construct; (h, i) scaffold implantation and tissue regeneration (Mota et al. 2012).

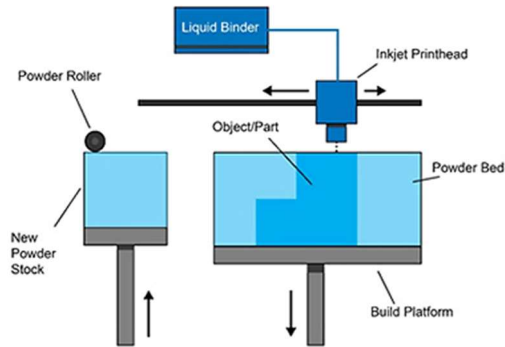
The possibility of rapidly producing tissue-engineered constructs meeting patient specific requirements, in terms of tissue defect size and geometry as well as autologous biological features, makes AM techniques a powerful way of enhancing clinical routine procedures. During the development of AM technology there have been numerous different terms and definitions in use, often with reference to specific application areas and trademarks. This is often ambiguous and confusing which hampers communication and wider application of this technology. For instance, the term 3D Printing (3DP) is used as a synonym for all AM processes, and at the same as a synonym of an individual process often called binder jetting (Table 1. 2). There are actually several individual processes which vary in their method of layer manufacturing and differ depending on the material used.

Hence, together, the American Society for Testing Materials (ASTM) and the International Organization for Standardization (ISO) created a standard in 2015, ISO/ASTM 52900-15, Additive Manufacturing – General Principles – Terminology, which established the following definition for AM: “A process of joining materials to make parts from 3D model data, usually layer upon layer, as opposed to subtractive and formative manufacturing methodologies.” Machining and grinding processes qualify as subtractive methodologies, while extrusion, forging, rolling, casting, etc. qualify as formative methodologies [STANDARD]. This International Standard has been developed on the basis of a partnership agreement between ISO and ASTM International with the aim to create a common set of ISO/ASTM standards on Additive Manufacturing. The objective of this standardization of terminology for AM is to facilitate communication between people involved in this field of technology on a world-wide basis. In this standard the range of AM processes is further classified into seven categories, based on how material is joined together, as described in Table 1. 2.

Table 1. 2. Range of AM processes classified into seven categories, based on how material is joined together accordingly to the ISO/ASTM 52900-15 standard. Adapted from (S. Shirazi et al. 2015; M. Tarik Arafat Xu Li 2014; Additive Manufacturing group from Loughborough University 2015).

AM techniques	Description
<p>VAT polymerisation or Stereolithography (SLA)</p>  <p>The diagram illustrates the Stereolithography (SLA) process. A blue laser beam is directed at a vat filled with yellow photo resin. The laser cures a layer of resin, forming an 'Object (cured)' in blue. A 'Y Platform' moves vertically, indicated by a double-headed arrow, to position the next layer of resin for curing. The vat is labeled 'Vat' and the resin is labeled 'Photo resin'.</p>	<p>SLA uses a vat of liquid photopolymer resin, out of which the model is constructed layer by layer. An ultraviolet (UV) light is used to cure or harden the resin where required, using a process of photo polymerisation, whilst a platform moves the object being made downwards after each new layer is cured. As the process uses liquid to form objects, there is no structural support from the material during the build phase, unlike powder based methods, where support is given from the unbound material.</p>
<p>Powder Bed Fusion (PBF):</p>  <p>The diagram illustrates the Powder Bed Fusion (PBF) process. A 'Laser or Electron Beam' is directed at a 'Powder Bed'. A 'Powder Roller' moves a 'New Powder Stock' into the bed. An 'Object/Part' is being built on a 'Build Platform'. The unfused powder surrounding the consolidated part acts as a support material for overhanging features.</p>	<p>PBF processes involve the spreading of the powder material over previous layers. There are different mechanisms to enable this, including a roller or a blade. A hopper or a reservoir below of aside the bed provides fresh material supply. A laser or electron beam are the sources used to fuse material powder together, whereas the unfused powder surrounding the consolidated part acts as a support material for overhanging features. It includes : Direct Metal Laser Sintering (DMLS), Electron beam melting (EBM), Selective heat sintering (SHS), Selective laser melting (SLM) and Selective laser sintering (SLS).</p>

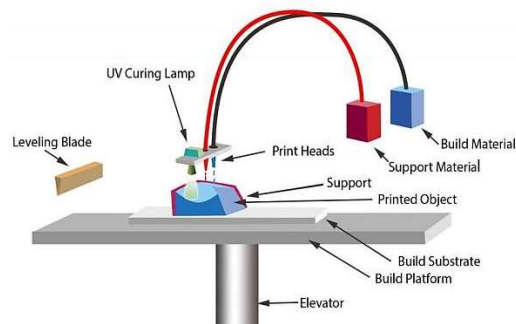
Binder Jetting (BJ) or Three-Dimensional Printing (3DP) *



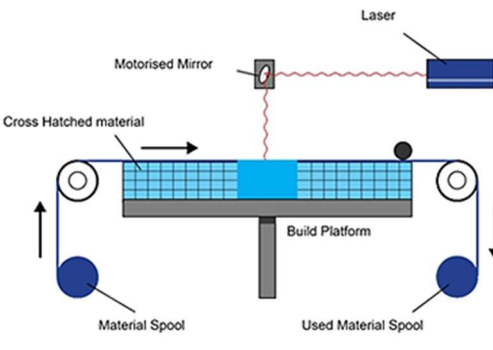
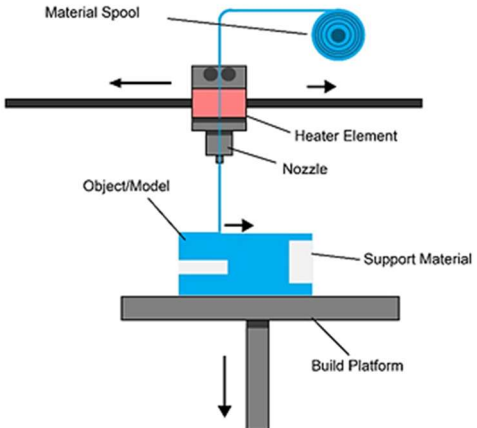
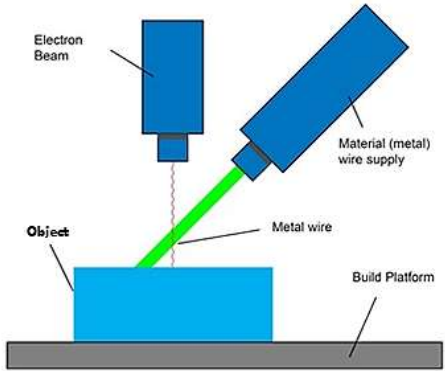
**The technology is often referred to as 3DP technology and is copyrighted under this name.*

The binder jetting process uses two materials: a powder based material and a binder that acts as an adhesive between powder layers. The binder (normally organic) is usually in liquid form or as a powdered form incorporated in the build material that is always in powder form. Liquid bonding agents are selectively applied onto thin layers of powdered material to build up parts layer by layer. A print head moves horizontally along the x and y axes of the machine and deposits alternating layers of the build material and the binding material or the material that promotes binding (in case binder is incorporated in the blend). After each layer, the object being printed is lowered on its build platform. After printing, the obtained parts (called green parts) are typically fired in a furnace after printing to sinter the particles and remove the binder system. As with other powder based manufacturing methods, the object being printed is self-supported within the powder bed and is removed from the unbound powder once completed.

Material Jetting



Droplets of materials are deposited layer by layer to make parts. Common varieties include jetting a photocurable resin and curing it with UV light, as well as jetting thermally molten materials that then solidify in ambient temperatures.

<p>Sheet Lamination</p>  <p>The diagram illustrates the Sheet Lamination process. A 'Material Spool' on the left feeds a 'Cross Hatched material' into a 'Build Platform'. A 'Motorised Mirror' directs a 'Laser' beam onto the material as it moves. The material is then wound onto a 'Used Material Spool' on the right. The cross-hatching is used for easy removal post-build.</p>	<p>Sheet lamination processes include ultrasonic additive manufacturing (UAM) and laminated object manufacturing (LOM). UAM process uses sheets or ribbons of metal (aluminium, copper, stainless steel and titanium), which are bound together using ultrasonic welding. The process does require additional machining and removal of the unbound metal, often during the welding process. LOM process uses a similar layer by layer approach but uses paper as material and adhesive instead of welding. A cross hatching method is used during the printing process to allow for easy removal post build.</p>
<p>Material Extrusion</p>  <p>The diagram shows the Material Extrusion process. A 'Material Spool' feeds material into a 'Nozzle' which is heated by a 'Heater Element'. The extruded material forms an 'Object/Model' on a 'Build Platform'. 'Support Material' is also extruded to support the main object.</p>	<p>With this technique, a material (usually thermoplastic) is melted and extruded into layers through a nozzle moving in the XY plane. This method provides for the rapid printing of parts, but also requires the printing of supports. The required supports are made of another substance that is removed after manufacturing. It is limited to only a few types of materials (thermoplastic based).</p>
<p>Directed Energy Deposition (DED)</p>  <p>The diagram depicts the Directed Energy Deposition (DED) process. An 'Electron Beam' is directed at a 'Material (metal) wire supply'. The wire is fed into a 'Metal wire' which is then deposited onto an 'Object' on a 'Build Platform'.</p>	<p>Powder or wire is fed into a melt pool which has been generated on the surface of the part where it adheres to the underlying part or layers by using an energy source such as laser or electron beam. This is essentially a form of automated build-up welding</p>

Each AM technique has its features, such as Fused deposition modelling (FDM) or Fused Filament Fabrication (FFF) requires thermoplastic polymers, stereolithography (SLA)

requires the use of radical initiated polymerization, and binder jetting involves the use of solvents and binders in a powder based system. The binder jetting process employs inkjet head (IJH) technology for processing materials. In this system, the head prints a liquid binder onto thin layers of powders based on object profiles that have been generated by software. Two kinds of heads can be used in IJH systems: piezoelectric and thermal heads, with different performances. Each inkjet technique has some points which can be categorized as availability, printing speed, accuracy of printed parts, and functional cost. Thermal inkjet printers have some advantages, including availability, higher print speed, and lower cost of parts fabrication compared with piezoelectric inkjet printers (S. F. S. Shirazi et al. 2015). Regarding PBF processes, selective laser sintering (SLS) and direct metal laser sintering (DMLS) are essentially the same thing, with SLS used to refer to the process as applied to a variety of materials—plastics, glass, ceramics—whereas DMLS refers to the process as applied to metal alloys. But sintering (SLS) is distinguished from melting (SLM) because sintering processes do not fully melt the powder, but heat it to the point that the powder can fuse together on a molecular level. The idea of sintering is to join particles together without melting them, thus the porosity of the printed part can be controlled with SLS. On the other hand, SLM can do the same as sintering and go one further, by using the laser to achieve a full melt, meaning the powder is not merely fused together, but is melted into a homogenous part. There are two types of laser sources that are commonly used for laser sintering. Lasers with different wavelengths are selected to match the absorption characteristics of the corresponding powder granules. One is a continuous wave CO₂ laser with a wavelength of 10.6 μm , which is particularly suitable for processing thermal curing plastics. The other is a continuous wave ytterbium (Yb) fibre laser with a wavelength of $\sim 1.1 \mu\text{m}$, which is commonly used for processing metals (Qian & Shen 2013).

Accordingly to the ISO/ASTM 52900-15 standard, AM processes are also divided in two groups: (i) the single-step processes (also called ‘direct’ processes), in which parts are fabricated in a single operation where the basic geometrical shape and basic material properties of the intended product are achieved simultaneously and (ii) the multi-step processes (also called ‘indirect’ processes), in which the parts are fabricated in two or more operations where the first typically provides the basic geometric shape and the following consolidates the part to the intended basic material properties. Most of the AM processes to shape ceramics are multi-step (indirect) processes, which make use of a sacrificial binder material to shape ceramic powder particles, that is removed in a subsequent de-binding furnace treatment. Some examples of single-step processes to shape ceramics are direct

energy deposition (DED) and powder bed fusion (PBF), comprising selective laser melting (SLM).

1.2.6. Ultrasonic welding

First patented in the 1960s, ultrasonic welding (UW) is a well-established method used in automotive, aircraft, packaging, and medical industries (Amanat et al. 2010). UW technology is a unique method of joining two parts together without using fasteners or adhesives because it uses the materials themselves to create the joint. UW uses low amplitude, high frequency vibration to create friction between the parts to be joined to generate enough heat to melt the plastic at the interface. The frequencies used are above the range of human hearing (20–40 kHz), hence the label ultrasonic.

The ultrasonic welding equipment is schematic described Fig.1. 11.A and the mechanism behind the use of ultrasonic energy to weld polymers is explained in the three steps of Fig.1. 11.B.

The basic process of welding can be described by the following steps:

1. One of the parts to be joined is fixed firmly within a stationary holding jig or fixture, while the mating part (orange plastic part in Fig.1. 11.A) is subjected to a sinusoidal-ultrasonic vibration perpendicular to the desired bond contact area.
2. Then using a welding tool called sonotrode (blue part in both Fig.1. 11.A and B) the high-frequency vibrations generated by the ultrasonic system, in combination with pressure, are transferred to the parts to be joined, leading to relative vibrations in the jointing zone (step 1 and 2 in Fig.1. 11.B).
3. Due to the friction between the parts and internal friction in the parts, heat is generated, causing the polymer to soften and melt at the interface. After switching off the ultrasound, the polymer solidifies as it cools down and forms a bond step 3 in Fig.1. 11.B)

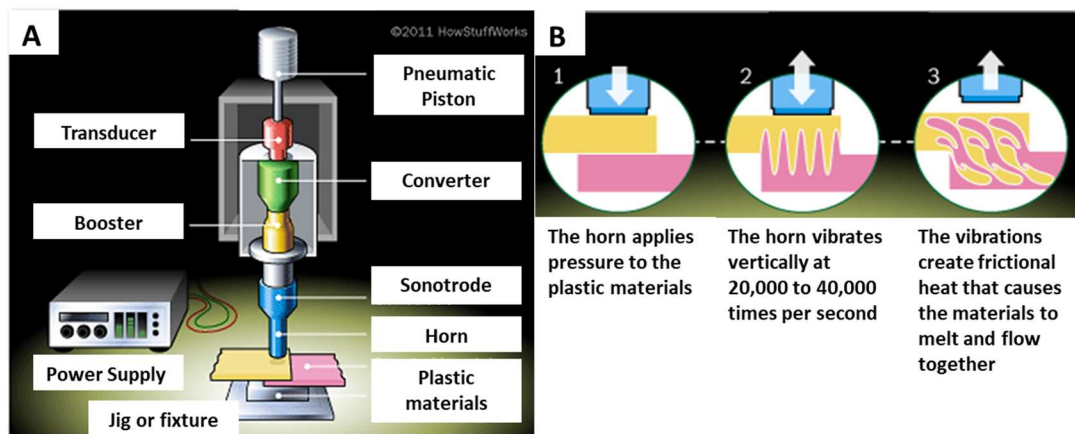


Fig.1. 11. Ultrasonic welding process schematic diagram. A. The ultrasonic welding equipment is represented by identifying the main parts and B. The ultrasonic welding process is represented in three steps (numbered 1 to 3), where the blue tip represents the sonotrode/horn, the white arrow the pressure applied direction and the orange and pink parts are the plastic parts being welded. Adapted from (Freudenrich 2011)

This way, a kind of glue is generated in approximately one second joining the two parts (Sackmann et al. 2015). Optimal transmission of ultrasonic energy to the joint and subsequent melting behaviour is therefore dependent on the geometry of the part, and on the ultrasonic absorption characteristics of the material.

Heat generated is normally highest at the joint surface due to surface asperities, which are subjected to greater strain and frictional force than the bulk material. Compared with other welding techniques, such as hot plate welding, spin welding and vibration welding, UW is the fastest known welding technique with weld times typically between as 0.1 to 1.0 seconds, and provides ease of automation (Troughton 2008).

This technique is particularly suited for assembling medical devices because it is a fast, clean, efficient and repeatable process. For instance, one promising technology to be used in orthopaedic surgery, is the use of ultrasonic welding of bioresorbable pins into trabecular bone. The trade name is SonicPin™ and it consists of a copolymer of Poly-(L-Lactid-co-D and L-Lactid) in a proportion of 70:30) with a diameter of 1.8 - 2.2 mm and is available in lengths of 18 – 22mm.

The ultrasonic aided fixation process of SonicPin™ is illustrated in Fig.1. 12.A-C, and it can be described in three steps:

- A) For application, the thermoplastic pin (SonicPin™) is fixed with its proximal thread on the ultrasound applicator (sonotrode) that drives the pin implant into the trabecular bone;
- B) Subsequently the pin can melt into a pre-drilled hole by application of a defined amount of ultrasound energy, this sets up shearing forces at the contact surface of the polymer, causing it to liquefy at pre-defined locations and to penetrate the trabecular bone, by filling its lacunes;

C) Finally, the liquid polymer is immediately quenched, resulting in a mechanically stable bond to the bone after only a few seconds.

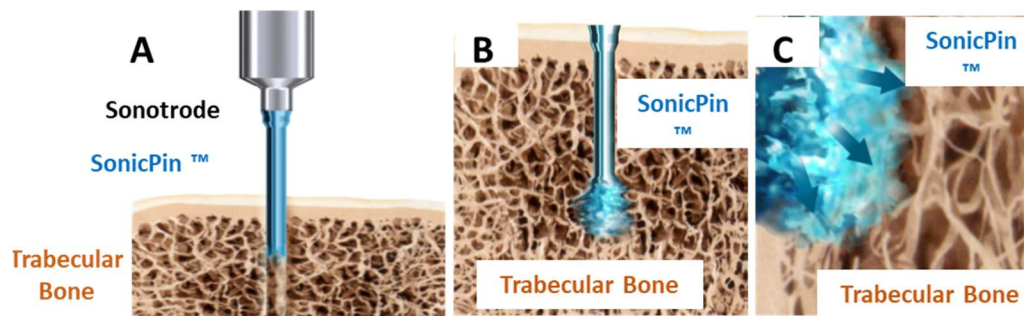


Fig.1. 12. Diagrams showing the use of the SonicPin system (Stryker GmbH), a) at implantation, mounted on the ultrasound applicator, b) after ultrasound energy being applied and the applicator, was removed c) showing the 'melting' of the pin into the trabecular bone by filling its lacunes (Neumann et al. 2013).

The short ultrasonic impulse and the localized melting of the polymer disturbs neither the bone healing nor the osteointegration as proven in numerous animal studies (Neumann et al. 2013; Heidenreich et al. 2011; Lee & Park 2013).

It improves the fixation performance through better integration of the implant within the surrounding trabecular bone (Heidenreich et al. 2011; Augat et al. 2015). Besides, the advantages of ultrasound-aided fixation include optimum operative handling, reduced insertion time, avoidance of fractures of the fixation elements, and higher three-dimensional load capacity (Augat et al. 2015).

1.3. Aim and Objectives

General Aim: This research work focused on developing a hybrid biopolymer-bioceramic composite structure for mimicking trabecular and cortical bone mechanical properties, and on developing the manufacturing processes required to make them.

Research has focussed on the use of two model materials to create a composite structure: a biodegradable polymer, polylactic acid (PLA), and a bioactive glass-ceramic, apatite wollastonite (AW).

To achieve the aim, the work was divided in 4 objectives:

OBJ1: Fabricate (FFF machine and laser cutting) and characterise (mechanical properties, *in vitro* degradation behaviour and morphology) of a polylactic acid (PLA) porous structure with designed porosity (trabecular bone analogue)

OBJ2: Fabricate (indirect 3DP) of a three dimensional (3D) porous apatite- wollastonite (AW), as previously reported by (Mancuso et al. 2017) (cortical bone analogue)

OBJ3: Fabricate a bonded PLA-AW hybrid composite structure with thermal bonding and ultrasonic welding

OBJ4: Characterise the interface morphology and shear strength of the assembled PLA-AW composite structure

1.4. Thesis outline

This thesis was organized in six chapters, as described in the following lines.

Chapter 1 consists on an introduction to the main problem that was the origin of this experimental work. It is addressed the urgent need of improving the current treatment for large bone defects and the aim and objectives were defined. It also presents a literature review of the main concepts used in this work. For instance, bone anatomy and properties together with conventional clinical approaches and scaffold-based treatments for bone healing were reviewed. In addition, additive manufacturing (AM) techniques were broadly mentioned, as the select manufacturing techniques in this study belong to the AM group.

Chapter 2 is devoted to general materials and methods used for characterising both PLA and AW and the fabricated structures in the next Chapters.

Chapter 3, Chapter 4 and Chapter 5 content is about the results obtained during objectives 1 to 3, respectively. Each one comprises an experimental details section employed to develop the work and an individual discussion section.

Then, Chapter 6 presents a general discussion, where the aim and objectives achievement are reviewed, together with a summary of outcomes and novelty obtained from Chapter 3 to Chapter 5. At the end, this chapter compiles all the conclusions obtained, leading to an evaluation of the thesis proposed and mainly to an answer to the initial question. And it is also proposed some future work that can be further developed on this subject/topic.

CHAPTER 2. Materials and Methods

2.1. Materials Choice Rationale

The model biopolymer and bioceramic materials used for assembling the hybrid composite structure were apatite-wollastonite (AW) and polylactic acid (PLA). The rationale behind the two biomaterials selection was based on the following reasons:

1. Both AW and PLA are well-known and accepted biomaterials for bone replacement applications:
 - i) AW is a bioactive glass-ceramic that comprises apatite and wollastonite microcrystalline phases embedded in a glassy matrix, improving the mechanical properties when compared to other bioceramics (Gerhardt & Boccaccini 2010). It has the ability to chemically integrate with surrounding bone *in vivo* (Blaker et al. 2003). This property is attributed to the presence of silicon (Si) that plays a key role in the metabolic events responsible for new bone formation the AW ability to promote bone formation and ingrowth (Montazerian & Dutra Zanotto 2016). Their clinical use comprises bone spacers and fillers in bulk and granular forms with dense and porous structures and also as artificial vertebrae and in vertebral discs in dense bulk form (Li et al. 2014; El-Meliegy & Noort 2012). Cerabone TM is a commercially available version of a glass-ceramic composed of AW. In the study of (Dyson et al. 2007), custom-designed AW scaffolds were fabricated with selective laser sintering (SLS) with the *in vitro* results indicating biocompatibility and osteo-supportive capacity. Moreover porous AW scaffolds (indirect SLS approach) described in (Xiao et al. 2008) were described with comparable biological properties to that of AW fabricated with other conventional methods. The *in vivo* degradation of AW scaffolds is affected by porosity of scaffold as reported by (Teramoto et al. 2005). For the AW scaffold with 70% porosity after a period of 36-weeks more than 80% of the scaffold was resorbed. Moreover the bulk mechanical properties of AW were described as a good match to the ones of cortical bone by (Currey 2008);

- ii) PLA, a biocompatible, and biodegradable aliphatic polyester available from renewable resources (Cailloux et al. 2014) have been used in numerous biomedical application such as sutures, pins, screws and drug delivery systems (Navarro et al. 2005). Among other polyesters such as PLGA and PGA, PLA displays the highest tensile stress (~55 MPa) and favourable ultimate elongation at breakage (30%–240%); hence, it has been broadly used for the fabrication of devices that are under constant tensile stress and high elongation (Manavitehrani et al. 2016). Furthermore, owing to PLA lack of bioactivity (Serra et al. 2014), for bone applications this polymer is usual combined with an inorganic phase into a composite (Serra et al. 2013).
- 2. Suitability of both materials of being processed with additive manufacturing techniques, and particularly low cost of both PLA material and fused filament fabrication (FFF) technique. Together with the knowledge of the existence of previously developed manufacturing route for AW porous structures fabrication that match cortical bone properties (Mancuso et al. 2017).
- 3. Possibility of controlled biodegradation rate of PLA by adjusting chemical composition and AW ability to release alkaline ions that might neutralise the acidic degradation by-products of PLA degradation process (Li & Chang 2004; Xiong 2002). In the study of (Cao et al. 2012), the presence of β - tricalcium phosphate (TCP) shown a pH buffering effect versus the detected pH decreased when compared to the PLA scaffold. Moreover, the incorporation of β -TCP enhanced *in vitro* osteoinductivity in a rabbit model. The presence of lactic acid as by-products of PLA degradation were described as affecting negatively the bone healing process after implantation due to the formation of a thin layer of fibrous tissue around the implant (Abert et al. 2016).

Besides combining these two biomaterials with the aim of improving each other as a composite material, the idea of a structural bonding rather than a reinforcement of the inorganic phase into an organic/polymeric matrix has the potential to overcome the concerns associated with dispersion and lack of integration between phases (Rakmae et al. 2012).

2.2. Materials

2.2.1. Polylactic acid (PLA)

Polylactic acid 2.85-3.00 mm natural colour filament (PLA, 4032D, Nature Works®) with an L-lactide: D-lactide ratio of 98:2 and a density of 1.24 g/cm³ was the material used for the experimental work.

2.2.2. Apatite-wollastonite (AW)

AW powders were supplied by GTS (Sheffield, UK) in two batches (AW1 and AW2). AW1 was ordered in October 2013 as a glass frit (1-2 mm) and AW2 was ordered in December 2015, with a requested particle size range of 40-200 µm.

2.2.3. Maltodextrin (MD)

Maltodextrin (MD) powders were purchased from Eon® (MD1) and from My Protein® (MD2).

2.2.4. Zb®60 binder

The zb®60 clear binder solution was purchased from Technology Supplies LTD and the approximate composition of zb®60 as percent by weight is presented in Table 2. 1.

Table 2. 1. Approximate composition as percent by weight (%) of binder zb®60 (Technologies Supplies LTD).

Component	Approximate weight %
Humectant	<10
Polymer	<4
Water	85-95

2.3. Material Processing

2.3.1. PLA

2.3.1.1. Fused Filament Fabrication (FFF) Process

The FFF process can be divided in three steps: A) design of the 3D model (CAD software), B) the 3D model in STL format file is exported to the slicing software and, at the end of build step, a gcode file is created, which contains the path/coordinates than can be recognized by

the printer to fabricate the design 3D model; C) then the gcode is sent to the printer and the thermoplastic polymer (PLA for this study) is extruded at a selected speed and temperature. Each one of the steps is described in detail as follows.

Design

A CAD software (Autodesk Inventor 2014, Autodesk, USA) was used for designing the PLA 3D porous models. As shown in *Fig.2. 1*, the design approach consisted in assembling porous layers with a selected layer height (LH) accordingly to a laydown pattern, in which each layer consisting of parallel filaments with a defined width (FW) and separated by a specific filament gap (FG).

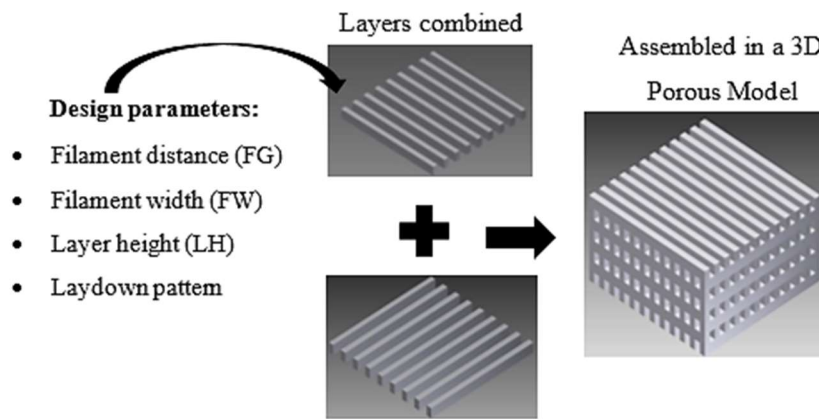


Fig.2. 1. Parameters defined during design of a 3D porous model with CAD drawings used for assembling the porous model.

The laydown pattern of 0/90 degrees was favoured to obtain a cube shaped porous structure to obtain a structure with equivalent accessibility from all three major axes. The number of combined layers (n) will depend on the desired thickness (T) of the final printed part and on the LH value: $T = nLH$.

Build

After 3D model design step, the file was exported in STL format to the build software (Cura, Ultimaker, Netherlands) where it was sliced into horizontal layers with a defined thickness (ST).

For the commercially FFF machine used in this study, the ST values ranged from a minimum of 0.06 mm (defined by FFF machine XYZ resolution) to a maximum of 0.4 mm (defined by FFF machine nozzle diameter). When a fully dense model is imported, the ST value represents the number of slices that the model will be converted to, influencing part quality

and fabrication time. For instance, lower ST values will result in more slices, higher part quality and longer fabrication times.

However, in this study, the imported 3D model was designed as an assembly of porous layers (Fig.2. 1), thus the slicing software interpreted this model differently than a dense one. For a three-dimensional porous model, the select ST value represented the number of slices of each layer characterised by a LH value (defined during the design step). For instance, if LH=0.60 mm and ST =0.20 mm (Fig.2. 2) one layer defined during design step would result in “three slices per layer” during FFF process. While if LH=0.50 mm and ST =0.25 mm, one layer defined during design step would result in “two slices per layer”.

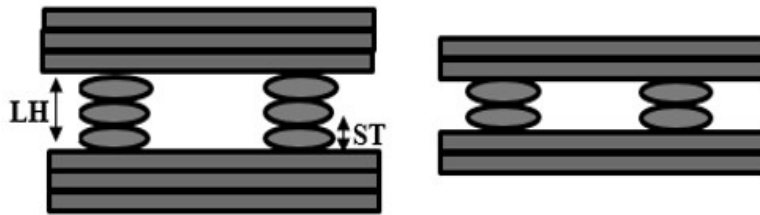


Fig.2. 2. Relation between slicing thickness (ST) (defined during build step) and layer height (LH) (defined during design step) resulting in three slices per layer approach.

Printing

At the end of build step, a gcode file was created, which contained the path/coordinates that can be recognized by the printer to fabricate the 3D model. Then the gcode was sent to the printer (Ultimaker 2, Fig.2. 3), which uses a temperature controlled nozzle ($\varnothing 0.4$ mm) to extrude the PLA and deposit the semi-molten material onto a platform in a layer by layer process.

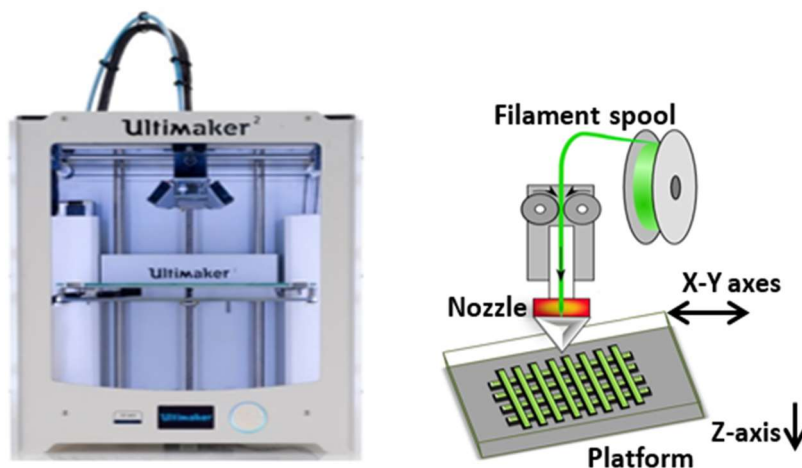


Fig.2. 3. Fused Filament Fabrication machine (FFF) commercially available machine (Ultimaker 2) used for fabricating PLA scaffolds and diagram explaining the process.

The filament is moved by two rollers and acts as a piston to drive the semi-molten material. At the end of each finished layer, the platform is lowered and the next layer is deposited (Fig.2. 3). The designed object is fabricated based solely on the precise deposition of thin layers that are made of parallel filaments deposited in X and Y directions. Parameters such as printing speed and printing temperature need to be carefully chosen to achieve a constant flow rate and consequently a constant filament width (FW) with a minimal fabrication time.

2.3.1.2. Laser cutting

The laser cutting (LS3020, HPC Laser LTD, UK) system represented in Fig.2. 4 was used to obtain smaller PLA scaffolds from a printed porous bar prepared with the FFF process described in the previous section. Hence, parameters, such as laser power and speed were optimised to obtain open pores structures with minimal polymer (PLA) melting.

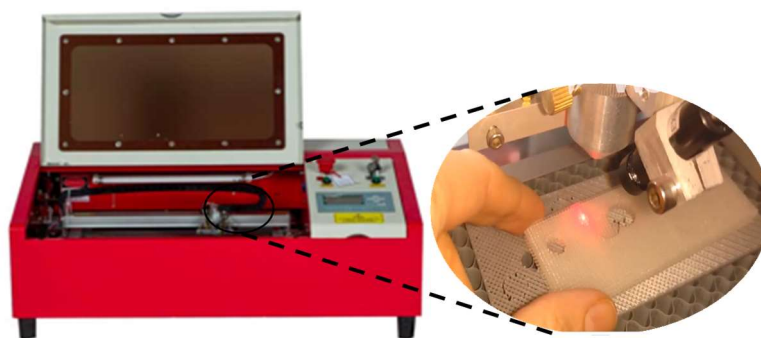


Fig.2. 4. A Laser cutting machine (LS3020, HPC Laser LTD, UK) used for fabricating PLA scaffolds from printed porous bar.

2.3.2. AW and MD

2.3.2.1. Milling and sieving

A one-bowl ball mill machine (Planetary Mono Mill Pulverisette 6, Fritsch GmbH, Germany) (Fig.2. 5.A) was used to grind AW batches and MD powders to the necessary fineness by friction and impact with alumina balls. After milling, the powders were sieved towards specific particle size ranges with a mechanical sieve shaker (Fig.2. 5.B).

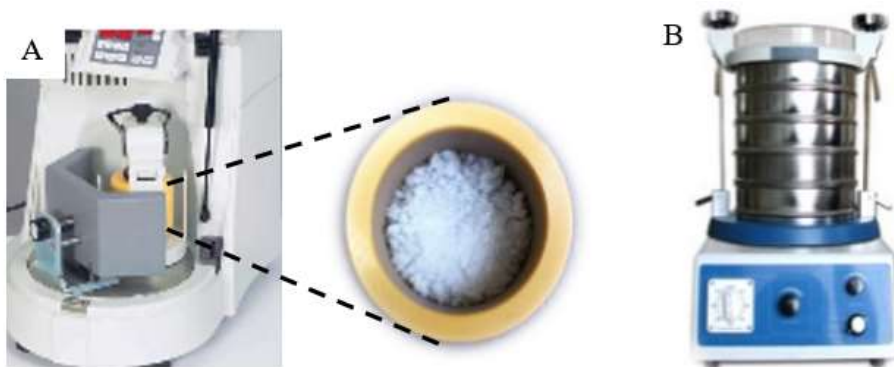


Fig.2. 5. Equipment used for preparing MD and AW powder: A. one-bowl ball mill machine and B. Mechanical Sieve shaker.

2.3.2.2. Roller mixing

Before the printing process, to achieve a homogeneous mixture, the two base materials (70wt.% of AW powders and 30wt.% of MD) were blended for 3h using a roller mixer (Stuart, SRT6, UK) (Fig.2. 6).



Fig.2. 6. Roller mixer used for mixing MD and AW powders into a powder blend.

2.3.2.3. Vacuum drying

The equipment used for vacuum drying the powders used during the indirect 3D-printing process was a vacuum oven (Svac1, Shel Lab®, US) (Fig.2. 7). For this study powders were dried during 4 hours with a set temperature of 60°C and a pressure of -29.4 in Hg (inches of mercury).



Fig.2. 7. Vacuum drying oven used in this study.

2.3.2.4. 3DP Process

In the present study, a commercial (ZPrinter 310 Plus 3D printer, Z Corp., USA) (Fig.2. 8.A) was used for processing the prepared powder blends into 3DP parts.

As highlighted in Fig.2. 8., the 3DP process can be described by the following steps: firstly, the black ink is purged out from the commercially available HP 10 print head (Fig.2. 8.B) and the binder (zb60 clear binder, Z Corp., USA) is added or refilled (Fig.2. 8.C). The next step is to prepare the build area by filling the feed container with powder and the air is removed from the powder by compacting the bed several times until it feels firm. By pressing the powder slowly with a tamp until a smooth, flat, and compact surface is obtained (Fig.2. 8.D). Then, using the control panel, the build piston is moved up until it stops and the feed piston is moved up until the surface of the powder reaches the top deck. Finally, the spread button is pressed to spread the powder onto the build area (Fig.2. 8.E). At this stage, everything is prepared for starting the 3DP process.

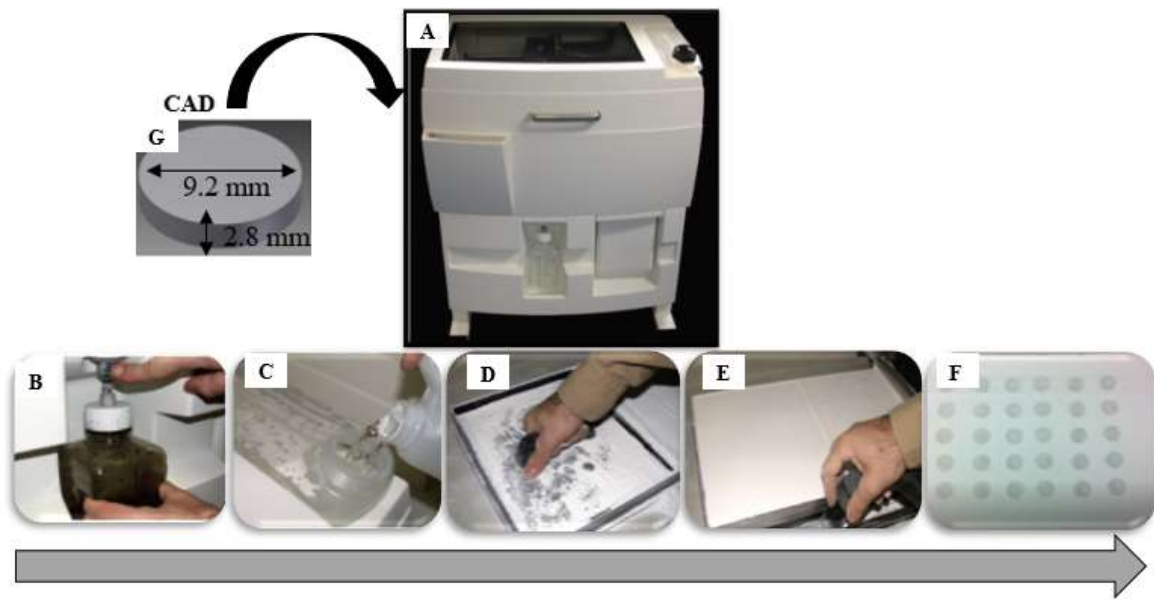


Fig.2. 8. 3D Printing process main steps and equipment: A. ZPrinter 310 Plus 3D printer (Z Corp., USA), B. Purging the print head, C. Refilling the binder bottle with ZB60, D. Powder compaction, E. Powder spreading from feed to build areas, F. Build area at the end of 3DP process and G. CAD model.

Sample geometry was controlled by design step of a 3D model, using a CAD software (Autodesk Inventor, Autodesk, USA). For this study discs (8 mm x 2 mm) were chosen for the testing geometry (Fig.2. 8.G). The CAD files were saved in *.STL file format, then transferred to the 3DP software that sliced the model into two-dimensional layers. The structures were then built layer by layer from the bottom of the part to the top (Fig.2. 8.F), with the printing parameters described by (Mancuso et al. 2017): a layer thickness of 0.1 mm

was used, the binder/volume ratio of the shell was 0.21 and that of the inner core of the layers was 0.1.

2.3.2.5. Post-Processing

Post-processing begins after creating the AW green part by 3DP and it consists of two steps: 1) de-powdering: after green parts were left to dry overnight, samples were taken out the build area and any unbounded powder particles were removed with an air blower, followed by 2) sintering cycle, where green parts were heated in a chamber furnace (Carbolite, 1200 °C, Company, City, Germany) in ambient air. The sintering step of green parts consists in burning off the MD binder, and consolidate the AW powder particles to obtain the desired mechanical properties, in order create a solid porous structure.

In this study the starting point for the thermal processing of 3DP AW green parts was the protocol developed by Xiao et al. (Xiao et al. 2008), represented as SINT I in Fig.2. 9: where samples are initially heated through up to 779°C at a heating rate of 10°C/min to burn off the binder and hold for one hour for nucleation and growth. Then temperatures increase up to 1150°C with a heating rate of 10°C/min to sinter the powder particles to get a stronger part but with a solid porous structure and hold for one hour, to allow crystal growth. Finally, the samples are left in the furnace to cool down with no controlled rate. Besides the heat treatment developed by Xiao et al. 2008 (SINT I), two other heat treatments (SINT II and SINT III) were evaluated in this study. The rationale behind the design of heat treatments SINT II and SINT III is explained based on the results obtained with SINT I, as described in the section 4.5.3.1. Sinterability study.

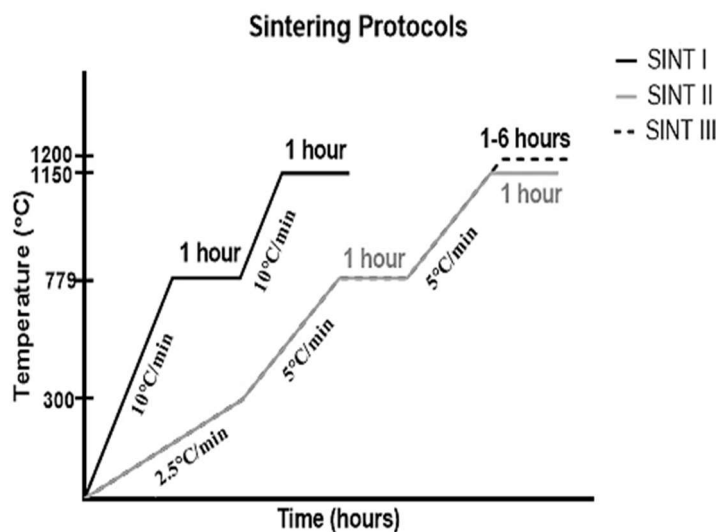


Fig.2. 9. Thermal post-processing cycles used in this study to sinter the 3DP green parts: SINT I is the protocol developed by (Xiao et al. 2008) and SINT II and SINT III were developed in this study.

2.3.3. PLA-AW Composite Structures Assembly

The composite structures were assembled with two approaches :1) thermal bonding and 2) ultrasonic welding, as described in the next sections.

Both approaches rely on the local melting of PLA, that integrates with the porous AW contacting surface once it cools down. The main difference between the two approaches was the principle used to promote adhesion between PLA and AW. For instance, the thermal bonding was just based on the softening effect of PLA upon contact with the pre-heated AW part. While the ultrasonic welding, uses ultrasonic energy that promotes friction and thus local PLA melting, leading to its integration with the AW part.

2.3.3.1. Thermal Bonding

The thermal bonding process is illustrated in the schematic diagram in Fig.2. 10.A-C and it consisted of preheating (A), bonding (B) and quenching (C) phases.

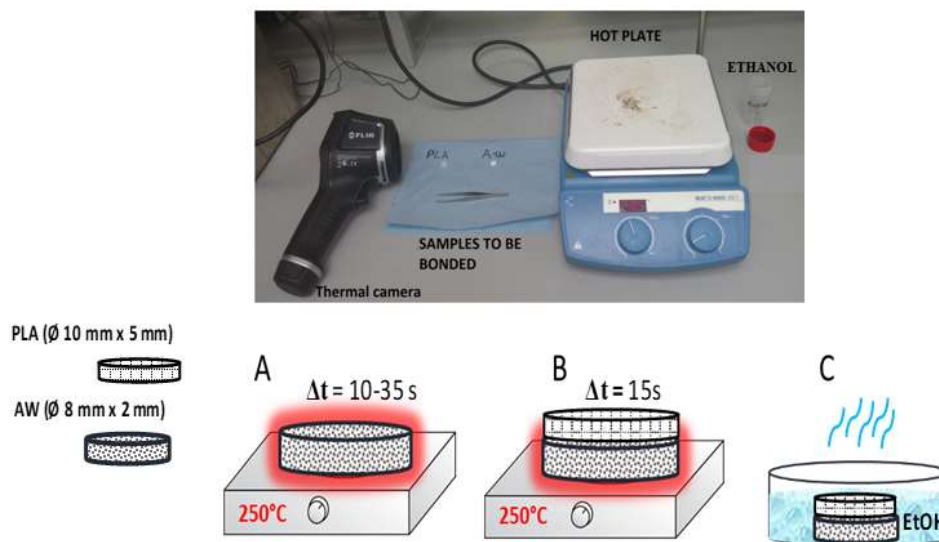


Fig.2. 10. Thermal Bonding of AW and PLA Composite Structures: Top image: set-up and bottom image: schematic diagram: A. AW Preheating, B. Bonding and C. Quenching.

Initially, the AW discs were placed on a standard laboratory hot plate set to 250°C and heated for 10-35 seconds and the surface temperature was monitored with a thermal camera (FLIR® E-Series, USA). A PLA disc was then positioned, as to be concentric, on the top surface of the AW disc. The PLA was allowed to thermally adhere to the surface of the AW for a set time of 15 seconds before being quenched in pure ethanol. The composite structures were then set aside to allow any ethanol remaining after quenching to evaporate.

2.3.3.2. Ultrasonic Welding

An ultrasonic welding machine (Sonics® 2050 model, Sonics®, USA), shown in Fig.2. 11.A was the equipment used in this approach. Depending on welded samples geometry, oval-shaped sonotrode (Fig.2. 11.B) or square shaped sonotrode (Fig.2. 11.C) were selected.

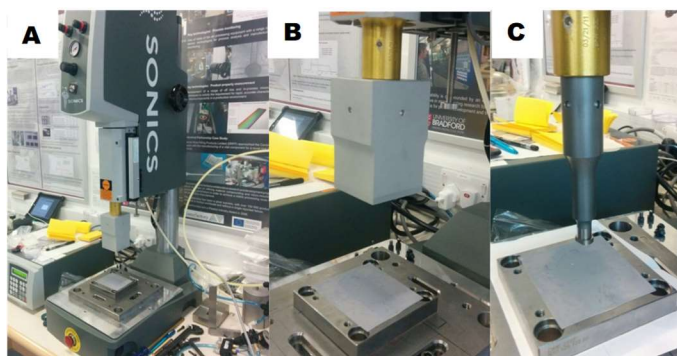


Fig.2. 11. Ultrasonic Welding machine from Bradford University used in this study: A. General overview of the set-up, B. square shaped sonotrode and C. oval shaped sonotrode.

During welding, the sonotrode vibrates at low amplitude and high frequency, for a set amount of time, transferring the energy to the contacting surfaces. The sonotrode starts at a selected distance from the sample and a set pressure, amplitude and energy are applied during welding for a set time.

2.4. Materials Characterisation

2.4.1. AW and MD

Various techniques were applied for the characterization of the AW and MD powders across different batches, including X-ray photoelectron spectroscopy (XPS) and X-ray fluorescence (XRF) to determine the surface and bulk composition of AW particles. Scanning electron microscopy (SEM) to visualize AW and MD particle morphology, x-ray diffraction (XRD) to check the amorphous nature of as-received AW glass and a laser diffractometry to determine the particle size distribution (PSD) of the AW and MD powders. The thermal properties and sintering behaviour of AW powders were studied with differential scanning calorimetry (DSC) and hot stage microscope (HSM).

After processing, the obtained AW structures morphology was characterised by SEM and crystallinity after sintering was obtained with XRD analysis. The mentioned techniques are described below.

2.4.1.1. X-ray Fluorescence (XRF)

AW batches were analysed by X-ray fluorescence analysis (XRF) to verify the stoichiometric composition of the prepared samples. A MagiX Super Q Version 3.0 Phillips X-ray fluorescence spectrometer (Philips, Netherlands) was used. This spectrometer is equipped with IQ+ analytical software used for qualitative and semi-quantitative analysis. Calibration curves were fitted from the certified standards consisted of natural and synthetic calcium phosphates and calcium silicates. For X-ray fluorescence analysis, the glass ceramic samples and standards were prepared as glass beads by lithium tetraborate fusion in a Perl'x2 machine (Philips, Netherlands). The powdered sample (0.3 g) and the flux (5.5 g of $\text{Li}_2\text{B}_4\text{O}_7$) were mixed and heated in a Pt-5 wt% Au crucible at 1100 °C. The molten mixture was cast as amorphous glass bead suitable for analysis.

Three replicates of each AW batch (AW1 and AW2) were prepared in Newcastle University by sieving powders towards < 53 μm particle size range and send to Glass Technology Services (GTS) Ltd (Sheffield, UK) that performed the analysis.

2.4.1.2. X-ray photoelectron spectroscopy (XPS)

To quantitatively evaluate the AW surface composition, X-ray Photoelectron Spectroscopy (XPS) analysis was performed using a Theta Probe Angle-Resolved X-ray Photoelectron Spectrometer System (Thermo Scientific, East Grinstead, UK).

The equipment used a micro-focused monochromatic $\text{AlK}\alpha$ X-ray source with an energy of 1486.6 eV, a 6.7mA emission current and 15 kV anode potential that operated with a 400 μm spot size (100 W power). Survey spectra were collected at take-off angles of 20° to 80° relative to the sample surface and pass energy of 200 eV, with the spectrometer operating in standard (not angle-resolved) lens mode.

The results were expressed as the average of three points of each sample surface. Data analysis and charge correction were carried out using Casa XPS software (Version 2.2.107). Samples (2-5 g) of each one of AW batches (AW1 and AW2) were prepared by sieving towards <20 μm particle size range and manual compacted in a double-taped aluminium foil substrate.

2.4.1.3. Differential Scanning Calorimetry (DSC)

Measurements were performed using a simultaneous thermal analysis (Labsys Evo, Setaram® Caluire, France). Samples were added to platinum crucibles and loaded into the chamber and

empty platinum crucible with the same weight as the sample crucible was used as reference. Samples were heated from 25°C to 1400 °C at a rate of 10 °C/min in argon atmosphere. Pure alumina powder (Sigma-Aldrich) was used as reference material and for baseline determination.

Melting temperatures (T_m) were obtained at the peak of melting endotherms and glass transition temperatures (T_g) were acquired at the inflection point of the specific heat capacity. Samples of approximately 30-50 mg in mass of each one of AW batches (AW1 and AW2) were prepared in three particle size ranges: 1) <20 µm, 2) 54-90 µm and 3) 90-200 µm.

2.4.1.4. Hot stage microscopy (HSM)

HSM allows the quantification of the shrinkage due to sintering by measuring the variation of the samples dimensions during a controlled heating process. The sintering process of the AW powders was monitored by hot stage microscopy (HSM) (Misura®, Expert System Solutions, Italy), performed in air atmosphere to simulate the chemo-environmental conditions of the furnace chamber.

The samples for HSM analysis were prepared by mixing AW powders (2-5g) with a small amount of distilled water (DI), enough to prepare a paste, followed by manually pressing the obtained paste into a small cylindrical die (2x3mm) which was then placed on an alumina support (10x15x1mm). The specimens were observed by a video-camera and the photos of their silhouettes were registered up to 1350°C at a heating rate of 10°C/min. The samples shrinkage was calculated at specific temperatures from the variation of the samples area, using the following equation (equation 1):

$$shrinkage (\%) = 1 - \frac{A_T}{A_0} \times 100 \quad (\text{Equation 1})$$

where A_0 (mm^2) is the area of the sample at room temperature and A_T (mm^2) is the area at temperature T (°C).

Samples (2-5g) of each one of AW batches (AW1 and AW2) were prepared in three replicates with two particle size ranges: 1) <20 µm, 2) a mix of 50% of <20 µm with 54-90 µm. Then one representative plot and silhouettes images acquired were selected for each condition.

2.4.1.5. Particle size distribution (PSD)

The powder particle size distribution of particles in a suspension (dry powder method) was measured by using the light scattering technique on a Malvern Mastersizer 3000 (UK) located

at Nottingham University. Laser diffraction is used to measure the size of particles through measuring the intensity of light scattered as a laser beam passes through a dispersed particulate sample. Data is then analysed to calculate the size of the particles that created the scattering pattern.

To define the distribution width, three values on the x-axis were obtained, the Dx (10), Dx (50), and Dx (90). The Dx (50), the median, has been defined above as the diameter where half of the population lies below this value. Similarly, 90 percent of the distribution lies below the Dx (90), and 10 percent of the population lies below the Dx (10).

Samples (10-20g) of AW and MD powders were analysed before and after preparing the powder blends. Three replicates of each sample were prepared in Newcastle University and send to a PhD student (Priscila Melo) that run the analysis.

2.4.1.6. Scanning Electron Microscope (SEM)

An electron microscope, (Philips XL30 ESEM FEG) was used across several AW processing stages: 1) AW and MD powders morphology and particle size distribution before and after powder blends preparation and 2) processed AW structures top microstructure before and after sintering.

For all analysed samples, before the imaging acquisition, the specimens were sputtered with a thin layer of gold (approximately 10nm, sputter time 40s, at 40mA), and afterwards analysed. All the images were taken at an operation voltage of 20 kV, and working distance between 5 and 10mm. The SEM software was used for 5 to 10 measurements of particle dimensions (length and width).

2.4.1.7. X-ray diffraction (XRD)

XRD analysis was performed using a PANalytical X'Pert Pro MPD, powered by a Philips PW3040/60 X-ray generator to investigate AW crystallinity.

Diffraction data was acquired by exposing powder samples to Cu-K α X-ray radiation, which has a characteristic wavelength (λ) of 1.5418Å. X-rays were generated from a Cu anode supplied with 40kV and a current of 40mA. The data was collected over a 2θ range between 5-80° 2θ , with a step size equal to 0.0334°, a counting time per step of 200 seconds using the scanning X'Celerator detector. Fixed anti-scatter and divergence slits of 1° were used together with a beam mask of 10mm. All scans were carried out in 'continuous' mode.

Phase identification was carried out by means of the PANalytical X'Pert HighScore Plus© software, in conjunction with the ICDD Powder Diffraction File 2 Database (2004), ICDD

Powder Diffraction File 4 - Minerals (2014) and the Crystallography Open Database (February 2013; www.crystallography.net).

Samples analysed consisted on:

1. As-received AW batches (AW1 and AW2) were prepared by sieving towards $<20\mu\text{m}$ particle size range to characterise different AW batches;
2. Sintered AW structures were crushed into powders within the sinterability study performed as described in 4.2.2.3. Post-processing: Powder Blends Sinterability Study.

2.4.2. PLA

PLA thermal properties and average molecular weight (M_w) across processing stages were characterised with DSC and gel permeation chromatography (GPC), respectively. After processing, PLA porous structure morphology was characterised with SEM and Micro-CT.

2.4.2.1. Differential Scanning Calorimetry (DSC)

Measurements were performed using a simultaneous thermal analysis (Labsys Evo, Setaram®) samples of approximately 30-50 mg in mass were added to aluminium pans and loaded into the chamber and empty aluminium pan with the same weight as the sample pan was used as reference. PLA samples were extracted at different processing stages: 1) PLA filament as-received, 2) extruded/printed (FFF) part and 3) from laser cut part.

All samples were heated and cooled twice from 30 to 220 °C at a rate of 10 °C /min under Argon atmosphere. The thermal values were measured in the first heating round to examine the properties of a specific part rather than the bulk polymer. As illustrated in Fig.2. 12, the melting temperatures (T_m) were obtained at the peak of melting endotherms and glass transition temperatures (T_g) were acquired at the inflection point of the specific heat capacity.

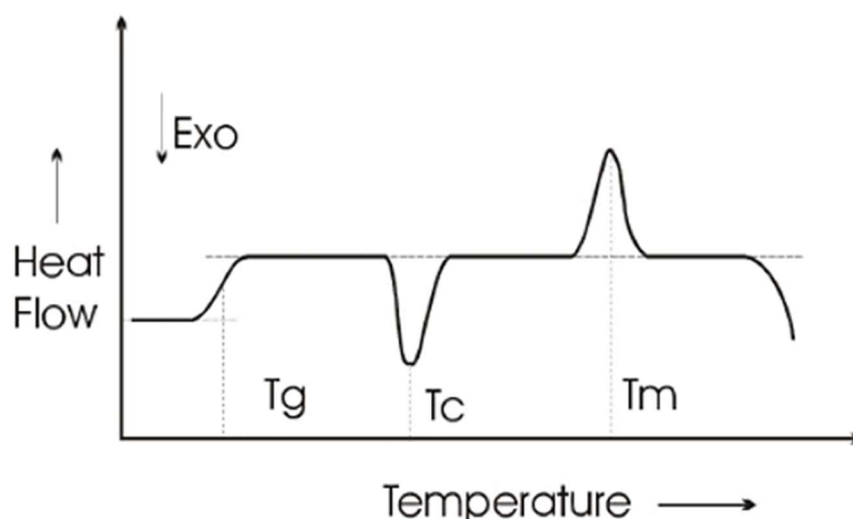


Fig.2. 12. Typical DSC curve for a polymer: T_g-glass transition, T_c-crystallisation temperature and T_m-Melting temperature.

2.4.2.2. Gel Permeation Chromatography (GPC)

PLA molecular weight distribution was determined by a gel permeation chromatograph (GPC) equipped with a refractive index (RI) detector (Viscotek VE3580). RI detectors work by assessing the difference in refractive index between the mobile phase and the pure solvent. Since the refractive index of polymers is usually constant above molecular weights of about 1,000 g/mol, the detector response is directly proportional to the sample concentration. The GPC contained two Varian PLgel 5 μ m MIXED-D columns running Dimethylformamide (DMF) with 0.1% LiBr as a solvent at a flow rate of 0.6 mL min⁻¹ at 50°C. First the PLA samples (approximately 8 mg) were dissolved in 2ml of DMF for 2-3 hours, until the polymer was completely dissolved. Then the samples were filtered through syringe filters (15 mm, 0.45 μ m pore size) and put into 2 ml vials. During GPC analysis, approximately 1 mL of each solution was injected into a 50 μ L injection loop and eluted in a series of configurations through a Styragel column refractor (Waters) at a flow rate of 0.6 mL min⁻¹. Polystyrene (PS) standards were used for determining the weight average molecular weight (M_w) and polydispersity (PDI). The PS standards were Polymer Labs EasyCal PS1-A and PS1-B each containing five polystyrenes of varying molecular masses.

PLA samples were extracted at different processing stages: 1) PLA filament as-received, 2) extruded/printed (FFF) part and 3) from laser cut part.

2.4.2.3. Micro Computed tomography (CT)

The fabricated PLA porous scaffolds were analysed with microcomputed tomography (micro-CT, Skyscan 1174, Bruker). Using the CT software, after the segmentation of the images, a 3D morphometric analysis was carried out to evaluate the pore distribution, porosity % and mean pore size. Samples were sent and analysed in Politecnico di Torino in the Institute of Materials Physics and Engineering, Applied Science and Technology Department in Italy.

2.4.2.4. Scanning Electron Microscope (SEM)

The same scanning electron microscope and protocol described above (2.4.1.6. Scanning Electron Microscope (SEM)) were used for characterising obtained PLA porous structures morphology.

2.4.3. PLA-AW Composite Structures

The interface of obtained PLA-AW composites structures was characterised in terms of morphology and interfacial shear strength.

2.4.3.1. Interface Morphology

PLA-AW composite samples were sectioned (IsoMet 5000 Linear Precision Saw, Buehler, Germany) (Fig.2. 13) with a diamond blade at a speed of 1550 RPM and a feed rate of 9.9mm/min. Then, the interface morphology was characterised by acquiring SEM images of the interface.

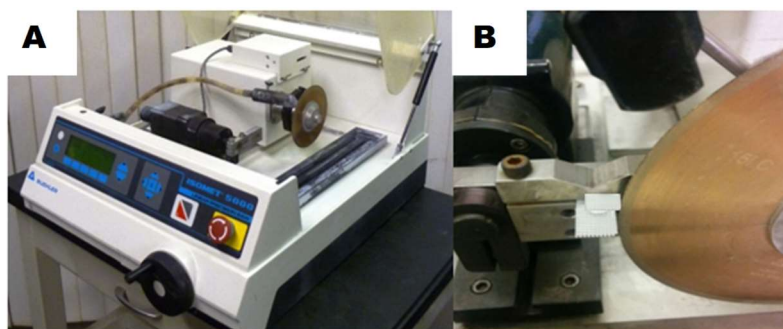


Fig.2. 13. A. Cutting equipment used in this study, IsoMet 5000 Linear Precision Saw from Buehler and B. PLA-AW sample being cross sectioned with a diamond blade.

2.4.3.2. Interfacial Shear Testing

The interfacial shear properties of the assembled composite constructs were determined by applying a shearing force at the interface region of these samples using a specially designed

jig (Fig.2. 14.B) added to an Instron Universal Testing machine (Fig.2. 14.A), this testing concept was previously described (St-Pierre et al. 2012; Allan et al. 2007). The rig design allows the secure fixation of the sample during testing while ensuring correct alignment of the scaffold between the machine's load cell and base platen. Ideally, pure shear load should be applied, and effects of compressive or tensile loads at the interface minimised.

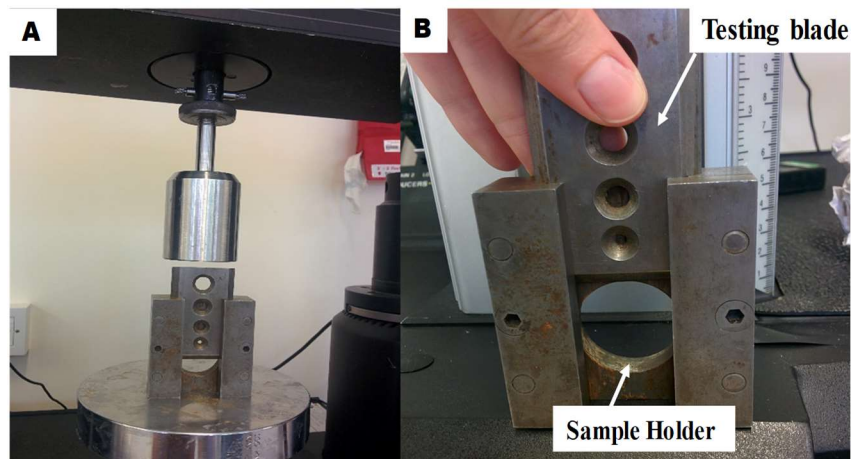


Fig.2. 14. Interfacial strength testing of assembled composite parts: A. Set-up of jig added in a universal testing machine and B. zoom in the personalised jig used.

Samples preparation (Fig.2. 15) involved embedding the composites structures in cold setting resin system that cured overnight (provided by Dental School).

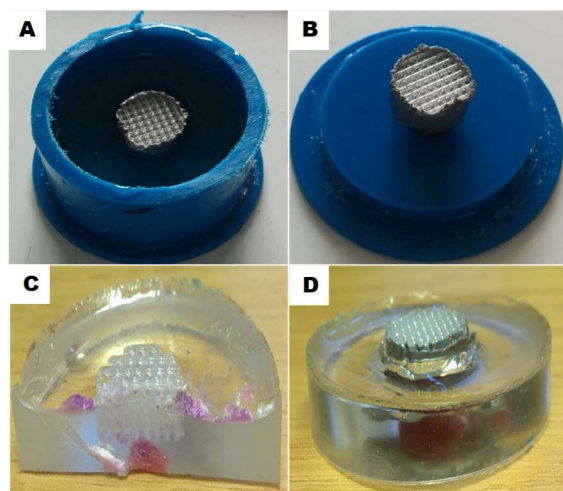


Fig.2. 15. Embedding protocol used for testing interfacial shear: A. Cold embedding 2-part HDPE moulds, B and C. Tape used for avoiding resin infiltration into the porous PLA part and D. Sample ready for testing.

Resin was mixed with a hardener to provide the mounting compound, and then the polymerization process took place overnight to form a block (Fig.2. 15.D) that would fit the sample holder (hole in the jig, Fig.2. 14.B). Cold embedding 2-part HDPE moulds (Fig.2. 15.A), with the same diameter but thicker than the hole in the jig (sample holder), were

provided. After embedding procedure, the resin surrounding the sample fit the hole in the jig, providing support during testing. The embedding procedure was optimised by adding some tape around the composite structure (Fig.2. 15.D), to avoid resin infiltration in the porous samples, as observed in Fig.2. 15.C.

Tests were performed at a crosshead speed of 1mm/min and force-displacement curves were acquired. Real-time monitoring was important as the aim was to terminate the test once the onset of initial failure occurred e.g. when a drop in the force-displacement curve occurred. In this regard, particular attention was paid to the shape of the force- displacement curve during testing so that the crosshead of the Instron machine would be stop at this point of the test, the load relaxed, thus allowing the sample to be removed immediately from the housing, for further sample characterisation.

The shear peak load at failure was determined as the point where initial failure occurred, corresponding to the highest point of the first perceived peak of the force–displacement curve, normally followed by a drop. An estimation of the interface shear strength was calculated using the peak shear load at failure divided by the total contacting area of approximately 50 mm² of the 8 mm diameter (AW disc) as reported in (St-Pierre et al. 2012).

For samples assembled with thermal bonding (TB), three samples were tested for each condition, whereas for the ultrasonic welded (UW) only two samples were tested due to time/samples preparation limitations.

2.5. Statistical analysis

The statistical significance of differences between means from the independent samples from experiments with 2 groups, was determined by an unpaired T-test. Whereas for experiments where more than 2 groups were analyzed, a one–way analysis of variance (ANOVA) followed by Tukey post hoc analysis was performed. Experimental results were considered statistical significant at 95 % confidence level ($*p<0.05$). All analyses were run using the Graph Pad Prism® software (Version 6.0; GraphPad Software, Inc., San Diego, CA). According the software, statistical difference was significant ($*p<0.05$), whereas P-values $< 0.001(**)$ were considered very significant. The results are presented as the mean \pm standard deviation (SD). For the mechanical characterisation results were presented as an average value of five measurements \pm SD.

CHAPTER 3. Manufacture and Characterisation of PLA Porous Structure

3.1. Introduction

A porous three-dimensional (3D) scaffold acts as a template for tissue regeneration, guiding cells to form functional and new tissue (Bose et al. 2012). Ideally a bone scaffold must be biocompatible, biodegradable, have the appropriate porosity range and interconnectivity, readily available and easy to manufacture (Grayson et al. 2008; Schaefer, Martin, G Jundt, et al. 2002; B Mollon et al. 2013). Several groups have reported the importance of scaffold pore size in successful bone ingrowth (Karageorgiou & Kaplan 2005).

Scaffolds with pores bigger than 0.3 mm were associated with greater penetration of mineralized tissue and cell migration towards the scaffold centre, stimulating nutrient supply and waste products removal (Murphy & O'Brien 2010; Jones et al. 2004). Fused filament fabrication (FFF) offers the ability to directly print 3D porous structures with pre-designed shape, solvent-free, controlled pore size and interconnected porosity. Also, commercially available FFF machines can be considered a low-cost system when compared to other AM techniques. However, one of the drawbacks of the FFF process is that fabricated 3D porous scaffolds are often characterised by closed edges instead of open porosity. At time of scaffold implantation, these closed edges can affect cell-biomaterial interaction by decreasing nutrients and waste products flow and affecting vascularization, which is essential for tissue growth (Park et al. 2011; Lu et al. 2000). The current solution for achieving a structure with surrounding open pores involves cutting the edges of the fabricated scaffold (Korpela et al. 2013).

Therefore, the aim of this study was to manufacture a scaffold with a controlled and open porosity by a two-step route: 1) 3D printing of a porous bar with a commercially available FFF machine, and 2) laser cutting smaller scaffolds from the 3D printed bar. In this study, laser cutting was used as an effective, precise and fast solution for obtaining scaffolds with desired-shape and open porosity from a pre-fabricated 3D printed porous bar.

To determine the applicability of the fabricated PLA scaffolds for bone tissue engineering, morphology and mechanical behaviour were assessed. A key issue when choosing a material for temporary tissue engineering templates is its degradation rate. It is highly desirable to ensure that the degradation rate matches the speed of new tissue regeneration at the defect site. Consequently, an *in vitro* degradation study in PBS at 37°C of the fabricated PLA scaffolds was carried out.

3.2. Scaffold fabrication

Scaffold fabrication was achieved by following the two-step manufacturing route, represented in Fig.3. 1.

Briefly, the first step consisted in printing PLA rectangular porous bars with a process called fused filament fabrication (FFF) that consists in three sub-steps (Design, Build and 3D Print). Each of the sub-steps requires parameters to be selected to obtain the desired final structure, e.g. during design, a CAD model is prepared and to obtain the build model, the correct slicing parameters need to be selected. Then the second step consisted in laser cut the discs ($\varnothing 10$ mm) from the printed bars to obtain structures with open pores. The details of each one of the steps and sub-steps are described in detail in the previous chapter: section 2.3.1.1. Fused Filament Fabrication (FFF) Process.

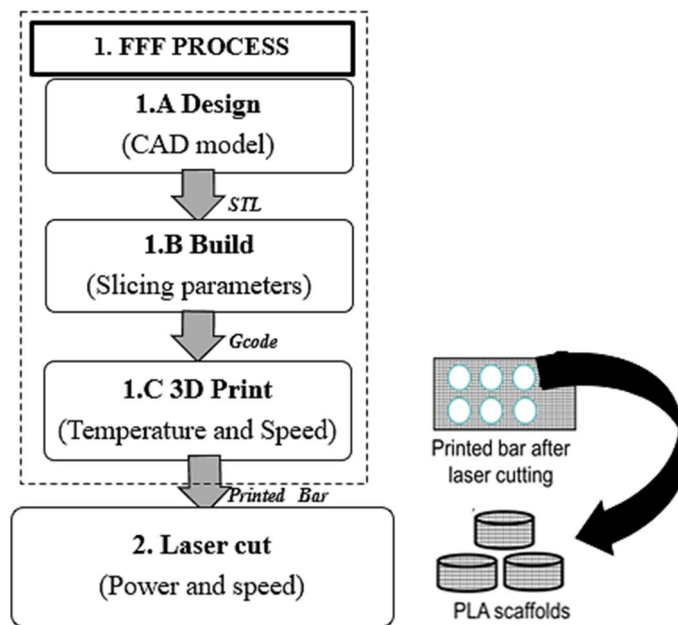


Fig.3. 1. PLA scaffolds manufacturing route steps and parameters that need to be selected for each step.

3.2.1. Fabrication Route Parameters

After performing a preliminary study where the FFF processing parameters were investigated (3.6. Results: Preliminary FFF study) the best combination of parameters was selected to obtain a pore size of 0.50 mm in XYZ-planes (Table 3. 1). The pore size selection was to meet the scaffold requirements to fit bone tissue engineering (Murphy & O'Brien 2010; Jones et al. 2004).

Table 3. 1.FFF and laser cutting processing parameters used in the manufacturing route.

	DESIGN	BUILD	PRINTING	LASER CUT (2x)			
Parameters	FG	LH	ST	Speed	Temperature	Power	Speed
Values	0.65	0.60	0.20	30 mm/s	210°C	12 W	6.50 mm/s

PLA porous rectangular bars (32 x 86 x 5mm) were prepared and each sample took approximately one hour for being printed. Then, ten PLA scaffolds (\varnothing 10 mm discs) were laser cut per printed bar with optimised parameters (Table 3. 1). The processing conditions used to cut the PLA rectangular porous plates were found to cut with a twice laser speed and power of 6.50 mm/s and 12 W, respectively.

3.2.2. Material Characterisation

Due to the shear stresses and melting that occur during printing and laser cutting procedures, PLA degradation may arise during processing. Therefore, PLA samples were extracted at the three PLA stages during scaffolds fabrication: 1) PLA filament, 2) Printed PLA and 3) Laser cut PLA. Then molecular weight (M_w), and thermal properties of PLA samples were respectively determined with gel permeation chromatograph (GPC) and thermal analyzer system (both techniques were described in 2.4.2. PLA).

3.3. Preliminary study: FFF Processing Parameters Investigation

This section represents the preliminary study that was carried out to investigate the FFF processing parameters influence on the obtained PLA printed porous bar. The aim of this investigation was to select the more adequate FFF parameters for fabrication of the PLA scaffold.

In more detail, Design, Build and Printing parameters (described in detail in 2.3.1.1. Fused Filament Fabrication (FFF) Process) influence on the morphology and mechanical properties of PLA porous structure was investigated (experiments described in Table 3. 2). The selected design values of FG and LH for experiment I and II were based on the desired final value of 0.50 mm for the pore size in XY-axes and XZ-axes. Then the values selected for experiment III, were based on the results obtained in the previous two experiments. Moreover the ST values for all experiments were selected to obtain the minimum number of slices per layer, within the equipment features (explained in detail in section Build from 2.3.1.1. Fused Filament Fabrication (FFF) Process).

Initially, the influence of FFF processing parameters on fabricated porous structures morphology (section 3.3.1. Morphology study) was evaluated for all the three experiments.

Then only for the experiments that showed significant differences in morphology (experiments II and III), the prepared porous structures tensile properties were evaluated (section 3.3.2. Tensile testing). For example, for experiment I, the goal was to evaluate the influence of printing speed on the morphology, therefore four samples were printed with each one representing one speed (8mm/s, 12mm/s, 20mm/s and 30 mm/s). Yet for this experiment, no mechanical testing was performed for the printed structures, because no differences in morphology were observed. On the other hand, for experiment II, the aim was to evaluate the influence of printing temperature on the morphology and four samples were printed with each one representing one temperature (190 °C, 200°C, 210°C and 220°C). Since differences in morphology were observed during experiment II, the porous structures mechanical properties were evaluated.

Table 3. 2. Influence of FFF processing parameters study on the morphology of obtained porous PLA structures. FG=filament gap, LH=layer height, ST=slice thickness, S= speed, T= temperature.

	Design		Build	Printing		Morphology	Tensile Testing
Experiments	FG	LH	ST	S (mm/s)	T (°C)	Number of samples	
I	0.50	0.50	0.25	8	210	1	NO
	0.50	0.50	0.25	12	210	1	
	0.50	0.50	0.25	20	210	1	
	0.50	0.50	0.25	30	210	1	
II	0.50	0.50	0.25	30	190	1	5
	0.50	0.50	0.25	30	200	1	5
	0.50	0.50	0.25	30	210	1	5
	0.50	0.50	0.25	30	220	1	5
III	0.65	0.60	0.20	30	210	1	5

3.3.1. Morphology study

PLA porous structures (20x20x5 mm) were prepared (as described in 2.3.1.1. Fused Filament Fabrication (FFF) Process) with the selected FFF parameters summarised in Table 3. 2. Then morphology of each of the printed structures was evaluated as described in (3.4.1. Morphology).

3.3.2. Tensile testing

Tensile testing samples were fabricated in the dumbbell-shaped standard form with dimensions conforming to ISO standard 527- 2 standard test method for tensile properties of plastics (International Organization for Standardization 2012) (Fig.3. 2.A). During the design step, the original CAD tensile model was modified with a layer by layer approach (Design in section 2.3.1.1. Fused Filament Fabrication (FFF) Process) for obtaining a porous tensile sample (Fig.3. 2.B) with controlled pore size in the XYZ.

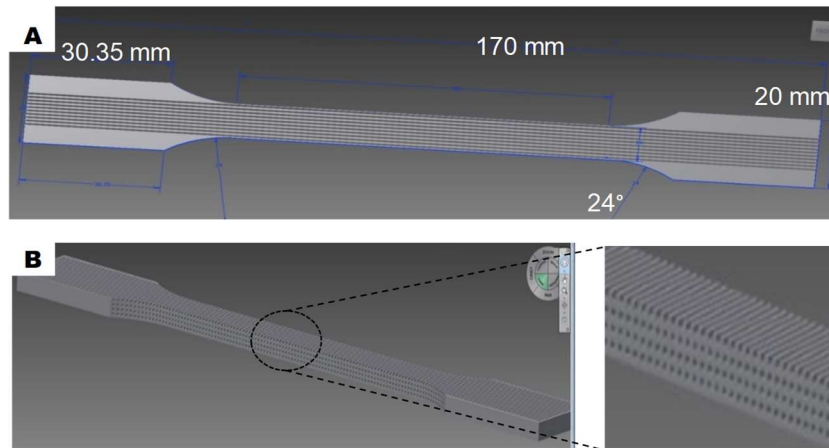


Fig.3. 2. CAD models obtained during porous tensile samples design: A. Dimensions in mm following the ISO standard 527- 2 specifications and B. Obtained tensile specimen with zoom image to highlight porous structure in the testing area.

The PLA samples with a notionally fully dense structure were also printed and tested to obtain the material tensile properties rather than the apparent/structural properties. As it is shown in Fig.3. 3, samples were tested in a Shimadzu model Autograph AG-X, by using a 50 kN load cell. The tests were carried out at a cross-head speed of 2 mm/min up to failure, where samples extension over the gauge length was recorded by an extensometer.

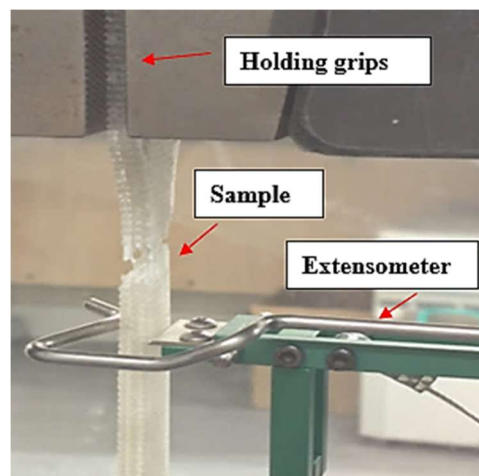


Fig.3. 3. Tensile test set-up with porous sample after failure.

A minimum of five specimens were tested for each condition and the stress-strain (σ - ϵ) curves were obtained by using the initial samples cross-sectional area or apparent area in the calculations. The apparent area was obtained by measuring the real cross-sectional area of the samples before testing, assuming a dense structure, rather than the real structure that is porous.

For porous structures, both the “apparent” Young Modulus (MPa) and the “apparent” tensile stress (MPa) were calculated from the stress-strain curve. The “apparent” Young Modulus was calculated as the slope of the initial linear portion of the stress-strain curve and the “apparent” tensile stress (MPa) was calculated as the peak stress before fracture.

3.4. Scaffolds Morphological and Mechanical Testing

3.4.1. Morphology

Morphological analysis was carried out with a scanning electron microscope (SEM) to visualize and evaluate the architecture of the obtained 3D structures and structural stability of the deposited filaments and layers. As highlighted in Fig.3. 4.A, from the top view images, pore size (PS) and filament width (FW) in the XY-axes were measured for the top layer, with this assumed to be indicative of pore sizes in the XY plane throughout the structure.

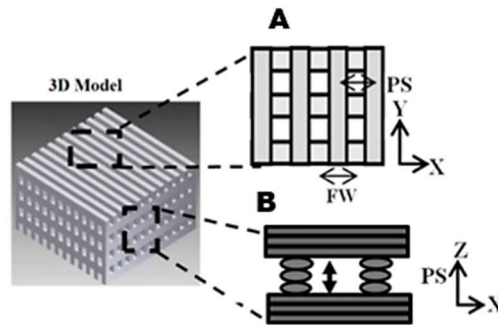


Fig.3. 4. 3D model of porous structure with: Top view or XY axes and b) Cross section or XZ axes with a 3-layer approach. PS=pore size and FW= filament width.

The PS in XZ-axes or PS in the transversal direction was measured from the cross-section images (Fig.3. 4.B) after cutting the sample with a scalpel. The PS and FW values were obtained by an average of five measurements and expressed as mean \pm standard deviation (SD).

The average PLA structures porosity (P) was evaluated by the following Equation 2:

$$P = 1 - \rho_{scaffold} / \rho_{material} \quad (\text{Equation 2})$$

Where ρ_{material} is the density of the material of which the scaffold is fabricated (PLA density= 1.24 g/cm³) and ρ_{scaffold} is the apparent density of the scaffold measured by dividing the weight by the volume of the scaffold.

The fabricated scaffolds were analysed with microcomputed tomography (micro-CT), as described in 2.4.2.3. Micro Computed tomography (CT).

3.4.2. Mechanical Testing

Compression properties of porous PLA samples at different stages of scaffold fabrication were investigated, to assess the influence of processing on the mechanical behavior.

Compression samples (10x10x20mm) were prepared with 2 routes: 1) porous samples were 3D printed with FFF machine and 2) samples were laser cut from printed porous bars. A third group of PLA samples with a notionally fully dense structure were also printed and tested to obtain the material compressive properties rather than the apparent/structural compressive properties. All samples groups were tested under axial compression by loading at a speed of 1mm/s with a 5 kN load cell up to a strain level of approximately 60%. The compression modulus was calculated from the stress-strain curve as the slope of the initial linear portion of the curve. Compressive strength at yield was determined from the first point on the stress-strain curve at which an increase in strain was observed without an increase in stress. For porous samples, the calculated properties were described as apparent or structural, because the cross-sectional area used for stress calculation was the dense one rather than the “real one”. The compression modulus and yield strength for any given set of specimens were obtained by an average of five measurements and expressed as mean \pm standard deviation (SD). To study the compression behavior of the prepared PLA scaffolds at structural level, a video-camera operating at high magnification (x90) was added to the testing set-up and videos were acquired during testing.

3.5. *In Vitro* Degradation Study

An *in vitro* degradation study of the porous PLA scaffolds (laser cut from printed bar) was carried out in PBS solution with 1.0 M concentration (Sigma-Aldrich®) under pH 7.0 at 37°C. Before immersion the samples were treated with air plasma by placing the scaffolds in a radiofrequency plasma chamber (PDC-32G, Harrick Plasma, USA) for 5 minutes with a medium inflow of air. Plasma cleaning was applied to obtain a more hydrophilic PLA surface, improving sample wetting upon immersion (Fig.3. 5.A and B). Afterwards the samples were

placed in 8ml weighing vials containing 4 ml PBS solution (Fig.3. 5.C) and were stored in an incubator (INCU-Line, VWR and Avantor, US) (Fig.3. 5.D) at 37°C for up to 10 weeks.

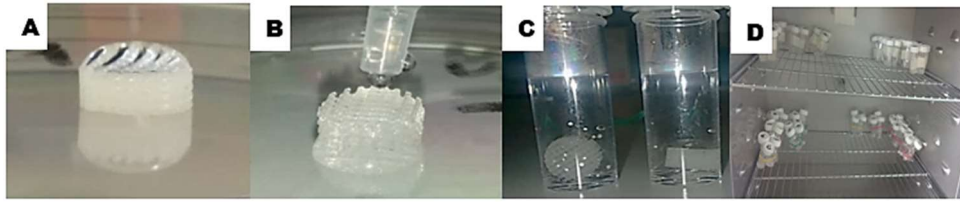


Fig.3. 5. PLA scaffold in vitro degradation study steps: A. Before air plasma treatment, B. After air plasma treatment, C. Scaffolds immersed in PBS vials and D. Vials inside incubator.

At weekly intervals, the pH of the PBS solution was measured by pH meter and then replaced with fresh PBS. At approximately 2-week intervals, 3 samples of each scaffold type were removed from the vials for characterization. Characterisation of samples consisted in assessing the compressive properties with samples still in a wet state (with the procedure described previously in 3.4.2. Mechanical Testing). Due to the destructive nature of compression testing, another group of samples was vacuum dried for 48h and was characterised in terms of scaffold morphological evolution (as described in 3.4.1. Morphology) and sample dry weight was recorded with an analytical balance. Moreover, a small amount of material was selectively taken to guarantee that it was representative from the PLA scaffold edges and dry samples molecular weight (M_w) was characterised with GPC (as described in 2.4.2.2. Gel Permeation Chromatography (GPC)).

3.6. Results: Preliminary FFF study

3.6.1. Morphology

The average pore size measurements in XYZ of porous PLA structures obtained in experiments I and II (printing parameters) and III (design parameters) were summarised in Table 3. 3. The obtained PLA porous structures SEM images of top view (acquired for all experiments) and cross section (acquired just for experiment II and III) are shown in Fig.3. 6, Fig.3. 7 and Fig.3. 8, respectively. The average pore size XZ measurements structures printed for experiment I were not performed because of the lack of differences observed in the pore size in XY.

Table 3. 3. Morphological features values of fabricated porous PLA structures. The presented values are an average of 3 measurements with \pm SD.

Printing Temperature (°C)	Speed (mm/s)	Designed pore size values (FG and LH) (mm)	Filament Width (FW) (mm)	Average Pore size XY (mm)	Average Pore size XZ (mm)
210	8	0.50 and 0.50	0.65 ± 0.02	0.29 ± 0.01	--
	12		0.65 ± 0.02	0.29 ± 0.01	--
	20		0.65 ± 0.03	0.29 ± 0.01	--
	30		0.64 ± 0.02	0.30 ± 0.01	--
190			0.62 ± 0.02	0.32 ± 0.01	0.32 ± 0.01
200			0.63 ± 0.03	0.31 ± 0.01	0.29 ± 0.004
210	30	0.50 and 0.50	0.64 ± 0.02	0.30 ± 0.01	0.29 ± 0.003
220			0.66 ± 0.02	0.29 ± 0.01	0.27 ± 0.01
210	30	0.65 and 0.60	0.64 ± 0.02	0.55 ± 0.02	0.52 ± 0.02

After printing with different speeds, the top view SEM images of prepared PLA porous structures (Fig.3. 6) did not show any significant differences. This was confirmed by the average pore size measurements that were ~ 0.29 mm (Table 3. 3). Moreover, it was observed that when printing temperature rise resulted in a slightly increase in filament width and in a pore size increase in both XY and XZ planes. Regarding cross section view (right side SEM images in Fig.3. 7) a printing temperature of 190°C resulted in slices distinction, whereas for 220°C there were visual signs of material degradation across and within layers (this was more evident on the samples at macro level, that presented burnt areas). Printing at 210°C resulted in uniform and improved inter-slices adhesion. Overall printing with different speeds and temperatures lead to an average pore size in XY and XZ around 0.29 to 0.32 mm (Table 3. 3), which was inferior than the value defined during design step (0.50mm).

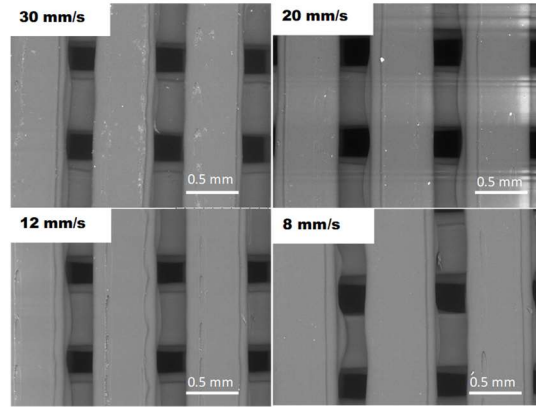


Fig.3. 6. SEM images (top view) obtained during experiment I: printing speed influence on morphology characterisation of porous structures prepared with constant values of FG and LH=0.50 mm, ST=0.25mm, T=210°C.

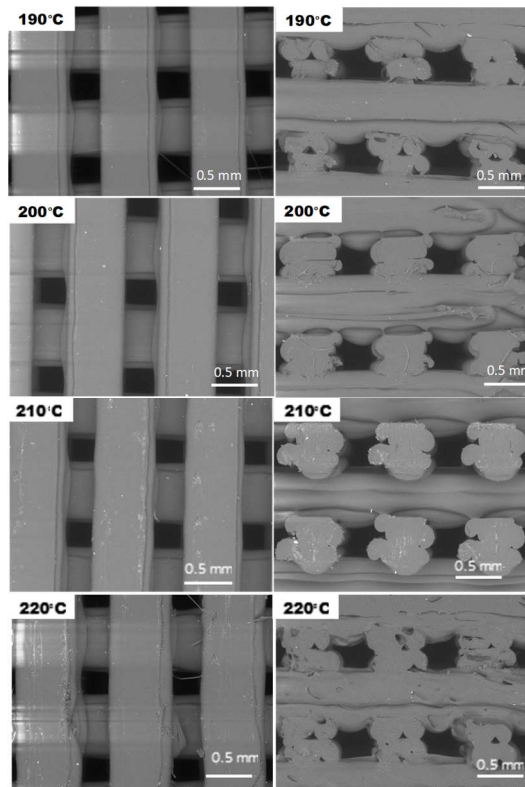


Fig.3. 7. SEM images (left: top view and right: cross section) obtained during experiment II: temperature influence on morphology of porous structures prepared with constant values of FG and LH=0.50 mm, ST=0.25mm, S=30 mm/s.

The resulting porous structures morphology when the design parameters (FG and LH) values were increased from 0.50 mm (Experiment I and II) to 0.65mm and 0.60 mm, as respectively shown in Fig.3. 7 and Fig.3. 8. This approach resulted in average pore size of ~0.55 and ~0.52 mm for XY and XZ planes which were very closed to the values defined during design for the FG and LH. Also, a 3-slice per layer approach was observed as defined during design, with excellent adhesion between stacked slices, as it was previously observed for the 2-slice per layer approach (Fig.3. 7: 210°C).

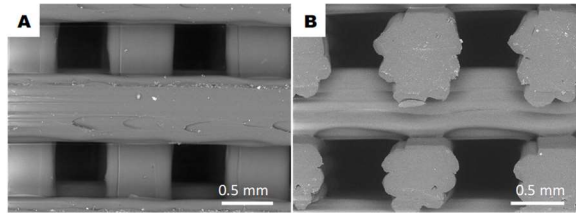


Fig.3. 8.SEM images (left: top view and right: cross section) obtained during experiment III: design and build parameters influence on morphology of porous structures prepared with constant values of $S=30$ mm/s and $T=210^{\circ}\text{C}$.

3.6.2. Tensile Testing

The influence of printing temperature and design parameters (experiment II and III, Table 3. 3.) in porous PLA structures tensile properties is illustrated in Fig.3. 9 and Fig.3. 10.

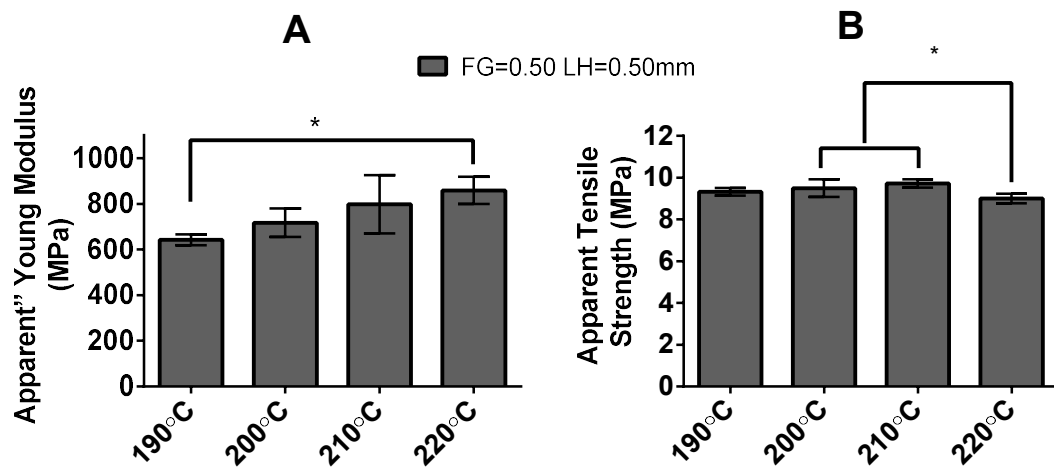


Fig.3. 9. Effect of printing temperature on tensile properties: A. Apparent Young Modulus and B. Apparent Tensile Strength.

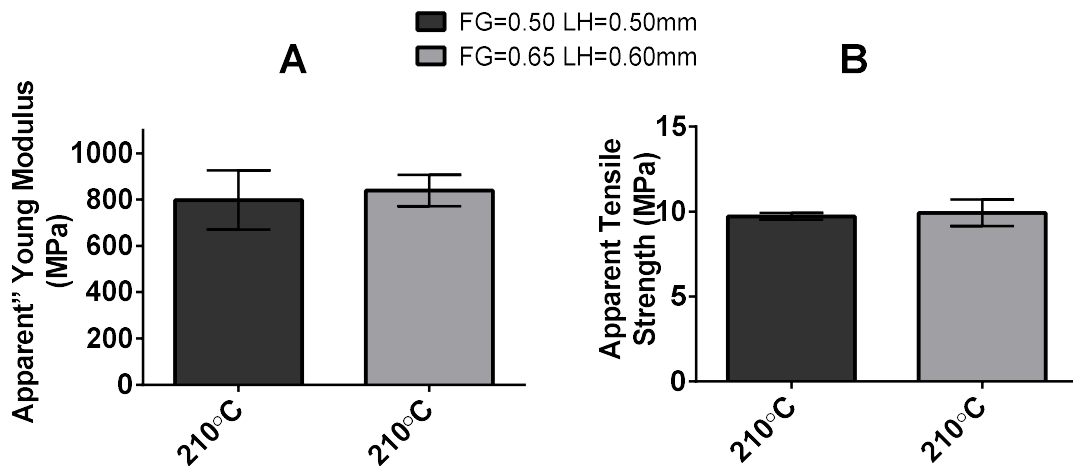


Fig.3. 10. Effect of design and build parameters on tensile properties: A. Apparent Young Modulus and B. Apparent Tensile Strength.

There was a significant decrease of Young Modulus of obtained PLA porous structures, when printing temperature decreased (Fig.3. 9). Regarding the tensile strength, a significant difference was found from 220°C to 200°C temperature range. On the other hand, the tensile

properties of porous PLA structures fabricated with different design parameters were very similar (Fig.3. 10).

Tensile properties of porous PLA structures were very statistically different than dense PLA samples printed with the same temperatures as shown in Fig.3. 11. Regarding the material properties (dense samples) rather than structural properties (porous samples), higher printing temperatures resulted in a significant increase in the tensile strength.

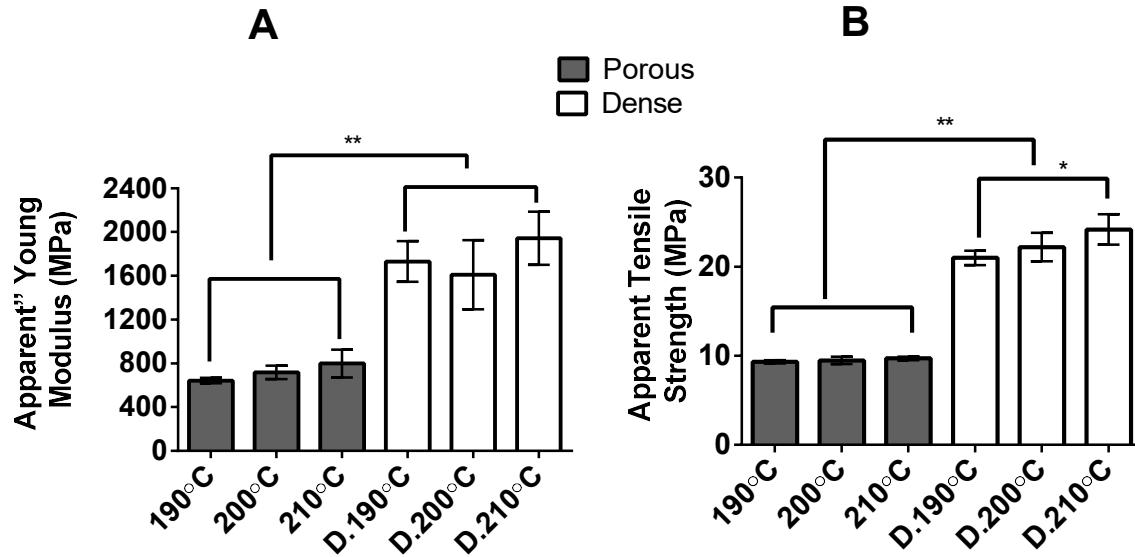


Fig.3. 11. Structural (porous) versus material(dense) tensile properties: A. Apparent Young Modulus and B. Apparent Tensile Strength. Porous samples design (LH and FG=0.50 mm).

3.7. Results: Scaffolds Fabrication

PLA scaffolds (Fig.3. 12.B) were successfully laser cut from a printed porous bar (Fig.3. 12.A). As observed in Fig.3. 12.b1, the laser cut samples presented a well-defined structure with open pores, while the printed samples showed smaller pores with non-uniform edges and pore size, highlighted by differences on Fig.3. 12.a1 and Fig.3. 12.a2.

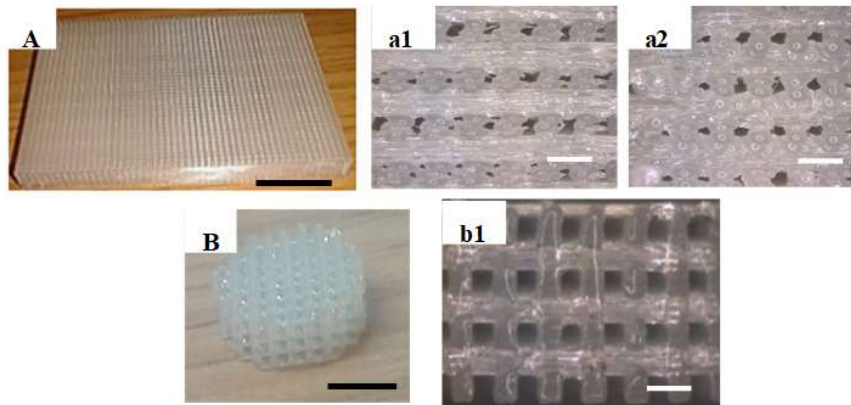


Fig.3. 12. PLA scaffold fabrication process. A. Porous PLA printed bar sample (experiment III) with zoom at edges a1 and a2, B. Laser cut disc from A. with b1. Laser cut disc surrounding edges. White scale bar represents 1mm and black bar represents 4mm.

3.8. Results: Material Characterisation

Table 3. 4 shows the results of DSC and GPC analysis of PLA at different processing stages. It can be observed that the M_w value of PLA decreased approximately 23% during FFF processing. The same trend was observed for the glass transition temperature that has shown a decrease from 68°C to 61°C. On the other hand, the slightly decrease of M_w , and T_g , observed after laser cutting was not significant.

Overall the values of PDI and TM did not point to any trend.

Table 3. 4. Values obtained from GPC (M_w and PDI) and DSC (T_g and TM) analysis of PLA at different stages of processing.

	M_w (Da)	PDI	T_g (°C)	TM (°C)
PLA.Filament	190 802	1.22	68	173
PLA. Printed Bar	147 717	1.29	61	172
Laser.Cut.PLA scaffold	144 352	1.33	62	171

3.9. Results: Morphological and Mechanical Behaviour of PLA scaffold

3.9.1. Morphology

SEM and micro-CT images of top view, cross section and edges of laser cut PLA scaffold are presented in Fig.3. 13.

From both top and cross-section views, it is possible to observe a uniform pore distribution and well-defined geometry. Also, in the cross-section view (Fig.3. 13.B and b), the scaffolds were characterised by a good interlayer adhesion and each layer is represented by 3 slices as defined during build step in the “3-slice per layer approach”. Different morphology was observed at the scaffold edges (Fig.3. 13.C and c) with a mix of pore geometries: together with the cubic pore observed in the cross-section images, a more rounded pore geometry, as pointed with arrows, was also observed.

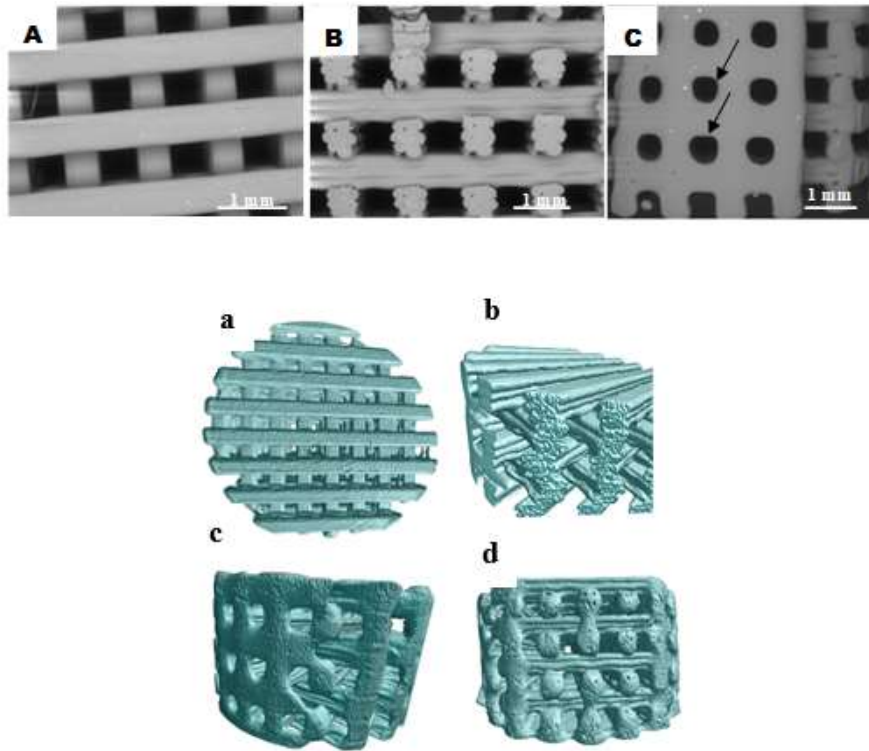


Fig.3. 13. Top images: SEM images (40x magnification) of laser cut PLA scaffold. A. Top view, B. Middle cross-section and C. scaffold edges with black arrow pointing towards rounded shape pores. Bottom images: Micro-CT analysis images of laser cut PLA scaffold. a. Top view b. Middle cross-section. c and d. scaffold edges.

The measured values of PS in XY and XZ axes, FW and porosity % are summarized in Table 3. 5. Similar values were observed after characterisation with SEM and micro-CT. After printing, it was observed that the PS in the XYX-axes were lower than the values set during design.

Table 3. 5. Design parameters and values obtained after fabrication of PLA scaffold. The presented values are an average of 5 measurements with \pm SD. * mean pore size

	Designed values (mm)	PLA scaffold (SEM)	PLA scaffold (μ -CT)
PS XY-plane	0.65	0.55 ± 0.02 mm	
PS XZ-plane	0.60	0.52 ± 0.01 mm	0.56 ± 0.02 mm*
FW	---	0.62 ± 0.01 mm	---
Porosity	---	$60\% \pm 1.00$	$53\% \pm 0.50$

3.9.2. Mechanical properties

The representative compression behaviour of the fabricated PLA scaffold and images acquired during testing at different stages and different time points (t) are represented in Fig.3. 14.

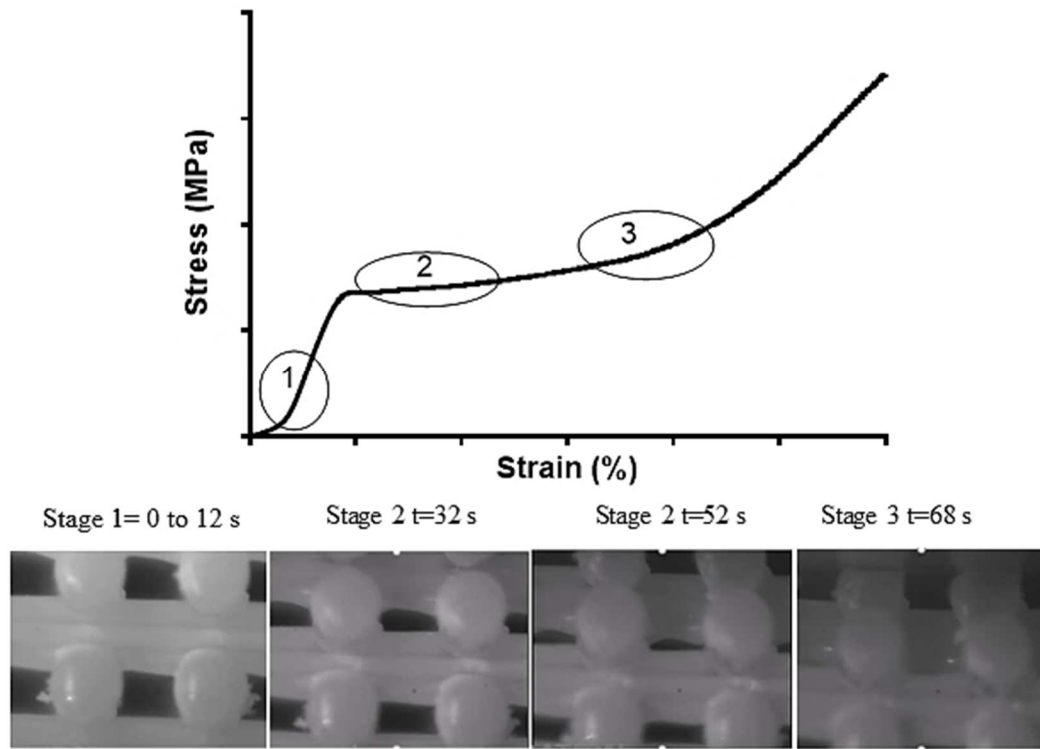


Fig.3. 14. Stress-strain curve stages of PLA scaffold under compression loading with images acquired during compression testing of PLA scaffolds at a unit cell or pores evolutions level. Each image is identified with the stage and time point (t) that was acquired. Each stage is described in detail in the text below.

Three stages were observed: 1) an initial linear elastic region followed by 2) a plateau of almost constant stress but increasing strain which is terminated by 3) an exponential increase in stress until the test ends. The unit cell or pore evolution is described for the PLA scaffolds as: 1) up to 12 seconds (end of stage 1) the pores do not move on the Z axis, 2) between 13 seconds until 67 seconds (stage 2) pores are compressed and decreased in height until 3) stage 3 starts at 68 seconds when pore's walls are touching each other causing the disappear of pores.

The influence of laser cutting after printing on compression properties was investigated and the compressive modulus and stress at yield values obtained are summarised in Fig.3. 15.A and B. When comparing the influence of the structural properties in the compression behaviour, PLA samples with more void space (pores) presented lower values. Regarding the influence of the fabrication steps, after laser cutting, the PLA presented significantly lower compressive properties with a decrease of ~27% in the compressive modulus and of ~35% in the stress at yield.

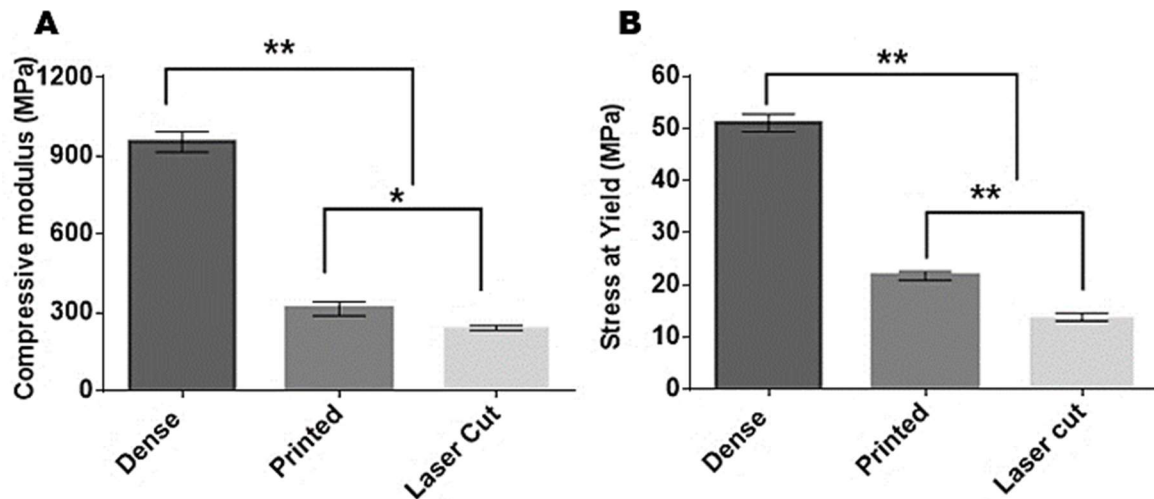


Fig.3. 15. Compression properties of dense PLA and porous PLA printed and PLA laser cut from a printed bar (PLA scaffold). A. Stress at yield and B. Compressive modulus. Average values were plotted with \pm SD.

3.10. Results: *In vitro* Degradation Study

The SEM images of PLA scaffolds cross-section (middle area of the scaffolds) after 10 weeks of immersion in PBS are shown in Fig.3. 16. b. No change in pore morphology and size up to 10 weeks of degradation in PBS was observed when compared to before degradation test. (Fig.3. 16.a). Regarding PLA scaffold edges (Fig.3. 16. A-H), differences were observed between samples at the starting point (week 0 in Fig.3. 16.A and D) and after 6 weeks (Fig.3. 16.B, E and G) and 10 weeks (Fig.3. 16.C, F and H) of immersion in PBS.

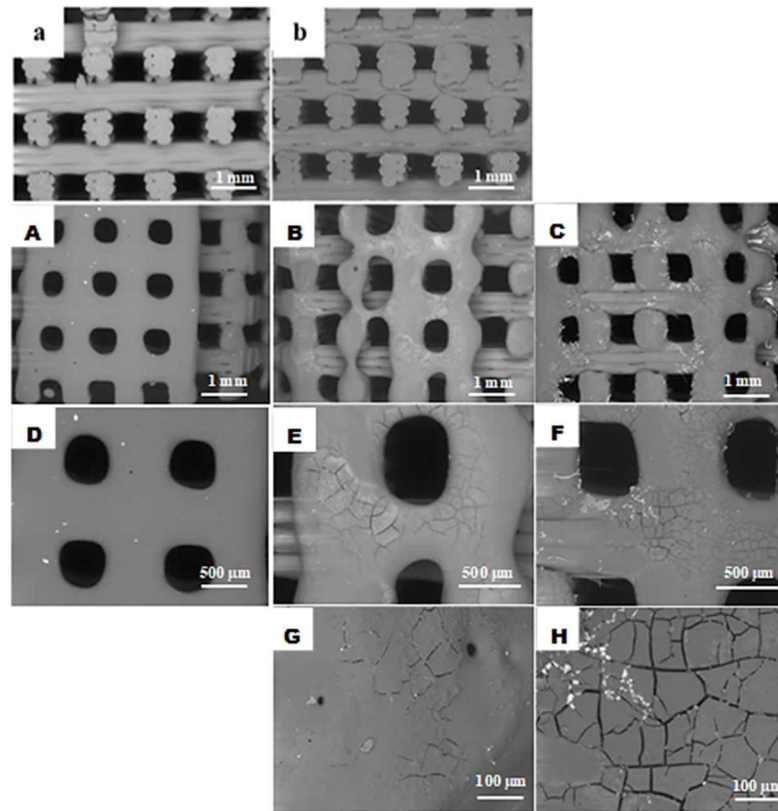


Fig.3. 16. SEM images of the PLA scaffolds: a. and b: Cross-section SEM images with 40X magnification of laser cut PLA scaffold before (week 0) and after immersion (week 10). A-H: SEM images of laser cut PLA scaffold edges at different PBS immersion times. A and D- before immersion at x30 and x60 magnifications. B, E and G. after 6 weeks at 30x, 60x and 300x magnifications and C, F and H. after 10 weeks at 30x, 60x and 300x magnifications.

The PLA scaffolds mass, the pH of PBS solution and average molecular weight (M_w) are shown in Fig.3. 17.A-C. The PLA scaffolds mass remained relatively constant throughout degradation period of 10 weeks. The PBS solution pH remained unchanged for up to 5 weeks around its initial value (pH~7), yet at week 6 it decreased to ~6.6 and it remained around this value until the end of 10-week study. The molecular weight (M_w) of PLA scaffold decrease 20 % after 6 weeks of immersion in PBS, whereas it showed a significant decrease of 15% change between week 8 and 10.

Compressive properties evolution is illustrated in Fig.3. 18.A-B. The compressive properties remained constant for 6 weeks. However, at week 8 there was a significant and anomalous increase in the compressive modulus from ~255 MPa to ~339 MPa that was still observed at week 10. Additionally, the stress at yield values showed a significant increase after 10 weeks of immersion in PBS.

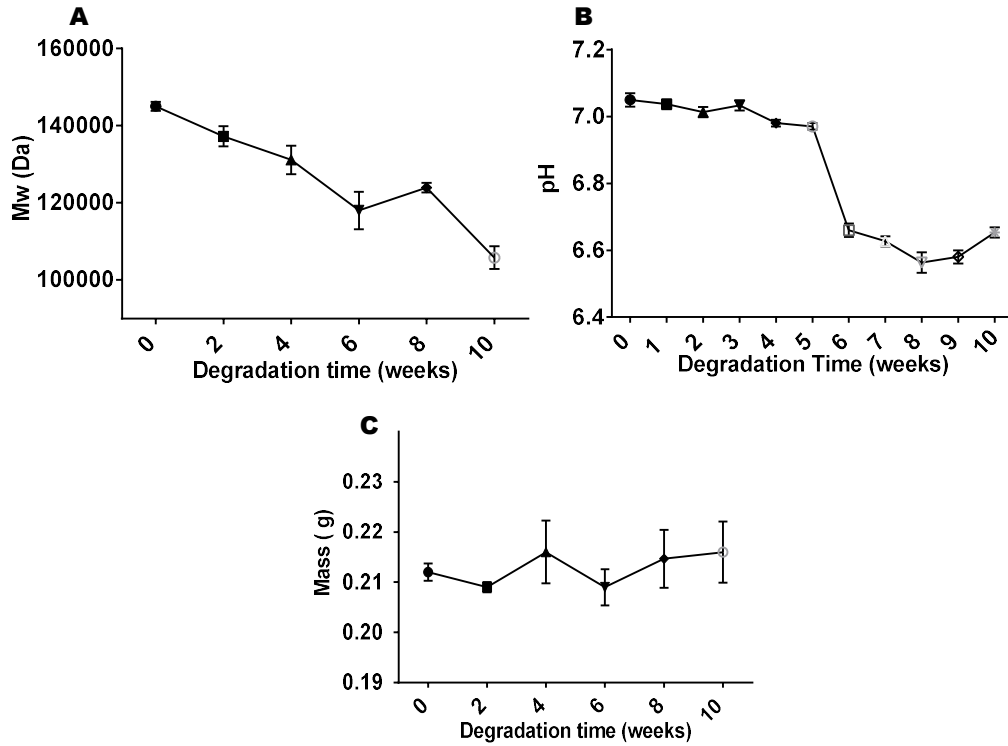


Fig.3. 17. PLA scaffold in vitro degradation study results obtained for: A. average molecular weight (Mw), B. PBS solution pH variation and C. Dry mass variation of porous PLA scaffolds.

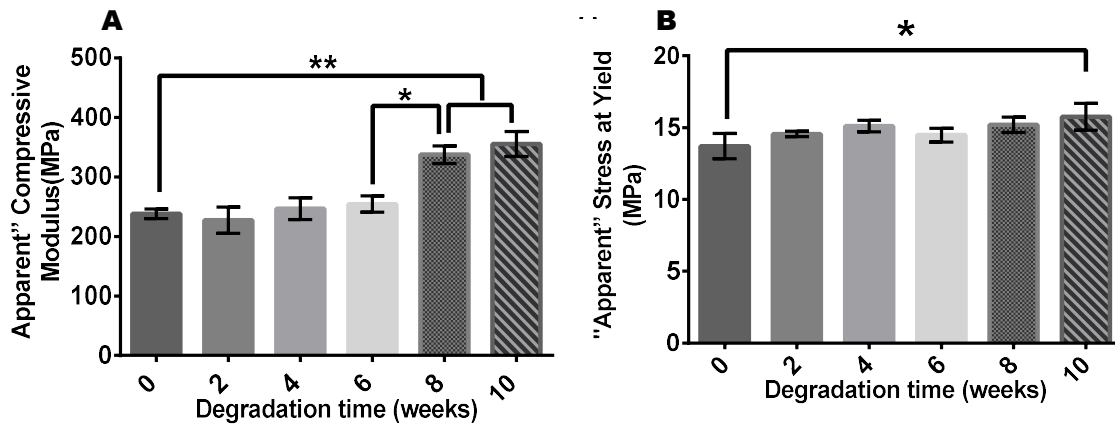


Fig.3. 18. Results from in vitro degradation study of PLA scaffolds in PBS at 37°C. A) Compressive modulus and B) Stress at yield. Average values of three replicates were plotted with \pm SD.

The PLA samples images acquired at the end of compression testing at different time points are illustrated in Fig.3. 19.

When evaluating the samples colour and structure after being removed from the vials every 2 weeks, before compression testing, the PLA scaffolds did not show any structural changes after being 10 weeks immersed in PBS. Yet after 2 weeks, samples changed their transparent appearance to an opaque colour (Fig.3. 19). However, after 4 weeks, the PLA scaffold changed gradually to transparent again (Fig.3. 19).

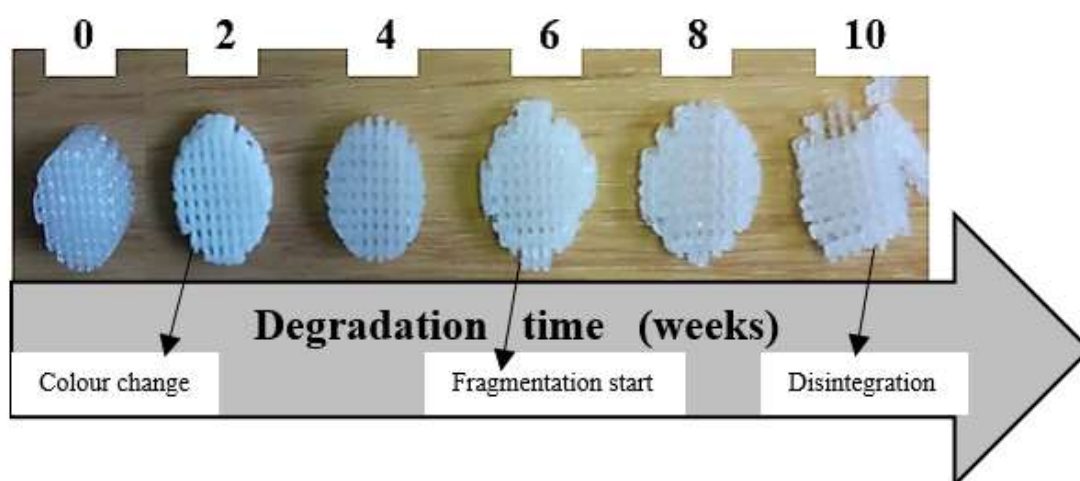


Fig.3. 19. Images acquired at the end of compression testing of PLA scaffolds at different time points from 0 weeks (no immersion) to 10 weeks (last time point).

Accordingly, the stress-strain curves up to 8 weeks (Fig.3. 20) remained like the one described in Fig.3. 14 (PLA scaffold before immersion in PBS) with 3 stages observed as pointed in the curves. Nevertheless, after immersion in PBS for 10 weeks, a different stress-strain curve was observed. While stage 1 and stage 2 were still observed (Fig.3. 20), stress plateau was followed by a decrease and another plateau in stress, and the stress exponential increase (stage 3) occurred at higher strain values.

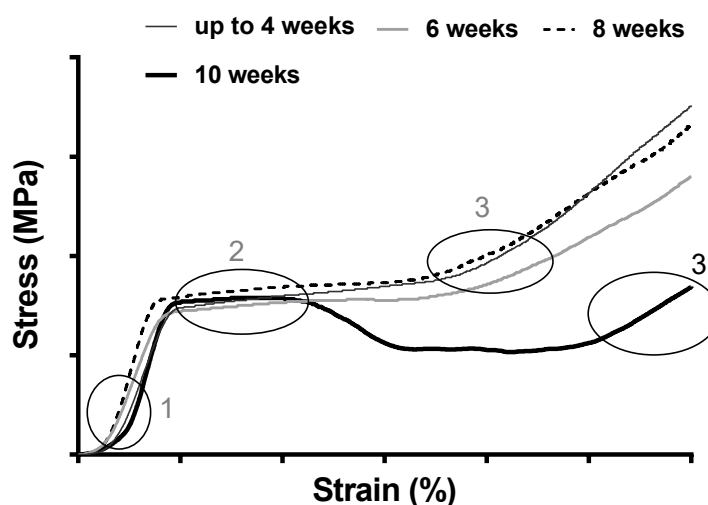


Fig.3. 20. Representative stress-strain curves of PLA scaffold during in vitro degradation study at different time points. The curves were divided in stages, as it was done previously: 1) initial linear elastic region followed by 2) plateau of almost constant stress with increasing strain which is terminated by 3) an exponential increase in stress until the test ends.

At the end of compression testing, PLA scaffolds (Fig.3. 19) did not show any significant structural differences up to 4 weeks. While for samples immersed for 6 and 8 weeks in PBS, minor material detachment from scaffold edges was observed and after 10 weeks, the PLA scaffold structure fall apart after compression testing.

Therefore, the images acquired at different time points during compression testing of samples immersed for 6 and 10 weeks in PBS were summarised in Fig.3. 21 and Fig.3. 22.

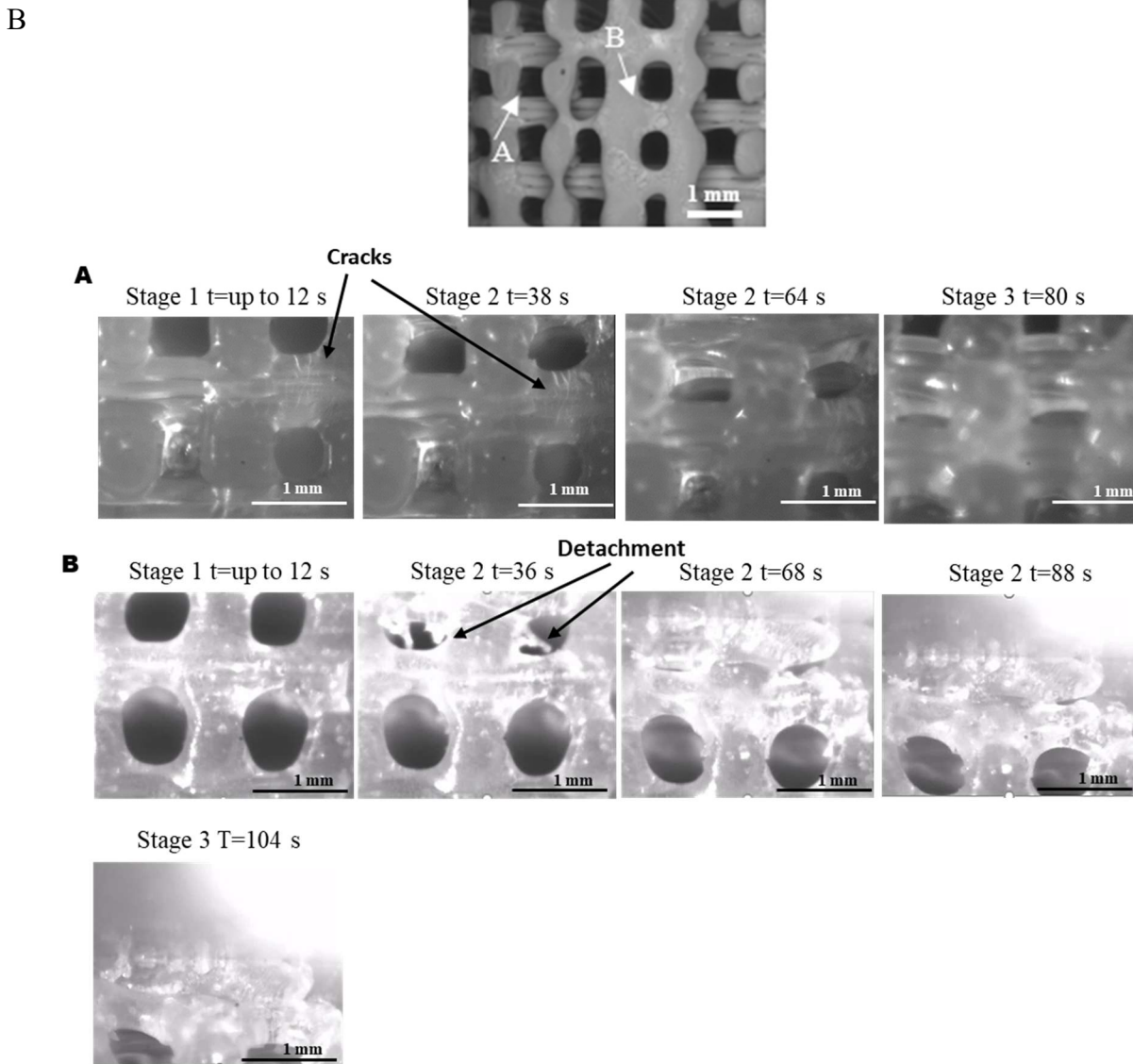


Fig.3. 21. PLA scaffold edges after 6 weeks of immersion on PBS. Top. SEM image with white arrows pointing towards different pore geometries areas and Bottom: Images acquired during compression testing stages of stress strain curves and time points (t). A. cubic pores with white arrows pointing towards cracks. And B. More rounded pores.

For PLA samples immersed for 6 weeks, two pore geometries characterised PLA scaffold edges, as previously observed in Fig.3. 16.B. Hence, during compression test, the behaviour of the two areas corresponding to each pore geometry was recorded (areas A and B, Fig.3. 21). For area A (cubic pore geometry), the PLA scaffold compression behaviour was the same as the one observed and described before immersion (images shown in Fig.3. 14). The only difference was the cracks observed around pores being compressed (identified with white arrows), that were previously identified in Fig.3. 16. Also, a small amount of water leaving

the material around the pores was observed after 12 seconds (end of stage 1), which is just visible during video watching and could not be represented in the images acquired. On the other hand, compression behaviour of area B (more rounded pore geometry) was characterised by material detachment observed during stage 2 from 36 to 68 seconds. Also, stage 2 was longer (from 12 to 104 seconds) than the one observed for area A and for the samples before immersion (Fig.3. 14)).

After being immersed for 10 weeks in PBS, PLA scaffolds edges were mostly characterised by one pore geometry type, as illustrated in top image Fig.3. 22. The compression behaviour followed the same trend previously observed for area A (6 weeks) where pores were compressed until failure. However, stage 1 ended at 16 seconds, contrary to area A that ended earlier at 12 seconds. Additionally, a bigger amount of water coming out of material being compressed was observed for PLA scaffolds immersed during 10 weeks in PBS versus the small amount observed during compression of sample immersed for 6 weeks.

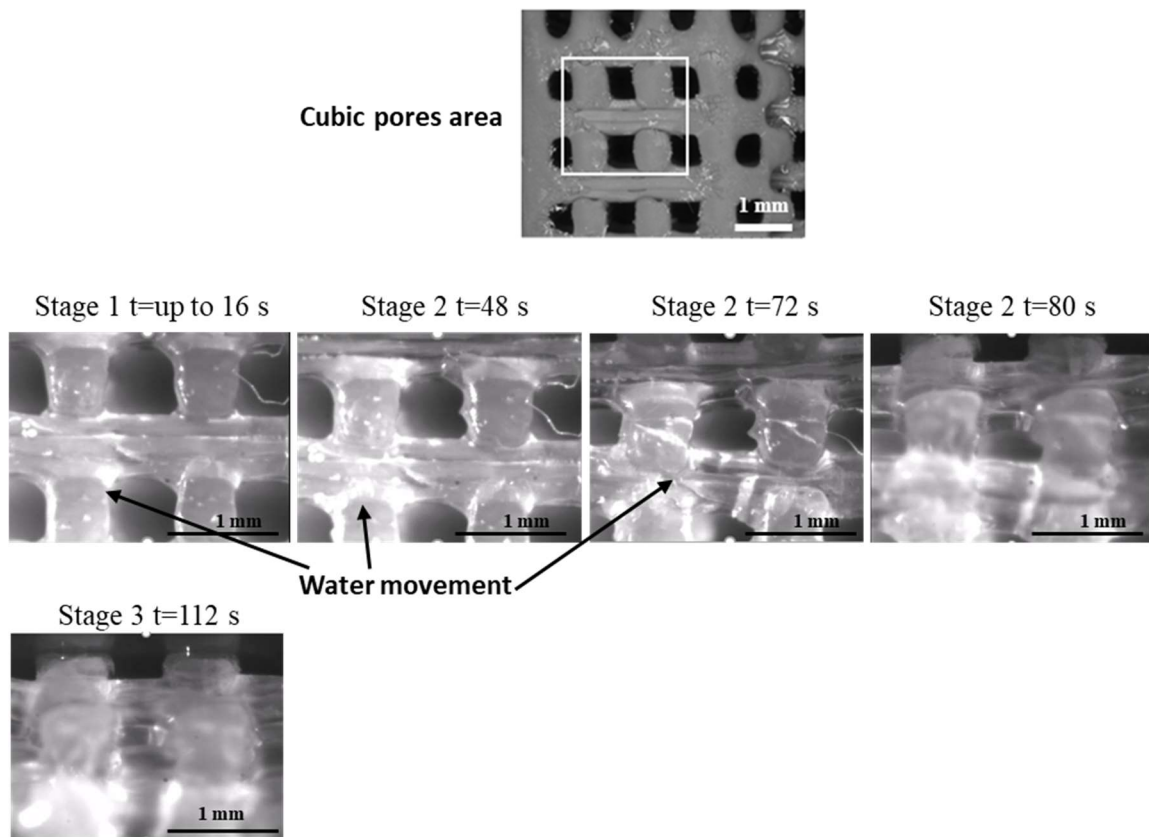


Fig.3. 22. PLA scaffold edges after 10 weeks of immersion on PBS. Top. SEM image and Bottom: Images acquired during compression testing stages observed in stress-strain curves and time points (t).

3.11. Discussion

3.11.1. Preliminary study: FFF Processing Parameters Investigation

This study focused on the investigation the FFF processing parameters influence on the obtained PLA porous structure morphology and tensile properties. Ultimately, the FFF processing parameters were selected for the fabrication of the PLA scaffold as described in section 3.2.1. Fabrication Route Parameters.

The resulting ~0.30 mm pore size values in XY-plane vs the “as designed” filament gap of 0.50 mm (Table 3. 3), can be explained by the increased obtained filament width value, as the sum of filament distance and pore size will be constant. Theoretically, the extruded filament width should accord with the nozzle diameter (which was 0.4 mm for the FFF machine used in this work) and be influenced by chosen printing parameters in less extent (Domingos et al. 2012; M E Hoque et al. 2011). For instance, a filament width values between ~0.30-0.43 mm was reported (Domingos et al. 2012) when extruding a starch-based polymer (PCL) through a 0.3 mm Ø nozzle with different printing parameters. Higher printing temperatures led to an increment in filament width from 0.33mm to 0.43 mm, pore width decreased from 0.67mm to 0.58 mm and pore height from 0.25mm to 0.18 mm. Also, printing speed increase from 8 to 12mm/s caused the narrowing of filaments from 0.37 mm to 0. 30 mm, resulting in structures with wider pores. This is also in line with the findings of Hoque et al. (M. E. Hoque et al. 2011), who have observed the same trend when extruding PLGA. Differing from the reported findings, in this study printing parameters did not influence the filament width and thus the pore size in XY-plane. Hence, compensation during design was implemented (experiment III) where filament gap was increased to 0.65 mm resulting in a pore size of ~0.50 mm on XY-plane. Furthermore, printing speed was selected as 30 mm/s towards minimum fabrication time, whereas temperature was selected based on the tensile properties study, as described next.

The measured average pore size in the XZ-plane of ~0.30mm was also inferior to the “as designed” LH of 0.50 mm (Table 3. 3). To overcome this, during design the layer height was increased to 0.60mm and the number of slices per layer was increase to three (as previously described in the study performed by (Serra et al. 2013), obtaining a ~0.52 mm pore size in the XZ-plane (Table 3. 3). Although printing temperature did not influence pore size valuees in the XZ planes (Table 3. 3), it did affect the interslice adhesion observed in the cross-section view. During FFF processing a thermoplastic polymer is extruded above its melting point and

higher temperatures decrease the material viscosity, which might explained the slices interaction/fusion during layers formation (Zein et al. 2002).

It was reported by (Steuben et al. 2015) that the FFF process is a complex multi-stage process governed by a large number of parameters that might affect particularly the bonding of layers, resulting in parts with ultimately different properties. Generally, it is desirable to print at the highest temperature possible to improve bonding between layers. In this study, the influence of printing temperature on structural tensile properties of porous PLA structures was studied with the obtained results summarised in Fig.3. 9 . Samples printed with 220°C (the highest temperature used), showed the lowest tensile strength when compared to printing temperatures of 210°C and 200°C, that might be explained by material degradation (observed at macro level when samples were observed after printing). The pore size in XY decrease with increasing printing temperature (Table 3. 3) was suggested to contribute to the Young Modulus values significant increase, by theoretically decreasing the sample porosity, as reported by (Wang & Wang 2006) . At first instance, there was no influence of design and build parameters on tensile properties (Fig.3. 10). As described before, two group of samples with differences in morphology were obtained, when design and build parameters were studied: group 1 (~pore size of 0.30 mm on XYZ planes) and group 2 (~pore size of 0.52 mm on XYZ planes). It was expected that the increase in pore size values in XYZ and thus higher porosity, would contribute to lower mechanical properties (Li et al. 2015). Nevertheless, the higher number of 3 slices per layer approach of group 2 when compared to 2 slices per layer of group 1, could contribute to stronger interslice bonding and thus explain the enhancement in tensile properties. Consequently, it might have balanced the resulting higher porosity by showing similar tensile properties between the groups.

PLA material tensile properties rather than structural properties were evaluated by preparing dense tensile samples (Fig.3. 11). When the influence of printing temperature on PLA tensile strength was studied, higher temperatures (210 °C vs 190°C) resulted in higher tensile strength values (Fig.3. 11). Which might be explained by superior interlayer bonding due to lower viscosity of extruded PLA. When compared to a similar study where dense PLA samples were FFF processed with a printing temperature of 200°C (Steuben et al. 2015), the reported average tensile strength values of 49.3 MPa were higher than the ones (~25 MPa) reported here. Material properties and FFF parameters, rather than printing temperature could easily explain differences obtained. Consequently, 210°C was selected as the maximum printing temperature without observing material degradation and allowing printing speeds as high as

30 mm/s. Also, when a printing temperature of 200°C was selected, the maximum speed value allowed without lack of extrusion was lowered.

3.11.2. PLA scaffold fabrication and characterisation

Regarding PLA scaffold fabrication, the decrease in the glass transition temperature during PLA FFF fabrication (Table 3. 4) was also observed by Dietmar et al. (Dietmar et al. 2012) and it was attributed to polymer degradation during extrusion. Also the observed decrease in molecular weight and an increase in polydispersity after FFF processing was previously reported as indicator of polymer thermal degradation (Yen et al. 2009). Nevertheless, the decreased molecular weight after processing could accelerate the *in vivo* degradation rate of fabricated PLA scaffold, which might be beneficial for its application in bone tissue repair. The reported Poly(DLlactide) degradation time was of 12 to 16 months (Middleton & Tipton 2000). While it was suggested for load-bearing tissues such bone, 3D scaffold should retain its mechanical properties for 5–6 months (tissue is mature enough to support itself) and then gradually lose its physical properties over a period of 2 years (Dietmar W. Hutmacher et al. 2001). The importance of biomaterial degradation rate and extent is a crucial for bone repair and regeneration. The degradation capability of biomaterials implanted allows for space to be produced for newly forming bone tissue to not only grow along the implant surface but also to infiltrate the scaffolds matrix along with new blood vessels, needed to provide with oxygen that is mandatory for survival of the regenerating tissues. It is crucial for the biodegradable scaffold to retain its strength during the healing period so as to provide fixation at the fracture site but degrade after the healing as completed (Sheikh et al. 2015).

Therefore the mechanical properties of 3D structures are an important feature when considering the scaffold application in bone tissue engineering (Middleton & Tipton 2000; Polo-Corrales et al. 2014). In this study, the PLA scaffold compression behavior was investigated and three regimes were observed as shown in Fig.3. 14. The images acquired during compression testing were very important for understanding the specific mechanism behind cell deformation in porous structures. In the first stage, the pore walls contribute to the resistance to the compressive load, which results in an elastic response to the load and thus pores did not decrease in height. In stage 2, the pores started collapsing by elastic buckling of the walls, as observed by pore height decreasing until they disappeared. At stage 3 the large increase in modulus is explained by the scaffolds now being effectively fully dense and further deformation compressing the material itself, as highlighted by the pores absence when this stage started. The compression behaviour found in this work agrees with the typically

foam behavior observed in other polymeric scaffold studies (Ghassemieh 2008; D W Hutmacher et al. 2001).

According to the compression test results summarized in Fig.3. 15, PLA laser cutting process led to a significant decrease in both stress at yield and compressive modulus. This behaviour could be caused mainly by differences in morphology. The more open porosity means that there is some “redundant” material at the edges of the scaffold, which will not be load bearing. However, for a relatively small sacrifice in mechanical properties the higher open porosity could facilitate nutrients supply and waste removal and thus enhance vascularization and cell survival into the inner part of the scaffold (Murphy & O’Brien 2010). The typical compressive strength of trabecular bone ranges from 2 to 12 MPa, and its modulus is in the range of 0.1–5 GPa (Wu et al. 2014) , suggesting that the fabricated laser cut PLA scaffolds would be appropriate for this application. Also, in a similar study (Xiong et al. 2001) a PLA scaffold fabricated with precise extrusion at 160°C, with average porosity % ~60% and 200-500 µm pore size, was characterised by a lower compressive modulus of 195 MPa and compressive strength of 8.5 MPa when compared to the 255 MPa and 14 MPa obtained in this study.

3.11.3. *In Vitro Degradation Behaviour*

The degradation behaviour of a polymeric scaffold is crucial for the long-term *in vivo* performance and it may affect a range of processes such as cell growth, tissue regeneration, and host response (Lu et al. 2000). PLA degradation is described by a simple hydrolysis of the lactide ester bonds into lactic acid in contact with water, which is eventually removed from the body by normal metabolic pathways (Lu et al. 2000).

When PLA is exposed to aqueous media such as PBS, water molecules attack the ester linkages, breaking long polymer backbone chains into shorter ones (Onuma & Serruys 2011). Ester linkage cleaving by hydrolysis results in hydroxyl and carboxylic acid groups formation, resulting in a decrease in the polymer molecular weight (M_w) (Lu et al. 2000). Because the ester linkages are cleaved randomly along the polymer backbone, relatively few water-soluble fragments form initially (Onuma & Serruys 2011). The reduction in molecular weight produces an increase in hydrophilicity but not necessarily changes in physical properties or mass (Duek et al. 1999). As degradation time increases, the M_w decrease leads to a reduction in physical properties and the formation of water-soluble fragments that decrease local pH. These water-soluble fragments diffuse away from the polymer and are ultimately hydrolysed to lactic acid, which are processed through normal metabolic pathways.

The rate of hydrolysis depends on factors such as the size, the monomer composition and degree of crystallinity of the polymer (Duek et al. 1999). For instance, non-porous structures undergo degradation more rapidly than porous ones, because the latter facilitate dissolving and spread of the degradation products throughout the aqueous medium, thus discouraging self-catalysis behaviour (Odelius et al. 2011)

In this study, fabricated PLA scaffolds were immersed in PBS solution for 10 weeks and structures were characterised every 2 weeks and pH was monitored weekly (Fig.3. 17.B). The continuous Mw decrease starting at week 0 (Fig.3. 17.A), suggested PLA degradation initiation due to hydrolysis in PBS, with consequent cleavage of the ester bonds, thus formation of shorter chains. At week 6, the pH decreased from 7.4 to 6.6 together with a sharp decrease in Mw value, suggesting that shorter chain by-products were formed with water solubility (Odelius et al. 2011). Thus, pH decrease is described an indicator of polymer degradation evolution (Huang et al. 2013; Andersson et al. 2010).

The PLA scaffolds colour change from transparent to opaque (Fig.3. 19) might be attributed to sample crystallinity increase due to hydrolysis occurring selectively in the amorphous regions of the polymer (Duek et al. 1999). This would explain the reduction in molecular weight without a loss in physical properties and mass as the PLA scaffold was still held together by the crystalline regions. Further characterisation, such as DSC analysis would be helpful towards deep understanding of suggested mechanism. With DSC analysis, the glass transition temperatures of PLA would be measured used as an indicator of crystallinity % change. This was observed in the PLA (both PLA and PLLA/PDLA stereo complex) *in vitro* degradation study performed by (Andersson et al. 2010) , where the glass transition temperature (T_g) increased with degradation time. It was explained by a more stable structure, where only small amounts of amorphous material remained more protected in the crystallites. Also, surface degradation was suggested by (Wu & Ding 2005) for explaining how PDLA porous scaffolds survived intact and the weight remained constant, while molecular weight decrease exponentially throughout entire degradation period. In agreement, in this study the PLA scaffold edges were characterised by cracks formation at week 6 (SEM images, Fig.3. 16.E and G), while the middle was intact (SEM images, Fig.3. 16.B), indicating water erosion happening preferentially at scaffold outside areas/surface. Furthermore, after 10 weeks in PBS, the PLA scaffold, the number of observed cracks increased (Fig.3. 16.F and H) and the Mw showed a sharp decrease (Fig.3. 17.A). The fabrication route used in this study, could explain the PLA scaffold edges higher tendency to erosion, due to PLA thermal degradation caused during the laser cutting step. In summary, understanding of the mechanical properties

and how they change during degradation is very helpful for effective prediction of the degradation process so that one can design devices for load bearing applications.

Besides the dry PLA scaffold performed characterisation, every two weeks, the compression properties were investigated for scaffolds in wet state. Up to 8 weeks, mechanical properties remained unchanged and were represented by similar stress-strain curves (Fig.3. 20) and thus similar compression behaviour, that was previously described for dry samples (Fig.3. 14). It is suspected that compressing properties of scaffolds remained stable as a result of unchanged mass loss during 10 weeks (Felfel et al. 2016). Nevertheless, images acquired from the edges of PLA scaffold during compression, revealed that the two pore morphologies identified in both SEM images (Fig.3. 13.A-C) and three-dimensional pore characterisation micro-CT (Fig.3. 13.a-c), were characterised by different cell-unit deformation mechanisms (Fig.3. 21.A and B). The more rounded pore geometry showed material detachment after 6 weeks and longer stage 2, suggesting that pores took longer to collapse. The compression behaviour of more cubic pore geometry gave evidence of water absorption by PLA in areas visible affected by cracks, that left the PLA porous structure during compression. Furthermore, after 10 weeks of immersion in PBS, an anomalous increase of compression modulus (Fig.3. 18.A), change in the stress-strain curve (Fig.3. 20) and scaffold destruction after testing (Fig.3. 19) were observed. This might be elucidated by the increased presence of surface cracks at the PLA scaffold edges, enabling both fluid penetration and leakage of the degradation products, accelerating the hydrolysis process (Navarro et al. 2005). This agreed with Mw sharpest increase observed throughout 10 weeks. Moreover, the enhancement of the water penetration through the increase number cracks in the PLA scaffold edges when compared to week 6. Thus, water presence within the structure added load resistance to the PLA scaffold, explaining longer stage 1 (Fig.3. 22).

3.12. Conclusions

FFF process was successfully used in the fabrication of porous PLA structures characterised by a pore size in XYZ that was dictated by the design parameters. To obtain a 0.50 mm pore size in the XY plane, a compensation approach for filament gap value was implemented having in account the larger than expected extruded filament in this study. Parallely, to obtain a 0.50 mm pore size in the XZ plane, three slices per layer with increased height of 0.60 mm was the selected approach. Overall the FFF parameters for obtaining a porous PLA structure with 0.50 mm in all planes were optimised.

Additive manufacturing, in particular the FFF low-cost system used in this work, is suitable for fabricating 3-D porous structures with controlled pore sizes of greater than 500 μm and interconnected porosity. Laser cutting of 3D printed PLA scaffolds did not affect the molecular weight and thermal properties of the polymer, but did slightly decrease in the mechanical properties by removing the capacity for some material within the structure to support load. However, the PLA scaffolds compressive properties were found to be appropriate for trabecular bone applications.

After being immersed for 10 weeks in PBS at 37°C, laser cut PLA scaffolds did not show any significant decrease in weight and compressive properties values, because material degradation was occurring at the scaffold edges. Higher compression modulus and different stress-strain curves observed for 10 weeks of immersion in PBS were explained by water infiltration facilitated by cracks presence at scaffold edges. The degradation study demonstrated that the implant would be stable for a long enough period to allow for bone ingrowth.

Overall the 2-step manufacturing route used in this work led to the fabrication of promising, mechanically stable scaffolds with well-defined and open architectures for trabecular bone applications.

CHAPTER 4. Design and characterisation of a 3DP AW structure

4.1. Introduction

This chapter summarises work on the development of porous apatite wollastonite (AW) structures processed with indirect three-dimensional printing (3DP). The original aim of the work reported here was to create AW porous discs for performing bonding studies. However, the initial results differed significantly from previous results with this material, thus a more in-depth study of the processing route was required. A general study on indirect 3DP of AW parts was previously reported by (Mancuso et al. 2017) with the following optimised powder-binder system: 70% AW and 30% MD. For this study, the same powder-binder system was assessed, however bimodal and trimodal powder blends were also investigated.

4.2. Materials Processing Route

4.2.1. Starting materials processing and characterisation

The starting materials (AW and MD powders as-received described in section 2.2. Materials) were prepared separately by milling and sieving (as described in section 2.3.2.1. Milling and sieving) to obtain the desired particle size ranges needed for blend formulation. This process was optimised for each AW batch and MD, as described below.

AW1 glass frit was milled and sieved in a 2-step process, with the following parameters: 1) programming for 2 repetitions of rotational speed of 400 rpm for 2 min, followed by sieving towards powder in the $> 90\mu\text{m}$, $53\text{-}90\mu\text{m}$ and $< 53\mu\text{m}$ particle size ranges and 2) then the powder on the $> 90\mu\text{m}$ range was milled by programming for 2 repetitions of rotational speed of 410 rpm for 2 min. This process was repeated until the amounts of each particle size range needed for preparing the powder blends was obtained. AW2 powders were sieved to obtain the $54\text{-}90\mu\text{m}$ range and the remaining $>90\mu\text{m}$ powder was milled twice with 390 rpm for 2 min to obtain the smaller particle size ranges of $>20\mu\text{m}$ and $20\text{-}53\mu\text{m}$.

MD was used in three particle size ranges: $< 53\mu\text{m}$, $20\text{-}53\mu\text{m}$ and $<20\mu\text{m}$. The $<53\mu\text{m}$ and $20\text{-}53\mu\text{m}$ powders were obtained by sieving the MD powder as-received. To obtain the $<20\mu\text{m}$ powder, milling was required. The milling parameters were optimised to avoid the overheating of the ceramic bowl and thus material melting. The resultant processing conditions were that 200g of powder was milled with three repetitions of rotational speed of 390 rpm for 1 min.

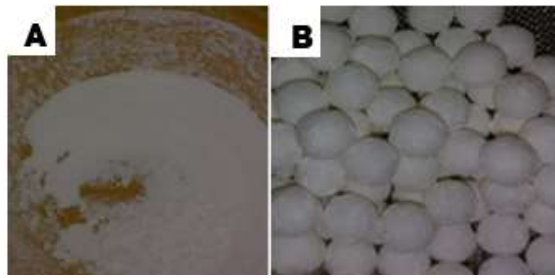


Fig.4. 1.Maltodextrin (MD) powder after milling with 400 RPM for 2 min: A) Ceramic bowl with MD melting and B) Milling balls with MD adhesion.

After processed into the desired particle size ranges, both AW and MD powders (described in section 2.2. Materials) were characterised with the techniques described in section 2.4.1. AW and MD.

4.2.2. Indirect 3DP

The indirect 3DP process can be subdivided in 3 steps: 1) powder blend preparation, 2) 3DP with prepared powder blends to obtain the green parts and 3) post processing of green parts to obtain the sintered 3DP parts.

In Table 4. 1, the steps are briefly described and the characterisation techniques and/or methods used in each step are summarised. Then, in the following sections, each step was explained in more detail.

Table 4. 1. Table describing the steps performed during AW indirect 3DP processing.

Steps	Process	Characterisation
Powder blend preparation	Mix AW and MD	Particle size distribution
	into 8 formulations	Particle morphology
3DP	CAD model design	Printability study
	Powder blend & binder	
Post-Processing	De-powdering	Sinterability study with phase
	Thermal treatment	identification

4.2.2.1. Powder Blends Preparation

Powder blends of AW and MD were prepared by mixing different ratios by weight and different particle size range with the roller mixing process described in section 2.3.2.2. Roller mixing. The formulation for each prepared powder blend is summarised in section 4.3.

Powder Blends Rationale. The powder blends were always prepared with a minimum quantity

of about 500 g of material, requirement of the 3D printer used in this study. Before the 3DP process the powder blend was vacuum dried (as described in section 2.3.2.3. Vacuum drying) for removing any moisture from the powders during the processing steps.

4.2.2.2. 3DP: Powder Blends Printability study

This procedure served to assess and compare the prepared powder blends by 3DP them with the process described in 2.3.2.4. 3DP Process. The prepared powder blends printability was qualitatively assessed, as following:

- 1) During 3DP process the flowability of the powders blends from the feed area into the build area and recoating of spread layers were observed and classified into: low, sufficient or high.
- 2) 3DP green parts quality was evaluated (3 replicates for each powder blend), by i) checking if the obtained parts were mechanically strong for handling, followed by ii) photographing in a reproducible manner to evaluate geometry and classifying them as not satisfactory, acceptable, good and excellent.
- 3) 3DP green parts microstructure was characterised with SEM images.

As the quality of the printed parts differed only slightly across different powder blends, no further characterization of green parts was performed.

4.2.2.3. Post-processing: Powder Blends Sinterability Study

The prepared powder blends that were successfully 3DP into green parts (as described in 2.3.2.4. 3DP Process) moved to thermal post-processing step with the described sintering process and protocols (as described in 2.3.2.5. Post-Processing).

After sintering, the obtained parts were qualitatively characterised accordingly to the following parameters: i) consolidation, through visual inspection to assess if part was mechanically strong enough to be handled and ii) microstructure characterisation by SEM. To assess and compare the consolidation obtained for sintered parts, a classification system was created as summarised in Table 4. 2.

Table 4. 2. Consolidation levels classification used for powder blends sinterability study.

Levels				
	-1	0	1	2
Consolidation	No	Yes, with shrinkage	Yes, with partial swelling	Yes, with high swelling level

Briefly, the consolidation levels after sintering were classified from level -1 (sample not strong enough to be handled), level 0 (sample consolidated, with shrinkage observed in X, Y and Z), level -1 and level -2 (samples consolidated with swelling observed specially on Z axis).

For this study, parts prepared with different batches were selected to assess the influence of raw material batch sintering protocols on crystallinity. In detail, AW1.1 and AW2.1 sintered parts crystallinity was assessed for representing AW1 and AW2 batches, respectively, as described in 2.4.1.7. X-ray diffraction (XRD).

4.2.2.4. De-binding studies

This study was to understand the MD burning out mechanism in the green parts during the heat treatment developed by *Xiao et al. 2008* . It involved two stages:

- 1) MD burning study, where initially a MD powder sample ($< 90 \mu\text{m}$) was heated up to set temperatures between 200°C to 300°C , at a heating rate of $10^{\circ}\text{C}/\text{min}$ and sample colour evolution was observed. Secondly, the MD particle size (PS) and heating rate (HR) influence on the burning process were investigated. It consisted in heating MD with different PS ($<20\mu\text{m}$ and $20\text{-}53 \mu\text{m}$) up to 310°C at different HR of $2.5^{\circ}\text{C}/\text{min}$, $5^{\circ}\text{C}/\text{min}$ and $10^{\circ}\text{C}/\text{min}$ and the swelling level was observed.
- 2) A de-binding study of the 3DP green parts, where the green parts (AW1.1) were heated at set temperatures of 310°C , 400°C and 779°C , at heating rate of $10^{\circ}\text{C}/\text{min}$ with no previous VD and $2.5^{\circ}\text{C}/\text{min}$ with previous VD and sample colour evolution and structure were observed.

4.3. Powder Blends Rationale

The eight powder blends formulations (Table 4. 3) prepared with AW (AW1 and AW2) and MD powders (MD1 and MD2), each one containing different weight ratios of different particles sizes ranges. The powder blends names contain information about the AW batch used (AW1 or AW2) and they were numbered accordingly to the formulation order. The powder blends were formulated always based in the results obtained with the previous blend, in the following way:

- Powder blends prepared with AW1 with zero in the name code, represent the first formulations prepared: AW1.01* and AW1.02* were previously reported in (Mancuso et al. 2017) and were used as the starting point. Differences in the results from those

previously obtained by (Mancuso et al. 2017) led to the formulation of AW1.03, AW1.1 and AW1.2.

- Powder blends prepared with AW2: AW2.1 and AW2.2 were prepared with the same formulations that AW1.1, AW1.2 for comparison, and AW2.3 was formulated based on results obtained from AW2.1 and AW2.2.

*Table 4. 3. Powder blends (PB) formulations prepared for this study. *Powder blends formulations reported by (Mancuso et al. 2017).*

Blend	70%AW (µm)		30%MD (µm)
AW1.01*	< 53		MD1 < 53
AW1.02*	55% 54-90	15% < 53	MD1 < 53
AW1.03	55% 54-90	15% < 20	MD1 < 20
AW1.1	45% 54-90	25 %< 20	MD1 < 20
AW1.2	40% 54-90	30%< 20	MD2 < 53
AW2.1	45% 54-90	25%< 20	MD1 < 53
AW2.2	40% 54-90	30%< 20	MD2 < 53
AW2.3	30% 54-90	25%< 20-53	15%%< 20
			MD2 20-53

4.4. Results: Starting Materials Characterisation after Processing

4.4.1. Morphological (SEM) and Particle size distribution (PSD)

The SEM images of AW powders after processing towards specific particle size ranges are shown in Fig.4. 2.A-D. For powders in the 54-90 µm range (Fig.4. 2.A and B), the average value of five measurements of particle width (W) and length (L) was calculated as shown on the top right corner of each SEM image. In general AW powders were characterised by a non-spherical and angular morphology, with AW2 particles Fig.4. 2.B and C) showing a more elongated morphology and higher aspect ratio. This was confirmed by the calculated L/W ratio of 2.3 for AW2 powders when compared to 1.2 for the AW1 powders. The quantitatively results of particle size distribution after powders processing are summarised in Table 4. 4.

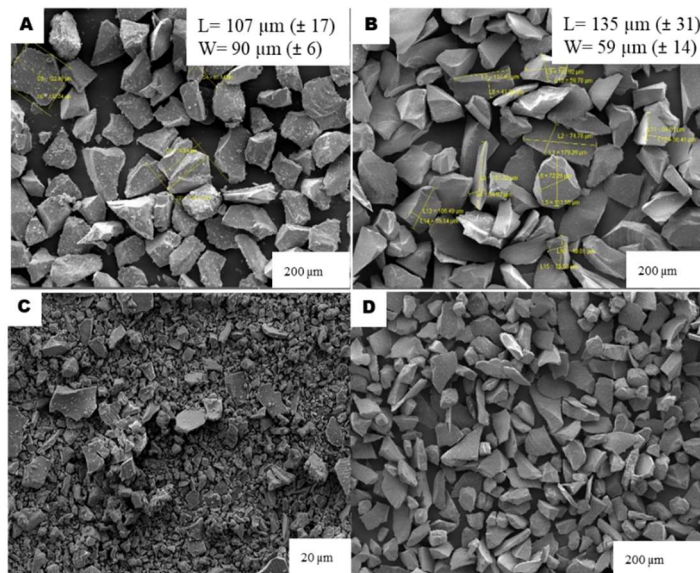


Fig.4. 2. SEM images of AW batches after processing towards specific particle size ranges: A. AW1 54-90 μm , B. AW2 54-90 μm , C AW1 <20 μm and D. AW2 20-53 μm . (The L and W values were not measured for images C and D).

Table 4. 4. Particle size distribution (PSD) of AW1, AW2 and MD powders after processing. Average values with \pm SD were reported.

AW	D _x (10) (μm)	D _x (50) (μm)	D _x (90) (μm)
AW1 <20	0.63 (0.03)	6.17 (0.38)	25.9 (3.48)
AW2 < 20	0.83 (0.09)	7.20 (0.78)	21.7 (0.68)
AW1 54-90	64.2 (0.51)	101 (0.52)	159 (0.68)
AW2 54-90	61.6 (1.33)	101 (2.26)	166 (5.03)
AW2 20-53	36.7 (0.23)	60.7 (0.11)	96.1 (0.13)
MD < 53	5.71 (0.06)	30.0 (0.12)	69.0 (0.25)
MD 20-53	20.5 (0.56)	48.1 (0.54)	95.9 (0.47)

AW2.54-90 μm and AW2.20-53 μm powders were characterised by a homogenous particle size distribution as observed in Fig.4. 2.B and D. Regarding the desired particle size versus the one obtained after processing: AW2.54-90 μm and AW2 .20-53 powders μm were characterised by an average particle size of $D_x(50) \sim 101 \mu\text{m}$ and ($D_x(50) \sim 60.7 \mu\text{m}$ (Table 4. 4), which were higher than the expected $\sim 72 \mu\text{m}$ and $\sim 35 \mu\text{m}$. This was also observed in the AW2.54-90 μm SEM images width and length average values between 60 μm to 135 μm . On the other hand, powders AW1 <20 μm were characterised by a heterogeneous particle size distribution with a mix of particle sizes (Fig.4. 2.C). Regarding particle size distribution values, both AW1 and AW2 powders <20 μm were characterised by an average particle size $D_x(50)$ value of $\sim 6\text{-}7 \mu\text{m}$ (Table 4. 4) as desired.

For the processed MD powders, (Fig.4. 3.A-C) some tendency for particle agglomeration was noticed, especially on the $< 20\mu\text{m}$ powders. MD2 powders were characterised by a more elongated and irregular morphology when compared to MD1 powders. Regarding the particle size distribution of MD powders, although the average particle size of MD 20-53 μm powders was higher than expected, the number of particles on the sub 20 μm was less than 10% (Table 4. 4).

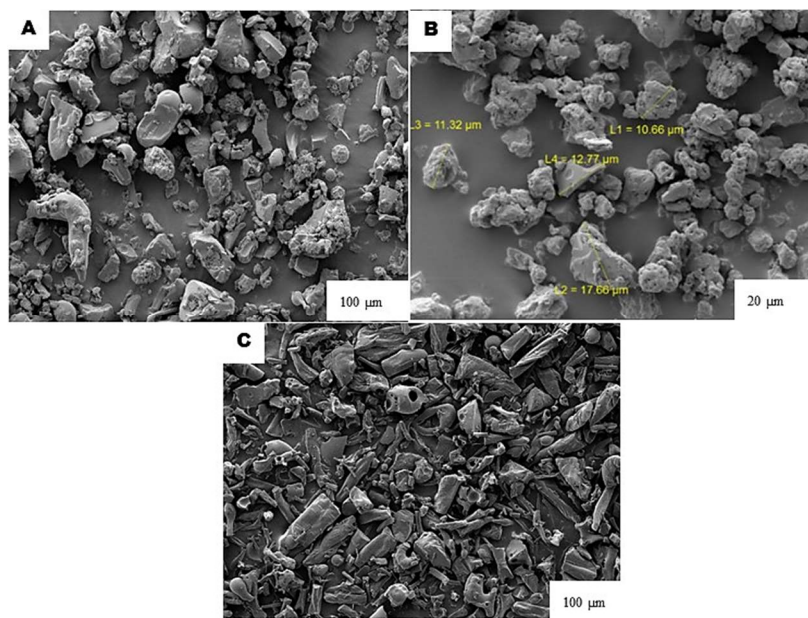


Fig.4. 3. SEM images of MD after processing towards specific particle size ranges: A. MD1 $< 53 \mu\text{m}$ after sieving B. MD1 $< 20 \mu\text{m}$ after milling and sieving and C. MD2.20-53 μm after sieving.

4.4.2. Bulk Chemical characterisation (XRF)

Table 4. 5 displays the composition and weight ratio of AW1 and AW2 obtained after XRF analysis.

Table 4. 5. X-ray fluorescence analysis of AW batches (provided by the company GTS).

(wt%)	MgO	CaO	SiO ₂	P ₂ O ₅	CaF ₂	K ₂ O	SrO	Fe ₂ O ₃	Al ₂ O ₃	ZrO ₂
AW 1	3.72	48.42	33.12	13.79	-	0.03	0.02	0.10	0.68	0.01
AW 2	3.68	44.81	35.49	15.47	0.19	-	0.02	0.09	0.14	-

4.4.3. Surface Chemical characterisation (XPS)

In Fig.4. 4 the XPS spectra representative of AW1 and AW2 batches is shown and in Table 4. 6 the atomic percentage was calculated for each one of the batches. Besides the expected Si, O, P and Ca peaks, from AW glass composition (Fig.4. 4) a C1s peaks was observed. This is

attributed to the adsorption of hydrocarbon impurities in the samples surface (Serra et al. 2003) and when the atomic percentage (%) was calculated, this element was excluded from calculations. As highlighted in Table 4. 6, no significant differences between the AW batches were observed in terms of surface chemical composition.

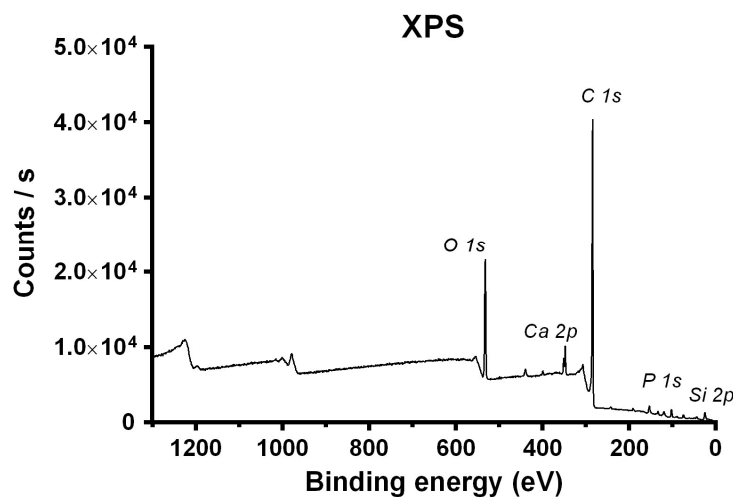


Fig.4. 4. Representative survey XPS spectrum of AW1 and AW2 batches.

Table 4. 6. Surface elemental composition (% atomic concentration) of AW batches as measured by XPS analysis of survey spectra, without carbon peak.

Atomic %	Ca2p	Si2p	P1s	O1s
Binding energy peak	346.73	101.7	132.77	531.44
AW1	15.89 (0.41)	19.99 (1.00)	7.59 (0.29)	56.49 (0.68)
AW2	15.72 (0.58)	21.49 (1.28)	9.26 (0.54)	53.72 (0.61)

4.4.4. Crystallinity (XRD)

The XRD patterns of both AW1 and AW2 batches (Fig.4. 5.A) showed one main broad diffraction peak (centre 30°, 2θ). The inset provided in Fig.4. 5.B highlights the weak diffraction peaks observed just for AW1 batch, which can be assigned to a crystalline phase hydroxylapatite phase (●: $\text{Ca}_{10}(\text{PO}_4)_6(\text{OH})_2$), accordingly to the fitting software.

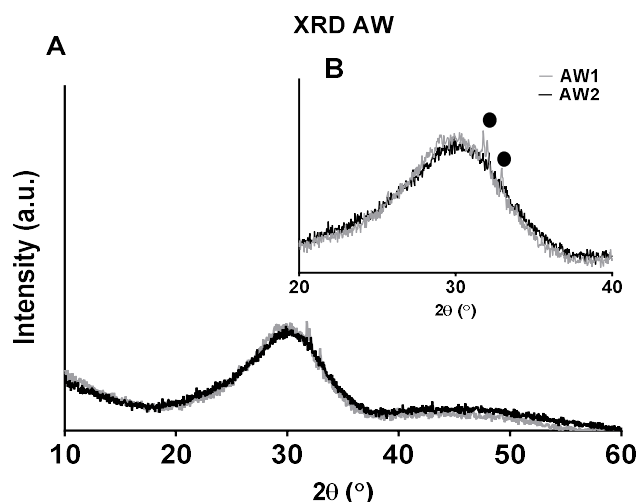


Fig.4. 5. X-ray diffraction pattern of AW batches as received: A. full data was plotted and B. Inset, with hydroxylapatite phase (●) identification.

4.4.5. Thermal characterisation (DSC)

Results from DSC analysis carried out on AW1 and AW2 batches are graphically displayed in Fig.4. 6.A-B and the thermal events such as glass transition temperature (T_g), onset crystallisation temperature (T_x), crystallisation peaks (T_c) and first melting peak (T_m) are summarised in Table 4. 7. For each AW batch, 3 different samples were prepared and analysed to assess the influence of particle size on the thermal events. The particle sizes range of interest for this study were selected as $< 20\mu\text{m}$, $54\text{-}90\mu\text{m}$ and $90\text{-}200\mu\text{m}$.

From Fig.4. 6. A-B, the glass transition temperature does not change significantly across the batches and particle sizes: AW1 ($T_g=743^\circ\text{C}\text{-}745^\circ\text{C}$) and AW2 ($T_g=740^\circ\text{C}\text{-}741^\circ\text{C}$). As summarised in Table 4. 7, the first crystallisation peak (T_{c1}) is between $855^\circ\text{C}\text{-}908^\circ\text{C}$ for AW1 and between $840^\circ\text{C}\text{-}860^\circ\text{C}$ for AW2, while the second peak (T_{c2}) is around $913^\circ\text{C}\text{-}1002^\circ\text{C}$ for AW1 and $920^\circ\text{C}\text{-}960^\circ\text{C}$ for AW2. It can be observed that AW2 crystallisation temperatures are characterised by lower and narrower ranges over different particle sizes when compared to AW1. Moreover, AW1 shows a strong influence of the particle size on the crystallisation behaviour, crystallisation temperatures increase with the increase in the particle size, e.g. T_{c1} and T_{c2} for AW1. $<20\mu\text{m}$ are the lowest temperatures observed. On the other hand, for AW2, the particle size seems to play a role on the second crystallisation event (T_{c2}). Regarding the melting peak temperatures, it is observed that AW1 shows a broader range of temperatures for different particle size that varies from 1226°C to 1260°C , whereas AW2 samples melting event ranges around 1260°C .

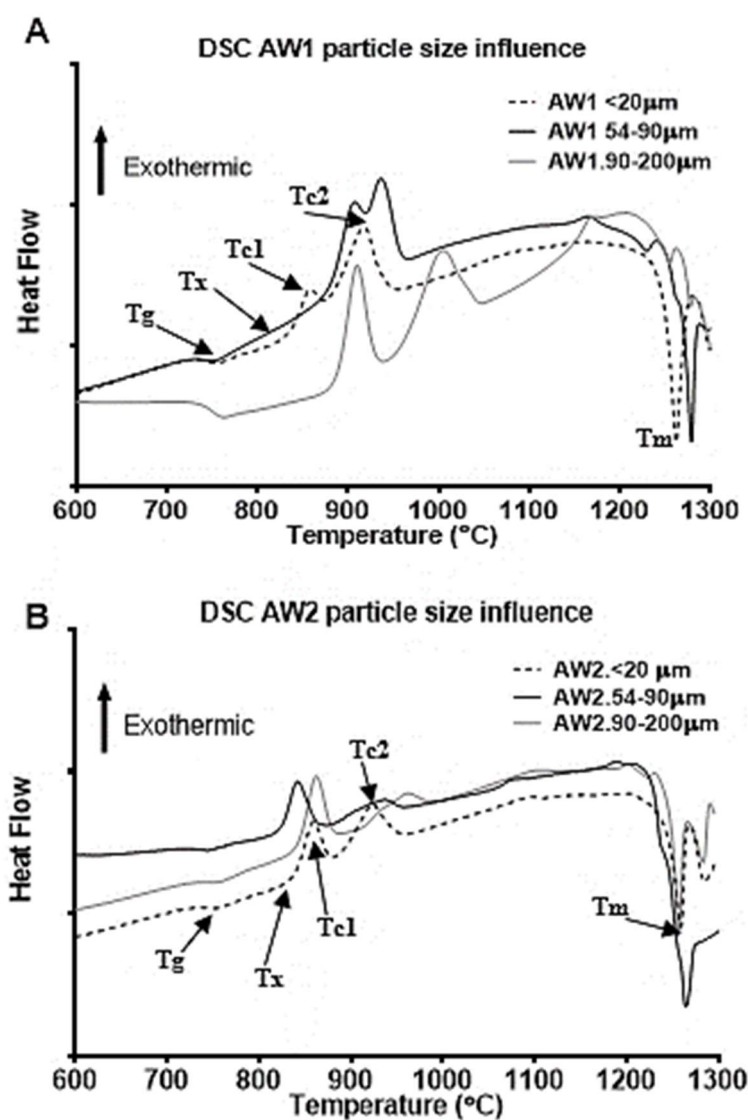


Fig.4. 6. DSC patterns of AW batches with different particle size: A. AW1 and B.AW2. The thermal transitions were identified for the AW1 and AW2 <20 μm , as an example.

Table 4. 7. Thermal events summary from DSC patterns of AW1 and AW2 with different particle sizes. *T_m was selected as the first melting peak temperature and T_x is the onset crystallisation temperature.

Samples	T _g (°C)	T _x (°C)	T _{c1} (°C)	T _{c2} (°C)	T _m * (°C)
AW1.90-200 μm	745	875	908	1002	1253
AW1.54-90 μm	742	862	903	934	1226
AW1. <20 μm	743	831	855	913	1260
AW2. 90-200 μm	741	835	860	960	1256
AW2.54-90 μm	740	814	840	930	1262
AW2. <20 μm	740	827	856	920	1257

4.4.6. Hot stage microscopy (HSM)

A quantitative evaluation of the variations of AW glass (AW1 and AW2) shrinkage with different particle size as a function of increasing temperature can be derived from the curves plotted in Fig.4. 7.A. An inset of the AW shrinkage curves in the 1200°C-1325°C temperature interval is shown in Fig.4. 7.B for highlighting the main differences spotted in Fig.4. 7.A.

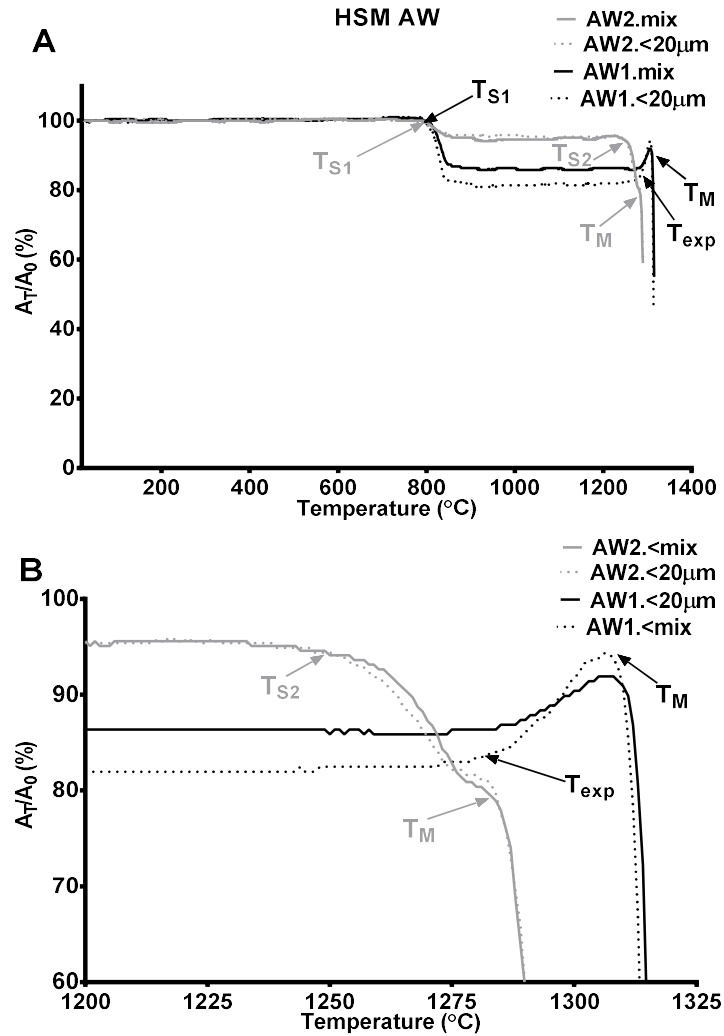


Fig.4. 7. Shrinkage of AW1 and AW2 glass samples with different particle sizes obtained by HSM: A. Full temperature range analysed and B. Inset depicting the shrinkage behaviour between 1200°C - 1325°C. The main thermal events of samples <20µm are pointed with grey arrows (AW2) and black arrows (AW1).

The main thermal events such as shrinkage temperature intervals (T_{S1} and T_{S2}) and the shrinkage amount (S1 and S2), expansion temperature interval (T_{exp}) and expansion amount (Exp), and melting temperature interval (T_M) were summarised in Table 4. 8, and identified in the plotted curves of Fig.4. 7.A-B. The changes in sample areas during the AW heating process can be observed as silhouettes recorded during HSM experiment for AW1 and AW2 less than 20µm, in Fig.4. 8.A and B, respectively.

Table 4. 8. Thermal events summary from HSM curves of AW1 and AW2 with different particle sizes.

Samples	T _{S1} (°C)	S1 (%)	T _{Exp} (°C)	Exp (%)	T _{S2} (°C)	S2 (%)	T _M (°C)
AW1.<20µm	786-850	18.0	1272-1306	11.8			1308-1314
AW1.mix	791-857	13.6	1289-1308	5.5			1310-1315
AW2.<20µm	788-848	4.1			1239-1279	13.3	1280-1290
AW2.mix	793-858	5.0			1233-1279	14.6	1279-1290

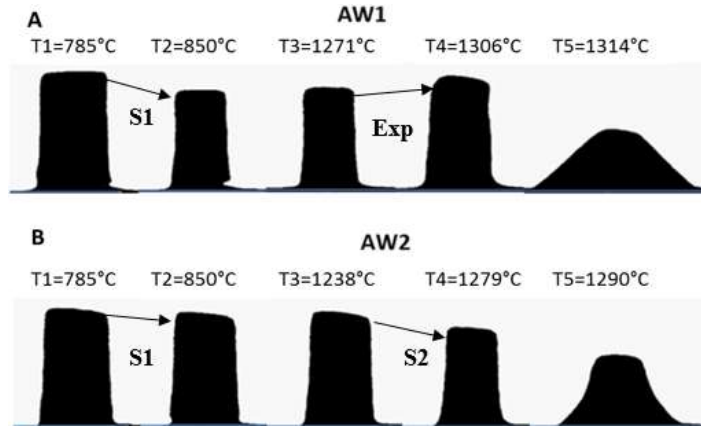


Fig.4. 8. HSM images of a cylindrical AW samples (<20 µm) at different characteristic temperatures during sintering for: A. AW1 and B. AW2. The sintering and expansion events are pointed with arrows for each AW batch.

The sintering behaviour of AW1 and AW2 samples, based in HSM results, can be divided in 5 stages/intervals:

- 1) The samples exhibited no geometrical variation (maintaining their initial rectangular silhouettes, as observed in the 1st silhouette of Fig.4. 8.A and B up to T_{S1} interval starting temperatures as shown in Table 4. 8.
- 2) The first shrinkage interval (T_{S1} shown in Table 4. 8, and 1st and 2nd silhouette of Fig.4. 8. A and B) was influenced by the AW batch and particle size. For instance, AW samples <20 µm showed earlier TS1, where AW1. <20 µm started at 786°C and AW2. <20 µm started at 788°C, while AW1.mix TS1 interval started at 791°C and at 793°C for AW2.mix. When comparing the batches, AW1 samples showed higher S1% values, where the particle size played a significant role, when compared to AW2 samples, e.g. AW1 samples showed a shrinkage of 13.6% (AW1.mix) to 18.0% (AW1. <20 µm) when compared to 4.1% (AW2. <20 µm) and 5% (AW2.mix) observed for AW2 samples (2nd silhouette of Fig.4. 8.A and B).

- 3) A plateau interval (T_2 to T_3 , 2nd and 3rd silhouette of Fig.4. 8.A and B) in samples area up to 1233°C -1239°C is observed for AW2 and up to 1272°C AW1. <20 μ m and up to 1289°C AW1.mix.
- 4) This stage (T_3 to T_4 , 3rd and 4th silhouette of Fig.4. 8.A and B) was characterised by the plateau end and it was different for AW1 and AW2 batches. AW1 samples showed an expansion event (T_{Exp} in Table 4. 8) where AW1.mix samples expanded 6% up to 1308°C and AW1. <20 μ m samples expanded 12% up to 1306°C. On the other hand, AW2 samples showed no expansion event occurring, instead a second sintering event (TS_2 in Table 4. 8.) occurred in the 1233°C-1280°C interval with a shrinkage of ~ 13.3% and 14.6% for AW2. <20 μ m. and AW2.mix.
- 5) When the temperature increased above T_M , a rapid distortion of the sample silhouettes was observed. For AW1, samples start melting at 1308°C and in less than 10°C, there is a prompt melting and distortion of the sample towards values lower than 60% (5th silhouette of Fig.4. 8.A). While for AW2 batch, samples start melting earlier at ~1280°C, in which samples reach values lower than 60% shrinkage at 1290°C (5th silhouette of Fig.4. 8.B).

4.5. Results: Indirect 3DP

This section presents the results obtained with the indirect 3DP of the prepared powder blends formulations summarised in section 4.3. Powder Blends Rationale.

4.5.1. Powder Blends Characterisation

4.5.1.1. SEM and PSD

In the SEM images of prepared powder blends (Fig.4. 9) AW particles were characterised by an irregular shape with sharp edges. While MD particles have a more globular morphology, and show some tendency for agglomeration (specifically observed for powder blend AW1.1). As for AW2.3 powder blend, it was characterised by high aspect ratio AW (very long) particles and irregular morphology MD particles when compared to more globular MD1. This irregular morphology of MD2 was previously observed in SEM images of MD2 (Fig.4. 3).

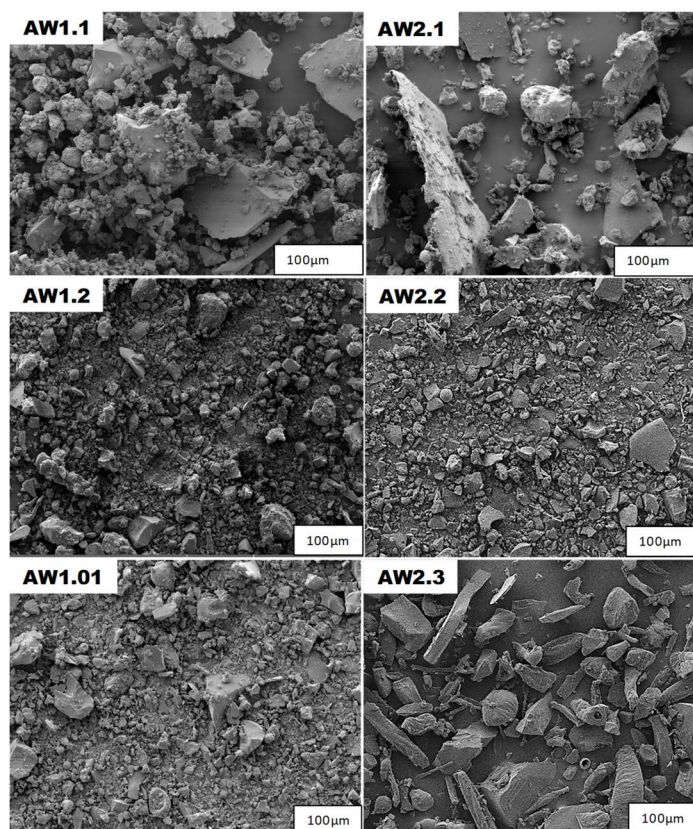


Fig.4. 9. SEM images of prepared AW powder blends. Powder blends AW1.02 and AW1.03 are not shown here because they could not be processed.

The powder blend PSD curves are shown in Fig.4. 10, where curves with the same formulation prepared with different AW batches were plotted together, e.g. AW1.1 and AW2.1. Main size class peaks can be identified for all analysed powder blends curves and the intensity of main peaks was added to each curve. Accordingly, to the number of size classes peaks, powder blends were classified as trimodal (AW1.1, AW2.1, AW1.2 and AW2.2) and bimodal (AW1.01 and AW2.3, Fig.4. 10). The values obtained from the curves analysis, such as $D_x(10)$, $D_x(50)$ and $D_x(90)$ were summarised in Table 4. 9.

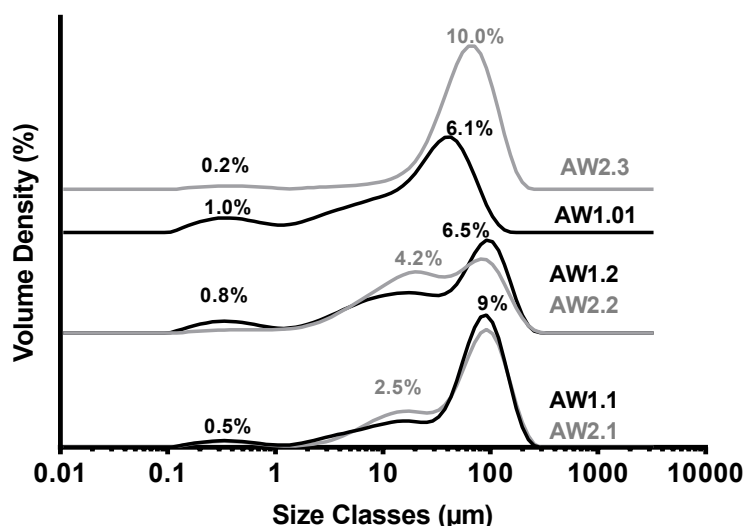


Fig.4. 10. Differential particle size distribution curves of prepared AW powder blends, where main peaks volume density% was quantified.

Table 4. 9. Particle size distribution (PSD) of prepared powder blends.

Powder Blend	D_x (10) (μm)	D_x (50) (μm)	D_x (90) (μm)
AW1. 1	4.89 (0.31)	65.1 (0.76)	135 (0.73)
AW2. 1	6.49 (0.14)	60.6 (1.48)	139 (1.27)
AW1. 2	2.04 (0.21)	36.5 (3.38)	128 (2.30)
AW2. 2	4.93 (9.34)	29.8 (1.87)	117 (2.75)
AW2. 3	19.2 (1.55)	57.8 (1.93)	115(3.55)
AW1.01	0.86 (0.08)	23.1 (0.36)	64.4 (0.74)

Powder blends prepared with the same formulation but with different AW batches presented similar particle size distribution from both SEM (Fig.4. 9) and PSD curves (Fig.4. 10) results. For instance, AW1.1 and AW2.1 had almost identical curves (Fig.4. 10.), with similar average particle size D_x (50) values (Table 4. 9) of ~65.1 μm and 60.6 μm respectively. AW1.2 and AW2.1 presented similar PSD curves, where AW1.2 was characterised by smoother transition between peaks (as observed for AW1.1 and AW2.1) whereas AW2.2 had an abrupt transition between first and second peak. Following the same trend, D_x (50) values (Table 4. 9) were slightly different of ~36.5 μm (AW1.2) and ~29.8 μm (AW2.2). Moreover, when compared to the other blends, AW1.01 presented the lowest values of D_x (50) of 23.1 μm (Table 4. 9) and the highest density of particles smaller than 1 μm (1st peak with a 1.0% volume density), that was dictated by the powder blend formulation in which AW and MD<53 μm. On the other hand, powder blend AW2.3 was close to be classified as monomodal, due to the low density of particles smaller than 1 μm (1st peak with 0.2% volume density) and a very intense 2nd peak, representing most of particles in the 10-100 μm range (Fig.4. 10).

4.5.2. 3DP: Powder Blends Printability Study

4.5.2.1. Powder Blends Flowability

The qualitative results obtained upon 3DP process observation of each one of the powder blends are summarised in Table 4. 10.

Table 4. 10. Summary of flowability results of prepared powder blends. (*) When printing AW2.2 minor issues related with insufficient recoating were observed.

Powder blend	Flowability	Observation/Details
AW1.01	Low	Powder was not spread uniformly/insufficient recoating
AW1.02	Too High	Powder was impossible to compact at initial stages
AW1.03	High	Powder bed major instability with misaligned layers
AW1.1	Sufficient	Powder and binder spread uniformly
AW1.2	Sufficient	Powder and binder spread uniformly
AW2.1	Sufficient	Powder and binder spread uniformly
AW2.2	Sufficient	Powder and binder spread uniformly
AW2.3	Sufficient	Powder and binder spread uniformly

From the eight powders blends, five of them (AW1.1, AW1.2, AW2.1, AW2.2 and AW2.3) were classified with sufficient flowability. On the other hand, AW1.02 was the only one impossible to process due to its high level of flowability and lower bed packing density, where the powders could not be compacted in the feeding area (one of the mandatory steps before starting the 3DP process, as described in section 2.3.2.4. 3DP Process). Hence, green parts were not available for this blend. Similarly, AW1.03 had high flowability, where the layers recoating was very uniform but shifted regarding the previous layer, but parts were possible to be attained. Finally, for AW1.01 low flowability was observed when the layers were not spread uniformly on the top of a binder jetted area of the previous layer.

4.5.2.2. Green Parts Quality and microstructure (SEM)

The second criteria used for assessing the powder blends printability was the quality of the obtained 3DP green parts. Firstly, the green parts obtained (except for AW1.02) were all characterised as strong enough to be handled. This was followed, by their geometry qualitative evaluation on regards to the CAD model (disc shaped) as summarised in Table 4. 11. The representative images examples of the green parts obtained for each powder blend are shown in Fig.4. 11.A-D.

Table 4. 11. Qualitative assessment of green parts quality.

Powder blend	GP quality	Observation/Details
AW1.01	Not acceptable	Irregular shape and surface
AW1.03	Not acceptable	Irregular shape with major layers' misalignment
AW1.1	Satisfactory	Shape very close to a disc with minor layers' misalignment
AW1.2	Good	Disc shape and regular surface
AW2.1	Excellent	Disc shape and regular surface
AW2.2	Good	Disc shape and regular surface
AW2.3	Good	Disc shape and regular surface



Fig.4. 11. Representative green parts, 3DP with the following powder blends: A. AW1.01, B. AW1.03 C. AW1.1 and D. Representative sample for AW1.2 AW2.1, AW2.2 and AW2.3.

The SEM images of the green parts prepared with different blends can be observed in Fig.4. 12. All green parts microstructure was characterised by a surrounding homogeneous matrix of MD with AW particles represented by the lighter areas, except for AW1.1, where the MD matrix seems less regular with some spaces in between. AW1.01 green parts are the ones with smaller AW particles, while AW1.1, AW2.1 and AW2.3 seem to have a higher number of big particles. AW1.2 and AW2.2 green parts present similar AW particle size distribution.

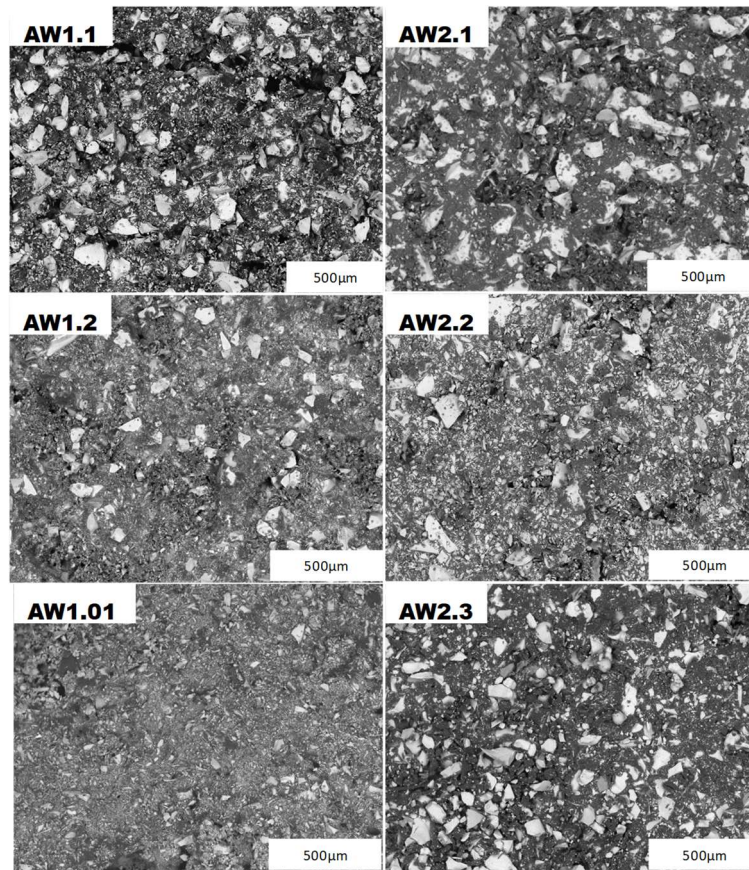


Fig.4. 12..3DP Green parts microstructure prepared with different powder blends formulation.

4.5.3. Post-Processing: Powder Blends Sinterability Study

4.5.3.1. Sinterability study

Consolidation of sintered parts

Consolidation results obtained for each powder blend sintered with different heating protocols were summarised in Table 4. 12. The images of samples after sintering, with an example of each level of consolidation were provided in Fig.4. 13.A-C.

*Table 4. 12. Consolidation levels obtained after sintering powder blends with different heating protocols: -1=no consolidation, 0=consolidation with shrinkage, 1 and 2=swelling and high swelling. VD=vacuum dry powder before processing. *samples were stronger*

Powder Blends				
Protocols	AW1.01/AW1.1/AW1.2	AW2.1	AW2.2	AW2.3
SINTI	1 (VD) and 2	-1	-1	
SINTII	0 (VD) and 1	-1	-1	-1
SINTIII.1h		0	0 (VD) and 1	0
SINTIII.6h		0*		0*

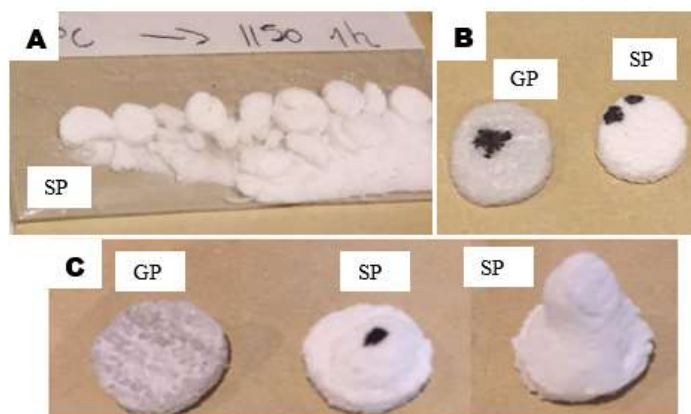


Fig.4. 13. Representative images of obtained consolidation levels: A. Level -1, sintered sample can't be handled, B. Level 0, sintered sample with shrinkage and C. Level 1 and 2, sintered sample with partial and high swelling. GP=green part and SP=sintered part.

Parts printed using powder blends prepared with AW2 (AW2.1, AW2.2 and AW2.3) did not consolidate when sintered up to 1150°C, independently of the heating rate of 10°C/min (SINT I) or 5°C/min (SINTII). There was a minor improvement when samples were sintered with slower heating rates (SINT II) where samples were less powder-ish but still very fragile to be handled (level -1, Fig.4. 13.A). On the other hand, powder blends prepared with AW1 (AW1.01, AW1.1 and AW1.2) consolidated with SINT I yet parts swelling was observed (Fig.4. 13.C). In more detail, consolidation results of SINT I provided in Table 4. 12, show that the swelling level was attenuated by VD protocol. Additionally, when a slower sintering rate of 5°C/min and vacuum drying procedure were combined, the swelling effect observed in both AW1 and AW2 samples was mitigated. The swelling effect was never observed for both AW2.1 and AW2.3 sintered parts, where AW2.1 was never vacuum dried and AW2.3 was always vacuum dried. Consolidation of AW2 parts was only observed after sintering up to 1200°C (SINTIII), where AW2.2 parts were strongly consolidated after one-hour sintering (SINTIII.1h). Whereas AW2.1 and AW2.3 were strongly consolidated after longer sintering time of six hours (SINTIII.6h). The results obtained in a more in-depth study on the effect of the heating rate on de-binding mechanism of AW1.1 samples are presented in the next section 4.5.4. De-binding studies.

Microstructure of sintered parts (SEM)

The microstructure of samples prepared with powder blends with the same formulation (AW1.1 with AW2.1 and AW1.2 with AW2.2) sintered with heating protocol SINTII are shown in Fig.4. 14. Similar microstructures were obtained when the same powder blends were sintered with SINT I and SINT II.

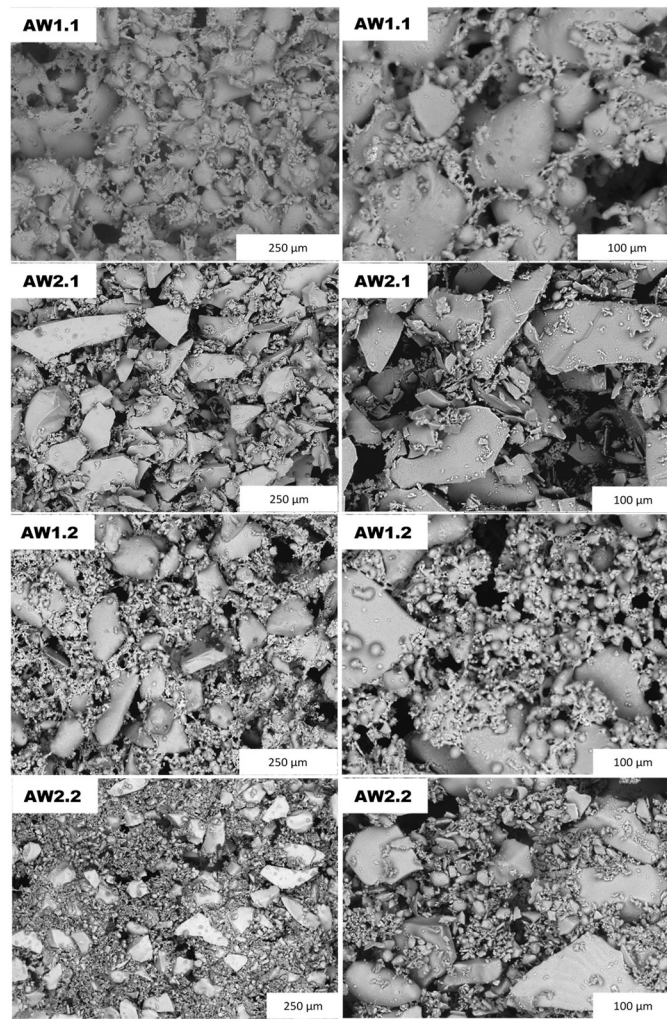


Fig.4. 14. Microstructure images (SEM) of AW1.1, AW2.1, AW1.2 and AW2.2 parts sintered with SINT II at different magnification: images on the left with a magnification of 200x and images on the right with a magnification of 600x.

After sintering, parts microstructure consisted in AW particles with different sizes and shapes, with no trace of the MD previously observed in the green parts (Fig.4. 14). However, samples prepared with the same formulation but different AW batches presented different microstructure regarding AW particles morphology evolution stages (angular, rounded or globular) across different particle size ranges (small to large). For instance, AW1.1 sintered parts (Fig.4. 14. at lower magnification SEM images) were characterised by an interconnected structure, where both small and large AW particles shape changed from the initial angular towards a globular one. Whereas for AW2.1 parts sintered with the same protocol, there was no evidence of AW particle shape change at any size range. Similarly, AW1.2 sintered parts showed evolution of large AW particles towards rounded edges, while small particles had a globular shape and promoted the observed interconnected network (higher magnification SEM image, Fig.4. 14). Instead AW2.2 sintered parts showed large particles with no evidence of shape evolution and small particles may be classified as rounded.

Only powder blends prepared with AW2 batch were sintered with SINT III for one hour (AW2.1, AW2.2 and AW2.3) and six hours (AW2.1 and AW2.3), as presented in Fig.4. 15 and Fig.4. 16, respectively.

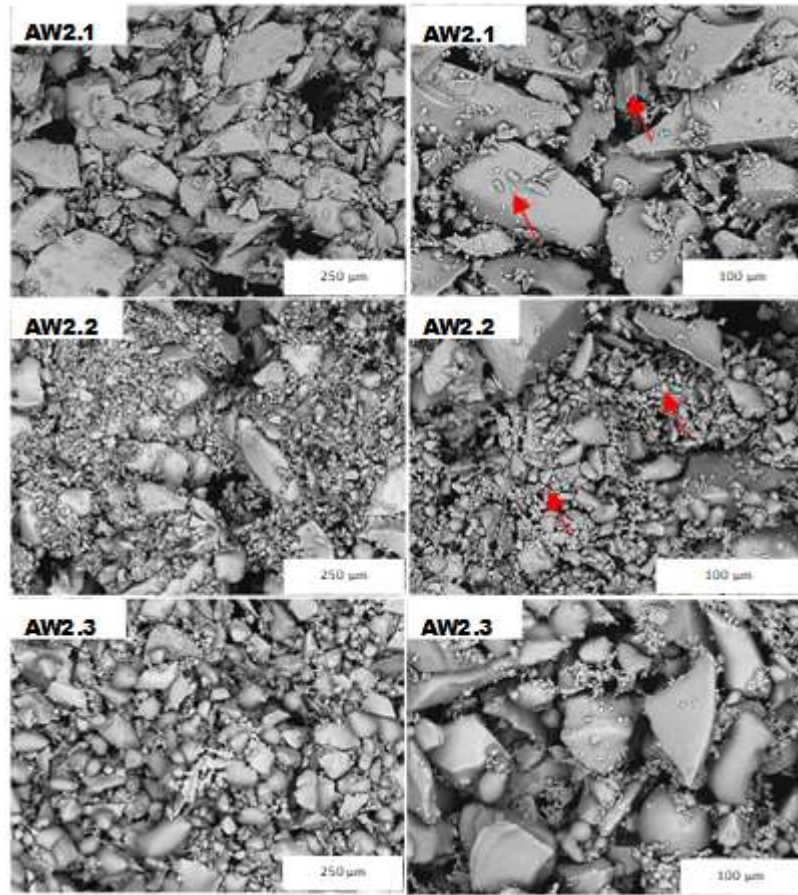


Fig.4. 15. Microstructure images (SEM) of AW2.1, AW2.2, AW2.3 parts sintered with SINT III for 1 hour at different magnification: images on the left with a magnification of 200x and images on the right with a magnification of 600x. Red arrows are pointing towards globular shape particles.

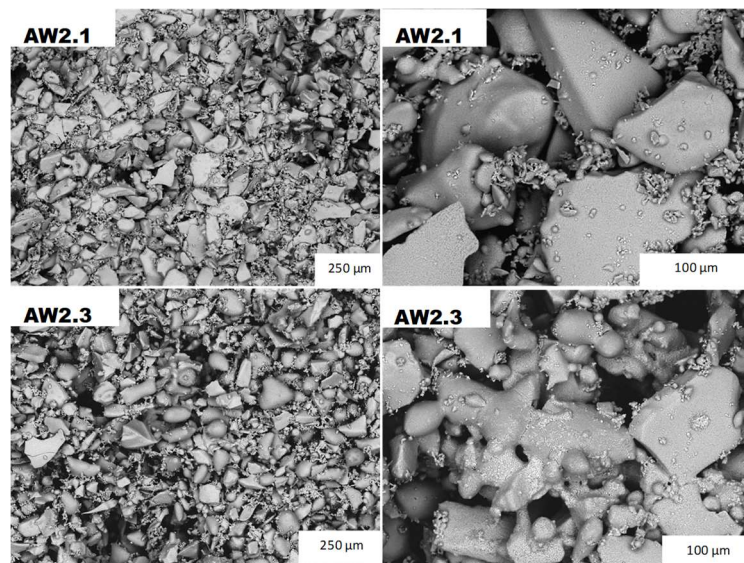


Fig.4. 16. Microstructure images (SEM) of AW2.1 and AW2.3 parts sintered with SINT III for 6 hours at different magnification: left (lower) and right (higher).

Sintering up to higher temperatures (1200°C) for one-hour lead to a minor particle shape evolution of small (AW2.1 and AW2.2) and medium size (just observed for AW2.2) particles towards a globular shape (red arrows), while big particles remained unchanged. When comparing the high magnification SEM images in Fig.4. 15, the particle change evolution was more obvious for AW2.2, characterised by a larger number of particles in the small and medium size range.

It was only when AW2.1 samples were sintered up to 1200°C for six hours (Fig.4. 16) that the big particles showed some rounded edges with small particles acting as interconnection points. AW2.3 samples microstructure observed in Fig.4. 16. was more homogeneous than AW2.2 and AW2.1 powder blend parts. For example, AW2.3 was characterised by particles shapes and size uniformity, whereas AW2.1 and AW2.2 showed a contrast between small and big particles with differences in shape evolution. Additionally, the sintering time played a key role in observed AW2.3 microstructure, where longer heating time promoted particle shape change and development of an interconnected network.

Crystallinity (XRD) after sintering

The XRD spectra of AW1.1 (AW1 representative) and AW2.1 (AW2 representative) samples after sintering with SINT I (green), SINT II (grey) and SINT III for two (black) and six hours (blue) are shown in Fig.4. 17. The crystalline phases identified after XRD pattern fitting were AW batch dependent, thus they were just plotted once for AW1 and AW2.

After sintering with the same protocol SINT II (grey pattern in Fig.4. 17), three predominant crystalline phases of whitlockite (●) wollastonite (■) and hydroxylapatite (▲) were identified for AW1 XRD diffraction peaks. In the case of AW2, the XRD patterns were characterised by weaker diffraction peaks that can be attributed to two predominantly phases of whitlockite (●) and wollastonite (■). The amount of the wollastonite (■) and whitlockite (●) crystalline phases increased when AW1 was sintered at slower rates, as indicated by increasing diffraction peak heights (SINT I and SINT II, green and grey patterns in Fig.4. 17). Similar diffraction patterns (grey and black patterns) were obtained for AW2 samples, when sintering up to temperatures of 1150°C or 1200°C for one hour. On the other hand, AW2 diffraction patterns showed an increase in the main wollastonite (■) peak ($2\theta=30^\circ$) intensity when sintering time was increase from one to six hours ((SINT III.1h and SINT III.6h, grey and blue pattern in Fig.4. 17).

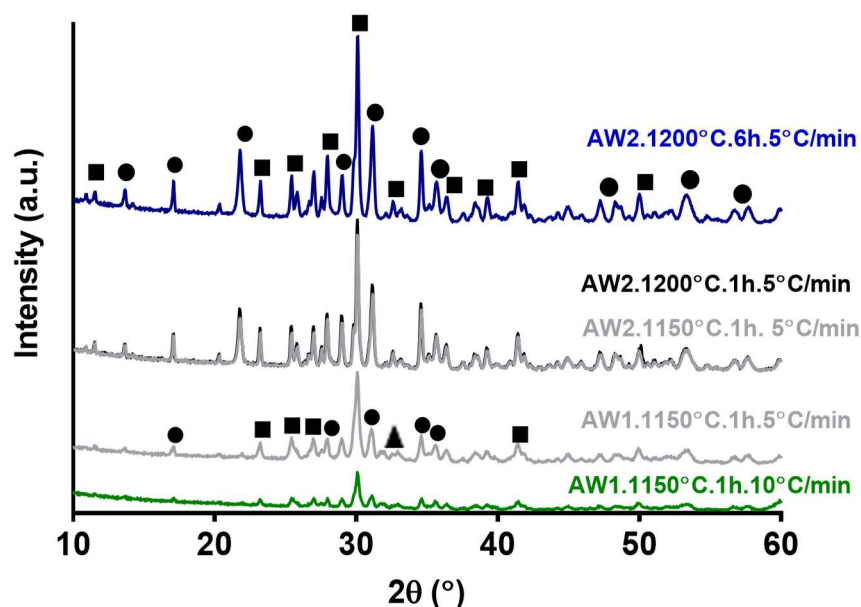


Fig.4. 17. Influence of sintering protocol on the X-ray diffraction (XRD) spectra of AW1 and AW2 batches. From bottom to top: green and light grey spectra are comparing the influence of heating rate on the AW1 sintering process; dark grey and black spectra are comparing the influence of temperature increase on the AW2 sintering process and blue spectra when compared to the dark spectra is showing the influence of time in the sintering process of AW2. Crystalline phases identified as: Whitlockite (●), Wollastonite (■) and Hydroxylapatite (▲).

4.5.4. De-binding studies

Maltodextrin (MD) Burning Study

When MD <90 μm was heated up to set temperatures at 10°C/min (Fig.4. 18), it was observed that MD burning point was between 290°C and 300°C, with MD burn and swollen at 300°C.

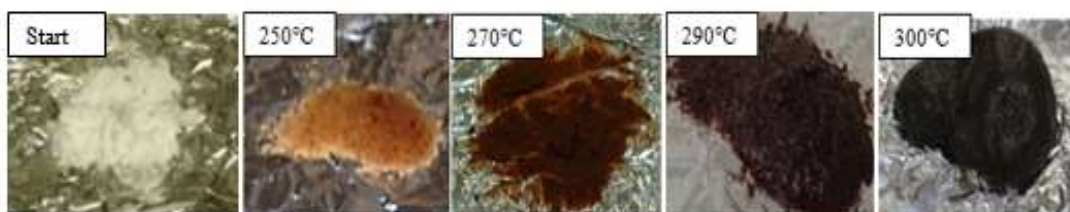


Fig.4. 18. Maltodextrin burning study at 10°C/min up to set temperatures as described in each image.

The influence of the heating rate on the MD < 53 μm burning process can be observed in Fig.4. 19.A-C. When the MD samples were heated at the 10°C/min Fig.4. 19.A) the final structure swelling was observed, whereas at the the slowest heating rate of 2.5°C/min (Fig.4. 19.C) the swelling was not noticed.

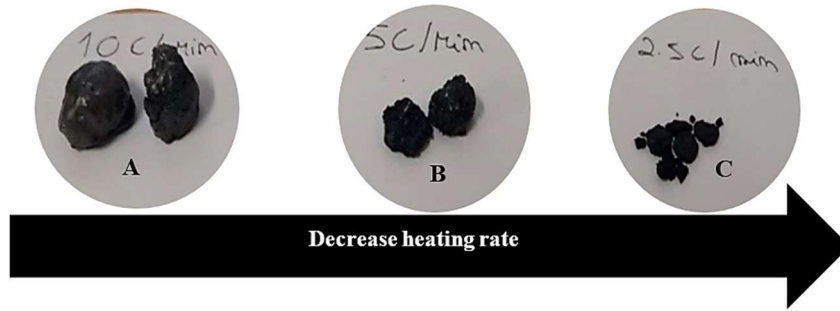


Fig.4. 19. Maltodextrin $<53\ \mu\text{m}$ pictures after heating up to 330°C at different heating rates: A. $10^\circ\text{C}/\text{min}$, B. $5^\circ\text{C}/\text{min}$ and C. $2.5^\circ\text{C}/\text{min}$.

The combined influence of the PS and HR on the MD burning out process are shown in Fig.4. 20.A-D. It was observed that when MD $<20\ \mu\text{m}$ (Fig.4. 20.A and C) was heated up to the burning temperature, the final structure was always swollen, yet lower heating rates leading to less swelling. Whereas, when MD $20\text{-}53\ \mu\text{m}$ was heated at the lowest rates were used no MD swelling was observed (Fig.4. 20.D).

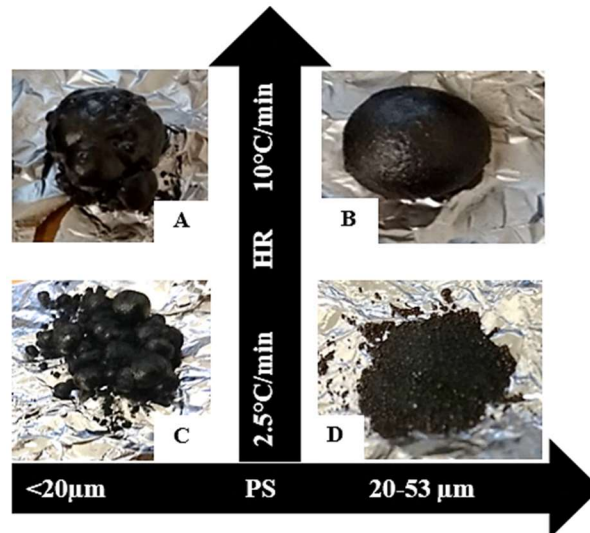


Fig.4. 20. Influence of MD particle size (PS) and heating rate (HR) on MD burning out up to 330°C :
0-A. PS= $<20\ \mu\text{m}$ and HR= $10^\circ\text{C}/\text{min}$, B. PS= $20\text{-}53\ \mu\text{m}$ and HR= $10^\circ\text{C}/\text{min}$, C. PS= $<20\ \mu\text{m}$ and HR= $2.5^\circ\text{C}/\text{min}$ and D. PS= $20\text{-}53\ \mu\text{m}$ and HR= $2.5^\circ\text{C}/\text{min}$.

Maltodextrin (MD) Burning Out process of 3DP green parts

The de-binding or MD burning out process of 3DP green parts was initially investigated to understand the swelling effect observed (Fig.4. 13.C) after sintering with SINT I. Thus, 3DP AW1.1 green parts were heated $10^\circ\text{C}/\text{min}$ up set temperatures as shown in Fig.4. 21.A-C. When samples were heated up to temperatures equal and higher than 310°C a swollen structure was observed when compared to the flat initial green part. Also, when the

temperature increased from 310°C to 779°C, a colour evolution from black-grey- white was noticed.

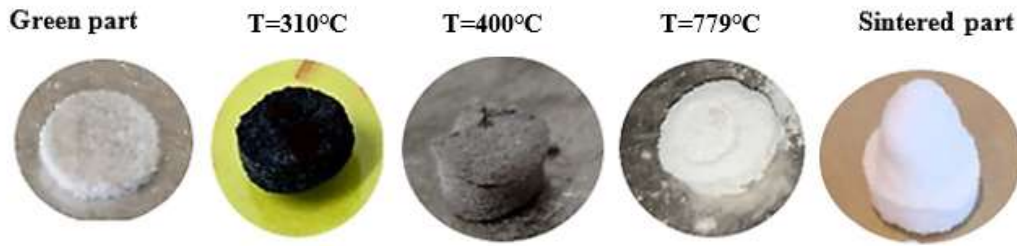


Fig.4. 21. AW1.1 3DP green parts de-biding study at 10°C/min up to different temperatures.

Then, the same heating protocol at a slower rate of 2.5°C/min was applied to previously vacuum dried AW1.1 3DP samples. As shown in Fig.4. 22, when heating was stop at 400°C, samples were black coloured and darker than the ones observed for the faster heating rate (Fig.4. 21). Moreover, no swelling was observed at any stage when samples were heated at a heating rate of 2.5°C/min. The heating rate effect on decreasing or mitigating the swelling level agreed with the results showed in sinterability study of previous section (4.5.3.1. Sinterability study).

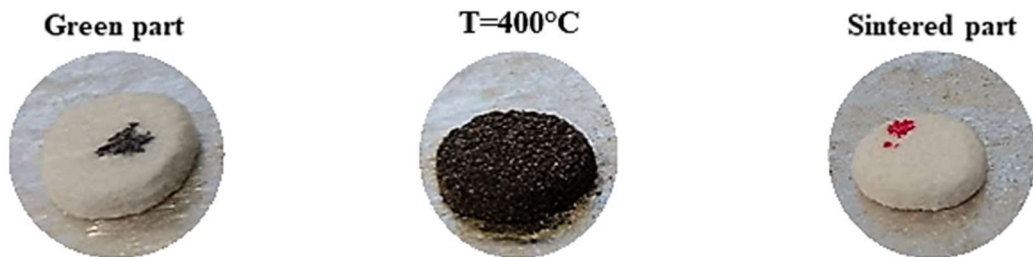


Fig.4. 22. Vacuum dried AW1.1 3DP green parts images acquired during de-biding study at 2.5°C/min up.

4.6. Discussion

4.6.1. Comparison with Previous Work

The goal of this study was to use indirect 3DP process for the preparation of AW porous discs required for a bonding study. For that purpose, an approach previously reported by (Mancuso et al. 2017) was selected, where powder blends (70% AW mixed with 30% MD) with specific formulations were successfully processed by indirect 3D printing into porous AW three-dimensional structures.

For this study, AW1.01 and AW1.02 blends (Table 4. 3) were prepared with the same formulation (AW4 and AW5, reported in (Mancuso et al. 2017)). However, when the same material (AW1 batch) and approach (3DP and sintering with SINT I) were used to prepare and process powder blends with the same formulation, different results were obtained.

Powder blends (AW4 and AW5) were successfully 3DP and sintered with different geometries as shown in Fig.4. 23.A-B (Mancuso et al. 2017). On the other hand, AW1.02 (same formulation as AW5) was impossible to process with 3DP due to high flowability and low bed packing density. Also, AW1.01 (the same formulation as AW4) processing resulted in 3DP green parts with bad quality (Fig.4. 11.A) and in swollen parts after sintering with SINT I (Fig.4. 23.C). Additionally, after sintering with SINT I, lack of consolidation was also observed for AW2 powder blends (AW2.1, AW2.2 and AW2.3) as observed by resulting powder-ish samples (Fig.4. 13.A).

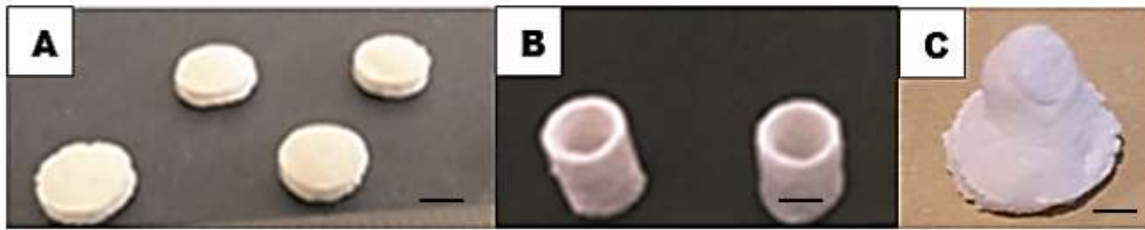


Fig.4. 23. Comparison images of sintered parts prepared with indirect 3DP process in different studies: A. AW4 (70% AW<53 μ m and 30% MD<53 μ m) (Mancuso et al. 2017), B. AW5 (55% AW 54-90 μ m, 15% AW< 53 μ m and 30% MD<53 μ m) (Mancuso et al. 2017) and C. AW1.01 (70% AW<53 μ m and 30% MD<53 μ m) (this study). Black scale bar represents 4 mm.

Moreover, different microstructures (SEM images) were obtained in the two studies after sintering with the same protocol (SINT I). For instance, an intermediate stage of sintering (Fig.4. 24.A) was evident for AW4 samples (prepared by (Mancuso et al. 2017)) as cohesive necks grown at the particle contacts (German 1996; Denry & Holloway 2014). While for AW1.1 samples (Fig.4. 24.B), an initial stage of sintering was reached, where grain boundaries are still visible for large particles and neck growth occurs for small and medium particles (German 1996).

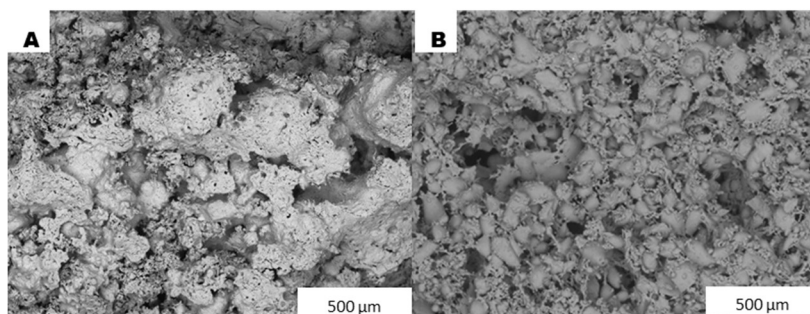


Fig.4. 24. SEM images of 3DP parts microstructures prepared in different studies , after sintering with the same protocol (SINT I): A. AW4 (70% AW<53 μ m and 30% MD<53 μ m)(Mancuso et al. 2017). B. AW1.1 (this study).

As described, the initial results differed significantly from previous results with this material in two main points: printability and sinterability of prepared powder blends. Hence a more in-depth study of the processing route was required and it will be discussed as follows:

- 1) Printability study of prepared powder blends
- 2) Sinterability study of prepared powder blends that presented good printability in 1)
- 3) Printability and sinterability of AW2.3, that was the last blends formulated based on the results obtained in the previous steps 1) and 2)

4.6.2. Processability of different powder blends formulations

4.6.2.1 Printability study

During 3DP processing, powders flowability is an essential parameter for achieving high 3DP resolution, where sufficient flowability of powders allows the roller to build up thin layers. Whereas low flowability and powder agglomeration decreases fabrication resolution due to insufficient recoating. Conversely, too high flowability as observed in does not provide sufficient powder bed stability for 3DP processing (S. F. S. Shirazi et al. 2015; Bai et al. 2017).

It could be observed that there was a direct relationship between flowability and resulting green parts quality: where the flowability was described as sufficient (AW1.1, AW1.2) the resulting parts Fig.4. 11.D were classified with good and excellent quality. On the other hand, when the flowability was classified as low (AW1.01), the resulting parts were characterised by an irregular surface with the presence of powder particles that could not be removed during the de-powdering step. When flowability was high (AW1.03), samples shape was deviated from the desired disc shaped geometry due to misaligned layers.

In the work reported in (Butscher et al. 2012), a linear correlation between powders average particle size ($D_x(50)$) and flowability was found. Simultaneously, it has been demonstrated that the powder particle size distribution is the most important topological characteristic in affecting powder bed packing and flowability (Utela et al. 2008; Zhou et al. 2017). Powder morphology was also described as a factor influencing powder flowability in less extent (Utela et al. 2008), however in this study it was not a controllable parameter.

AW1.01 low flowability could be explained by the presence of large amount of fine and very fine powders, resulting in particle agglomerates. This can be observed in the particle size distribution curve (Fig.4. 10), where 10% of particles were smaller than $0.86\ \mu\text{m}$ and 50% were smaller than $23.1\ \mu\text{m}$. In the work of (Utela et al. 2008) it was described that fine powders ($<20\ \mu\text{m}$) tend to agglomerate due to van der Waal's forces, where interparticle

forces can dominate gravitational forces, dramatically reducing flowability. In more detail, the mechanical spreading of very fine powders ($\sim 1\text{ }\mu\text{m}$) in dry state can be problematic and deposition is only possible as a low percentage in a predominantly coarser powders formulation. On the other hand, too high flowability of AW1.02 powder blend can be explained by its formulation where more than 55% is in the 54-90 μm , expecting a coarse nature powder that represented an unstable powder bed for 3DP (Utela et al. 2008).

Additionally, as reported in Table 4. 4 and confirmed by the SEM images and measurements (Fig.4. 2.A), AW1. 54-90 μm had an average particle size of 101 μm higher than the expected 72 μm , contributing to the coarser nature of AW1.02 powder blend. This can be explained by the sieving process of the observed high aspect ratio AW particles (SEM images and measurements in Fig.4. 2.A). A sieve will tend to emphasize the second smallest dimension because of the way particles must orient themselves to pass through the mesh opening.

Therefore, powder blends AW1.03, AW1.1, AW1.2 were formulated in this study (Table 4. 3) based on the results obtained with AW1.02 powder blend 3DP process. The strategy for improving powder blends flowability consisted in decreasing the powder blend average particle size and balancing the ratio between coarse (54-90 μm) and fine particles ($<20\text{ }\mu\text{m}$).

For instance, AW1.03 was formulated by decreasing both MD and AW particle size from $<53\text{ }\mu\text{m}$ to $<20\text{ }\mu\text{m}$ range. During AW1.03 3DP processing (see section Powder Blends Flowability) powders compaction and parts processing was possible, suggesting that flowability level was lowered. However, the obtained green parts were characterised by major layer displacement (Fig.4. 11.B), indicating that powder blends flowability was still not adequate for 3DP processing requirements. Consequently, AW1.1 formulation represented an effort to decrease flowability by decreasing AW coarse powders (54-90 μm) amount from 55% to 45%. During 3DP processing of AW1.1, the observed powders flowability was decreased to a point where it was classified as sufficient, yet resulting green parts were characterised by minor layer misalignment (Fig.4. 11.C).

At this point, since one third of the blend consisted in MD powders, the MD particle size role on the prepared powder blends flowability was investigated. For instance, when MD particle size was decreased from $<53\text{ }\mu\text{m}$ to $<20\text{ }\mu\text{m}$, particles tendency for agglomeration was observed in both MD alone (Fig.4. 3.B) and in AW1.1 powder blend (Fig.4. 9.A). The presence of agglomerates bigger than the individual particle size, might have influenced the powder blend flowability, hence green parts quality. Also, MD in the $<20\text{ }\mu\text{m}$ particle size range with increased surface area is more prone to moisture uptake (Largo Avila et al. 2015), which can influence the powder behaviour when very thin layers are deposited (Spierings et

al. 2016). These findings support the work published by (Sun et al. 2017), who reported that during 3DP, finer particles were susceptible to Van der Waal's force and moisture effects resulting in agglomeration.

Therefore, AW1.2 was formulated to re-establish the MD <53 μm particle size range and the coarser powder (54-90 μm) amount was adjusted from 45% to 40%. Resulting in a significant decrease from 65 μm to 37 μm of the average particle size (Table 4. 9). Hence, AW1.2 printability was successful with the powder blend flowability described as sufficient and the resulting good quality green parts as shown in Fig.4. 11.D.

Powder blends formulations AW2.1 and AW2.2 (Table 4. 3) were prepared with AW2 batch with the same formulation as powder blends AW1.1 and AW1.2. prepared with AW1 batch. A minor difference in the MD particle size from <20 μm to <53 μm can be observed between AW1.1 and AW2.1 formulation.

AW2.1 presented the best printability results (see section 4.5.2. 3DP: Powder Blends Printability Study), among all powder blends. When compared to AW1.1 with the same formulation, excellent green parts quality related to the superior AW2.1 flowability could be explained by the absence of MD agglomerates (Fig.4. 9). On the other hand, AW2.2 powders flowability was slightly inferior when compared to AW1.2, where minor lack of layer recoating was observed. This could be explained by AW2.2 lower average particle size value of $D_x(50) \sim 30 \mu\text{m}$ when compared to AW1.2 $D_x(50) \sim 37 \mu\text{m}$. Accordingly, it was the lowest value after AW1.01 $D_x(50) \sim 23 \mu\text{m}$ (Table 4. 9).

It can be suggested that the same powder blends formulations used in (Mancuso et al. 2017), might have originated powder blends with different particle size distribution, explaining differences in flowability and thus 3DP outcome. For example, depending on the as-received powder processing conditions (e.g. milling and sieving parameters), the obtained powder blend particle size distribution can vary. Thus, a step by step particle size distribution characterisation during powder blends preparation, would help towards a more consistent preparation process. The lack of particle size distribution data for the powder blends prepared by (Mancuso et al. 2017) makes it impossible to compare with the results obtained here.

4.6.2.2. Sinterability Study

In this study, the heating protocol SINT I, previously reported by (Mancuso et al. 2017) was the starting point for sintering the successfully 3DP parts (AW1.1, AW1.2, AW2.1 and AW2.2). When the sinterability of prepared powder blends with SINT I was investigated,

swelling behaviour and lack of consolidation were observed. Thus, this section reports the outcomes obtaining during:

- 1) Swelling behaviour investigation and the development of new heating protocol SINT II to obtain ideally consolidated samples (level 0 with no swelling, Table 4. 2)
- 2) Lack of consolidation obtained for AW2 sintered parts and the development of new heating protocol SINT III to obtain ideally a microstructure similar to the one reported by (Mancuso et al. 2017).

Swelling Behaviour

Based on the data observed in Table 4. 12, sintering AW1 powder blends (AW1.1, AW1.2) with SINT I, resulted in parts consolidation with partial and high swelling level Fig.4. 13.C. Sintered parts swelling was also observed for glass-ceramic scaffolds fabricated with polyethylene (PE) burning-out method (Bretcanu et al. 2014). This method involved the preparation of green bodies by mixing PE with glass particles, followed by a thermal treatment that involved a de-binding step (PE burning out) and a sintering step (glass particles sintering). The swelling across Z axis was attributed to the removal of the organic phase as gaseous products that flowed from the bottom to the top of the samples (Bretcanu et al. 2014). Hence, a de-binding study (described in 4.2.2.4. De-binding studies) was performed to understand at what point the samples started to swell in this study. As observed in Fig.4. 21, samples were already swollen at 310°C and 400°C, suggesting that indeed the swelling was related with MD burning out step. Also, the sample colour evolution is an indicative of MD burning out process, where the black colour represents the material burnt out but it is still within the structure, while at 779°C the white colour is explained by the complete “burning out of MD out of the structure”, leaving just the AW behind. The grey colour observed at 400°C is an intermediate phase, where the MD “burning out of the structure” process was still on going. Accordingly, the same swelling effect was observed after heating MD up to burning point temperatures (Fig.4. 18). Absorption of moisture is well accepted in maltodextrins know by their hygroscopic behaviour (Wang & Zhou 2013), where storage environment relative humidity is critical. According to (Chronakis 1998) when exposed to environments at low relative humidities (40% to 60%) for 18 days, MD attained equilibrium moisture level without undergoing any visible textural changes. Whereas when MD was stored above 75% relative humidity it changed from powder to a ‘sorption gel’. When water interacts with MD, a certain amount of water is absorbed in the system as part of the gel formation and characterised as ‘bound’ water, while the remaining, which does not interact with the polymer, could be

denoted as pure ‘free’ water (Chronakis 1998). No textural changes were observed for the MD powders in this study, thus vacuum drying was a step added to the powder blends preparation as an attempt to remove the free water absorbed by MD during storage or powders preparation. As observed in Table 4. 12 sintering with SINT I of previously vacuum drying AW1 powder blends resulted in swelling effect attenuation from high to partial level. Additionally, the swelling effect was attenuated when MD was burnt at slower heating rate (Fig.4. 19) and it was mitigated when the lowest heating rate of 2.5°C/min was used. Also, during the de-binding study (Fig.4. 22), it was observed that when green parts prepared with vacuum dried powder blends were heated at HR of 2.5°C/min, no swelling was observed. Interestingly, the black colour of the sample heated up to 400°C (Fig.4. 22), suggested MD burning out process was slower when compared to the grey-ish samples (Fig.4. 21) obtained when faster heating rate were used.

Based on these results, heat treatment SINT II was designed to avoid the swelling with a two-phase de-binding step : i) up to 350°C at a heating rate of 2.5°C/min, while the MD structure and any other residues, e.g. water is burning out within and out of the structure and ii) from 350°C to 779°C at a heating rate of 5°C/min, when the MD is burning out of the structure and disappears. The outcome of SINT II and vacuum drying powder blends before processing resulted in swelling mitigation, as described in Table 4. 12.

Lack of Consolidation

Microstructural variations were an important mean of monitoring the sintering process that is typically described as followed: particle rearrangement and interparticle new contact formation (adhesion), followed by the initial and intermediate sintering stage with interparticle neck growth and evolution (mass transport by viscous flow for amorphous structures) ending with a final stage of grain growth (German 1996).

After sintering with SINT I or SINT II, AW1.1 and AW1.2 microstructure (Fig.4. 25.B) revealed necking growth between contacting AW particles, promoting samples consolidation after MD burnt out. AW particles changed their shape to spherical which is an indicator that sintering is taking place, as described in (Siligardi et al. 2000).

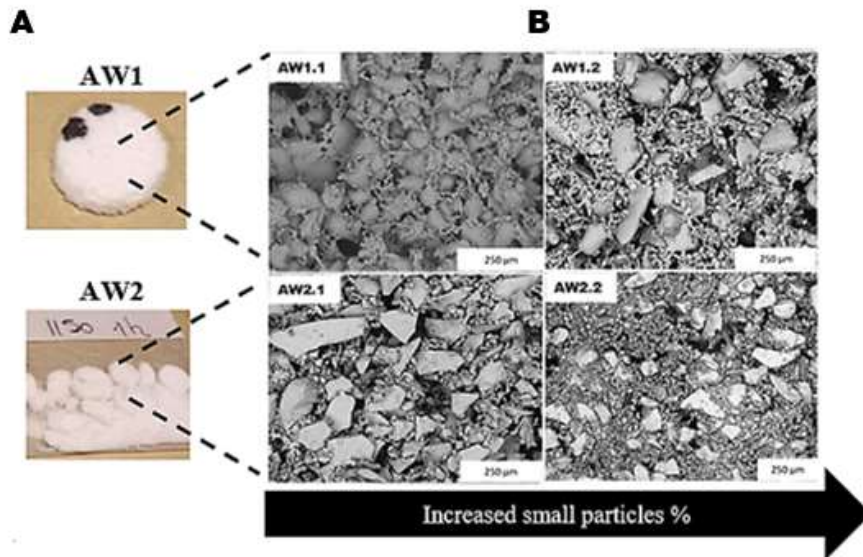


Fig.4. 25. Different consolidation results and microstructure (SEM images) obtained after sintering (SINT I or SINT II) parts prepared with AW1 (top images) and AW2 (bottom images).

It is interesting to note that the higher percentage of small particles added to AW1.2 formulation, led to differences in the sintered microstructure when compared to AW1.1. In binder jetting, by adopting bimodal powder mixtures where small particles fill the interstices of large particles, there is an increase in powder bed density and flowability when compared to mono-sized mixtures (German 1992). Yet the presence of large particles significantly lowers the driving force for sintering by reduction of surface energy when compared to high sintering rate of fine powders (Bai et al. 2017; German 1992). Hence for AW1.2 (Fig.4. 25.B), there was an observed decreased interparticle contact that might be explained by small particles cluster formation and faster sintering rate, inhibiting large particles sintering (German 1996).

As observed in Fig.4. 25.A , parts prepared with AW2 powder blends did not consolidate after sintering up to 1150°C (SINT I and SINT II), differing from the results obtained with AW1 powder blends with the same formulations. As noticed in the microstructure of AW2 sintered parts Fig.4. 25.B, lack of consolidation can be explained by absence of AW particles sintering, thus, after de-binding the AW particles were not bonded. AW2.2 formulation with observed small particles organised in clusters (Fig.4. 25.B), did not sinter as observed in same formulation with AW1 batch (AW1.2), pointing towards sintering behaviour differences between AW1 and AW2 batches, as confirmed by the results presented in 4.4.6. Hot stage microscopy (HSM).

AW1 batch was characterised by a one-step sintering behaviour with maximum shrinkage observed between 780°C -860°C, that begun shortly after glass transition temperature (identified as ~745°C in Table 4. 8), when viscous flow sintering starts (Siligardi et al. 2000).

The sintering was influenced by the particle size, where large particles addition decreased shrinkage from 18% to 13% (German 1992). The plateau observed at end of sintering up to $\sim 1280^{\circ}\text{C}$, was attributed to crystallisation processes, during which the viscosity increases, inhibiting viscous flow sintering (Montedo et al. 2009). Respectively, it is in good agreement with the DSC patterns (Fig.4. 6), where crystallisation occurred between $\sim 830^{\circ}\text{C}$ and 950°C . Additionally, the AW1 XRD data (Fig.4. 17) after sintering with SINT I (heating rate $10^{\circ}\text{C}/\text{min}$) confirmed the glass-ceramic nature of the obtained samples with crystal phases identified as wollastonite (calcium silicate) and whitlockite (calcium phosphate). The same crystalline phases were identified by (Chang et al. 2000) after AW sintering. Moreover, when heating rate was decreased to $5^{\circ}\text{C}/\text{min}$ (SINT II) the resulting XRD peaks intensity increased and a new crystalline phase was identified (Fig.4. 17), suggesting that heating rate influenced AW1 crystallisation process. It was reported by (Likitvanichkul & Lacourse 1998) that AW slower heating processes resulted in crystallisation peaks shift to lower temperatures. Finally, considering that full densification was already achieved (Calver et al. 2004), the AW1 expansion event (Exp in Table 4. 8) observed before melting, might be attributed to a late crystallisation (Baino et al. 2013). The particle size influence on the expansion amount can be explained by the crystallisation mechanism nature. AW1 surface crystallisation mechanism was implicit, where smaller particles with higher surface have more tendency for crystallisation (Calver et al. 2004), in agreement with the observed dependence of the crystallisation peaks temperature on particle size (Table 4. 7).

When a glass is heated above the glass transition temperature (T_g) sintering and crystallisation processes take place either one at a time or simultaneously (Siligardi et al. 2000). The desired order of events in a glass powder sintering process occurs when the sintering stage comes to an end before crystallisation begins (Siligardi et al. 2000; Boccaccini et al. 2007). As described above, AW1 glass particles maximum shrinkage (sintering event) occurred before crystallisation started, resulting in consolidated structures after sintering AW1.1 and AW1.2 3DP samples up to 1150°C .

On the other hand, AW2 batch (HSM curve, Fig.4. 8) was characterised by a two-step sintering behaviour with a first sintering event with a shrinkage of 4-5% happening between 780°C - 860°C and a second sintering event, where maximum shrinkage of 13%-15% was observed at higher temperatures of 1233°C - 1279°C . Also, there is a plateau observed between the two sintering events, described as crystallisation event in agreement with the exothermic peaks temperatures around 814°C - 950°C shown in AW2 DSC patterns (Fig.4. 6). The glass-ceramic nature of the obtained samples after sintering with SINT II (Fig.4. 17)

was confirmed by the XRD spectra with crystal phases identified as wollastonite (calcium silicate) and whitlockite (calcium phosphate). Accordingly, to the described HSM results and the lack of sintering observed in AW2 microstructure (Fig.4. 25) it can be suggested that the first sintering stage was interrupted by crystallisation start. This second sintering event has also been found by (Montedo et al. 2009; Baino et al. 2013) and described as the viscous flow sintering of the remaining amorphous part of the partially crystallised material. Moreover, as suggested by (Boccaccini et al. 2007) it was also possible that liquid phase sintering through diffusion by dissolution/ precipitation took place. This explanation is supported by the suspected low quantity of remaining glass phase (XRD in Fig.4. 17) that would not allow the significant shrinkage observed in this study. The AW2 more intense crystalline peaks when compared to AW1 after sintering with the same protocol (SINT II) suggest different crystallisation mechanisms between the AW batches. Correspondingly, AW1 and AW2 crystallisation mechanism was investigated by observing the DSC patterns (Fig.4. 6) of different particle size samples (Likitvanichkul & Lacourse 1998). While both AW1 crystallisation peaks were shifted to lower temperatures with particle size decrease, indicating surface crystallisation tendency for both crystalline phases formed. AW2 first crystallisation peak, showed no influence of particle size, indicating bulk crystallisation mechanism whereas surface nucleation was suspected for the second crystalline phase (Likitvanichkul & Lacourse 1998).

Sinterability, that represents a measure of the ability of sintering versus crystallisation of glass powders during heating was calculated for the AW1 and AW2 samples (Table 4. 13) as:

$$S_c = T_x - T_{Ms} \quad (\text{Equation 3})$$

Where T_x is the onset of crystallisation (obtained from DSC analysis in Table 4. 7) and T_{Ms} is the maximum shrinkage temperature (obtained from HSM analysis in Table 4. 8). The greater the S_c , the more independent are the kinetics of crystallisation and sintering processes (Baino et al. 2013). Therefore, higher AW1 S_c value indicated a better sintering behaviour involving final sample higher densification.

Table 4. 13. Thermal events obtained from HSM and DSC results used for calculating sinterability (S_c).

Samples	$T_x(^{\circ}\text{C})$	$T_{Ms} (^{\circ}\text{C})$	S_c
AW1.<20μm	831	910	-79
AW2.<20μm	827	1280	-453

Moreover, HSM results can be very useful in guiding the selection of sintering window in glass powders processing. As described by (Baino et al. 2013), if glass-ceramic structures are required and/or crystallisation occurs before densification is completed (as observed for AW2), the sintering temperature should be chosen in the range between the maximum densification and the melting onset. For instance, for AW1, the sintering window would be between 860°C and 1308°C that was in agreement with the consolidated samples obtained after heat treated with SINT I and SINT II, where the sintering step was defined as 779°C to 1150° C. Whereas, for AW2 temperatures between 1239°C to 1280°C should be considered to obtain consolidated samples. However, the furnace equipment used in this study had a maximum temperature limit of 1200°C, thus SINT III (1200°C for one or six hours) was designed as an attempt to improve sinterability of AW2.

When temperature was increased to 1200°C for one-hour, consolidated AW2.1 and AW2.2 samples were obtained (Table 4. 12) yet characterised by differences in sintered microstructure (Fig.4. 15). For AW2.2 parts, the predominant presence of small particles, resulted in a sintered network that was enough for obtaining strong samples. On the other hand, Fig.4. 15 showed no direct necking between large particles in AW2.1 parts, wherein the small particles inserted in a large skeletal structure had a negligible effect on the sintering response (German 1992; Bai et al. 2017).

Consequently, increasing AW2.1 sintering time to six hours was the key factor for observing sintering evidence with some large particle rounding (Fig.4. 16). Furthermore, longer sintering time resulted mainly in increased wollastonite (■) peak intensity (Fig.4. 17), suggesting larger crystal growth as described by (Cannillo et al. 2009) when AW heat treatment time was increased.

Nevertheless, the working temperature limit defined by the equipment did not allow further sintering of AW2.1 printed parts to meet the optimum sintering temperature defined by the HSM results.

Overall, besides playing a key role in printability, the large-small particle size ratio was also important for both AW1 and AW2 sintering process. For example, AW1.1 formulation characterised by a 45% large-25% small ratio resulted in a sintered microstructure with necking observed across small and large particles. On the other hand, small particles increase to 30% (AW1.2) resulted in clusters formation sintering at faster rate, decreasing interparticle contact between large particles.

For AW2 powder blends, the lower AW2 batch sinterability was the main cause behind lack of AW particles sintering, however large-small particle ratio played a role in less extent. For AW2.1 powder blend (45% large-25% small), faster sintering effect of small AW2 particles was neglected due to main large AW2 particles skeleton. For AW2.2 the same effect observed in AW1.2 was described, with the difference that small AW2 particles were less sintered than AW1 ones.

4.6.2.3. AW2.3

After sintering with SINT III both AW2.1 and AW2.2 powder blends were consolidated and strong enough to be handled. However sintered parts microstructure was yet far away from the sintering intermediate stage observed for AW1.1 parts, where necking growth between AW1 particles was attained.

Therefore, as an attempt to overcome the inferior AW2 batch sinterability, an intermediate particle size range (20-53 μm) was added to AW2.3 powder blend formulation. After sintering up to 1200°C for six hours (Fig.4. 16), an interconnected AW2.3 microstructure with some evidence of AW2 necking and merging was observed. When compared to AW2.1, where there is a limited sign of direct necking due to large particle radii, the added 20-53 μm particles increased interparticle contact and improved sintered density (Bai et al. 2017) . Furthermore, AW2.3 powder blend printability was comparable to the one observed for AW1.2 powder blend formulation. This might be explained by the similar obtained average particle size of $\sim 60\text{ }\mu\text{m}$ (AW2.1) and $\sim 58\text{ }\mu\text{m}$ (AW2.3).

Moreover, swelling behaviour was not observed after AW2.3 sintering because vacuum drying of prepared powder blends before processing and slower de-biding step (SINT II and SINT III) were implemented. Also, AW2.3 was formulated with maltodextrin in the 20-53 μm , to avoid the exacerbated swelling effect observed when sub-20 μm maltodextrin was present in the powder blend formulation (described in detail in section Swelling Behaviour).

4.7. Conclusions

In this study, bimodal mixtures with 40 to 45% of large AW particles and 25 to 30% of small AW particles resulted in good flowability and enough bed packing density needed for successful 3DP process. However, flowability differences across powder blends with the same formulation pointed towards the importance of the average particle size ($D_x(50)$) values. The combination of bimodal mixtures with appropriate large-small particle ratios and $D_x(50)$ values between 37 μm to 61 μm (AW1.2, AW2.1) resulted in the best printability outcome. At

the same time, maltodextrin (30% of formulation) in the sub-20 μm particle size range should be avoided due to its agglomeration and moisture uptake tendency that negatively affects powder flowability.

Parts swelling and lack of consolidation were the issues observed during sintering of 3DP powder blends (AW1.1, AW1.2, AW2.1 and AW2.2). Swelling behaviour was attributed to moisture uptake explained by the hygroscopic nature of maltodextrin and it was mitigated by a combination of three factors: vacuum dry, a slower de-binding rate and excluding sub-20 μm MD particles. Additionally, prepared powder blends were stored in vacuum sealed containers as an extra measure to prevent moisture uptake.

Lack of consolidation and un-sintered AW particles were only observed after sintering AW2 powder blends up 1150°C (SINT II), indicating that the main cause was differences across AW batches. Based on the obtained AW batches characterisation (HSM and DSC), it was attributed to lower AW2 sinterability(S_C) when compared to AW1 and explained by sintering and crystallisation events competition (Baino et al. 2013). Moreover, 1239°C-1280°C was the suggested AW2 optimum sintering window, while 1200°C was the maximum temperature allowed for the furnace used in this study. Thus, within the equipment limits, influence of sintering temperature and time in AW2 particle sintering was investigated. Samples consolidation was observed with increased sintering temperature, yet at a microstructural level, AW particles sintering was particle size dependent.

Further work to improve sintering of AW2 powder blends will consist in conducting experiments in a furnace that allows higher temperature range, that can fulfil the AW2 sintering window (1239°C-1280°C).

CHAPTER 5. PLA-AW Hybrid Composite Structure

5. 1. Introduction

The varying mechanical properties of bone throughout its volume means that it is difficult for a synthetic implant formed from a single material to match the anisotropic properties in different regions. Furthermore, discrete anatomical regions such as cortical, sub-chondral and trabecular bone each have their own unique mechanical properties and architectures (Keaveny & Hayes 1993; Li & Aspden 1997).

Ceramic-polymer composites have been proposed as bone implants most commonly as particulate reinforced polymer structures (Rezwan et al. 2006), either solid or porous. This produces a material which has the strength of the polymer phase and a slightly higher modulus than the polymer phase, which for most biopolymers is normally a good match to the mechanical properties of trabecular bone. However, the wide range of variation in properties of natural bone is such that they may be better reproduced by bringing together two distinct structures made from two different biomaterials.

The aim for this chapter was to develop an innovative process for the fabrication of a hybrid biopolymer-bioceramic composite structure that would meet the complex anatomical requirements of bone implants.

The macro-scale composite structure has been produced by combining two structures: 1) macroporous poly (lactic acid) (PLA) structure (developed/described in Chapter 3), with mechanical properties which match those of trabecular bone, together with 2) microporous apatite-wollastonite glass-ceramic (AW), with mechanical properties which approach those of cortical bone. The AW scaffolds used in this study were fabricated by Naif Alharbi as described in (Mancuso et al., 2017) with the formulation AW1.02 described in Table 4. 3 and sintering protocol SINTI described in 2.3.2.5. Post-Processing.

Ultrasonic welding (UW) technology is a unique method of joining two parts together without using fasteners or adhesives because it uses the material to create the joint. This technique is particularly suited for assembling medical devices because it is a fast, clean, efficient and repeatable process. To obtain these advantages, however, a weldable material needs to be selected, fixtures need to be developed, and the weld process parameters need to be optimised. Overall two different approaches were selected for combining PLA with AW: i) ultrasonic welding and ii) thermal fusion. First, it was crucial to assess the suitability of both techniques for generating the PLA-AW interface without damaging any of the components during process. Then, the obtained interface and mechanism behind it was investigated by SEM and

the biocomposite integration was mechanically evaluated with a designed interfacial shear stress device.

5.2. Materials

As illustrated in Fig.5. 1.A and B, the structures used for assembling the composite were: 1) AW porous discs with 8 mm diameter and either 1.8 mm or 2.5 mm thick developed by (Mancuso et al. 2017) and 2) the PLA scaffolds discs (Ø10 mmx 5 mm), developed in Chapter 3. The rationale behind the design of AW and PLA parts that are characterised by different thicknesses was for AW to mimic the thinner cortical bone structure, whereas the PLA was to mimic the thicker trabecular bone structure.

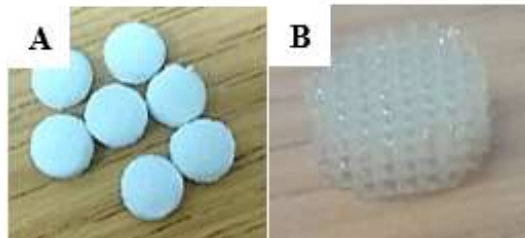


Fig.5. 1. Porous structures used for the hybrid composite assembly: A. AW discs and B. PLA scaffolds.

5.3. Ultrasonic Welding Preliminary Study

In order to successfully ultrasonic weld two dissimilar materials, the following welding parameters need to be selected: the ultrasonic wave properties such as amplitude, energy, the weld and hold time and the distance and pressure applied by the sonotrode.

Therefore, the first step of this process was to select the combination of welding parameters values needed for assembling the PLA-AW composite structure (described in detail in 2.3.3.2. Ultrasonic Welding). Consequently, a preliminary study was performed, where the ultrasonic welding process parameters influence on resulting bonded structures were investigated, as described in this section.

The influence of the ultrasonic welding parameters (Table 5. 1) on the welding process (described in section 2.3.3.2. Ultrasonic Welding) of the following materials/structures combination was assessed: 1) dense PLA- dense PLA, 2) porous PLA-porous PLA, 3) dense PLA- AW and 4) porous PLA- AW.

Table 5. 1. Ultrasonic welding parameters and values used in this study.

	Amplitude	Energy	Weld &	Distance	Press
	(%)	(J)	Hold time (s)	(mm)	(Psi)
Values	20-60%	50-300 J	5.5 & 2.5	0.1- 0.8	10-20

As depicted in Fig.5. 2.A. and C-E, the PLA parts used in this study were fabricated as described in section 2.3.1.1. Fused Filament Fabrication (FFF) Process with three geometries selected to test different material combinations.

For instance, dense PLA-dense PLA combination was assessed with PLA parts with square geometry (50x50x5 mm) with smaller dense pads (15x15 mm in the four corners for the testing approach, as shown in Fig.5. 2.A (showing the two parts to be welded) and B (showing how the parts are positioned in the welding machine and ready to be welded). Whereas, for testing the welding of PLA and AW (Fig.5. 2.D and E), a simple square PLA dense or porous pad (20x20x2mm) was fabricated to test the dense PLA- AW approach. Finally, a porous PLA box with 30x30x3mm with a Ø 8.5 mm hole (Fig.5. 2.C) was also fabricated that allowed the AW discs to be inserted before welding and to be constrained during welding process.

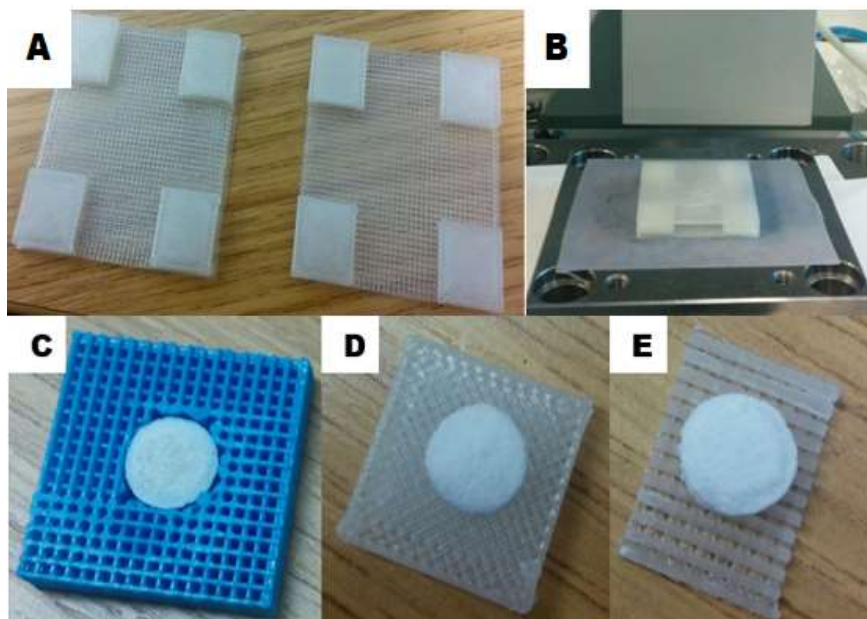


Fig.5. 2. Images showing the material combinations and geometries used in the preliminary study: A. Dense PLA samples with square and pads geometry, B. PLA dense samples aligned before welding. C. Porous PLA box with a Ø 8.5 mm hole to inset the AW disc, D. Dense PLA-AW and Porous PLA-AW.

The welding set-up for assembling the PLA-AW structures is shown in Fig.5. 3., and it consists in two tensile bars acting as temporary fixture to constrain the AW disc during welding and then the PLA part is positioned on the top of the AW disc to be in direct contact with the sonotrode.

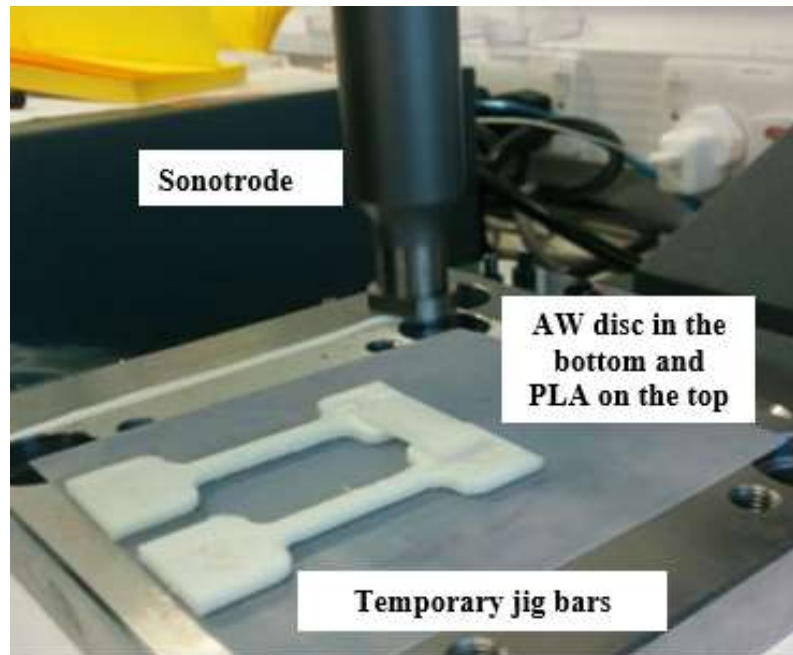


Fig.5. 3. Preliminary study set-up for welding PLA-AW samples. The AW disc is positioned in between two bars to constrain the sample during the welding process, then the PLA pad is positioned on the top.

5.4. Results: Composite Structures Assembly

5.4.1. Thermal Bonding

During thermal bonding, the first step consisted in positioning the AW sample in a pre-heated hot plate (250°C) for different times and to measure the AW sample surface temperature with a thermal camera, as summarised in *Table 5. 2*. For the thermal images acquired during AW heating procedure (Fig.5. 4.A-D), the blue area in the middle represents the AW sample and the surrounding yellow-red area represents the hot plate. The colour scale is located at the right area of the image, where blue represent the lowest temperature and yellow to red highest ones. The temperature was always measure at the AW sample centre and it was represented by the darkest blue or lowest temperature across all images areas.

Even though the target for AW surface temperature was 250 °C and as observed in thermal images (Fig.5. 4) the measured hot plate temperature was around that value; the AW surface measured temperature was never higher than 228°C (*Table 5. 2*). Moreover, AW surface was slightly burnt after heating the AW sample for 35 seconds, while a heating time of 10 seconds resulted in the lowest surface temperature. Thus, AW heating times of 15 and 25 seconds were selected for preparing the PLA-AW composite structures (Fig.5. 5) in this study and further characterisation is presented in section 5.5. Results: Composite Structures Characterisation.

Table 5. 2. Influence of heating time on an AW disc surface temperature measured with a thermal camera.

Heating time (s)	Aw disc surface temperature (°C)
10	180 ± 2
15	193 ± 2
25	215 ± 2
35	228 ± 2

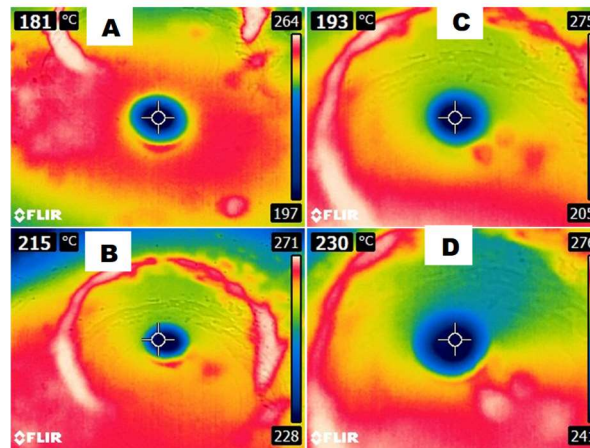


Fig.5. 4. Thermal images acquired during AW disc heating procedure. AW sample was placed in hot plate pre-heated at 250°C for different heating times: A.10 seconds, B. 15 seconds, C. 25 seconds and D. 35 seconds.



Fig.5. 5. Representative image of thermal bonded PLA-AW composite structure.

5.4.2. Ultrasonic Welding

5.4.2.1. Preliminary study

The ultrasonic welding parameters values that allowed the assembly of the PLA-PLA (both dense and porous structures) and PLA-AW (both dense and porous PLA) were summarised in Table 5. 3. The weld and hold times were selected as 5.5 s and 2.5 s for all the combined structures, whereas all the other parameters depended on the selected material/structure. For instance, lower pressure, distance and energy were selected when the AW parts were present.

When 20 psi pressure was applied and distance from sonotrode to the samples of 0.8 mm were selected for welding PLA-AW, it resulted in broken AW parts. On the other hand, higher amplitude was selected during welding process of dense PLA parts.

Table 5. 3. Ultrasonic welding parameters values selected for each material and structure combination of PLA and AW.

Samples	Amplitude (%)	Energy (J)	Weld & Hold time (s)	Distance (mm)	Pressure (Psi)
PLA-PLA (porous)	40	300	5.5 & 2.5	0.8	20
PLA-PLA (dense)	60	250	5.5 & 2.5	0.8	20
Dense PLA-AW	60	50	5.5 & 2.5	0.1	10
Porous PLA-AW	40	50	5.5 & 2.5	0.1	10

The obtained dense PLA- PLA and porous PLA-PLA structures are illustrated in Fig.5. 6.A. As pointed in Fig.5. 6.B and b, a welding line was observed (red arrows) between the bonded PLA porous structures and the pores were not affected by the selected process parameters (mainly pressure).

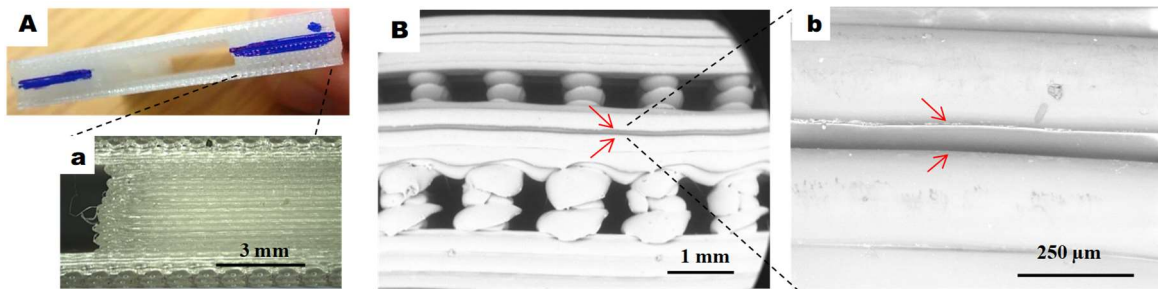


Fig.5. 6. Ultrasonic welding of PLA structures: A and a. Stereomicroscope images of dense PLA-PLA (increasing magnification), B and b. SEM images of porous PLA-PLA (increasing magnification) with red arrows pointing towards the welding line.

Independently of PLA structure (porous or dense), it was observed that AW discs with a thickness inferior to 2 mm could not be welded without surface fracturing (Fig.5. 7) even when lower pressure and distance values were selected. Thus, for all ultrasonic welding studies, AW discs with 2.5 mm thickness were fabricated.

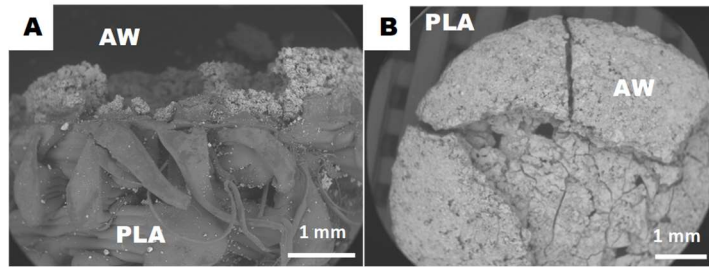


Fig.5. 7. SEM images of ultrasonic welded porous PLA- AW (2mm thick) composite: A. Cross-section view and B. top view. PLA and AW samples were identified in the image.

Ultrasonic welding of dense PLA and AW (2.5 mm thick samples) originated a continuous interface, where the PLA was moulded to lodge the AW disc (Fig.5. 8).

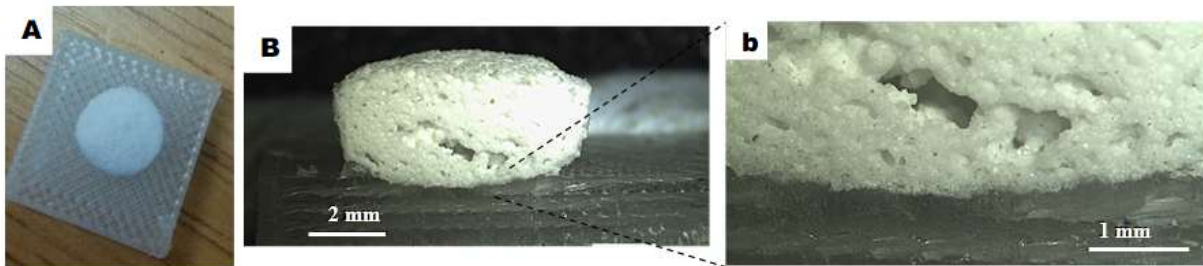


Fig.5. 8. Ultrasonic welding of dense PLA with AW disc (2.5 mm thick sample): A Stereomicroscope image of obtained structure and B and b. Cross section images of obtained structure (increasing magnification).

The porous PLA and AW discs were successfully welded, in both geometries tested: i) simple square geometry (Fig.5. 9.A) and ii) box with hole geometry (Fig.5. 9.B and C). The obtained interface (Fig.5. 9.c) was similar to the one observed for the dense PLA-AW welding (Fig.5. 8.b)



Fig.5. 9. Stereomicroscope images of ultrasonic welded porous PLA with AW (2.5 mm thick sample): A. Simple PLA squared geometry, B. PLA porous box with AW disc inserted and C and c. Cross section images of structure obtained in B (increasing magnification).

5.4.2.2. Final Geometry Assembly

One of the outcomes of the preliminary study (previous section) was the need to fabricate a specific aluminium fixture (Fig.5. 10.B) with predefined dimensions (Fig.5. 10.A) for holding the PLA and AW samples during welding, avoiding misalignment of samples. During welding, the AW disc was positioned on the bottom of the aluminium fixture and the PLA

was mounted on the top (Fig.5. 10.B) and positioned in a way that was aligned with the sonotrode (Fig.5. 10.C). The selected welding parameters were based on the results obtained in the preliminary study (Table 5. 3) for the porous PLA-AW bonding. The obtained composite macrostructure was similar to the one obtained with thermal bonding approach (Fig.5. 5).

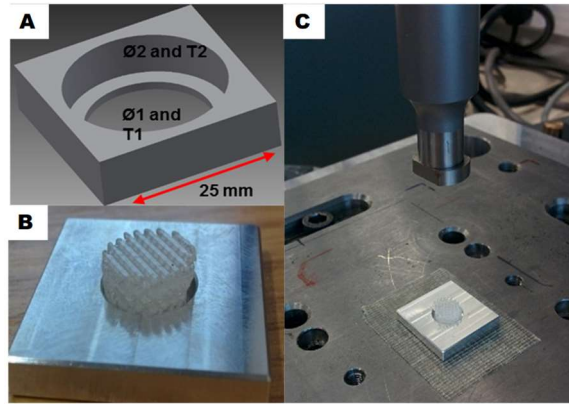


Fig.5. 10. Ultrasonic welding set-up used in this study: A. CAD model of designed fixture and B. fabricated fixture with PLA and AW and C. final welding set-up.

5.5. Results: Composite Structures Characterisation

5.5.1. Interface Morphology

SEM images of obtained interface of thermal bonded composites structures with different AW pre- heating times are shown in Fig.5. 11.A-F.

Pre-heating the AW sample for 25 seconds before positioning PLA sample on the top of it, resulted in superior integration between bonded PLA and AW, highlighted by the depth of infiltration of PLA into the porous AW structure (Fig.5. 11.D-F). On the other hand, shorter pre-heating times, resulted in inferior integration between PLA and AW structures (Fig.5. 11.C).

PLA-AW interface resulting from ultrasonic welding (Fig.5. 12. A-C) was very similar to the one described for thermal bonded samples prepared with longer AW pre-heating times (Fig.5. 11.F). At the edges, the interface was characterised by aligned AW and PLA samples.

After assembling the composite structure with two different approaches, differences on the porous PLA structure were observed. After thermal bonding, with no regards to pre-heating times, PLA pores height was affected, especially on the edges of the structure Fig.5. 11.A and D. Whereas no PLA porous samples structural alterations were observed in the ultrasonic welded composites.

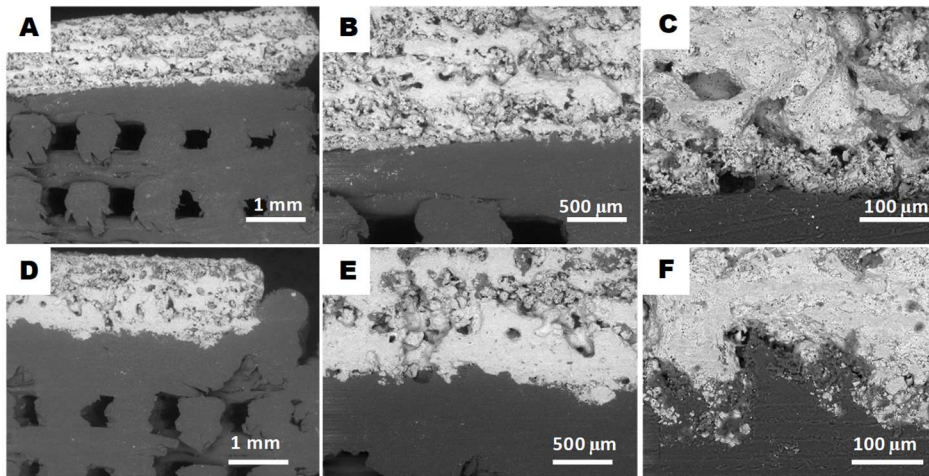


Fig.5. 11. Cross-section SEM images of thermal bonded PLA-AW composites interface with increasing magnification when AW was pre-heated for: A-C.15 seconds and D-F.25 seconds. No SEM images of sample edges were acquired.

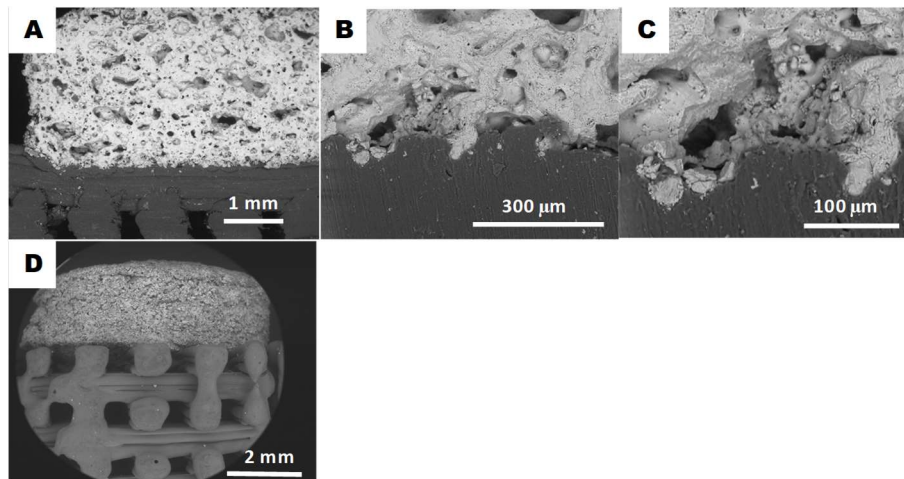


Fig.5. 12. SEM images of ultrasonic welded PLA-AW composites interface: A-C cross section with increasing magnification and D. Sample edges.

5.5.2. Interfacial Shear Testing

The representative force-displacement curves acquired during interfacial shear testing of prepared composite structures with thermal bonding (TB) and ultrasonic welding (UW) can be observed in Fig.5. 13.B . The average values of shear peak load were summarised in Table 5. 4 and interfacial shear strength values are presented in Fig.5. 14.

The force-displacement curves were influenced by the approach and parameters used for assembling the composites structures being tested. For instance, ultrasonic welded (UW) samples presented the highest values for shear peak load (~131 N, Table 5. 4), while samples thermal bonded with lower AW pre-heating times (TB.15.15) had the lowest shear resistance (~19 N, Table 5. 4). Also, after failure, ultrasonic welded samples presented a sudden force drop, whereas thermal bonded structures showed a slower decrease in force values, hence higher displacement values were observed.

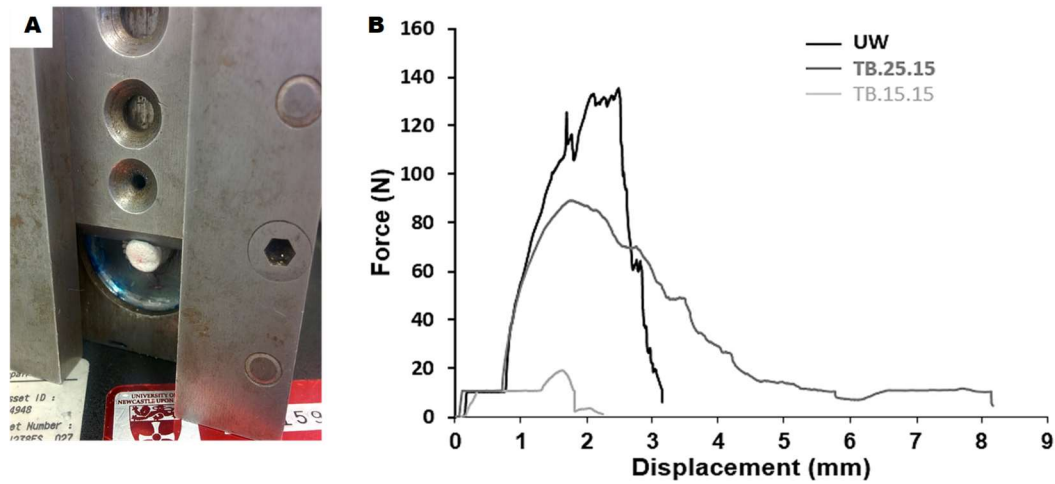


Fig.5. 13. Interfacial shear strength testing of composite structures: A. Structure embedded in resin during testing, with blade hitting the interface. B. Representative force-displacement curves acquired during testing.

Table 5. 4. Average values ($n=3$ for TB and $n=2$ for UW) of interfacial shear properties calculated from load-displacement curves.

	TB.15.15	TB.25.15	UW
Peak Load (N)	18.77 ± 3.03	96.33 ± 9.07	130.67 ± 25.03

Interfacial shear strength values (Fig.5. 14) were proportional to AW pre-heating times, with higher shear strength values for longer AW pre-heating times (TB.25.15). There was a significant difference on the interfacial shear strength values of thermal bonded samples with lower AW pre-heating times (TB.15.15) versus the ultrasonic welded samples (UW).

Simultaneously, interfacial shear strength of thermal bonded samples with longer AW pre-heating times (TB.25.15) did not show significant differences from the ultrasonic welded samples (UW).

After shear testing, different failure mechanisms were observed for the three samples group, as illustrated in Fig.5. 15.A-C. Within thermal bonded samples, failure occurred at the interface for composite structures obtained from shorter AW pre-heating times (TB.15.15, Fig.5. 15.A), whereas failure occurred at PLA structure as highlighted by the PLA filaments attached to the AW (Fig.5. 15.B). On the other hand, ultrasonic welded samples failed due to AW delamination with what was left from AW structure still attached to the PLA structure (Fig.5. 15.C).

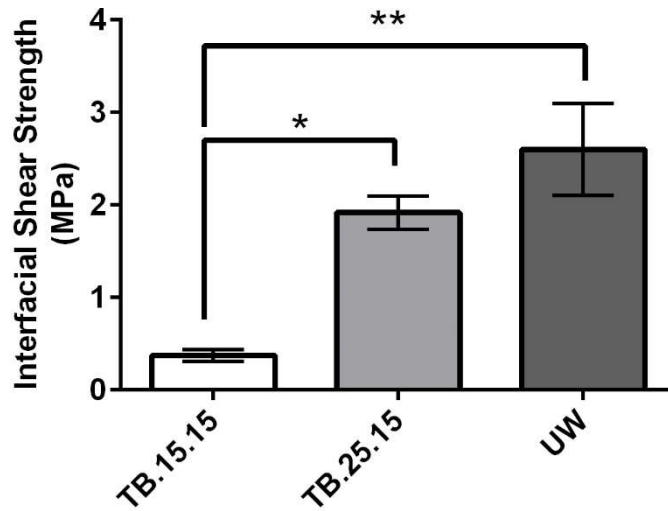


Fig.5. 14. Average ($n=3$ or 2) interfacial shear strength values obtained for composite structures prepared with different approaches/parameters.

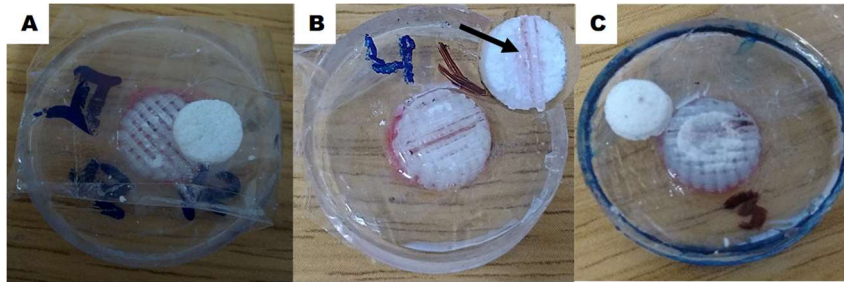


Fig.5. 15. PLA-AW composite structures, assembled with different approaches/parameters, after shear testing: A. thermal bonded (TB) with 15 seconds AW pre-heating, B. Thermal bonded (TB) with 25 seconds AW pre-heating and E. Ultrasonic welded (UW).

5.6. Discussion

Most approaches to bone engineering developed until date, do not take into account tissue structure complexity that integrates both trabecular and cortical bone characterised by individual morphology and mechanical properties (Nooeaid et al. 2014). At the same time, a strong attachment of a soft structure to a rigid material is usually difficult to obtain due to the mismatch of the corresponding mechanical properties (Hollenstein et al. 2013; Taboas et al. 2003).

This study reports the outcomes of assembling pre-fabricated parts (PLA and AW porous samples) into a hybrid composite structure. Both structures were previously described in Chapter 3 and Chapter 4 as adequate trabecular and cortical bone analogues, hence good candidates for this study.

Two approaches were selected for assembling PLA and AW into an integrated composite system, namely ultrasonic welding and thermal bonding. The optimisation of both

approaches, by means of selecting the most adequate parameters that would not damage any of the parts, while aiming at a strong interface, where described in section 5.4. Results: Composite Structures Assembly.

Regarding thermal bonding process, AW pre-heating time was a key parameter for achieving a surface temperature that would allow PLA to locally melt and bond to AW. A pre-heating time window between 15 to 25 seconds, leading to a 193°C-215°C AW surface temperature, was described as adequate for achieving PLA and AW structures bonding. At the same time, AW pre-heating time influenced the obtained interface morphology with longer times leading to a higher integration level (Fig.5. 11). This was explained by PLA local melting behaviour at temperatures higher than 170°C (Rodrigues et al. 2016), that was intensified by longer heating times and thus more time to absorb thermal energy and infiltrate the AW porous structure. Consequently, the PLA porous structure was affected, with pores height decrease, resulted from AW “sinking” effect that was favoured by PLA softening. Furthermore, the higher shear resistance values observed for the thermal bonded samples with longer AW pre-heating times can be explained by superior PLA-AW integration. Also, the observed failure mechanism, with PLA attached to the delaminated AW structure, suggests that PLA-AW interface was stronger than the PLA-PLA extruded layers adhesion obtained during FFF process (Scaffaro et al. 2016; Levingstone et al. 2014). On contrary, when shorter AW pre-heating times were selected, the obtained PLA-AW structure showed lower interface strength values with failure occurring at the composite interface.

Regarding the ultrasonic welding bonding approach, during optimisation it was realised that in a first instance applied pressure, sonotrode distance and AW thickness were the key parameters for a successful bonding of PLA and AW, without destroying the brittle AW structure. The mechanism behind the bonding achieved between two dissimilar structures was the friction generated at the interface that converts kinetic energy into thermal energy, which is sufficient high to locally melt and soften PLA part (Zhang et al. 2011). Together with the applied pressure, the molten PLA penetrates the porous ceramic part, and when the polymer cools down, an bond is formed at the interface (Sackmann et al. 2015). It was observed that the most important parameter for obtaining a strong weld was the total amount of energy applied and the amplitude of the sonotrode. This can be explained by the basic theory of ultrasonic welding, where the strength of a given weld joint depends upon the total amount of energy (Solvay 2010; Industrial 2015):

$$\text{Energy (e)} = \text{Power (p)} \times \text{Time (t)} \text{ (Equation 4)}$$

$$\text{Power (p)} = \text{Force (f)} \times \text{Velocity (v)} \text{ (Equation 5)}$$

The force (f) is derived from applied pressure and velocity (v) is derived from frequency and amplitude of the vibration. The heat generated at the joint is proportional to the square of the amplitude. Therefore, a change in amplitude had a great impact on the obtained weld strength (Troughton 2008). When two dense PLA parts were welded, higher pressure need to be applied to obtain a strong weld, avoiding easy manually separation of the parts after welding. Regarding the composite interfacial shear strength, PLA-AW composite structures obtained with ultrasonic welding approach were characterised by higher interfacial shear strength values when compared to the thermal bonded structures prepared with shorter AW pre-heating times (Fig.5. 14). There was a correlation between the interfacial shear strength values, and the observed interface morphology (Fig.5. 11 and Fig.5. 12). For example, superior PLA-AW integration levels of ultrasonic welded samples resulted in higher bonding strength values. Parallely, an insight into the failure mechanism of tested samples (Fig.5. 15) pointed towards stronger integration of PLA-AW structures assembled with ultrasonic welding. Failure occurred at AW sample (Fig.5. 15.C), suggesting that the interfacial strength was greater than the tensile strength of the individual samples (Levingstone et al. 2014). Furthermore, when compared to other bi or multi-layered systems, assembled with other approaches, ultrasonic welded samples presented higher interfacial shear strength values around 2.5 MPa, representing promising results for tissue interface engineering applications (Schaefer, Martin, G. Jundt, et al. 2002; Sherwood et al. 2002). For instance, the shearing resistance of three-layered porous PLA/PEG scaffold with gradient porosity fabricated with melt mixing and salt water leaching, was reported as 0.35 MPa (Scaffaro et al. 2016). A bi-layered collagen and hydroxyapatite-based scaffold for osteochondral repair developed by (Levingstone et al. 2014) with a novel “iterative layering” freeze-drying technique was characterised by a shear strength of ~0.02 MPa. Also, bioceramic-hydrogel structure (PEG/ β -TCP) designed for osteochondral scaffold applications and fabricated with three-dimensional printing (Bian et al. 2012) was characterised by an interfacial shear strength of ~0.45 MPa. In another study (Allan et al. 2007), native osteochondral samples (bone-cartilage interface) were harvested from a bovine joint and shear strength was tested, with reported values of shear peak load at failure of ~57.1 N lower to the ones reported here in the range of ~97-130 N (Table 5. 4).

5.7. Osseointegration Study of PLA-AW Composite Structures

Furthermore, to explore the potential of the developed hybrid composite structure for mimicking the complex bone architecture, the *in vivo* performance of the PLA-AW structure (samples prepared with the thermal bonding approach) was investigated in a parallel study reported in (Tcacencu et al. 2018).

After implantation in a rat calvarial defect model, the composite structure showed the largest amount of the newly formed bone *in vivo* (Fig.5. 16), when compared to PLA and/or AW porous structures alone. It was suggested that the presence of the osteoinductive AW structure stimulating bone growth in the larger pores of the adjacent PLA structure, might explain the obtained outcome. Moreover, the composite structure showed no signs of delamination during the reported *in vivo* study, in agreement with the high interfacial shear strength values obtained in Chapter 7. This was attributed to good initial bonding between PLA and AW, slow resorption rates of the two materials, allied to excellent osseointegration.

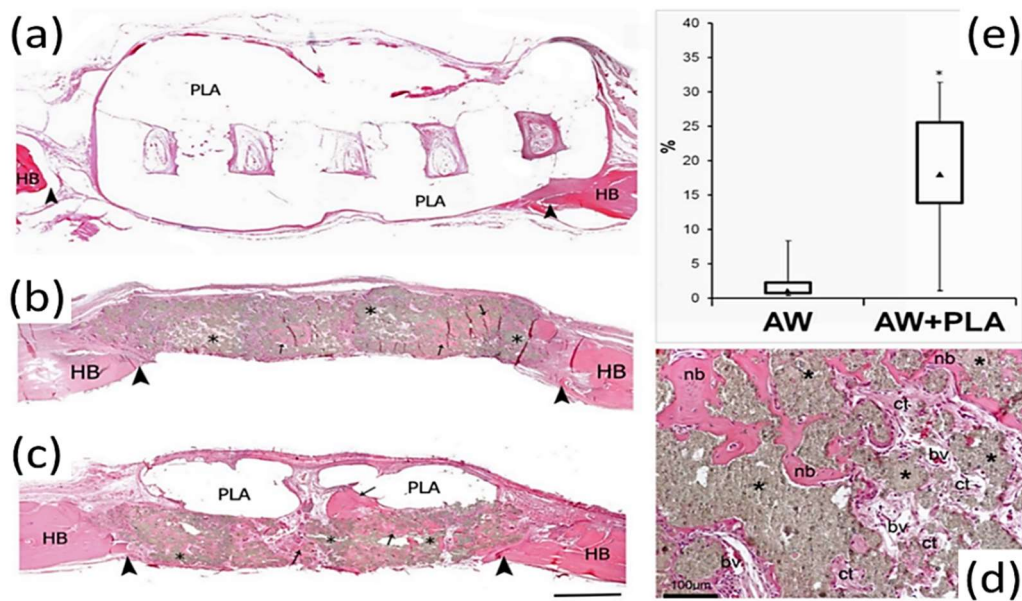


Fig.5. 16. Histological images stained with Haematoxylin and Eosin, illustrating the general morphological aspect of the calvarial defect repair. (a) – PLA alone; (b) – AW alone; (c) – AW/PLA; Scale bar = 1 mm; HB – host bone; defect margins indicated by arrow heads; * – residual AW; (d) – representative image of enlarged area of the AW; nb – new bone; bv – blood vessel; ct – connective tissue; Scale bar = 100 μm; (e) Box plots (maximum, third quartile, median, first quartile, minimum; * $P < 0.05$) representing the percentage of the newly formed bone in the calvarial defects treated with AW or AW+PLA discs.

5.8. Conclusions

A novel PLA-AW hybrid composite structure was created here by bonding the two structures together via two approaches, where thermal and ultrasonic energy were key.

Despite different energy sources were used for the bonding approaches, the obtained interface was created by the PLA locally melting and infiltration into the AW structure, providing mechanical adhesion through physical interlocking of the materials.

The high interfacial shear strength values obtained in this study (0.5 to 2.5 MPa) indicated that physical bonding generated by both thermal bonding and ultrasonic welding approaches, might be considered a promising way to avoid delamination of different layers in multiple layers tissue engineering scaffold (Bian et al. 2012).

Overall, when comparing the two bonding approaches for potential medical devices assembly, ultrasonic welding might provide a faster, cleaner and more scalable approach.

CHAPTER 6. Final Remarks

6.1. Outcomes and Novelty

The aim of this thesis was integrated in the MeDe (Medical Devices innovation) research challenges and focused on fabricating a hybrid biopolymer-bioceramic composite structure for mimicking the complex bone-tissue organisation repair, and on developing the manufacturing process required to make them.

To achieve the aim, the work was divided in four objectives:

OBJ1: Fabricate and characterise a polylactic acid (PLA) porous structure with designed porosity (trabecular bone analogue), as described in Chapter 3;

OBJ2: Fabricate a three dimensional (3D) porous apatite- wollastonite (AW), as previously reported by (Mancuso et al. 2017) (cortical bone analogue), as described in Chapter 4;

OBJ3: Fabricate a bonded PLA-AW hybrid composite structure and **OBJ4:** Characterise the obtained PLA-AW composite, as described in Chapter 5.

Overall, all the objectives were achieved, except for OBJ2, that was redefined towards a better understanding of the binder jetting 3DP fabrication route of AW porous structures. The key outcomes obtained for each one of the objectives and the novelty associated with these findings were summarised in the following tables.

Table 6. 1. Summary of outcomes and novelty obtained in Chapter 3.

Outcomes	Novelty
<ul style="list-style-type: none"> A 2-step manufacturing route was developed for creating PLA porous structures with controlled (0.5 mm) and open porosity. 	<ul style="list-style-type: none"> Laser cutting step was added to conventional FFF fabrication technique used for porous structures fabrication, enabling the creation of a PLA structure with surrounding open porosity.
<ul style="list-style-type: none"> Morphology, mechanical properties and <i>in vitro</i> degradation study results pointed towards suitable trabecular bone analogue 	<ul style="list-style-type: none"> Paper was published on this topic
<ul style="list-style-type: none"> Mechanical properties evolution with increasing immersion time (<i>in vitro</i> degradation study) was influenced by: i) differences in pore geometry ii) preferential material degradation at the edges. 	<ul style="list-style-type: none"> <i>In vitro</i> degradation study of fabricated PLA porous structures was performed with <i>in situ</i> video recording of compression behaviour at a cellular unit level (pores).
<ul style="list-style-type: none"> Preferential PLA degradation on the surrounding/edges of fabricated PLA porous structure was observed, during <i>in vitro</i> degradation study. This was explained by the thermal degradation on the structure edges that occurred during laser cut step. Degraded material was more prone to water interaction/erosion, as observed by the cracks formation and propagation with longer immersion times. 	<ul style="list-style-type: none"> The described PLA degradation mechanism in PBS was reported for the first time, where only material located at the edges was affected by hydrolysis, while the rest of the structure remained intact.

Table 6. 2. Summary of outcomes and novelty obtained in Chapter 4.

Outcomes	Novelty
<ul style="list-style-type: none"> Swelling behaviour and lack of samples consolidation were the issues reported when the work developed by (Mancuso et al. 2017) was replicated, thus the scope of this chapter was updated to a better understanding of the indirect 3DP process for creating AW porous structure. 	<ul style="list-style-type: none"> Extra knowledge was gathered on glass-ceramics powder properties (e.g. AW) and their influence on the 3DP process or other powder based techniques and sinterability Deeper understanding of the indirect 3DP process and the steps involved in the fabrication of a porous AW
<ul style="list-style-type: none"> The combination of bimodal mixtures with 40-45% large particles amount and Dx (50) values between 37 μm to 61 μm resulted in the best printability outcome. 	
<ul style="list-style-type: none"> Lack of consolidation was only observed after AW2 parts sintering and this was attributed to its lower sinterability(S_C). The suggested AW2 optimum sintering window was 1239°C-1280°C, which was above the maximum temperature (1200°C) allowed for furnace used in this study. AW particles sintering was particle size dependent and improved in minor scale by sintering time and temperature 	
<ul style="list-style-type: none"> Swelling behaviour was attributed to moisture uptake (maltodextrin) and it was mitigated with three measures: vacuum dry, a slower de-binding rate and excluding sub-20 μm MD particles. 	

Table 6. 3. Summary of outcomes and novelty obtained in Chapter 5.

Outcomes	Novelty
<ul style="list-style-type: none"> Both bonding approaches (thermal (TB) and ultrasonic welding (UW)) were optimised towards the selection of key parameters to obtain an integrated composite structure Similar bonding mechanism was found for both approaches: PLA was locally softened (due to thermal energy generated by friction (UW) or direct contact with pre-heated AW sample (TB)), infiltrating the AW microporous structure. While in UW process, applied pressure was the key parameter to avoid AW parts damage, in TB, AW pre-heating times had a direct influence on obtained interface morphology. 	<ul style="list-style-type: none"> A novel macroscale composite structure concept was developed, created by the assembly of two individual pre-fabricated parts Ultrasonic welding used for the first time as a tool for bonding two dissimilar materials like PLA and AW
<ul style="list-style-type: none"> Failure mechanism of tested composite structures was different for samples with similar interface properties: while TB with longer AW pre-heating times failed at PLA structure, the UW failed at AW structure level Superior PLA-AW integration of UW and TB (with higher pre-heating AW times) resulted in higher interfacial shear strength values, supported by failure mechanism that did not occur at interface, when compared to weaker TB (shorter pre-heating times) 	<ul style="list-style-type: none"> A novel set-up for assessing the interfacial bonding strength of assembled composite structures was developed Obtained interfacial shear strength values of TB with (higher AW pre-heating times) and UW composites structures were higher than the average values of layered systems found in literature up to date
<ul style="list-style-type: none"> Promising results were obtained for the osseointegration study of the PLA-AW composites structure assembled with TB For potential bone applications, faster, cleaner and more scalable UW approach would be the selected bonding approach 	<ul style="list-style-type: none"> Paper was published in this topic

6.2. Conclusions and Recommendations

Finally, the aim of fabricating a hybrid PLA-AW composite structure was accomplished and preliminary physical characterisation of the obtained interface suggested that a strong interface was created with both bonding approaches. A combination of mechanical properties and porosity was achieved, going beyond the range of properties that could be achieved from a single composite material.

It was concluded that macro-scale composites offer an alternative route to the fabrication of bioactive bone implants which can provide a match to both cortical and trabecular bone properties over millimetre length scales.

Further work to improve sintering of AW2 powder blends will consist in conducting experiments in a furnace that allows higher temperature range, that can fulfil the AW2 sintering window (1239°C-1280°C).

The promising *in vivo* performance of thermal bonded PLA AW composite structures, suggested that there is scope for further characterisation of ultrasonic welded structures.

Besides testing the *in vivo* performance, a more in depth study to investigate the influence of ultrasonic welding parameters on obtained interface properties is suggested.

References

- Abert, J. et al., 2016. Degradation and swelling issues of poly-(d,l-lactide)/ β -tricalcium phosphate/calcium carbonate composites for bone replacement. *Journal of the Mechanical Behavior of Biomedical Materials*.
- Additive Manufacturing group from Loughborough University, 2015. The 7 Categories of Additive Manufacturing. Available at:
<http://www.lboro.ac.uk/research/amrg/about/the7categoriesofadditivemanufacturing/>.
- Allan, K.S. et al., 2007. Formation of biphasic constructs containing cartilage with a calcified zone interface. *Tissue engineering*.
- Almeida, C.R. et al., 2014. Impact of 3-D printed PLA- and chitosan-based scaffolds on human monocyte/macrophage responses: Unraveling the effect of 3-D structures on inflammation. *Acta Biomaterialia*, 10(2), pp.613–622. Available at:
<http://www.sciencedirect.com/science/article/pii/S1742706113005527>.
- Amanat, N., James, N.L. & McKenzie, D.R., 2010. Welding methods for joining thermoplastic polymers for the hermetic enclosure of medical devices. *Medical Engineering & Physics*, 32(7), pp.690–699. Available at:
<http://www.sciencedirect.com/science/article/pii/S1350453310000858>.
- Andersson, S.R. et al., 2010. Polylactide Stereocomplexation Leads to Higher Hydrolytic Stability but More Acidic Hydrolysis Product Pattern. *Biomacromolecules*.
- Arnoldi, J. et al., 2012. In vivo tissue response to ultrasound assisted application of biodegradable pins into cortical and cancellous bone structures: a histological and densitometric analysis in rabbits. *J Biomater Sci Polym Ed*, 23(5), pp.663–676.
- Augat, P. et al., 2015. Fixation performance of an ultrasonically fused, bioresorbable osteosynthesis implant: A biomechanical and biocompatibility study. *Journal of Biomedical Materials Research Part B: Applied Biomaterials*, 104(1), pp.170–179. Available at: <https://onlinelibrary.wiley.com/doi/abs/10.1002/jbm.b.33382>.
- Bai, Y., Wagner, G. & Williams, C.B., 2017. Effect of Particle Size Distribution on Powder Packing and Sintering in Binder Jetting Additive Manufacturing of Metals. *Journal of Manufacturing Science and Engineering*, 139(8), p.6.

- Baino, F. et al., 2013. Optimization of composition, structure and mechanical strength of bioactive 3-D glass-ceramic scaffolds for bone substitution. *Journal of Biomaterials Applications*, 27(7), pp.872–890. Available at: <http://dx.doi.org/10.1177/0885328211429193>.
- Baldini, N. et al., 2009. Bone repair and regeneration. In *Bone Repair Biomaterials*.
- Bernstein, A. et al., 2013. Microporous calcium phosphate ceramics as tissue engineering scaffolds for the repair of osteochondral defects: Histological results. *Acta biomaterialia*, 9(7), p.7490—7505. Available at: <https://doi.org/10.1016/j.actbio.2013.03.021>.
- Bian, W. et al., 2012. Fabrication of a bio-inspired beta-Tricalcium phosphate/collagen scaffold based on ceramic stereolithography and gel casting for osteochondral tissue engineering. *Rapid Prototyping Journal*.
- Blaker, J.J. et al., 2003. In vitro evaluation of novel bioactive composites based on Bioglass-filled polylactide foams for bone tissue engineering scaffolds. *Journal of biomedical materials research. Part A*.
- Blokhuis, T.J. & Arts, J.J.C., 2011. Bioactive and osteoinductive bone graft substitutes: Definitions, facts and myths. *Injury*, 42(SUPPL. 2).
- Boccaccini, A.R. et al., 2007. Sintering, crystallisation and biodegradation behaviour of Bioglass-derived glass-ceramics. *Faraday discussions*.
- Bosch, C., Melsen, B. & Vargervik, K., 1998. Importance of the critical-size bone defect in testing bone-regenerating materials. *The Journal of craniofacial surgery*, 9(4), pp.310–316.
- Bose, S., Roy, M. & Bandyopadhyay, A., 2012. Recent advances in bone tissue engineering scaffolds. *Trends in Biotechnology*.
- Brahatheeswaran Dhandayuthapani Toru Maekawa D. Sakthi Kumar, Y.Y., 2011. Polymeric Scaffolds in Tissue Engineering Application: A Review. *International Journal of Polymer Science*, 2011. Available at: <http://dx.doi.org/10.1155/2011/290602>.
- Bretcanu, O. et al., 2014. Novel resorbable glass-ceramic scaffolds for hard tissue engineering: From the parent phosphate glass to its bone-like macroporous derivatives.

Journal of Biomaterials Applications, 28(9), pp.1287–1303. Available at:
<http://dx.doi.org/10.1177/0885328213506759>.

Butscher, A. et al., 2012. Printability of calcium phosphate powders for three-dimensional printing of tissue engineering scaffolds. *Acta Biomaterialia*, 8(1), pp.373–385. Available at: <http://www.sciencedirect.com/science/article/pii/S1742706111003801> [Accessed October 14, 2016].

Butscher, A. et al., 2011. Structural and material approaches to bone tissue engineering in powder-based three-dimensional printing. *Acta Biomaterialia*, 7(3), pp.907–920.

Cailloux, J. et al., 2014. Sheets of branched poly(lactic acid) obtained by one-step reactive extrusion-calendering process: Physical aging and fracture behavior. *Journal of Materials Science*.

Calver, A., Hill, R.G. & Stamboulis, A., 2004. Influence of fluorine content on the crystallization behavior of apatite-wollastonite glass-ceramics. *Journal of Materials Science*, 39(7), pp.2601–2603. Available at:
<http://dx.doi.org/10.1023/B:JMSC.0000020038.79675.0f>.

Campana, V. et al., 2014. Bone substitutes in orthopaedic surgery: from basic science to clinical practice. In *J Mater Sci Mater Med*. pp. 2445–2461.

Cannillo, V. et al., 2009. Thermal and physical characterisation of apatite/wollastonite bioactive glass–ceramics. *Journal of the European Ceramic Society*, 29(4), pp.611–619. Available at: <http://www.sciencedirect.com/science/article/pii/S0955221908003476> [Accessed March 31, 2017].

Cao, L. et al., 2012. Degradation and osteogenic potential of a novel poly(lactic acid)/nano-sized β -tricalcium phosphate scaffold. *International Journal of Nanomedicine*.

Castilho, M. et al., 2014. Direct 3D powder printing of biphasic calcium phosphate scaffolds for substitution of complex bone defects. *Biofabrication*, 6(1), p.015006. Available at: <http://stacks.iop.org/1758-5090/6/i=1/a=015006?key=crossref.19977f83c201136f8220e44d5549f4f5>.

Chan, B.P. & Leong, K.W., 2008. Scaffolding in tissue engineering: general approaches and tissue-specific considerations. *European Spine Journal*, 17(Suppl 4), pp.467–479.

Available at: <http://www.ncbi.nlm.nih.gov/pmc/articles/PMC2587658/>.

Chang, C.K., Mao, D.L. & Wu, J.S., 2000. Characteristics of crystals precipitated in sintered apatite/wollastonite glass ceramics. *Ceramics International*, 26(7), pp.779–785.

Available at: <http://www.sciencedirect.com/science/article/pii/S0272884200000195>.

Chartrain, N.A., Williams, C.B. & Whittington, A.R., 2018. A review on fabricating tissue scaffolds using vat photopolymerization. *Acta Biomaterialia*, 74, pp.90–111. Available at: <http://www.sciencedirect.com/science/article/pii/S1742706118302794>.

Chronakis, I.S., 1998. On the Molecular Characteristics, Compositional Properties, and Structural-Functional Mechanisms of Maltodextrins: A Review. *Critical Reviews in Food Science and Nutrition*, 38(7), pp.599–637. Available at: <http://dx.doi.org/10.1080/10408699891274327>.

Cowan, C.M. et al., 2004. Adipose-derived adult stromal cells heal critical-size mouse calvarial defects. *Nature Biotechnology*, 22(5), pp.560–567. Available at: <http://www.nature.com/doifinder/10.1038/nbt958>.

Currey, J., 2008. *The structure and mechanical properties of bone*. In: Kokubo, T. (ed.) *Bioceramics and their clinical applications*,

Da, H. et al., 2013. The impact of compact layer in biphasic scaffold on osteochondral tissue engineering. *PLoS One*, 8(1).

Denry, I. & Holloway, J.A., 2014. Low temperature sintering of fluorapatite glass-ceramics. *Dental Materials*, 30(2), pp.112–121. Available at: <http://linkinghub.elsevier.com/retrieve/pii/S0109564113004697> [Accessed August 2, 2017].

Deschaseaux, F., Sensébé, L. & Heymann, D., 2009. Mechanisms of bone repair and regeneration. *Trends in Molecular Medicine*.

Detting, X. et al., 2010. Osteochondral repair using porous poly(lactide-co-glycolide)/nano-hydroxyapatite hybrid scaffolds with undifferentiated mesenchymal stem cells in a rat model. *Journal of Biomedical Materials Research Part A*, 94A(1), pp.259–270. Available at: <https://onlinelibrary.wiley.com/doi/abs/10.1002/jbm.a.32691>.

- Dietmar, D., Sandra, C. & Dominik, R., 2012. Suitability of PLA/TCP for fused deposition modeling. *Rapid Prototyping Journal*, 18(6), pp.500–507. Available at: <http://www.emeraldinsight.com/doi/abs/10.1108/13552541211272045>.
- Diez-Pascual, A.M., 2017. Tissue Engineering Bionanocomposites Based on Poly(propylene fumarate). *Polymers*, 9(7).
- Domingos, M. et al., 2012. Effect of process parameters on the morphological and mechanical properties of 3D Bioextruded poly(ϵ -caprolactone) scaffolds. *Rapid Prototyping Journal*.
- Duek, E.A., Zavaglia, C.A. & Belangero, W., 1999. In vitro study of poly(lactic acid) pin degradation. *Polymer*.
- Dyson, J. a et al., 2007. Development of custom-built bone scaffolds using mesenchymal stem cells and apatite-wollastonite glass-ceramics. *Tissue engineering*.
- El-Meliegy, E. & Noort, R. Van, 2012. *Glasses and glass ceramics for medical applications*,
- Felfel, R.M. et al., 2016. *In vitro* degradation and mechanical properties of PLA-PCL copolymer unit cell scaffolds generated by two-photon polymerization. *Biomedical Materials*, 11(1), p.015011. Available at: <http://stacks.iop.org/1748-605X/11/i=1/a=015011?key=crossref.fdaa59b902f3ce986c2583e675d171b6>.
- Florencio-Silva, R. et al., 2015. Biology of Bone Tissue: Structure, Function, and Factors That Influence Bone Cells. *BioMed Research International*, 2015.
- Freudenrich, C., 2011. How Ultrasonic Welding Works. , pp.1–9. Available at: <https://science.howstuffworks.com/ultrasonic-welding2.htm> [Accessed August 20, 2006].
- Fujita, H. et al., 2000. Porous apatite-wollastonite glass-ceramic as an intramedullary plug. *The Journal of bone and joint surgery. British volume*.
- Gerhardt, L.-C. & Boccaccini, A.R., 2010. Bioactive Glass and Glass-Ceramic Scaffolds for Bone Tissue Engineering. *Materials*.
- German, R.M., 1992. Prediction of sintered density for bimodal powder mixtures. *Metallurgical Transactions A*, 23(5), pp.1455–1465. Available at:

<https://doi.org/10.1007/BF02647329>.

German, R.M., 1996. *Sintering theory and practice*,

Ghassemieh, E., 2008. Morphology and compression behaviour of biodegradable scaffolds produced by the sintering process. *Proc Inst Mech Eng H*, 222(8), pp.1247–1262.

Gomes, C.M. et al., 2014. Designing apatite-wollastonite (AW) porous scaffolds by powder-based 3D printing. *High Value Manufacturing: Advanced Research in Virtual and Rapid Prototyping*.

Gong, J.K., Arnold, J.S. & Cohn, S.H., 1964. Composition of trabecular and cortical bone. *The Anatomical Record*, 149(3), pp.325–331.

Goulet, J.A. et al., 1997. Autogenous iliac crest bone graft. Complications and functional assessment. *Clinical orthopaedics and related research*, june(339), pp.76–81. Available at: <http://www.ncbi.nlm.nih.gov/pubmed/9186204>.

Grayson, W.L. et al., 2008. Engineering custom-designed osteochondral tissue grafts. *Trends in Biotechnology*, 26(4), pp.181–189. Available at: <http://www.sciencedirect.com/science/article/pii/S0167779908000577>.

Hao, L. & Harris, R., 2008. Customised Implants for Bone Replacement and Growth. In P. Bártolo & B. Bidanda, eds. *Bio-Materials and Prototyping Applications in Medicine*. Springer US, pp. 79–107. Available at: http://dx.doi.org/10.1007/978-0-387-47683-4_6.

Heidenreich, D. et al., 2011. The use of BoneWelding(R) technology in spinal surgery: an experimental study in sheep. *Eur Spine J*, 20(11), pp.1821–1836.

Henslee, A.M. et al., 2012. Development of a Biodegradable Bone Cement for Craniofacial Applications. *J Biomed Mater Res A*, 100(9), pp.2252–2259.

Ho, S.T.B. et al., 2010. The Evaluation of a Biphasic Osteochondral Implant Coupled with an Electrospun Membrane in a Large Animal Model. *Tissue Engineering Part A*, 16(4), pp.1123–1141. Available at: <https://doi.org/10.1089/ten.tea.2009.0471>.

Hollenstein, J. et al., 2013. Mechanical evaluation of a tissue-engineered zone of calcification in a bone-hydrogel osteochondral construct. *Computer methods in biomechanics and*

- Holmes, B. et al., 2014. Development of Novel Three-Dimensional Printed Scaffolds for Osteochondral Regeneration. *Tissue Engineering Part A*, 21(1–2), pp.403–415. Available at: <http://dx.doi.org/10.1089/ten.tea.2014.0138>.
- Hoque, M.E. et al., 2011. Process optimization to improve the processing of poly (DL-lactide-co- glycolide) into 3D tissue engineering scaffolds. In *IFMBE Proceedings*.
- Hoque, M.E. et al., 2011. Process Optimization to Improve the Processing of Poly (DL-lactide-co-glycolide) into 3D Tissue Engineering Scaffolds. In N. Osman et al., eds. *5th Kuala Lumpur International Conference on Biomedical Engineering 2011*. Springer Berlin Heidelberg, pp. 836–840. Available at: http://dx.doi.org/10.1007/978-3-642-21729-6_204.
- Huang, J. et al., 2013. Investigation of the *In Vitro* Degradation of a Novel Polylactide/Nanohydroxyapatite Composite for Artificial Bone. *Journal of Nanomaterials*.
- Hutmacher, D.W. et al., 2001. Mechanical properties and cell cultural response of polycaprolactone scaffolds designed and fabricated via fused deposition modeling. *Journal of Biomedical Materials Research*.
- Hutmacher, D.W. et al., 2001. Mechanical properties and cell cultural response of polycaprolactone scaffolds designed and fabricated via fused deposition modeling. *J Biomed Mater Res*, 55(2), pp.203–216.
- Hutmacher, D.W., Sittinger, M. & Risbud, M. V, 2004. Scaffold-based tissue engineering: rationale for computer-aided design and solid free-form fabrication systems. *Trends in Biotechnology*, 22(7), pp.354–362. Available at: <http://www.sciencedirect.com/science/article/pii/S0167779904001428>.
- Ikeda, R. et al., 2009. The effect of porosity and mechanical property of a synthetic polymer scaffold on repair of osteochondral defects. *International Orthopaedics*, 33(3), pp.821–828. Available at: <http://dx.doi.org/10.1007/s00264-008-0532-0>.
- Industrial, E., 2015. Amplitude reference guide. *Branson Ultrasonics Corporation*. Available at: <http://www.emersonindustrial.com/en->

US/documentcenter/BransonUltrasonics/Plastic Joining/Ultrasonics/Technologies/TL-2_Amplitude_Reference_Guide.pdf.

Insomphun, C. et al., 2017. Influence of Hydroxyl Groups on the Cell Viability of Polyhydroxyalkanoate (PHA) Scaffolds for Tissue Engineering. *ACS Biomaterials Science & Engineering*, 3, p.3064–3075.

International Organization for Standardization, 2012. ISO 527-2:2012: Plastics: determination of tensile properties. In *ISO standard*.

Jack, Z. & Lin, L., 2011. Biomimetic Structured Porogen Freeform Fabrication System for Tissue Engineering.

Jones, A.C. et al., 2004. Analysis of 3D bone ingrowth into polymer scaffolds via micro-computed tomography imaging. *Biomaterials*.

K., L.A. et al., 2009. Design of a multiphase osteochondral scaffold. I. Control of chemical composition. *Journal of Biomedical Materials Research Part A*, 92A(3), pp.1057–1065. Available at: <https://onlinelibrary.wiley.com/doi/abs/10.1002/jbm.a.32415>.

Kalita, S.J. et al., 2003. Development of controlled porosity polymer-ceramic composite scaffolds via fused deposition modeling. *Materials Science and Engineering: C*, 23(5), pp.611–620. Available at: <http://www.sciencedirect.com/science/article/pii/S0928493103000523>.

Kane, R. & Ma, P.X., 2013. Mimicking the nanostructure of bone matrix to regenerate bone. *Materials Today*, 16(11), pp.418–423. Available at: <http://www.sciencedirect.com/science/article/pii/S1369702113003775> [Accessed September 20, 2017].

Karageorgiou, V. & Kaplan, D., 2005. Porosity of 3D biomaterial scaffolds and osteogenesis. *Biomaterials*, 26(27), pp.5474–5491. Available at: <http://www.sciencedirect.com/science/article/pii/S0142961205001511>.

Keaveny, T.M. & Hayes, W.C., 1993. Mechanical Properties of Cortical and Trabecular Bone. *Bone growth*.

Khan, Y. et al., 2008. *Tissue Engineering of Bone: Material and Matrix Considerations*,

Available at: http://jbjs.org/jbjsam/90/Supplement_1/36.full.pdf.

- Kohane, D.S. & Langer, R., 2008. Polymeric Biomaterials in Tissue Engineering. *Pediatr Res*, 63(5), pp.487–491. Available at: <http://dx.doi.org/10.1203/01.pdr.0000305937.26105.e7>.
- Kokubo, T., 1991. Bioactive glass ceramics: properties and applications. *Biomaterials*, 12(2), pp.155–163. Available at: <http://linkinghub.elsevier.com/retrieve/pii/014296129190194F> [Accessed March 31, 2017].
- Kondo, N. et al., 2005. Bone formation and resorption of highly purified β -tricalcium phosphate in the rat femoral condyle. *Biomaterials*, 26(28), pp.5600–5608. Available at: <http://www.sciencedirect.com/science/article/pii/S0142961205001924>.
- Korpela, J. et al., 2013. Biodegradable and bioactive porous scaffold structures prepared using fused deposition modeling. *Journal of Biomedical Materials Research Part B: Applied Biomaterials*, 101B(4), pp.610–619. Available at: <http://doi.wiley.com/10.1002/jbm.b.32863> [Accessed August 22, 2017].
- Kumar, G. & Narayan, B., 2014. Morbidity at bone graft donor sites. In *Classic Papers in Orthopaedics*. pp. 503–505.
- Kurien, T., Pearson, R.G. & Scammell, B.E., 2013. Bone graft substitutes currently available in orthopaedic practice: The evidence for their use. *Bone and Joint Journal*, 95 B(5), pp.583–597.
- L. Hench, L. et al., 2000. Bioactive Materials to Control Cell Cycle. *Material Research Innovations*, 3, pp.313–323.
- Largo Avila, E., Cortes Rodriguez, M. & Ciro Velasquez, H.J., 2015. Influence of Maltodextrin and Spray Drying Process Conditions on Sugarcane Juice Powder Quality. *Revista Facultad Nacional de Agronomía, Medellín*, 68(1), pp.7509–7520.
- Lee, J.A. et al., 2015. In vivo biocompatibility of custom-fabricated apatite-wollastonite-mesenchymal stromal cell constructs. *Journal of Biomedical Materials Research - Part A*.
- Levingstone, T.J. et al., 2014. A biomimetic multi-layered collagen-based scaffold for

- osteocondral repair. *Acta Biomaterialia*, 10(5), pp.1996–2004. Available at: <http://www.sciencedirect.com/science/article/pii/S1742706114000087>.
- Li, B. & Aspden, R.M., 1997. Mechanical and material properties of the subchondral bone plate from the femoral head of patients with osteoarthritis or osteoporosis. *Annals of the rheumatic diseases*.
- Li, H.Y. & Chang, J., 2004. Preparation and characterization of bioactive and biodegradable Wollastonite/poly(D,L-lactic acid) composite scaffolds. *Journal of Materials Science-Materials in Medicine*.
- Li, J.J., Kaplan, D.L. & Zreiqat, H., 2014. Scaffold-based regeneration of skeletal tissues to meet clinical challenges. *Journal of Materials Chemistry B: Materials for biology and medicine*.
- Li, Y., Lim, C.T. & Kotaki, M., 2015. Study on structural and mechanical properties of porous PLA nanofibers electrospun by channel-based electrospinning system. *Polymer (United Kingdom)*.
- Li, Z., Yang, J. & Loh, X.J., 2016. Polyhydroxyalkanoates: opening doors for a sustainable future. *NPG Asia Materials*, 8(e265).
- Likitvanichkul, S. & Lacourse, W.C., 1998. Apatite--wollastonite glass-ceramics part I Crystallization kinetics by differential thermal analysis. *Journal of Materials Science*, 33(24), pp.5901–5904. Available at: <http://dx.doi.org/10.1023/A:1004491107420>.
- Little, N., Rogers, B. & Flannery, M., 2011. Bone formation, remodelling and healing. *Surgery*, 29(4), pp.141–145.
- Liu, M. et al., 2013. Tissue Engineering Stratified Scaffolds for Articular Cartilage and Subchondral Bone Defects Repair. *Orthopedics*.
- Lu, L. et al., 2000. In vitro degradation of porous poly(L-lactic acid) foams. *Biomaterials*.
- M. Tarik Arafat Xu Li, I.G., 2014. State of the art and future direction of additive manufactured scaffolds-based bone tissue engineering. *Rapid Prototyping Journal*, 20(1), pp.13–26.

- M. Tarik Arafat Xu Li, I.G., 2014. State of the art and future direction of additive manufactured scaffolds-based bone tissue engineering. *Rapid Prototyping Journal*, 20(1), pp.13–26.
- Manavitehrani, I. et al., 2016. Biomedical Applications of Biodegradable Polyesters. *Polymers*, 8(1).
- Mancuso, E. et al., 2017. Three-dimensional printing of porous load-bearing bioceramic scaffolds. *Proceedings of the Institution of Mechanical Engineers, Part H: Journal of Engineering in Medicine*, 231(6), pp.575–585. Available at: <http://dx.doi.org/10.1177/0954411916682984>.
- Martino, A. Di, Sittering, M. & Risbud, M. V, 2005. Chitosan: A versatile biopolymer for orthopaedic tissue-engineering. *Biomaterials*, 26(30), pp.5983–5990. Available at: <http://www.sciencedirect.com/science/article/pii/S0142961205002309>.
- Mateos-Timoneda, M.A., 2009. Polymers for bone repair. In *Bone Repair Biomaterials*. Woodhead publishing, pp. 231–251.
- Middleton, J.C. & Tipton, A.J., 2000. Synthetic biodegradable polymers as orthopedic devices. *Biomaterials*.
- Miot, S. et al., 2012. Influence of in vitro maturation of engineered cartilage on the outcome of osteochondral repair in a goat model. *Eur Cell Mater.*, 5(23), pp.222–236.
- Mohan, N. et al., 2011. Continuous Gradients of Material Composition and Growth Factors for Effective Regeneration of the Osteochondral Interface. *Tissue Engineering Part A*.
- Mollon, B. et al., 2013. The clinical status of cartilage tissue regeneration. *Osteoarthritis and Cartilage*, 21(12), pp.1824–1833. Available at: <http://www.sciencedirect.com/science/article/pii/S1063458413009424>.
- Mollon, B. et al., 2013. The clinical status of cartilage tissue regeneration in humans. *Osteoarthritis and Cartilage*.
- Montazerian, M. & Dutra Zanotto, E., 2016. History and trends of bioactive glass-ceramics. *Journal of Biomedical Materials Research - Part A*.

- Montedo, O.R.K. et al., 2009. Sintering behavior of LZSA glass-ceramics. *Materials Research*, 12(2), pp.197–200. Available at:
http://www.scielo.br/scielo.php?script=sci_arttext&pid=S1516-14392009000200014&lng=en&tlng=en [Accessed June 28, 2017].
- Mota, C. et al., 2012. Additive manufacturing techniques for the production of tissue engineering constructs. *Journal of Tissue Engineering and regenerative medicine*, 9(3), pp.174–190. Available at: <http://dx.doi.org/10.1002/term.1635>.
- Murphy, C.M. & O'Brien, F.J., 2010. Understanding the effect of mean pore size on cell activity in collagen-glycosaminoglycan scaffolds. *Cell Adhesion and Migration*.
- Nandi, S.K. et al., 2010. Orthopaedic applications of bone graft & graft substitutes: A review. *Indian Journal of Medical Research*, 132(7), pp.15–30.
- National Programme on Technology Enhanced Learning), 2014. MODULE 6. FIBRES FOR MEDICAL APPLICATIONS. Available at:
[http://www.nptel.ac.in/courses/116102006/module6/chapter 6.1.html](http://www.nptel.ac.in/courses/116102006/module6/chapter%206.1.html).
- Navarro, M. et al., 2005. In vitro degradation behavior of a novel bioresorbable composite material based on PLA and a soluble CaP glass. *Acta Biomaterialia*.
- Neumann, H. et al., 2013. Refixation of osteochondral fractures by ultrasound-activated, resorbable pins: An ovine in vivo study. *Bone & Joint Research*, 2(2), pp.26–32. Available at: <http://www.ncbi.nlm.nih.gov/pmc/articles/PMC3626216/>.
- Nooeaid, P. et al., 2012. Osteochondral tissue engineering: scaffolds, stem cells and applications. *Journal of Cellular and Molecular Medicine*, 16(10), pp.2247–2270. Available at: <http://dx.doi.org/10.1111/j.1582-4934.2012.01571.x>.
- Nooeaid, P. et al., 2014. Technologies for multilayered scaffolds suitable for interface tissue engineering. *Advanced Engineering Materials*.
- O'Brien, F.J., 2011. Biomaterials & scaffolds for tissue engineering. *Materials Today*, 14(3), pp.88–95. Available at:
<http://www.sciencedirect.com/science/article/pii/S136970211170058X>.
- Odelius, K. et al., 2011. Porosity and pore size regulate the degradation product profile of

polylactide. *Biomacromolecules*.

Onuma, Y. & Serruys, P.W., 2011. Bioresorbable Scaffold. *Circulation*, 123(7), pp.779–797.
Available at: <http://circ.ahajournals.org/content/123/7/779>.

Oryan, A. et al., 2014. Bone regenerative medicine: classic options, novel strategies, and future directions. *Journal of Orthopaedic Surgery and Research*, 9(1), p.18. Available at: <http://josr-online.biomedcentral.com/articles/10.1186/1749-799X-9-18>.

Pape, H.C., Evans, A. & Kobbe, P., 2010. Autologous bone graft: properties and techniques. *Journal of orthopaedic trauma*, 24 Suppl 1(March), pp.S36-40. Available at: <http://www.ncbi.nlm.nih.gov/pubmed/20182233>.

Park, S.A., Lee, S.H. & Kim, W.D., 2011. Fabrication of porous polycaprolactone/hydroxyapatite (PCL/HA) blend scaffolds using a 3D plotting system for bone tissue engineering. *Bioprocess and Biosystems Engineering*.

Pei, M. et al., 2009. Repair of full-thickness femoral condyle cartilage defects using allogeneic synovial cell-engineered tissue constructs. *Osteoarthritis and Cartilage*, 17(6), pp.714–722. Available at: <http://www.sciencedirect.com/science/article/pii/S1063458408003737>.

Perez, R.A. et al., 2015. Therapeutically relevant aspects in bone repair and regeneration. *Materials Today*, 18(10), pp.573–589. Available at: <http://www.sciencedirect.com/science/article/pii/S1369702115002102>.

Pilia, M., Guda, T. & Appleford, M., 2013. Development of Composite Scaffolds for Load-Bearing Segmental Bone Defects. *BioMed Research International*.

Polo-Corrales, L., Latorre-Esteves, M. & Ramirez-Vick, J.E., 2014. Scaffold Design for Bone Regeneration. *Journal of Nanoscience and Nanotechnology*.

Prasadh, S. & Wong, R.C.W., 2018. Unraveling the mechanical strength of biomaterials used as a bone scaffold in oral and maxillofacial defects. *Oral Science International*, 15(2), pp.48–55. Available at: <http://www.sciencedirect.com/science/article/pii/S1348864318300053>.

Qian, B. & Shen, Z., 2013. Laser sintering of ceramics. *Journal of Asian Ceramic Societies*,

- 1(4), pp.315–321. Available at:
<https://www.sciencedirect.com/science/article/pii/S2187076413000584> [Accessed July 18, 2018].
- Rakmae, S. et al., 2012. Effect of silane coupling agent treated bovine bone based carbonated hydroxyapatite on in vitro degradation behavior and bioactivity of PLA composites. *Materials Science and Engineering C*.
- Razak, S.I.A., Sharif, N.F.A. & Rahman, W.A.W.A., 2012. Biodegradable polymers and their bone applications: A review. *Int. J. Basic Appl. Sci.*, 12, pp.31–49.
- Rezwan, K. et al., 2006. Biodegradable and bioactive porous polymer/inorganic composite scaffolds for bone tissue engineering. *Biomaterials*.
- Rodrigues, N. et al., 2016. Manufacture and Characterisation of Porous PLA Scaffolds. *Procedia CIRP*, 49, pp.33–38. Available at:
<http://www.sciencedirect.com/science/article/pii/S2212827115007842>.
- Rogers, G. & Greene, A., 2012. Autogenous bone graft: basic science and clinical implications. *Journal of Craniofacial Surgery*, 23(1), pp.323–327. Available at:
http://journals.lww.com/jcraniofacialsurgery/Abstract/2012/01000/Autogenous_Bone_Graft___Basic_Science_and_Clinical.76.aspx.
- Roohani-Esfahani, S.-I., Newman, P. & Zreiqat, H., 2016. Design and Fabrication of 3D printed Scaffolds with a Mechanical Strength Comparable to Cortical Bone to Repair Large Bone Defects. *Scientific Reports*, 6, p.19468. Available at:
<http://dx.doi.org/10.1038/srep19468>.
- Sackmann, J. et al., 2015. Review on ultrasonic fabrication of polymer micro devices. *Ultrasonics*, 56(0), pp.189–200. Available at:
<http://www.sciencedirect.com/science/article/pii/S0041624X14002297>.
- Sadat-Shojai, M., 2015. Calcium Phosphate–Reinforced Polyester Nanocomposites for Bone Regeneration Applications. , pp.1–34.
- Samavedi, S., Whittington, A.R. & Goldstein, A.S., 2013. Calcium phosphate ceramics in bone tissue engineering: A review of properties and their influence on cell behavior. *Acta Biomaterialia*, 9(9), pp.8037–8045. Available at:

<http://www.sciencedirect.com/science/article/pii/S1742706113002985>.

Saravanan, S., Leena, R.S. & Selvamurugan, N., 2016. Chitosan based biocomposite scaffolds for bone tissue engineering. *International Journal of Biological Macromolecules*, 93, pp.1354–1365. Available at:

<http://www.sciencedirect.com/science/article/pii/S0141813016301155>.

Scaffaro, R. et al., 2016. Preparation of three-layered porous PLA/PEG scaffold: Relationship between morphology, mechanical behavior and cell permeability. *Journal of the Mechanical Behavior of Biomedical Materials*.

Schaefer, D., Martin, I., Jundt, G., et al., 2002. Tissue-engineered composites for the repair of large osteochondral defects. *Arthritis & Rheumatism*, 46(9), pp.2524–2534. Available at: <http://dx.doi.org/10.1002/art.10493>.

Schaefer, D., Martin, I., Jundt, G., et al., 2002. Tissue-engineered composites for the repair of large osteochondral defects. *Arthritis and Rheumatism*.

Scotti, C. et al., 2010. Engineering human cell-based, functionally integrated osteochondral grafts by biological bonding of engineered cartilage tissues to bony scaffolds. *Biomaterials*, 31(8), pp.2252–2259. Available at: <http://www.sciencedirect.com/science/article/pii/S0142961209013544>.

Seol, Y.-J. et al., 2004. Chitosan sponges as tissue engineering scaffolds for bone formation. *Biotechnology Letters*, 26(13), pp.1037–1041. Available at: <https://doi.org/10.1023/B:BILE.0000032962.79531.f0>.

Serra, J. et al., 2003. FTIR and XPS studies of bioactive silica based glasses. *Journal of Non-Crystalline Solids*, 332(1), pp.20–27. Available at: <http://www.sciencedirect.com/science/article/pii/S0022309303006860> [Accessed May 31, 2017].

Serra, T. et al., 2014. Relevance of PEG in PLA-based blends for tissue engineering 3D-printed scaffolds. *Materials Science and Engineering C*.

Serra, T., Planell, J.A. & Navarro, M., 2013. High-resolution PLA-based composite scaffolds via 3-D printing technology. *Acta Biomaterialia*.

- Sheikh, Z. et al., 2015. Biodegradable materials for bone repair and tissue engineering applications. *Materials*.
- Sherwood, J.K. et al., 2002. A three-dimensional osteochondral composite scaffold for articular cartilage repair. *Biomaterials*, 23(24), pp.4739–4751.
- Shi, X. et al., 2007. In vitro cytotoxicity of single-walled carbon nanotube/biodegradable polymer nanocomposites. *Journal of Biomedical Materials Research Part A*, 86A(3), pp.813–823. Available at: <https://onlinelibrary.wiley.com/doi/abs/10.1002/jbm.a.31671>.
- Shirazi, S. et al., 2015. A review on powder-based additive manufacturing for tissue engineering: selective laser sintering and inkjet 3D printing. *Science and Technology of Advanced Materials*, 16(3), p.033502. Available at: <http://www.tandfonline.com/doi/full/10.1088/1468-6996/16/3/033502>.
- Shirazi, S.F.S. et al., 2015. A review on powder-based additive manufacturing for tissue engineering: selective laser sintering and inkjet 3D printing. *Science and Technology of Advanced Materials*, 16(3), p.33502. Available at: <http://stacks.iop.org/1468-6996/16/i=3/a=033502>.
- Siligardi, C., D'Arrigo, M.C. & Leoneli, C., 2000. Sintering behavior of glass-ceramic frits. *American Ceramic Society bulletin*, 79(9), pp.88–92. Available at: <http://cat.inist.fr/?aModele=afficheN&cpsidt=1479643> [Accessed June 28, 2017].
- Solvay, 2010. Ultrasonic welding. *Technical bulletin*, pp.1–4. Available at: https://www.solvay.com/en/binaries/Ultrasonic-Welding_EN-199453.pdf.
- Spierings, A.B. et al., 2016. Powder flowability characterisation methodology for powder-bed-based metal additive manufacturing. *Progress in Additive Manufacturing*, 1(1), pp.9–20. Available at: <http://dx.doi.org/10.1007/s40964-015-0001-4>.
- St-Pierre, J.P. et al., 2012. The incorporation of a zone of calcified cartilage improves the interfacial shear strength between in vitro-formed cartilage and the underlying substrate. *Acta Biomaterialia*.
- Steuben, J., Van Bossuyt, D.L. & Turner, C., 2015. Design for Fused Filament Fabrication Additive Manufacturing. In *Volume 4: 20th Design for Manufacturing and the Life Cycle Conference; 9th International Conference on Micro- and Nanosystems*.

- Van Der Stok, J. et al., 2013. Selective laser melting-produced porous titanium scaffolds regenerate bone in critical size cortical bone defects. *Journal of Orthopaedic Research*, 31(5), pp.792–799.
- Sun, C. et al., 2017. Effect of particle size gradation on the performance of glass-ceramic 3D printing process. *Ceramics International*, 43(1), pp.578–584. Available at: <http://linkinghub.elsevier.com/retrieve/pii/S027288421631728X> [Accessed July 30, 2017].
- Taboas, J.M. et al., 2003. Indirect solid free form fabrication of local and global porous, biomimetic and composite 3D polymer-ceramic scaffolds. *Biomaterials*.
- Tcacencu, I. et al., 2018. Osseointegration of porous apatite-wollastonite and poly(lactic acid) composite structures created using 3D printing techniques. *Materials Science and Engineering: C*, 90, pp.1–7. Available at: <https://www.sciencedirect.com/science/article/pii/S0928493117326590?via%3Dihub> [Accessed May 9, 2018].
- Teramoto, H. et al., 2005. Resorption of Apatite-wollastonite containing glass-ceramic and β -tricalcium phosphate in vivo. *Acta Medica Okayama*.
- Thavornnyutikarn, B. et al., 2014. Bone tissue engineering scaffolding: computer-aided scaffolding techniques. *Progress in Biomaterials*.
- Troughton, M.J., 2008. *Handbook of Plastics Joining: A Practical Guide*,
- Utela, B. et al., 2008. A review of process development steps for new material systems in three dimensional printing (3DP). *Journal of Manufacturing Processes*, 10(2), pp.96–104.
- Varghese, S. & Elisseeff, J.H., 2006. Hydrogels for Musculoskeletal Tissue Engineering. In C. Werner, ed. *Polymers for Regenerative Medicine*. Berlin, Heidelberg: Springer Berlin Heidelberg, pp. 95–144. Available at: https://doi.org/10.1007/12_072.
- Wakitani, S. et al., 1994. Mesenchymal cell-based repair of large, full-thickness defects of articular cartilage. *J Bone Joint Surg Am.*, 76(4), pp.579–92.
- Wang, M. & Wang, M., 2006. Composite Scaffolds for Bone Tissue Engineering. *American*

- Wang, W. & Zhou, W., 2013. Water Adsorption and Glass Transition of Spray-Dried Soy Sauce Powders Using Maltodextrins as Carrier. *Food and Bioprocess Technology*, 6(10), pp.2791–2799. Available at: <https://doi.org/10.1007/s11947-012-0992-5>.
- Wegst, U.G.K. et al., 2014. Bioinspired structural materials. *Nature Materials*, 14(1), pp.23–36. Available at: <http://www.nature.com/doifinder/10.1038/nmat4089>.
- Weinand, C. et al., 2006. Hydrogel- β -TCP scaffolds and stem cells for tissue engineering bone. *Bone*, 38(4), pp.555–563. Available at: <http://www.sciencedirect.com/science/article/pii/S8756328205004114>.
- Wu, L. & Ding, J., 2005. Effects of porosity and pore size on in vitro degradation of three-dimensional porous poly(D,L-lactide-co-glycolide) scaffolds for tissue engineering. *Journal of Biomedical Materials Research Part A*, 75A(4), pp.767–777. Available at: <http://dx.doi.org/10.1002/jbm.a.30487>.
- Wu, S. et al., 2014. Biomimetic porous scaffolds for bone tissue engineering. *Materials Science and Engineering R*.
- Xiao, K. et al., 2008. Indirect selective laser sintering of apatite—wollastonite glass—ceramic. *Proceedings of the Institution of Mechanical Engineers, Part H: Journal of Engineering in Medicine*, 222(7), pp.1107–1114. Available at: <http://dx.doi.org/10.1243/09544119JEIM411>.
- Xiong, Z. et al., 2001. Fabrication of porous poly(L-lactic acid) scaffolds for bone tissue engineering via precise extrusion. *Scripta Materialia*.
- Xiong, Z., 2002. Fabrication of porous scaffolds for bone tissue engineering via low-temperature deposition. *Scripta Materialia*.
- Yaszemski, M.J. et al., 1996. Evolution of bone transplantation: Molecular, cellular and tissue strategies to engineer human bone. *Biomaterials*, 17(2), pp.175–185.
- Yen, H.J. et al., 2009. Evaluation of chondrocyte growth in the highly porous scaffolds made by fused deposition manufacturing (FDM) filled with type II collagen. *Biomedical Microdevices*.

- Younger, E.M. & Chapman, M.W., 1989. Morbidity at bone graft donor sites. *Journal of orthopaedic trauma*, 3(3), pp.192–195.
- Zein, I. et al., 2002. Fused deposition modeling of novel scaffold architectures for tissue engineering applications. *Biomaterials*, 23(4), pp.1169–1185. Available at: <http://www.sciencedirect.com/science/article/pii/S0142961201002320>.
- Zhang, G. et al., 2011. Ultrasonic weld properties of heterogeneous polymers: Polylactide and poly (methyl methacrylate). *Journal of Materials Processing Technology*.
- Zhang, R. & Ma, P., 2000. Synthetic nano-fibrillar extracellular matrices with predesigned macroporous architectures. *J Biomed Mater Res*, 52(2), pp.430–8.
- Zhou, Z. et al., 2017. Effects of poly (ϵ -caprolactone) coating on the properties of three-dimensional printed porous structures. *Journal of the Mechanical Behavior of Biomedical Materials*, 70, pp.68–83. Available at: <http://dx.doi.org/10.1016/j.jmbbm.2016.04.035>.

Appendix

Appendix A. Academic Contribution

Honours and Awards

- **May 2015:** Best Presentation Postgraduate Research Conference 2015 entitled “Manufacture and Assembly of Biopolymer-bioceramic hybrid composites” In: School of Mechanical and Systems Engineering, Newcastle University, UK
- **September 2014:** The CIRP-UK Best Presentation Award 2014 entitled “Materials Processing for the Manufacture of Hybrid Biopolymer-Bioceramic Medical Devices at the Point of Need” The International Academy for Production Engineering, In: EPSRC Manufacturing the Future conference 2014, Glasgow, Scotland, UK
- **May 2014:** Best Presentation Postgraduate Research Conference 2014 entitled “Manufacture and Characterisation of Porous PLA scaffolds” In: School of Mechanical and Systems Engineering, Newcastle University, UK
o October 2013: Ph.D. student grant provided by EPSRC Mede Innovation in medical to develop in clinic manufacturing approaches for large osteochondral defects.

Research Outreach

Publications:

- Rodrigues N, Benning M, Ferreira AM, Dixon L, Dalgarno K. Manufacture and Characterisation of Porous PLA Scaffolds. *Procedia CIRP* 2016, 49: 33-38 Doi: <http://dx.doi.org/10.1016/j.procir.2015.07.025>
- Tcacencu I., Rodrigues N., Alharbi N., Benning M., Toumpaniari S., Mancuso E. Osseointegration of porous apatite-wollastonite and poly(lactic acid) composite structures created using 3D printing techniques. *Materials Science and Engineering: C* 2018, 90:1-7 Doi: [10.1016/J.MSEC.2018.04.022](https://doi.org/10.1016/J.MSEC.2018.04.022)

My research has led to several oral presentations (personally presented) at international conferences and 4 oral presentations as invited speaker.

Selected communication in international meetings (oral presentation by the candidate)

[1] N. Rodrigues, J. Munguia. M. Benning, N. Alharbi, K. Dalgarno. Hybrid Biopolymer-Bioceramic Composite for Bone and Joint Repair. In: European Materials Research Society (E-MRS, fall meeting), Poland, September 15-18th 2014.

[2] N. Rodrigues, J. Munguia. M. Benning, N.Alharbi, K. Dalgarno. Materials Processing for the Manufacture of Hybrid Biopolymer-Bioceramic Medical Devices at the Point of Need. In: 3rd EPSRC Manufacturing the Future, Glasgow, Scotland September 23rd-24th 2014.

[3] N. Rodrigues, J. Munguia. M. Benning, N.Alharbi, K. Dalgarno. In-Clinic Manufacture of Hybrid Biopolymer-Bioceramic Medical Devices. In: The International Symposium on Frontiers In Biomedical Polymers, Trento, Italy July 8th-11th 2015.

[4] N. Rodrigues, J. Munguia. M. Benning, AM. Duarte, L. Dixon, K. Dalgarno. Manufacture and characterisation of porous PLA scaffolds. In: The Second CIRP Conference on Bio Manufacturing, Manchester, UK, July 29th -31st 2015.

Invited speaker

[1] N. Rodrigues, J. Munguia. M. Benning, K. Dalgarno. Manufacture and Assembly of Biopolymer Bioceramic Hybrid Composites . In: "MeDe Annual Conference", Newcastle-Upon-Tyne, UK January 28th, 2016.

[2] N. Rodrigues, J. Munguia. M. Benning, AM. Duarte, L. Dixon, K. Dalgarno. Manufacture and characterisation of porous PLA scaffolds. In: "MeDe Innovation Guest Lecture Series #2" Seminar, Leeds, UK September 30th, 2015.

[3] N. Rodrigues, M. Benning, S. Partridge, K. Dalgarno. MeDe Research Challenge 2: Manufacturing at the point of need. In: 1st MeDe ECR Workshop at the University of Bradford, UK, May 11th, 2015.

[4] N. Rodrigues, J. Munguia. M. Benning, K. Dalgarno. Manufacture of Hybrid Composites Structures at the Point of Need. In: New Strategies for Treating MSK Disorders: In-clinic Manufacture & Minimally Invasive Implantation of Material (research workshop) , Newcastle, UK October 30th ,2014.